

Methane-Concentrated Oxy-Fuel Calciner for Calcium-Looping

by

Arian Ebneyamini

B.Sc., Isfahan University of Technology, 2015

M.A.Sc., University of Ottawa, 2017

A THESIS SUBMITTED IN PARTIAL FULFILLMENT OF THE
REQUIREMENTS FOR THE DEGREE OF

DOCTOR OF PHILOSOPHY

in

The Faculty of Graduate and Postdoctoral Studies
(Chemical and Biological Engineering)

THE UNIVERSITY OF BRITISH COLUMBIA

(Vancouver)

August 2020

© Arian Ebneyamini, 2020

The following individuals certify that they have read, and recommend to the Faculty of Graduate and Postdoctoral Studies for acceptance, a dissertation entitled:

Methane-Concentrated Oxy-Fuel Calciner for Calcium-Looping

submitted by Arian Ebneyamini in partial fulfillment of the requirements for
the degree of Doctor of Philosophy
In Chemical and Biological Engineering

Examining Committee

Dr. John R. Grace, Chemical and Biological Engineering

Co-Supervisor

Dr. Naoko Ellis, Chemical and Biological Engineering

Co-Supervisor

Dr. C. Jim Lim, Chemical and Biological Engineering

Co-Supervisor

Dr. Cigdem Eskicioglu, Civil Engineering

University Examiner

Dr. Anthony Wachs, Chemical and Biological Engineering

University Examiner

Additional Supervisory Committee Members:

Dr. Fariborz Taghipour, Chemical and Biological Engineering

Supervisory Committee Member

Dr. Andres Mahecha-Botero, Senior Process Engineer in NORAM Ltd.

Supervisory Committee Member

Abstract

Greenhouse gas emissions (mostly CO₂) have resulted from massive fuel consumption over recent decades, with devastating effects on humans, climate, and wildlife. Cost-effective environmentally-friendly energy sources and carbon capture are required to diminish the destructive effects of CO₂ emissions. Calcium-looping, a process based on reversible solid-gas carbonation and calcination, utilizing lime-based sorbents to capture CO₂ at elevated temperatures, is an emerging carbon capture technology, also applicable for enhanced hydrogen production. A key challenge in this continuous process is the high temperature needed for cyclical sorbent regeneration (*via* limestone calcination). This adversely affects the thermal/energy efficiency of the process, while also leading to sorbent deactivation during first calcination-carbonation cycles. Investigations are required to enhance current knowledge on limestone calcination conditions in calcium-looping, while also identifying alternative low-temperature technologies for sorbent regeneration.

This thesis proposes a novel methane-concentrated oxy-fuel calciner, combining methane combustion, reforming and limestone calcination in a single reactor. The process is shown to be capable of autothermal syngas-producing sorbent regeneration with *in situ* CO₂ utilization, reducing the CO₂ concentration within the reactor, thereby decreasing the calcination temperature. The thermodynamic and kinetic performances of the process are evaluated by means of reactor simulations. Appropriate ranges of conditions are determined for autothermal, coke-free and complete limestone calcination. Increasing temperature and nitrogen concentration in air are shown to enhance limestone calcination, whereas elevating pressure and CaCO₃/gas feed ratio hinder sorbent conversion. A design methodology is suggested to determine appropriate operating conditions and/or reactor dimensions for this sorbent regeneration technology. Potential practical constraints of the process (e.g. safe operation and catalyst instability) are also briefly discussed. The thesis examines three potential applications of the process: sorbent-enhanced steam methane reforming, ammonia production without air separation, and Ca(OH)₂/CaCO₃ co-calcination. Thermogravimetric analysis is employed to assess the effect of sorbent regeneration conditions (especially partial calcination) on the cyclic CO₂ capture capability of lime-based sorbents. Increasing calcination temperature is shown to

reduce sorbent reactivity, while extending calcination duration and exposing limestone to high temperature without reaction did not appreciably change sorbent performance. Partially calcined sorbents are found to offer smoother CO₂ uptake over extended calcination-carbonation cycles.

Lay Summary

My work focused on the regeneration of lime-based sorbents for CO₂ capture. A novel technology is introduced, capable of autothermal synthesis-gas-producing sorbent regeneration at relatively mild temperatures. The proposed process also benefits from CO₂ utilization, reducing greenhouse gas emissions.

Preface

At the time of writing this thesis, three articles have been published, two others have been accepted and are awaiting publication, and two others are under preparation. In addition, the author is scheduled to give research talks at two international conferences in the future.

The author proposed the idea of methane-concentrated oxy-fuel calcination, carried out all stages of the research described in the published and submitted papers, prepared responses to the reviewers, and handled correspondence with the journal editors. The co-authors supervised the work and made appropriate revisions.

The author proposed studying the effect of partial limestone calcination on the carbon capture capability of lime-based sorbents, and conducted most of the thermogravimetric analysis tests. Two fellow students, John Zezhong Li and Jun Young Kim, helped in carrying out experiments and analyzing the results. The author prepared the first draft of the paper, which was slightly modified by these two students. The other co-authors supervised the work and made required revisions on the manuscript.

The author proposed writing a review paper on the limestone calcination, and managed the work load distribution between four participating students. The paper is currently under preparation, and will be submitted to an appropriate peer-reviewed journal. Part of this future paper, solely written by the author, is presented in Chapter 1 of this thesis.

Below is the list of journal publications, corresponding to the chapters of this thesis:

CHAPTER 1

- **A. Ebneyamini**, Z.J. Li , B.L. Cheng, J.Y. Kim, J.R. Grace, C.J. Lim, N. Ellis, Limestone Calcination Review, Under Preparation.

CHAPTER 2

- **A. Ebneyamini**, Z.J. Li, J.R. Grace, J.Y. Kim, C.J. Lim, N. Ellis, Effects of calcination temperature and extent on the CO₂ carrying capacity of lime-based sorbents, Under Preparation.

CHAPTER 3

- **A. Ebneyamini**, B.L. Cheng, J.Y. Kim, Z.J. Li, J.R. Grace, C.J. Lim, N. Ellis, Equilibrium analysis of the pressurized sorbent regeneration using combined methane reforming, combustion and calcination process, accepted for presentation and inclusion in the proceeding of the “13th International Conference in Fluidized Bed Technology”, Vancouver (2021).
- **A. Ebneyamini**, J.R. Grace, C.J. Lim, N. Ellis, S.S.E.H. Elnashaie, Simulation of limestone calcination for calcium looping: Potential for autothermal and hydrogen-producing sorbent regeneration, “*Industrial Engineering Chemistry Research*” 58 (2019) 8636–8655. <https://doi.org/10.1021/acs.iecr.9b00668>.
- **A. Ebneyamini**, J.R. Grace, C.J. Lim, N. Ellis, S.S.E.H. Elnashaie, A. Mahecha-Botero, Simulation of autothermal hydrogen-producing limestone calcination for calcium looping in turbulent fluidized bed reactors, “*Chemical Engineering Science*” 212 (2020) 115353. <https://doi.org/https://doi.org/10.1016/j.ces.2019.115353>.

CHAPTER 4

- **A. Ebneyamini**, J. Grace, N. Ellis, C.J. Lim, Toward autothermal and hydrogen-producing sorbent regeneration for calcium-looping, accepted for publication in March, 2020 in “*Canadian Journal of Chemical Engineering*”, <https://doi.org/10.1002/cjce.23847>.

CHAPTER 5

- **A. Ebneyamini**, J. Grace, N. Ellis, C.J. Lim, Simulation of sorbent-enhanced steam methane reforming and limestone calcination in dual turbulent fluidized bed reactors, “*Energy and Fuels*”. <https://doi.org/10.1021/acs.energyfuels.0c01093>

CHAPTER 6

- **A. Ebneyamini**, J.Y. Kim, Z.J. Li, J. Grace, N. Ellis, C.J. Lim, Sorbent steam reactivation and methane-concentrated calcination for calcium-looping carbon capture: Compatibilities and limitations, “*Journal of Industrial and Engineering Chemistry*” 87 (2020) 40-45. <https://doi.org/10.1016/j.jiec.2020.03.012>

CHAPTER 7

- **A. Ebneyamini**, Z.J. Li, J.Y. Kim, J. Grace, N. Ellis, C.J. Lim, Co-production of lime and syngas for ammonia synthesis without air separation, submitted.

Table of Contents

Abstract.....	iii
Lay Summary	v
Preface.....	vi
Table of Contents	ix
List of Tables	xv
List of Figures.....	xvii
Nomenclature	xxvi
Abbreviations	xxxii
Acknowledgments	xxxiii
Dedication	xxxiv
CHAPTER 1: Background	1
1.1. Energy Demand and Climate Change	1
1.2. Hydrogen.....	2
1.3. Steam Methane Reforming.....	3
1.4. Membrane-Assisted Steam Methane Reforming	5
1.5. Sorbent-Enhanced Steam Methane Reforming	5
1.6. Limestone Calcination.....	8
1.6.1. Background.....	8

1.6.2.	<i>Gaseous Media for Limestone Calcination</i>	10
1.6.2.1.	<i>Inert and Oxidant Gases</i>	10
1.6.2.2.	<i>CO₂</i>	13
1.6.2.3.	<i>Steam</i>	13
1.6.2.4.	<i>CO₂-Utilizing Media</i>	15
1.6.2.5.	<i>Oxy-Fuel Calciners</i>	19
1.7.	Thesis Scope and Objectives.....	23
CHAPTER 2: Effects of Calcination Temperature and Extent on CO₂ Carrying Capacity of Lime-Based Sorbents		26
2.1.	Introduction	26
2.2.	Experimental Details	27
2.3.	Results and Discussion.....	31
2.3.1	<i>Effect of Calcination-Carbonation Cycling</i>	31
2.3.2	<i>Effect of Calcination Temperature</i>	36
2.3.3	<i>Effect of Calcination Duration</i>	37
2.3.4	<i>Cyclic Sorbent Utilization in Equation Form</i>	42
2.4.	Conclusion.....	50
CHAPTER 3: Combined Methane Reforming, Combustion and Limestone Calcination – Thermodynamic Analysis		52
3.1.	Introduction	52

3.2.	Aspen Plus Simulation Setup	54
3.3.	Results and Discussion.....	56
3.3.1.	<i>Preliminary Performance Analysis</i>	56
3.3.2.	<i>Correlation for Autothermal MRC-CAL Operation</i>	59
3.3.3.	<i>Critical Limits of MRC-CAL Process</i>	61
3.3.4.	<i>Performance Analysis for Isothermal Operation</i>	65
3.3.5.	<i>Performance Analysis for Adiabatic Operation</i>	68
3.4.	Conclusion.....	70
CHAPTER 4: Simulation of Combined Methane Reforming, Combustion and Limestone Calcination in Turbulent Fluidized Bed Reactors		71
4.1.	Introduction	71
4.2.	Simulation Setup	73
4.3.	Results and Discussion.....	80
4.3.1.	<i>Simulation Results in Base Inputs</i>	80
4.3.2.	<i>Effect of Operating Temperature and Pressure</i>	81
4.3.3.	<i>Effect of CaCO₃/Total Gas Molar Feed Ratio</i>	86
4.3.4.	<i>Effect of Sorbent Residence Time</i>	89
4.3.5.	<i>Design Methodology</i>	90
4.4.	Conclusion.....	96

CHAPTER 5: Simulation of Sorbent-Enhanced Steam Methane Reforming and Limestone Calcination in Dual Turbulent Fluidized Bed Reactors 98

5. 1.	Introduction	98
5. 2.	Simulation Setup	100
5. 3.	Results and Discussion.....	103
5.3.1.	<i>Hydrodynamic, Base Input Data and Performance Metrics</i>	103
5.3.2.	<i>Simulation Results for Base Input Data</i>	105
5.3.3.	<i>Effects of Operating Temperature and Pressure</i>	106
5.3.4.	<i>Effect of Gaseous Feed Concentration</i>	108
5.3.5.	<i>Effect of CaO/Methane Feed Ratio</i>	110
5.3.6.	<i>Effect of Membrane Implementation</i>	113
5.3.7.	<i>Selection of the SE-SMR Operating Conditions</i>	116
5.3.8.	<i>Design of Sorbent Regenerator</i>	119
5. 4.	Conclusion.....	125

CHAPTER 6: Sorbent Steam Reactivation and Methane-Concentrated Calcination for Calcium-Looping Carbon Capture: Compatibilities and Limitations 127

6.1.	Introduction	127
6.2.	Simulation Setup	129
6.3.	Results and Discussion.....	130
6.3.1.	<i>Sorbent Hydrator</i>	130

6.3.2.	<i>MRC-CAL Sorbent Regeneration</i>	131
6.4.	Conclusions	136
CHAPTER 7:	Co-Production of Lime and Syngas for Ammonia Synthesis without Air Separation	137
7.1.	Introduction	137
7.2.	Correlation Development and Performance Metrics.....	140
7.3.	Simulation Setup	141
7.3.1.	<i>Thermodynamics Simulation</i>	141
7.3.2.	<i>Kinetic Simulation</i>	143
7.4.	Results and Discussion.....	144
7.4.1.	<i>Performance Analysis under Thermodynamic Equilibrium</i>	144
7.4.2.	<i>Kinetic Performance Analysis in Turbulent Fluidized Bed Reactors</i>	151
7.5.	Conclusions	155
CHAPTER 8:	Conclusions and Recommendations	156
8.1.	Conclusions	157
8.2.	Recommendations	161
Bibliography		167
Appendices		187
Appendix A:	Effect of Heating Rate on Cyclic CO ₂ Capture of Lime-Based Sorbents.....	187

Appendix B: Effect of Steam Reactivation on Cyclic CO ₂ Capture of Lime-Based Sorbents.....	188
Appendix C: Sensitivity Analysis of ADPFR Reactor Model.....	190
Appendix D: Supplementary Results for SE-SMR/Calciner Simulation.....	192
Appendix E: General Comparison and Suggested Range of Operating Conditions for MRC-CAL Process	194

List of Tables

Table 1.1. Main reactions in steam methane reforming [17]	3
Table 1.2. Reversible lime carbonation and limestone calcination reactions	6
Table 1.3. Main reactions involved in CaL-CLC process with Cu-based oxygen carrier	12
Table 1.4. Main reactions involved in calcination in methane	17
Table 1.5. Main reactions involved in calcination in ethanol/glycerol.....	18
Table 2.1. XRD measurement results for different limestones.....	28
Table 2.2. Summary of experimental conditions tested. (Measurement accuracy = +/- 5°C).....	30
Table 3.1. Stream properties for Aspen Plus simulations.....	55
Table 3.2. Block properties in Aspen Plus simulations	56
Table 4.1. Governing equations for kinetic simulations	75
Table 4.2. Reactions considered in kinetic simulations	75
Table 4.3. Rate parameters for reactions considered in kinetic simulations.....	76
Table 4.4. Correlations and supporting equations applied in kinetics simulations.....	76
Table 4.5. Metrics for evaluating the MRC-CAL performance.....	80
Table 4.6. Base inputs for kinetics simulations	80
Table 4.7. MRC-CAL design methodology.....	92
Table 5.1. Effects of operating conditions on the reactions involved in the SE-SMR process	99
Table 5.2. Governing equations for kinetic simulations	101
Table 5.3. Correlations and supporting equation applied for kinetics simulations.....	102
Table 5.4. Rate expressions for lime carbonation and hydrogen permeation.....	102
Table 5.5. Base input data and ranges considered in kinetic simulations.....	104

Table 5.6. Metrics applied for SE-SMR performance evaluation	105
Table 5.7. Simulated SE-SMR performance at selected operating conditions	119
Table 5.8. Performance of MRC-CAL and steam calciner for dual FBR's.....	122
Table 7.1. Metrics applied for SE-SMR performance evaluation	141
Table 7.2. Base inputs for kinetics simulations	144
Table D.1. Summary of Aspen Plus and kinetic simulation results for reformers	192
Table D.2. Summary of Aspen Plus and kinetic simulation results for calciners.....	193
Table E.1. Suggested range of operating conditions for oxy/air-fuel MRC-CAL processes	194

List of Figures

Figure 1.1. World primary energy supply by source, 1990-2017. Data adopted from [5]	1
Figure 1.2. Global demand for hydrogen, 1975-2015. Data adopted from [13].....	2
Figure 1.3. Hydrogen production by a conventional steam methane reforming plant	4
Figure 1.4. Schematic of the SE-SMR process in dual fluidized bed reactors	7
Figure 1.5. Thermodynamic equilibrium of CaO/CaCO ₃	7
Figure 1.6. Main criteria for limestone calciners	9
Figure 1.7. Limestone calcination in helium with solar-concentrated power.....	11
Figure 1.8. CaL-CLC process with Cu-based oxygen carrier [72]	12
Figure 1.9. Schematic of calcination in methane	17
Figure 1.10. Schematic of coal-based power plant with post-combustion CaL carbon capture...	21
Figure 2.1. Reproducibility of the cyclic thermogravimetric analysis results. For test conditions, see run 3 in Table 2.2. Red points are the average sorbent utilization achieved by three-time repetition of the cyclic TGA test. Blue error bars show plus and minus the calculated standard deviation at each calcination-carbonation cycle.	31
Figure 2.2. Typical sorbent conversion and temperature profile during cyclic calcination-carbonation tests. Stars show the fast-stage carbonation extent in each cycle. For test conditions, see run 3 in Table 2.2.....	32
Figure 2.3. Normalized (a) calcination; and (b) carbonation profiles at different calcination-carbonation cycles. For test conditions, see run 3 in Table 2.2.	34
Figure 2.4. CaCO ₃ molar fraction time variation during limestone calcination after different numbers of calcination-carbonation cycles. For test conditions, see run 3 in Table 2.2.	34

Figure 2.5. Normalized (a) calcination; and (b) carbonation rate profiles with different calcination-carbonation cycles. For test conditions, see run 3 in Table 2.2. 35

Figure 2.6. Effect of calcination temperature on: (a) cyclic sorbent (Strassburg) utilization; and (b) first-cycle calcination rate. Test conditions correspond to runs 1-5 in Table 2.2. Every third experimental data points is plotted in (a) for clearer presentation of the data. 37

Figure 2.7. Effects of calcination temperature and duration on the cyclic performance of Strassburg sorbents. For test conditions, see runs 1, 3 and 5-9 in Table 2.2. 38

Figure 2.8. Effect of partial calcination on cyclic: (a) carbonation; and (b) calcination extents. For test conditions see runs 1 and 6 in Table 2.2. Every third experimental data point is plotted for better viewing. 39

Figure 2.9. Effect of CO₂ pre-treatment on the cyclic performance of Strassburg sorbent. For test conditions, see runs 8 and 10 in Table 2.2. 40

Figure 2.10. Effect of partial and total calcination on: (a) single-cycle; and (b) cumulative CO₂ capture capacity of Strassburg sorbent. For test conditions see runs 1 and 6 in Table 2.2. Every third experimental data point is plotted for better viewing. 42

Figure 2.11. Arrhenius-type fitting of surface reduction constants (k) at different calcination temperatures. 44

Figure 2.12. Comparison of experimental data for totally calcined Strassburg sorbents with predictions of Equations (2.6) and (2.7) at different calcination temperatures. Every third experimental data point is plotted to give clearer plots. 44

Figure 2.13. Comparison of experimental data with the predictions of Equations (2.6)-(2.8) for run 6. Every third experimental data point is plotted for clearer presentation. 46

Figure 2.14. Comparison of experimental data and Equation (2.8) predictions for cyclic tests with periodically changing calcination duration during cycling (test conditions: (a) runs 11 and 13 (b) run 12 in Table 2.2). Every second experimental data point is plotted for better clarity.	47
Figure 2.15. (a) Effect of carbonation temperature on the Strassburg sorbent cyclic performance; (b) Comparison of method predictions and experimental results for partial calcination during isothermal cycling (test conditions: (a) runs 3 and 14; (b) run 15 in Table 2.2).	49
Figure 2.16. (a) Comparing cyclic performance of Strassburg and Cadomin limestones; (b) Comparing predictions and experimental results for partial calcination during isothermal cycling of Cadomin Limestone. (Test conditions: (a) runs 14 and 16; (b) run 17 in Table 2.2.).....	50
Figure 3.1. Reactions involved in the MRC-CAL process	53
Figure 3.2. Aspen Plus process flow sheet for simulating the MRC-CAL process. Block and stream properties are listed below in Tables 3.1 and 3.2.....	55
Figure 3.3. (a)–(e) Effect of temperature and feed concentration on MRC-CAL heat duty and sorbent conversion; (f) Effect of temperature on MRC-CAL off-gas H ₂ and CO concentration. (All results are for atmospheric pressure and CaCO ₃ /total gas molar feed ratio of 0.5. Panel (f) is for a methane-to-air feed ratio of 1.21.).....	58
Figure 3.4. Effect of methane feed concentration on MRC-CAL heat duty at different CaCO ₃ /gas feed ratios and at: (a) 800°C; (b) 850°C.	59
Figure 3.5. Required CH ₄ /Enriched-air molar feed ratio for autothermal MRC-CAL at 1-5 bars and 800-900°C (Maximum error of ± 0.4%)	60
Figure 3.6. MRC-CAL critical limits for atmospheric reactor operation. (Zone 1: endothermic/incomplete sorbent regeneration zone; zone 2: potential autothermal, coke-free, and complete calcination zone; zone 3: carbon generating zone).	64

Figure 3.7. MRC-CAL critical limits at high reactor pressures.....	65
Figure 3.8. Effect of operating pressure on: (a) sorbent conversion; and (b) MRC-CAL heat duty at fixed temperature of 850°C and different CaCO ₃ /total gas molar feed ratios.	66
Figure 3.9. Effect of operating pressure at fixed reactor temperature of 850°C and different CaCO ₃ /total gas molar feed ratios on the MRC-CAL: (a) CH ₄ conversion; (b) H ₂ yield.	67
Figure 3.10. Adiabatic and isothermal performance of MRC-CAL at different reactor pressures: (a) $\alpha=0.7$ and (b) $\alpha=0.9$. (Feed temperature = 850°C).....	69
Figure 3.11. Sankey diagram of MRC-CAL process.....	69
Figure 4.1. Schematic of MRC-CAL reactor model in turbulent fluidized bed reactors.....	74
Figure 4.2. Simulation algorithm for kinetic simulation.....	79
Figure 4.3. Simulated gases axial flow profiles at base input data in Table 4.6.....	81
Figure 4.4. Effects of temperature and pressure on sorbent conversion in: (a) MRC-CAL process; and (b) STEAM-CAL units. Other input data are identical to those in Table 4.6.....	82
Figure 4.5. Determination of “critical conversion” at reactor pressure of 3 bars: (a) CaCO ₃ /total gas molar feed ratio (α) = 0.5; and (b) reactor temperature of 850°C. Other input data are identical to those in Table 4.6.....	84
Figure 4.6. Effect of operating pressure on the “critical conversion” at: (a) CaCO ₃ /total gas molar feed ratio (α) = 0.5; and (b) reactor temperature of 850°C. Other input data are identical to those in Table 4.6.....	84
Figure 4.7. Effects of operating temperature and pressure on the MRC-CAL for: (a) methane conversion; and (b) hydrogen yield. Other input data are identical to those in Table 4.6.....	86

Figure 4.8. Effects of CaCO ₃ /total gas molar feed ratio and reactor pressure on the sorbent conversion in: (a) MRC-CAL; and (b) STEAM-CAL units. Other input data are identical to those in Table 4.6	87
Figure 4.9. Effects of CaCO ₃ /total gas molar feed ratio and reactor pressure on MRC-CAL: (a) methane conversion; (b) hydrogen yield. Other input data are identical to those in Table 4.6 ...	89
Figure 4.10. Effects of sorbent residence time and reactor pressure on: (a) sorbent conversion in MRC-CAL; and (b) reactor length. Other input data are identical to those in Table 4.6	90
Figure 4.11. (a) MRC-CAL graph for determination of design parameters at 1.1 bars; (b) MRC-CAL reactor design steps ($\tau = 10$ min).	92
Figure 4.12. MRC-CAL graphs for determination of design parameters at: (a) 2 bars; (b) 3 bars; (c) 4 bars; and (d) 5 bars ($\tau = 10$ min.)	93
Figure 5.1. General schematic of integrated SE-SMR/MRC-CAL process in dual FBR's.....	100
Figure 5.2. Boundaries of turbulent fluidization regime: (a) gas superficial velocity; (b) gas inlet flow rate for a reactor diameter of 75 mm.	104
Figure 5.3. (a) Gas flow rate axial profiles in SE-SMR reactor; (b) Reformer performance metrics, as defined in Table 5.6, in the presence and absence of lime sorbents. Input data are identical to those in Table 5.5.	106
Figure 5.4. Effects of reactor temperature and pressure on conversion of: (a) methane; and (b) sorbent in SE-SMR reactor. The other input data are identical to those in Table 5.5.	107
Figure 5.5. Effects of reactor temperature and pressure on: (a) hydrogen yield; and (b) dry off-gas hydrogen molar fraction in SE-SMR reactor. The other input data are identical to those in Table 5.5.	108

Figure 5.6. Effects of steam/methane ratio and operating pressure on: (a) methane conversion; (b) sorbent conversion in SE-SMR reactor. The rest of the input data are identical to those in Table 5.5.	109
Figure 5.7. Effects of steam/methane and operating pressure on: (a) hydrogen yield; and (b) dry off-gas hydrogen molar fraction in SE-SMR reactor. The other input data are identical to those in Table 5.5.	110
Figure 5.8. Effects of CaO/methane molar feed ratio and operating pressure on: (a) methane conversion; and (b) sorbent conversion in the SE-SMR reactor. The other input data are identical to those in Table 5.5.....	112
Figure 5.9. Effects of CaO/methane and operating pressure on: (a) hydrogen yield; and (b) dry off-gas hydrogen molar fraction in SE-SMR reactor. Other input data are identical to those in Table 5.5.	113
Figure 5.10. Effect of membrane addition on conversion of: (a) methane; and (b) sorbent in MA-SE-SMR reactor. The other input data are identical to those in Table 5.5.	114
Figure 5.11. Variation of hydrogen recovery with number of membrane tubes and reactor pressure. Other input data are identical to those in Table 5.5.....	114
Figure 5.12. Effect of membranes on: (a) hydrogen yield; and (b) dry off-gas hydrogen molar fraction in MA-SE-SMR reactor. The other input data are identical to those in Table 5.5.....	115
Figure 5.13. Effect of steam/methane molar feed ratio on SE-SMR: (a) hydrogen yield and dry off-gas hydrogen molar fraction; (b) hydrogen production rate, with $P = 3$ bars, $T = 650^{\circ}\text{C}$, $F_{\text{CaO,in}} = 0.21 \text{ mol}\cdot\text{s}^{-1}$. Other input data are identical to those in Table 5.5.	118

Figure 5.14. Effect of steam/methane molar feed ratio on SE-SMR hydrogen production index ($P = 3$ bars, $T = 650^{\circ}\text{C}$, $F_{\text{CaO},\text{in}} = 0.21 \text{ mol.s}^{-1}$). Other input data are identical to those in Table 5.5.	119
Figure 5.15. MRC-CAL (a) design parameters [69]; and (b) critical limits [137] at 3 bars.....	121
Figure 5.16. (a) Hydrogen yield; and (b) CO_2 emission of the SMR and SE-SMR processes, integrated with MRC-CAL and STEAM-CAL units. Reformer and calciner operating conditions are identical to those in Tables 5.7 and 5.8, respectively.	125
Figure 6.1 Schematics of calcium looping with sorbent hydrator/reactivation: (a) Three-integrated-reactors calcium looping; (b) Sorbent hydrator with steam superheater; and (c) MRC-CAL for $\text{CaCO}_3/\text{Ca}(\text{OH})_2$ co-calcination.....	128
Figure 6.2. Effects of water/CaO molar feed ratio on the hydrator off-gas temperature at: (a) different solid feed temperatures and fixed reactor pressure of 1 bar; and (b) different pressures for a fixed solid feed temperature of 600°C	131
Figure 6.3. (a) Required gaseous feed composition for the autothermal MRC-CAL operation with unary solid feed; and (b) Comparison of the Aspen Plus simulation results and Equation (6.3) predictions.....	133
Figure 6.4. Critical α limits for (a) $\text{Ca}(\text{OH})_2$; and (b) CaCO_3 decomposition via MRC-CAL process.....	134
Figure 6.5. Effect of solid feed composition on the MRC-CAL: (a) critical operation limits; and (b) H_2 and CO production yields (Reactor Pressure: 3 bars, Operating Temperature 800°C , Solid/total gas molar feed ratio: 0.5 for panel (b), Gas feed composition calculated by Equation (6.4))......	136
Figure 7.1. General schematic of a conventional ammonia plant.....	138

Figure 7.2. Schematic of the proposed ammonia plant.....	139
Figure 7.3. Process flowsheet for the Aspen Plus simulation.....	142
Figure 7.4. Flow chart of the applied calculation procedure in Aspen Plus simulation	143
Figure 7.5. Variation of the MRC-CAL heat duty at (a) 900C, 15 bars, 21% O ₂ in air and different α^* (b) 900C, 21% O ₂ in air and different pressures and α^* (c) 15 bars, 21% O ₂ in air and different temperatures α^* (d) 900C, 15 bars and $\alpha^* = 0.5$ and different O ₂ level in air. Panels (b)-(d) are limited to complete and coke-free limestone calcination conditions.	145
Figure 7.6. Effects of reactor temperature and pressure on the: (a) upper; and (b) lower α^* limits for complete and coke-free limestone calcination (21% O ₂ in air).....	146
Figure 7.7. Effect of air oxygen concentration on the MRC-CAL critical α^* limits at 5 bars....	147
Figure 7.8. Effects of: (a) reactor pressure (at T=900°C); and (b) reactor temperature (at P=3 bars) on syngas yield of the air-fuel MRC-CAL process at different CaCO ₃ /CH ₄ molar feed ratios, for 21 vol% O ₂ in air.	148
Figure 7.9. Effects of: (a) reactor pressure; and (b) reactor temperature on syngas H ₂ /CO ratio of the air-fuel MRC-CAL process at different CaCO ₃ /CH ₄ molar feed ratios. Other operating conditions are identical to those in Figure 7.8.	149
Figure 7.10. Effects of: (a) reactor pressure; and (b) reactor temperature on syngas H ₂ /N ₂ of the air-fuel MRC-CAL process at different CaCO ₃ /CH ₄ molar feed ratios. Other operating conditions are identical to those in Figure 7.8.....	150
Figure 7.11. Effects of: (a) reactor pressure; and (b) reactor temperature on required air oxygen concentration to achieve the syngas quality for the Haber-Bosch process. Other operating conditions are identical to those in Figure 7.8.	151

Figure 7.12. Effects of reactor temperature and pressure on the sorbent conversion of the MRC-CAL process at air oxygen concentration of: (a) 21 vol%; and (b) 40 vol%. Other input data are identical to those in Table 7.2.	152
Figure 7.13. Effects of reactor temperature and pressure on the syngas H ₂ /N ₂ of the MRC-CAL process at air oxygen concentration of: (a) 21 vol%; and (b) 40 vol%. Other input data are identical to those in Table 7.2.	153
Figure A.1. Effect of heating rate on the cyclic carbon capture capability of lime-based sorbents. Other tests conditions are identical to that for run 3 in Chapter 2.	187
Figure B.1. Effects of: (a) hydration temperature; and (b) steam concentration on the cyclic carbon capture capability of Strassburg limestone.	189
Figure B.2. Effects of: (a) hydration temperature; and (b) steam concentration on the cyclic sorbent hydration of Strassburg limestone.	189
Figure C.1. Effect of CaO density on the MRC-CAL off-gas concentration and sorbent conversion.	190
Figure C.2. Effect of CaCO ₃ density on the MRC-CAL off-gas molar concentration and sorbent conversion.	190
Figure C.3. Effect of the average particle diameter on the MRC-CAL off-gas molar concentration and sorbent conversion.	191
Figure E.1. Comparison of different gaseous media for limestone calcination.	194

Nomenclature

$A_{Occ,Mem}$	Cross-sectional area occupied by membrane tubes (m^2)
Ar	Archimedes number $= d_{Particle}^3 \cdot \rho_{Inlet-Gas} \cdot (\rho_{Solid} - \rho_{Inlet-Gas}) \cdot g \cdot \mu_{Inlet-Gas}^{-2}$ (-)
$A_{Reactor}$	Reactor cross-sectional area (m^2)
$A_{Reactor,z}$	Reactor free-membrane cross-sectional area (m^2)
C_p	Specific heat ($J.kg^{-1}.K^{-1}$)
D_a	Axial dispersion coefficient of gas ($m^2.s^{-1}$)
D_{CO_2}	Molecular diffusivity of CO ₂ ($m^2.s^{-1}$)
D_{Eff}	Effective CO ₂ diffusivity in sorbent ($m^2.s^{-1}$)
D_{H_2}	Molecular diffusivity of H ₂ ($m^2.s^{-1}$)
$D_{Inlet-Gas}$	Molecular diffusivity of inlet gas ($m^2.s^{-1}$)
$D_{Knudsen}$	Knudsen diffusion coefficient of CO ₂ in sorbent ($m^2.s^{-1}$)
$D_{Molecular}$	Molecular diffusion coefficient of CO ₂ in sorbent ($m^2.s^{-1}$)
D_{PL}	CO ₂ diffusivity in CaCO ₃ product layer ($m^2.s^{-1}$)
d_{Mem}	Membrane tube diameter (m)
d_N	Normalized utilization decay factor at cycle N in TGA tests (-)
$d_{Particle}$	Particle diameter (m)
$d_{Reactor}$	Reactor diameter (m)
$F_{CaCO_3,Calciner Feed}$	CaCO ₃ feed flow rate for calciner ($mol.s^{-1}$)
$F_{CaCO_3,Calciner Out}$	CaCO ₃ flow rate in calciner outlet ($mol.s^{-1}$)
$F_{CaO,Reformer Feed}$	CaO feed flow rate for reformer ($mol.s^{-1}$)
$F_{CaO,Reformer Out}$	CaO flow rate in reformer outlet ($mol.s^{-1}$)
$F_{CH_4,Calciner Fuel}$	Methane fuel flow rate for calciner ($mol.s^{-1}$)

$F_{CH_4,Reformer\ Fuel}$	Methane fuel flow rate for reformer ($mol.s^{-1}$)
$F_{CO_2,Calcliner\ Fuel}$	CO ₂ flow rate from fuel combustion for calciner ($mol.s^{-1}$)
$F_{CO_2,Des,Total}$	Total flow rate of CO ₂ released by calcination ($mol.s^{-1}$)
$F_{CO_2,Des,z}$	Local flow rate of CO ₂ released by calcination ($mol.s^{-1}$)
$F_{CO_2,Reformer\ Fuel}$	CO ₂ flow rate from fuel combustion for reformer ($mol.s^{-1}$)
$F_{CO_2,Sorb,Total}$	Total flow rate of CO ₂ removed by carbonation ($mol.s^{-1}$)
$F_{CO_2,Sorb,z}$	Local flow rate of CO ₂ removed by carbonation ($mol.s^{-1}$)
$F_{Gas,Calcliner\ Feed}$	Total calciner inlet gas flow rate ($mol.s^{-1}$)
$F_{Gas,Reformer\ Feed}$	Total reformer inlet gas flow rate ($mol.s^{-1}$)
$F_{H_2,Permeated}$	Hydrogen permeate flow rate for membrane reformer ($mol.s^{-1}$)
F_i	Molar flow rate of component i ($mol.s^{-1}$)
$F_{i,Calcliner\ Feed}$	Flow rate of component i in the calciner feed gas ($mol.s^{-1}$)
$F_{i,Calcliner\ Off-Gas}$	Flow rate of component i in calciner off-gas ($mol.s^{-1}$)
$F_{i,GasMix1}$	Flow rate of component i in stream GasMix1 in Aspen Plus simulations ($mol.s^{-1}$)
$F_{i,in}$	Flow rate of stream i as a feed for Aspen Plus simulations ($mol.s^{-1}$)
$F_{i,Reformer\ Feed}$	Flow rate of component i in the reformer feed gas ($mol.s^{-1}$)
$F_{i,Reformer\ Off-Gas}$	Flow rate of component i in reformer off-gas ($mol.s^{-1}$)
$F_{Reformer\ Off-Gas}$	Total reformer off-gas flow rate ($mol.s^{-1}$)
g	Acceleration of gravity ($m.s^{-2}$)
h	Dimensionless reactor length coordinate = $z.L_{Reactor}^{-1}$ (-)
h_{Mem}	Convective heat transfer coefficient in membrane tube ($W.m^{-2}.K^{-1}$)
$J_{H_2,z}$	Hydrogen permeation flux in membranes ($mol.m^{-2}.s^{-1}$)
$K_{i,j}$	Adsorption constant for component i in reaction j (<i>units vary</i>)
$K_{i,SMR}$	Adsorption constant for component i in SMR reactions, i (<i>units vary</i>)

K_j	Equilibrium constant for reaction j (bar^2)
$K_{p,j}$	Equilibrium constants for reaction j (<i>unit varies</i>)
k_d	Surface reduction constant (-)
$k_{g,Mem}$	External mass transfer coefficient for membrane tubes ($m.s^{-1}$)
$k_{g,Particle}$	External mass transfer coefficient for sorbent particles ($m.s^{-1}$)
$k_{h,Mem}$	Thermal conductivity of membrane tubes ($W.m^{-1}.K^{-1}$)
k_j	Reaction rate constant j (<i>units vary</i>)
L_{Mem}	Membrane length (m)
$L_{Reactor}$	Reactor length (m)
M_{CaCO_3}	CaCO ₃ molecular weight ($kg.mol^{-1}$)
M_{CaO}	CaO molecular weight ($kg.mol^{-1}$)
M_i	Molecular weight of component ($g.mole^{-1}$)
$m(t)$	Instantaneous weight of sample in TGA Tests (g)
$m_{in,i}$	Inlet mass flow rate of solid i : catalyst, CaO, CaCO ₃ ($kg.s^{-1}$)
$m_{in,Solid}$	Total mass flow rate of solid ($kg.s^{-1}$)
m_0	Weight of sample after secondary pretreatment in TGA Tests (g)
N	Number of cycles (-)
N_{Mem}	Number of membrane tubes (-)
Nu_{Mem}	Nusselt number for membrane tubes = $h_{Tube} \cdot L_{Mem} \cdot k_{h,Mem}^{-1}$ (-)
P	Pressure (bars)
$P(z)$	Local reactor pressure (<i>bars</i>)
\bar{P}_{CO_2}	Average CO ₂ partial pressure in reactor (<i>bars</i>)
$P_{CO_2,z}$	Local CO ₂ partial pressure in reactor (<i>bars</i>)
Pe	Peclet number = $U_{Superficial} \cdot L_{Reactor} \cdot D_a^{-1}$ (-)
P_{Eq,CO_2}	Partial pressure of CO ₂ in equilibrium with lime/limestone (<i>atm</i>)

$P_{H_2, Film, z}$	Local partial pressure of hydrogen in membrane film (<i>bars</i>)
$P_{H_2, Permeate}$	Partial pressure of hydrogen in membrane permeate side (<i>bars</i>)
$P_{H_2, Reformer, z}$	Local partial pressure of hydrogen in reformer (<i>bars</i>)
P_i	Partial pressure of component <i>i</i> (<i>bars</i>)
Pr_{Mem}	Prandtl number for single membrane tube = $\mu_{Gas} \cdot C_p \cdot k_{h, Tube}^{-1}$ (-)
R	Gas constant ($J \cdot mol^{-1} \cdot K^{-1}$)
Re_C	Reynolds number based on $U_C = \rho_{Gas} \cdot U_C \cdot d_{Particle} \cdot \mu_{Gas}^{-1}$ (-)
Re_{Mem}	Reynolds number for single tube = $\rho_{Inlet-Gas} \cdot U_{Superficial} \cdot d_{Mem} \cdot \mu_{Inlet-Gas}^{-1}$ (-)
$Re_{Particle}$	Reynolds number for particle = $\rho_{Inlet-Gas} \cdot U_{Superficial} \cdot d_{Particle} \cdot \mu_{Inlet-Gas}^{-1}$ (-)
Re_{Se}	Reynolds number based on $U_{Se} = \rho_{Gas} \cdot U_{Se} \cdot d_{Particle} \cdot \mu_{Gas}^{-1}$ (-)
r_j	Rate of reaction <i>j</i> (<i>unit varies</i>)
r_{pore}	Mean sorbent pore diameter (<i>m</i>)
S	Active surface area (m^2)
S_0	Initial active surface area (m^2)
S_r	Residual active surface area (m^2)
Sc_{inlet}	Schmidt number at reactor inlet = $\mu_{Inlet-Gas} \cdot D_{Inlet-Gas}^{-1} \cdot \rho_{Inlet-Gas}^{-1}$ (-)
Sc_{Mem}	Schmidt number for membrane tubes = $\mu_{Gas} \cdot D_{H_2}^{-1} \cdot \rho_{Gas}^{-1}$ (-)
$Sc_{Particle}$	Schmidt number for particles = $\mu_{Gas} \cdot D_{CO_2}^{-1} \cdot \rho_{Gas}^{-1}$ (-)
Sh_{Mem}	Sherwood number for single membrane tube = $k_{g, Mem} \cdot d_{Mem} \cdot D_{H_2}^{-1}$ (-)
$Sh_{Particle}$	Sherwood number for single membrane tube = $k_{g, Particle} \cdot d_{Particle} \cdot D_{CO_2}^{-1}$ (-)
T	Operating temperature (K - °C if specified elsewhere)
t	Time (min - s if specified elsewhere)
U_C	Transition velocity for bubbling/turbulent fluidization flow regimes ($m \cdot s^{-1}$)
$U_{gas, mixture, z}$	Local gas velocity inside the reactor ($m \cdot s^{-1}$)
U_{Se}	Transition velocity for turbulent/fast fluidization flow regimes ($m \cdot s^{-1}$)

$U_{\text{Superficial}}$	Superficial gas velocity ($m.s^{-1}$)
V_{Reactor}	Reactor volume (m^3)
$v_{\text{CaCO}_3, \text{bed}}$	Volume fraction of CaCO_3 in solid bed (-)
$v_{i,j}$	Stoichiometric number of component i in reaction j
X	Sorbent conversion (-)
$X(t)$	Instantaneous sorbent molar utilization/conversion in TGA tests (-)
X_{Calc}	Sorbent calcination extent (-)
$X_{\text{Calc}, N}$	Calcination extent at cycle N in TGA tests (-)
$X_{\text{Calc}, \text{Norm}, N}$	Normalized calcination extent at cycle N in TGA tests (-)
X_{Carb}	Sorbent carbonation Extent (-)
$X_{\text{Carb}, N}$	Carbonation extent at cycle N in TGA tests (-)
X_r	Residual sorbent molar utilization/conversion (-)
x_{CaCO_3}	CaCO_3 mole fraction in solid feed (-)
$y_{\text{H}_2, \text{Dry Reformer Off-Gas}}$	Dry reformer off-gas hydrogen molar fraction (-)
y_i	Mole fraction of component i in off-gas (-)
$y_{\text{O}_2, \text{Air}}$	Molar fraction of oxygen in air (-)
$y_{\text{O}_2, \text{Enriched-Air}}$	Molar fraction of oxygen in enriched-air (-)
$y_{\text{O}_2, \text{Target}}$	Target molar air oxygen molar fraction in Aspen Plus simulations (-)
z	Reactor length coordinate (m)

Greek Letters

α	CaCO_3 -to-total gas molar feed ratio (-)
α^*	CaCO_3 -to- CH_4 molar feed ratio (-)
β	Methane-to-enriched-air molar feed ratio (-)
β^*	95% of CH_4 -to-oxygen molar feed ratio (-)

$\Gamma_{Calc}(z)$	Desorption distribution factor (-)
$\Gamma_{Carb}(z)$	Sorption distribution factor (-)
$\Delta H_{25^{\circ}C}$	Standard enthalpy of reaction at 25°C ($kJ.mol^{-1}$)
δ	Active thickness of membrane tube (m)
ϵ_{bed}	Bed voidage (-)
ϵ_{pore}	Sorbent Porosity (-)
$\kappa_{H_2,Pd}$	Hydrogen permeability in palladium-based membranes ($mol.m^{-1}.s^{-1}.bar^{-0.5}$)
λ	Reactivity coefficient in ADPFR model solution
μ_{Gas}	Gas mixture viscosity ($Pa.s$)
$\mu_{Inlet-Gas}$	Inlet gas viscosity ($Pa.s$)
$\rho_{CaCO_3,bed}$	Limestone bed concentration ($kg.m^{-3}$)
ρ_{CaO}	Molar density of CaO ($mol.m^{-3}$)
$\rho_{Cat,bed}$	Catalyst bed concentration ($kg.m^{-3}$)
ρ_{Gas}	Gas mixture density ($kg.m^{-3}$)
$\rho_{Inlet-Gas}$	Inlet gas density ($kg.m^{-3}$)
ρ_{Solid}	Average solid (CaO, CaCO ₃ , Catalyst) density ($kg.m^{-3}$)
τ	Sorbent residence time (min)
$\bar{\tau}$	Sorbent tortuosity factor (-)

Subscripts

<i>Calc</i>	Calcination
<i>Cat</i>	Catalyst
<i>Carb</i>	Carbonation
<i>Eq</i>	Equilibrium
<i>in</i>	Inlet
<i>min</i>	Minimum
0	Value at reactor entrance ($z = 0$)

Abbreviations

ADPFR	Axially Dispersed Plug Flow Reactor
CaL	Calcium-Looping
CLC	Chemical Looping Combustion
CSTR	Continuous Stirred Tank Reactor
DMR	Dry Methane Reforming
FBR	Fluidized Bed Reactor
HPI	Hydrogen Production Index
MA-SE-SMR	Membrane-Assisted Sorbent-Enhanced Steam Methane Reforming
MA-WGS	Membrane-Assisted Water-Gas Shift
MRC-CAL	Combined Methane Reforming, Combustion and Limestone Calcination
OC	Oxygen Carrier
PFR	Plug Flow Reactor
PSA	Pressure Swing Adsorption
RWGS	Reverse Water-Gas Shift Reaction
SE-SMR	Sorbent-Enhanced Steam Methane Reforming
SMR	Steam Methane Reforming
STD	Standard
STEAM-CAL	Limestone Calcination in Steam
TGA	Thermogravimetric Analyzer
TPBVDE	Two-Point Boundary Value Differential Equation
TS	Temperature Swing
UFL	Upper Flammability Limit
WGS	Water-Gas Shift Reaction
XRD	X-Ray Diffraction

Acknowledgments

First and foremost, I would like to express my deepest appreciation to my beloved parents, Jalil Ebneyamini and Shahnaz Etminan, for their endless love, support and motivation throughout my life. I also want to express my sincere gratitude to my dear brother, Armin, for his constant support and kindness. I would not be the person I am today without their presence and encouragement.

Special thanks are owed to my supervisors, Dr. John Grace, Dr. Naoko Ellis, and Dr. Jim Lim, for giving me the opportunity of working in their research groups and for all the skills and knowledge I have gained throughout my Ph.D. program. It would absolutely not be possible to complete this thesis without their continuous support, insights and help.

I am sincerely grateful to my supervisory committee, Dr. Andres Mahecha-Botero and Dr. Fariborz Taghipour, whose penetrating questions directed me to address knowledge gaps and their potential solutions. I also would like to thank Dr. Said Elnashaie for his help and encouragement for reactor modeling.

I wish to show my gratitude to Dr. Dennis Lu and Dr. Robin Hughes for giving me the opportunity of visiting CanmetEnergy (Ottawa) and using their facilities.

I thank my colleagues and friends John Zezhong Li, Bill Long Cheng, and Jun Young Kim for their sincere friendship, constant presence and help which was truly valuable to make this research journey a very enjoyable experience.

I express my appreciation to Compute Canada for the opportunity to use a Cedar supercomputer.

I also acknowledge the financial support of the Natural Science and Engineering Research Council of Canada (NSERC) *via* their CREATE and Discovery Grant programs.

Dedication

*To my family for their endless love, support and
motivation throughout my life*

CHAPTER 1: Background

1.1. Energy Demand and Climate Change

Population and economic growth have raised the world's demand for energy, with traditional fossil fuels remaining the dominant source (Figure 1.1). Immense consumption of fossil fuels releases substantial amounts of greenhouse gases (especially CO₂) into the atmosphere, resulting in serious environmental consequences such as global warming, deforestation and acid rain [1,2]. International policies and agreements have sought reduction in CO₂ emissions, encouraging energy-related industries to utilize alternative energy sources, or capture and sequester CO₂ [3,4].

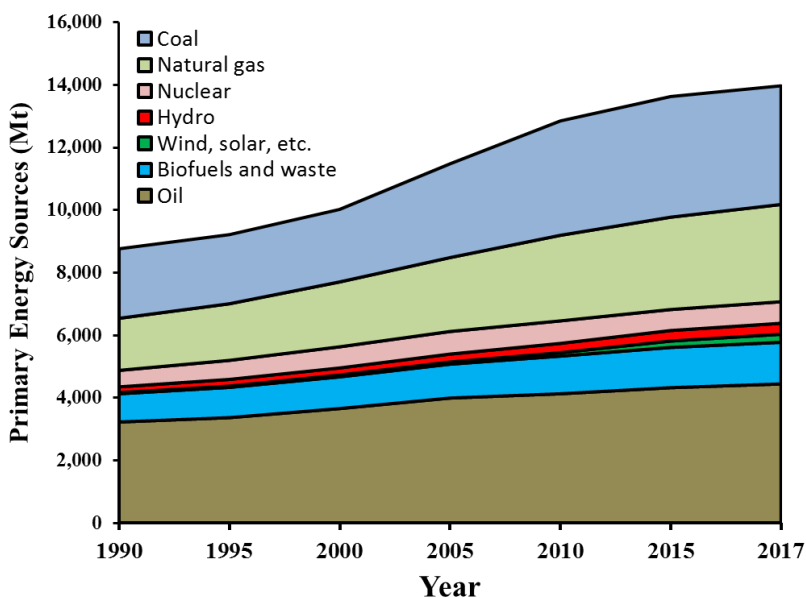


Figure 1.1. World primary energy supply by source, 1990-2017. Data adopted from [5]

Amine scrubbing by alkaline aqueous solutions is a carbon capture technology commonly used in industry. However, amine scrubbing processes emit amine solvents into the atmosphere, while also requiring high energy input to regenerate the amine [6]. Various environmental-friendly energy sources have been proposed to replace and contain the world's growing demand for clean

energy, including hydropower, biomass, geothermal, solar, wind and tidal energies [7]. However, these processes are geologically limited, and typically suffer from low conversion efficiencies. Alternative cost-effective energy sources and carbon capture technologies are imperative to diminish the undesired impact of CO₂ emission on the environment.

1.2. Hydrogen

Hydrogen is a promising fuel gas, also required in major industrial applications such as ammonia production, petroleum refining, proton exchange fuel cells, and metal alloying [8–10]. It has the highest gravimetric energy density, and produces steam when combusted. The world's demand for hydrogen has drastically increased during the past few decades, as shown in Figure 1.2. Considerable attention has been given to hydrogen as an eco-friendly alternative of the conventional hydrocarbon fuels [11]. However, pure hydrogen does not exist in nature and, therefore, must be synthesized from other sources (e.g. water, natural gas, biomass) [12].

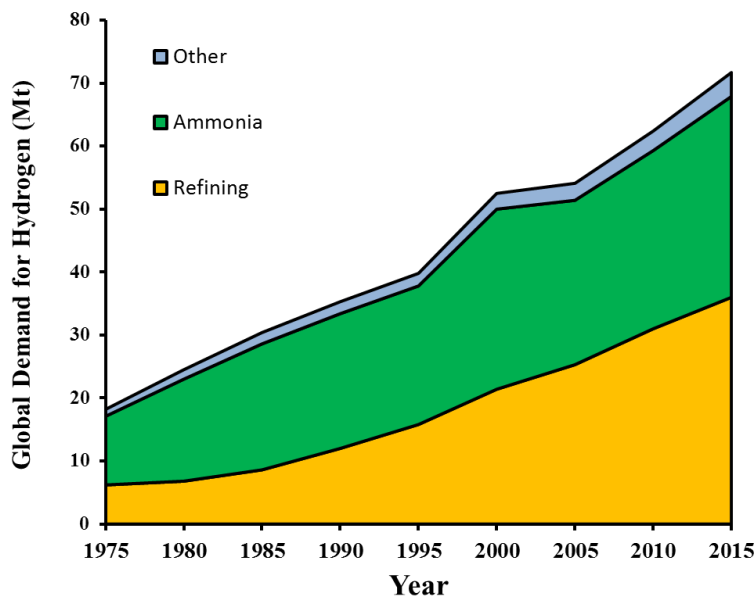


Figure 1.2. Global demand for hydrogen, 1975-2015. Data adopted from [13]

1.3. Steam Methane Reforming

Hydrogen can be produced by several processes, including bio/fossil fuel reforming or partial oxidation, biomass gasification, water electrolysis, plasma arc decomposition [14]. Conversion of hydrocarbons to hydrogen in the presence of steam was initially introduced during the 19th century. High-temperature catalytic steam methane reforming (SMR) is currently the most common industrial hydrogen production route [14,15]. The main reactions in this process are listed in Table 1.1. Note that several other reactions (e.g. methane cracking, Boudouard reaction, dry methane reforming) can also occur inside steam methane reformers [16]. Therefore, the operating conditions must be precisely controlled to optimize reformer productivity and product purity.

Table 1.1. Main reactions in steam methane reforming [17]

Reaction	Stoichiometry	$\Delta H_{25^\circ\text{C}}$ (kJ.mol ⁻¹)
Water-Gas Shift Reaction	$H_2O + CO \rightleftharpoons H_2 + CO_2$	-41.2
Steam Methane Reforming	$CH_4 + H_2O \rightleftharpoons 3H_2 + CO$	206.2
Overall Reaction	$CH_4 + 2H_2O \rightleftharpoons 4H_2 + CO_2$	165

Steam methane reforming is an endothermic process, thereby favoured at high operating temperatures. On the other hand, increasing the reactor pressure hinders SMR feedstock conversion, in agreement with Le Chatelier's principal. High reactor pressures and low operating temperatures are typically desired to facilitate heat recovery, increase energy efficiency, and reduce the cost of compression for downstream ammonia and methanol plants [16]. However, the thermodynamic equilibrium of the SMR reactions limits feedstock conversion, requiring temperatures >900°C to achieve suitable feedstock conversion. Such high temperatures can result in carbon formation and, consequently, catalyst deactivation by coke deposition [12].

Steam methane reforming gaseous products contain appreciable amounts of H_2 and steam, as well as some amounts of CO_2 , CO and unreacted CH_4 . The dry off-gas hydrogen concentration of the SMR process is typically below 80 vol%, mainly due to CO_2 generation inside the reactor (see Table 1.1). Downstream water-gas shift (WGS) reactor and pressure-swing adsorption (PSA) columns are then required if higher H_2 concentrations are needed, as shown schematically in Figure 1.3.

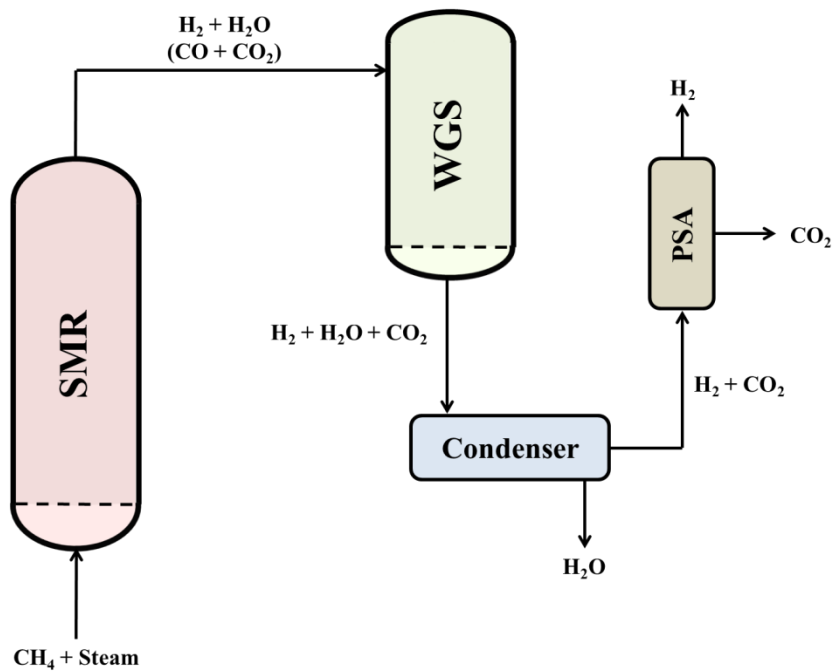


Figure 1.3. Hydrogen production by a conventional steam methane reforming plant

Recent studies have shown that *in situ* removal of H_2 and CO_2 can significantly enhance the performance of steam methane reformers at moderate reactor temperatures [9,12,15,17–20]. Removing H_2 and CO_2 from the reformer gas results in shifting the SMR thermodynamic equilibrium toward higher feedstock conversion and, consequently, enhanced hydrogen productivity. Further discussion is provided in Sections 1.4 and 1.5.

1.4. Membrane-Assisted Steam Methane Reforming

Hydrogen perm-selective membranes have been studied extensively to remove hydrogen from the reformer gaseous mixture [21–24]. This has been shown [9,16,17,19,25,26] to help shifting the reforming thermodynamic equilibrium, resulting in enhanced methane conversion at moderate reactor temperatures. A highly-concentrated hydrogen stream can then be withdrawn from the permeate side, to be used further in many downstream applications, especially proton-exchange fuel cells.

Palladium-based membranes are the most studied materials for high-temperature hydrogen removal [21–24]. Despite their high hydrogen selectivity and moderate permeability, Pd-based membranes are relatively expensive, and tend to lose their selectivity and mechanical stability at temperatures above 550-620°C [22,23]. Membrane swelling at low temperatures (e.g.<300°C) is another challenge attributed to Pd-based metallic membranes [11]. These membranes are also highly sensitive to poisoning when contacting species such as CO and sulfur compounds [27–30]. Alternative hydrogen-selective membrane materials, including nickel, cermet/cement and Vb metals, have been also studied for hydrogen separation at elevated temperatures [22,31–36]. However, these membranes typically suffer from low hydrogen permeability, low hydrogen selectivity, unfavourable reactivity (with other syngas species) and low mechanical stability [22].

1.5. Sorbent-Enhanced Steam Methane Reforming

The performance of steam methane reformers can be improved by *in situ* CO₂ removal from the reactor gaseous mixture. The improvement is due to enhanced methane conversion because of equilibrium shift (i.e., Le Chatelier's principal) by removing a large portion of the reforming

byproduct (CO₂). Sorbent enhancement can also reduce the required reforming temperature, thereby decreasing coke-formation and heat losses within the reactor [12].

Calcium-looping (CaL) is a promising high-temperature CO₂ separation technology, applicable for post-combustion carbon capture, biomass gasification and steam methane reforming [10,26,37–41]. This process utilizes calcined limestone (i.e., lime) as a CO₂ sorbent, removing carbon dioxide *via* reversible solid-gas lime carbonation (Table 1.2). Abundance, simplicity and low cost are the key advantages of lime particles as CO₂-acceptor sorbents [4,37,42–44]. In addition, exothermic carbonation of CaO-based sorbents can supply a large portion of the heat required for the endothermic SMR reactions, resulting in nearly autothermal reforming at mild operating temperatures [15]. Carbonated lime can then be calcined in a separate reactor, completing a loop for multi-cyclic operation.

Table 1.2. Reversible lime carbonation and limestone calcination reactions

Reaction	Stoichiometry	$\Delta H_{25^\circ\text{C}}$ (kJ.mol ⁻¹)
CaO Carbonation/CaCO ₃ Calcination	$\text{CaO}(s) + \text{CO}_2(g) \rightleftharpoons \text{CaCO}_3(s)$	-178

Conventional sorbent-enhanced steam methane reforming (SE-SMR) features two interconnected fluidized bed reactors: one as the limestone calciner and the other for methane reforming/lime carbonation (Figure 1.4). The CaO/CaCO₃ thermodynamic equilibrium is depicted in Figure 1.5. Lime carbonation benefits from mild operating temperatures and high CO₂ concentrations, whereas limestone calcination is favoured by elevated temperatures and CO₂-dilute gaseous media [10,26,37,38,40,41]. Ideally, a hydrogen-enriched gas leaves the SE-SMR reactor, while a concentrated CO₂ stream is desired from the limestone calciner. Note that the high concentration of the calciner off-gas is crucial for the next steps of CO₂ storage and sequestration [45].

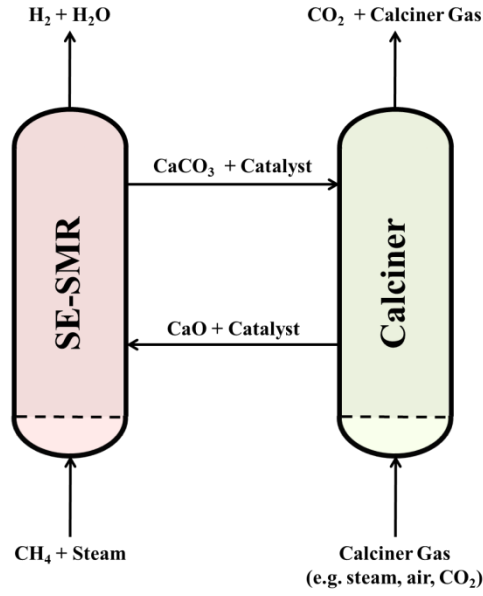


Figure 1.4. Schematic of the SE-SMR process in dual fluidized bed reactors

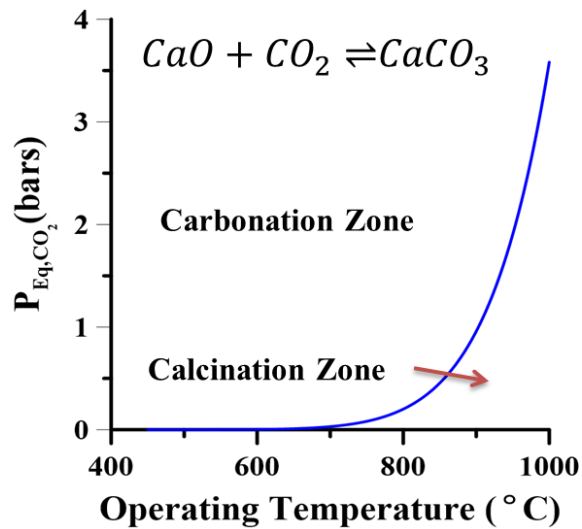


Figure 1.5. Thermodynamic equilibrium of CaO/CaCO₃

Temperature-swing (TS) is the typical sorption/desorption cyclic route in the CaL process, where the limestone calcination occurs at elevated temperatures (e.g. 850-920°C) [17]. Although TS provides rapid and complete calcination of spent sorbents, the high temperature in the calciner commonly changes the pore structure of the sorbents by shrinking the micro-pores, called

sintering. This reduces the active surface area of the sorbent, leading to a sharp decay in sorbent utilization during the first few calcination-carbonation cycles [4,43,46,47]. Various measures, including sorbent modification (e.g. by steam reactivation, doping and adding inert materials) and synthetic sorbents (e.g. Li_2ZrO_3), have been tested to prevent the decay of sorbent utilization, while enhancing CO_2 capture capability [4,47–50]. However, these modified/reactivated/synthetic sorbents are generally expensive compared to natural limestone, and are economically viable only if they show stable and high performance over many cycles (e.g. >10,000 cycles for Li_2ZrO_3) [37,41].

The pore evolution of lime-based sorbents depends strongly on the limestone calciner operating conditions. For instance, increasing the calciner temperature can significantly boost the rate of pore sintering, consequently accelerating decay of sorbent utilization [51,52]. Some studies [53–56] have shown that the porous structure of calcined limestone can also be affected by the gaseous medium (e.g. air, steam, CO_2). Further investigations are imperative to determine the optimal calciner operating conditions (temperature, calcination extent, and gaseous medium) for the CaL process.

1.6. Limestone Calcination

1.6.1. Background

Limestone calcination is an endothermic reaction, requiring elevated reactor temperatures (e.g. > 800°C). The performance of limestone calciners depends strongly on operational factors, including the heating supply, operating pressure, CO_2 partial pressure and reactor temperature. The energy required for calcination thermal processing can be supplied by burning fuels inside (direct) or outside (indirect) the reactor. Direct heating is typically preferred to decrease heat

losses, heat transfer resistance, temperature gradients, and reactor size. However, *in situ* burning of carbonaceous fuels (e.g. natural gas or coal) increases the CO₂ concentration within the reactor, inhibiting limestone calcination (see Figure 1.5). Similarly, elevating calciner pressure leads to higher CO₂ concentration within the reactor and therefore, lower calcination rate and extent. Note that high CO₂ concentration and reactor pressure are typically desired to reduce the cost of CO₂ purification and compression for carbon storage [37,57]. Although increasing the operating temperature can potentially enhance the rate of limestone calcination, it imposes several operational challenges (e.g. more sorbent sintering [51,52]).

Figure 1.6 summarizes the main criteria for the limestone calciners, as well as advantages and challenges associated with each individual factor. Limestone calciners are normally preferred to operate autothermally at high pressures, low temperature and high CO₂ concentrations. However, thermodynamics and kinetics of limestone calcination do not allow one to meet all these criteria simultaneously.

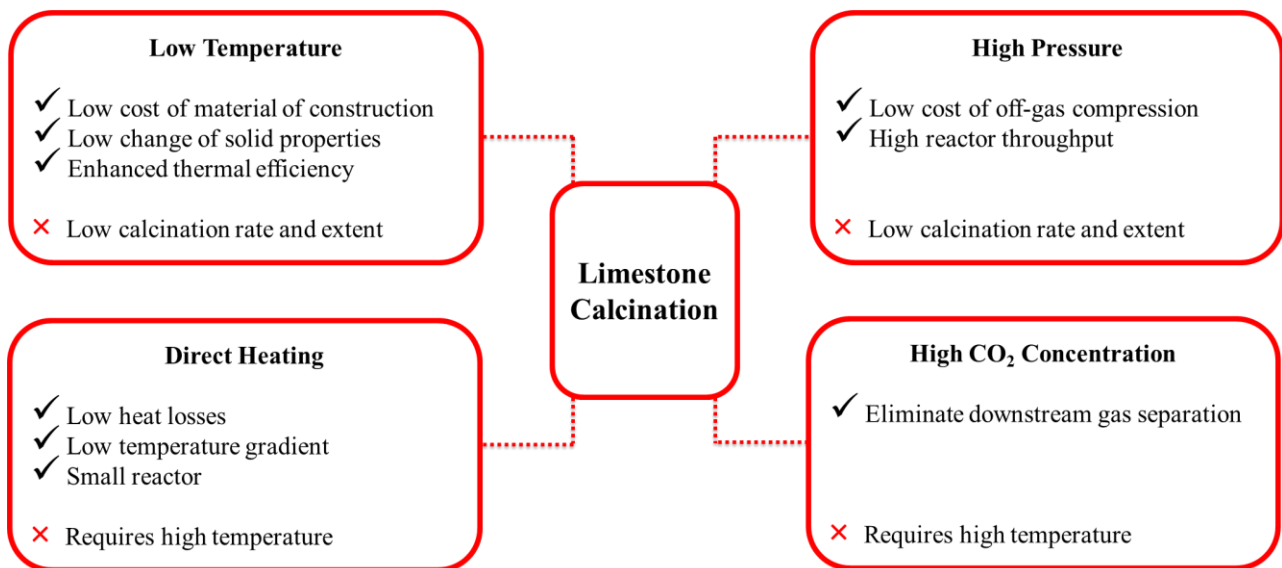


Figure 1.6. Main criteria for limestone calciners

1.6.2. Gaseous Media for Limestone Calcination

1.6.2.1. Inert and Oxidant Gases

Most fundamental studies have used air or N₂ as the calcination gaseous medium. This includes laboratory (e.g. thermogravimetric analysis, electrically heated foil and magnetic suspension balance [58–65]) and bench-scale (e.g. rotary kiln, fixed bed and fluidized bed reactors [59,66,67]) experimental setups. As mentioned above, the rate of limestone calcination depends heavily on the CO₂ concentration within the reaction zone [68]. Non-CO₂ sweeping gases can potentially dilute the reactor CO₂ concentration, thereby enhancing limestone calcination [4]. Therefore, operating in the presence of inert gases may offer satisfactory limestone calcination at relatively low reactor temperatures. Note that the positive impact of non-CO₂ gas-sweeping is directly a function of the CaCO₃/gas feed ratio, with more improvement achieved at higher inlet gas flow rates [69].

Limestone calcination in inert gases produces a dilute CO₂ off-gas, which must be purified prior to CO₂ sequestration. However, separating CO₂ from air and nitrogen is energy-intensive, imposing an energy penalty on the system. Alternatively, helium can be used as the calcination gaseous medium, and then removed by membrane separation (Figure 1.7). The separated helium can then be compressed and recycled into the limestone calciner, minimizing the helium required for continuous operation [58,70]. Higher thermal conductivity and CO₂ diffusivity in helium can also enhance limestone calcination at mild reactor temperatures [58]. Note that the energy required for calcination in these scenarios should be supplied by burning fuels, or by solar-concentrated power [58,70,71]. However, indirect heating by fuel combustion suffers from low thermal efficiency (e.g. more heat loss and temperature gradient), whereas the solar-concentrated

power supply is geographically limited, and needs specific considerations for overnight operations.

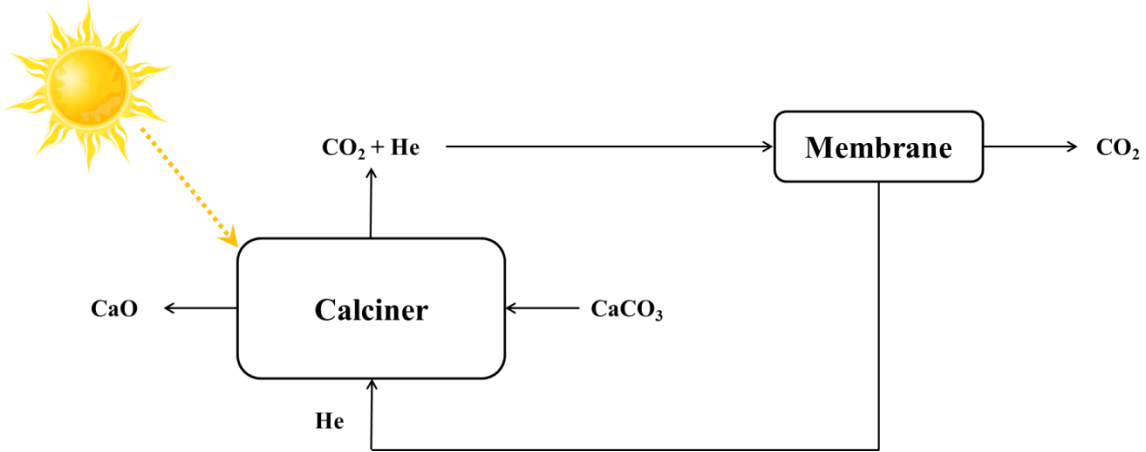


Figure 1.7. Limestone calcination in helium with solar-concentrated power

Some studies [72–75] have proposed integrating the CaL process with chemical looping combustion (CLC) systems, providing the limestone calcination energy by *in situ* metal (e.g. Ni and Cu) oxidation. The performance of the combined CaL-CLC process depends strongly on the oxygen carrier (OC), and the oxidation/calcination gaseous medium (air, steam, CO₂ or O₂). Air calcination/oxidation generates a dilute CO₂ off-gas, whereas metal oxidation can be endothermic in the presence of steam and CO₂ [74]. Instead, pure oxygen (in stoichiometric ratio) can be used to achieve autothermal operation and high off-gas CO₂ concentration simultaneously. However, excess oxygen is typically required to achieve satisfactory OC oxidation, as well as averting reactor failure by defluidization. This imposes an additional energy penalty on the system, mainly due to low energy efficiency of the cryogenic air separation units (25 kJ_{ele} per mole of O₂ [76]).

Limestone calcination can be also integrated with the exothermic CuO reduction (Table 1.3) in the presence of methane [72]. This potentially eliminates the need for downstream CO₂

separation, as methane oxidation generates mostly steam and CO₂. However, the high CO₂ concentration within calciner/reducer inhibits limestone calcination, implying the need for high reactor temperature. Note that this process (Figure 1.8) typically needs an additional air reactor to ensure satisfactory OC oxidation for multi-cyclic operation. The air reactor should preferably operate at mild temperatures, averting release of CO₂ (by limestone calcination) into the depleted air. Given the substantial decay of lime CO₂ carrying capacity over calcination-carbonation cycles, a significant limestone make-up flow would be required to maintain continuous operation. This implies the need for effective Cu/CaO separation in order to prevent purging of OC particles along with spent sorbents. More investigations are crucial to optimize the CaL-CLC process for practical applications.

Table 1.3. Main reactions involved in CaL-CLC process with Cu-based oxygen carrier

Reaction	Stoichiometry	$\Delta H_{25^\circ\text{C}} \text{ (kJ.mol}^{-1}\text{)}$
Limestone Calcination [18]	$\text{CaCO}_3 \rightleftharpoons \text{CaO} + \text{CO}_2$	178
CuO Reduction [72]	$4\text{CuO} + \text{CH}_4 \rightleftharpoons 4\text{Cu} + \text{CO}_2 + 2\text{H}_2\text{O}$	-156
Cu Oxidation [72]	$2\text{Cu} + \text{O}_2 \rightleftharpoons 2\text{CuO}$	-178

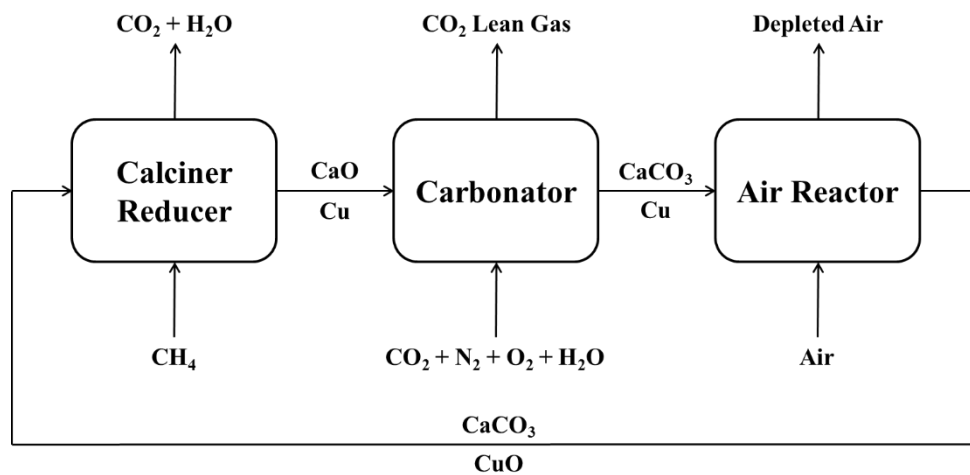


Figure 1.8. CaL-CLC process with Cu-based oxygen carrier [72]

1.6.2.2. *CO₂*

One alternative to conventional inert-gas calcination is to decompose the limestone in the presence of CO₂. This results in a highly-concentrated CO₂ off-gas, which can eliminate the need for downstream gas separation. In addition, a portion of the calciner off-gas can be cooled (integrated with heat recovery facilities, e.g. heat exchangers), compressed, and recycled to the limestone calciner [77]. However, increasing the CO₂ concentration inside the reactor reduces the limestone calcination rate and extent [3,62,67,78]. Therefore, higher reactor temperatures (e.g. > 900-950°C) than those for calcination in inert-gas (e.g. > 850°C) are required if CO₂ is the calcination gaseous medium [67]. The presence of CO₂ in the calciner can also promote loss of CaO surface area by pore sintering [53–56]. Given also the indirect heating requirement, CO₂ calcination may not be attractive for industrial limestone calciners.

1.6.2.3. *Steam*

Steam has been proposed to maintain a low CO₂ concentration within the reactor, while also producing a CO₂-concentrated stream after condensing the steam content of calciner off-gas. The presence of steam in the calciner also accelerates the rate of limestone decomposition by enhancing solid-gas heat transfer [79], weakening the CaO-CO₂ chemical bond [62,80,81], and forming a surface bicarbonate intermediate [58,82]. Enhanced limestone calcination rate can potentially reduce the required reactor temperature for satisfactory limestone calcination [62]. However, weaker sorbent structures in the presence of steam may lead to increased particle attrition and fragmentation, resulting in greater solid loss by entrainment [83]. Recent studies [58] have shown that the injection of steam at low concentrations (e.g. 1.25%) can notably enhance the rate of limestone calcination, without a negative impact on the mechanical strength of calcined limestone.

Morphological changes associated with limestone calcination in steam may also affect the performance of calcined limestone for successive carbon and sulfur capture. Rong et al. [84] found that adding steam during calcination slightly increased pore sintering, consequently reducing the cyclic carbon capture capability of calcined particles. Accelerated loss of surface area due to steam is similar to findings by Borgwardt [53]. In contrast, several studies have shown that steam injection during calcination can enhance the cyclic CO₂ and sulfur carrying capacity of calcined limestone [56,80,85,86]. The positive impact of steam has been linked to the creation of larger pore diameters (~50 nm) and reduced pore blockage by carbonation [85]. Champagne et al. [86] concluded that increasing the steam concentration in a limestone calciner results in both enhanced pore sintering and a shift of pore size toward larger diameters. This result was supported by detailed analysis of the fast and slow stage carbonation regimes at different reaction cycles. Enhanced pore sintering adversely affects the sorbent CO₂ carrying capacity, whereas larger pore diameter leads to lower diffusional resistance in the CaCO₃ product layer.

The effect of steam on the morphology of the calcined particles may also depend on the limestone impurities and particle size. Donat et al. [85] observed that different limestones behave differently during limestone calcination in steam, and explained this by means of different solid impurities. Rong et al. [84] claimed particle size to be a key factor for explaining observed contradiction between different experimental results. Chou et al. [87] showed that cyclic carbon capture capability of fine particles (4.3 vs. 217 μm) is more enhanced when injecting steam into calciner. In contrast, Champagne et al. [86] found that the performance of lime-based sorbents was independent of particle size (45-106 vs. 250-425 μm).

In summary, operation in the presence of steam can offer rapid limestone calcination at reduced temperatures. Injection of steam into a calciner may also enhance the carrying capacity of the calcined limestone for capture of CO₂ and SO₂. Nevertheless, steam generation is energy-consuming, imposing additional energy penalty on the system. Limestone calcination in steam is also endothermic, requiring indirect heating from the reactor wall. For some applications, metallic catalyst is fed into the calciner along with limestone particles (e.g. sorbent-enhanced methane reforming and water-gas shift reaction). High temperature steam in these processes can undesirably oxidize metallic catalysts, implying the need for catalyst regeneration and/or make-up flow. From a practical prospective, limestone calcination in steam would be attractive only if the calciner were to be used for non-catalytic processes (e.g. cement industry and post-combustion carbon capture), and if the steam could be supplied from a side process (e.g. a steam cycle).

1.6.2.4. CO₂-Utilizing Media

CO₂ utilization refers to the production of commercially attractive chemical compounds from carbon dioxide. Integration of limestone calcination with *in situ* CO₂ utilization can potentially preserve low CO₂ emissions, while generating a valuable byproduct. In addition, *in situ* CO₂ utilization can favourably reduce the CO₂ concentration within the reactor, enhancing the limestone calcination rate and reducing the reactor temperature.

Reller et al. [88] found that limestone calcination in the presence of hydrogen can substantially reduce the required calcination temperature (by at least 150°C), while also producing a gaseous mixture composed of methane and carbon monoxide. Similar observations were reported later by Jagadeesan et al. [89], who found co-production of lime and syngas (CO₂, CO, H₂, and CH₄) during limestone calcination in hydrogen. The use of a transition metal can accelerate limestone

decomposition, as well as catalyzing CO₂ conversion toward different gases. Jagadeesan et al. [89] reported 100% methane production by Co/CoO/CaO particles, and C1-C3 hydrocarbons generation in the presence of Fe-based transition metals [90]. Note that the performance of this process can also depend on the hydrogen partial pressure, with the CO and CH₄ selectivity decreasing and increasing with increasing hydrogen partial pressure, respectively [91].

Despite its advantages, hydrogen is not practically attractive as a calcination gaseous medium given its cost. Alternatively, methane can be applied in order to utilize the released CO₂ (from limestone calcination) for syngas production *via* dry methane reforming. A general schematic of the process is presented in Figure 1.9, with its main reactions listed in Table 1.4. A thermodynamic analysis by Nikulshina et al. [92] demonstrated that this process can be initiated at 1000 K, while temperatures > 1200 K are required for reaction completion. However, slow dry methane reforming inhibits the methane conversion in practice, and temperatures close to 2000 K are needed to achieve complete feedstock conversion. The authors claimed that increasing temperature, reducing gas inlet flow rate, elevating methane feed concentration and use of a catalyst can potentially enhance gaseous feedstock conversion during limestone calcination in presence of methane.

Kim et al. [93] studied the combined limestone calcination and methane dry reforming with a nickel-based catalyst under fluidization conditions. They obtained a moderate H₂/CO syngas molar ratio (~1.04-1.06) for dilute (720°C, balanced with nitrogen) and pure (900°C) methane feedstock. Coke formation was observed at mild reactor temperatures, which can eventually deactivate catalysts during continuous operation. Formation of coke at mild calciner temperatures was also reported by Dang et al. [94]. Catalyst deactivation by carbon deposition is a major challenge for industrial applications, requiring fresh catalyst make-up or costly

regeneration processes. Elevating the reactor temperature (e.g. to $>900^{\circ}\text{C}$), fabrication of catalyst with high oxygen storage capacity, bimetallic catalyst and limiting the operating time to calcination completion have been suggested to avoid coke formation during limestone calcination in presence of methane [93].

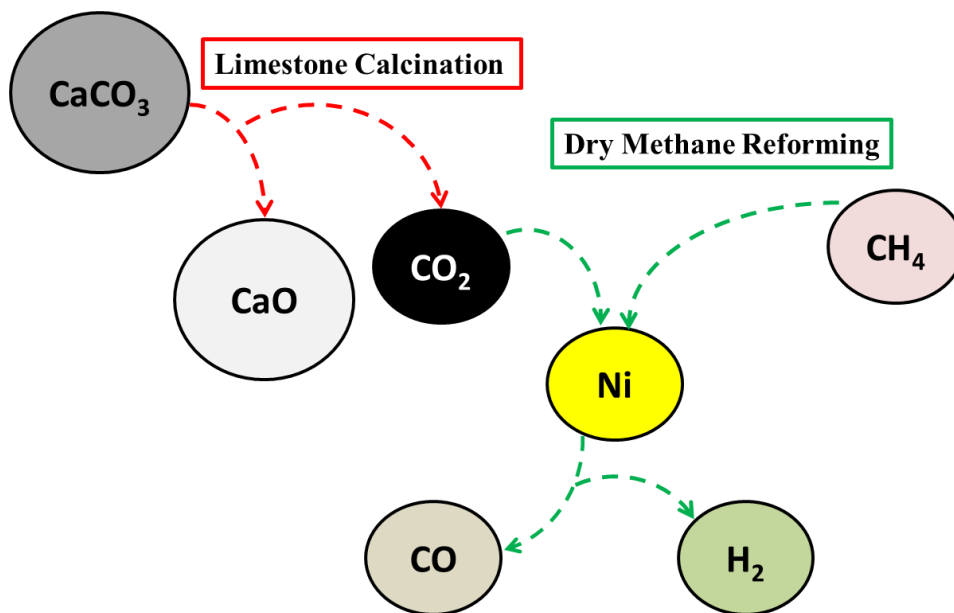


Figure 1.9. Schematic of calcination in methane

Table 1.4. Main reactions involved in calcination in methane

Reaction	Stoichiometry	$\Delta H_{25^{\circ}\text{C}} \text{ (kJ.mol}^{-1}\text{)}$
Limestone Calcination [18]	$\text{CaCO}_3 \rightleftharpoons \text{CaO} + \text{CO}_2$	178
Dry Methane Reforming [95]	$\text{CO}_2 + \text{CH}_4 \rightleftharpoons 2\text{CO} + 2\text{H}_2$	247
Methane Calcination*	$\text{CaCO}_3 + \text{CH}_4 \rightleftharpoons \text{CaO} + 2\text{CO} + 2\text{H}_2$	425

* Standard heat of reactions were calculated by summing the heats of reactions

Motivated by limited natural gas supply and non-uniform distribution of reserves, Dang et al. [96] studied the integration of limestone calcination with dry reforming of ethanol/glycerol mixtures. Crude glycerol is an attractive hydrogen donor which can be obtained as a byproduct

of biodiesel production. Although ethanol is not a major impurity in the crude glycerol, a mixture of glycerol and ethanol may be achieved during bioconversion of crude glycerol to ethanol. Table 1.5 demonstrates the main reactions involved in the limestone calcination combined with ethanol/glycerol dry reforming. Similar to limestone calcination in methane, Dang et al. [96] found that limestone decomposition in ethanol/glycerol mixture can offer a moderate H₂/CO syngas ratio (e.g. 1.2) in the presence of nickel-based catalysts. Nickel outperforms other metals (e.g. Co, Fe, Cu, Rh, Ru, and Pt), while its performance is similar to that for Pd-based catalyst. The authors did not observe any limestone calcination at temperatures below 700°C, and selected 765°C as the optimal operating temperature. Note that coke formation was also detected at low reactor temperatures. This could be avoided by increasing reactor temperature and/or limiting the reaction time. In addition, the variation of feedstock (glycerol + ethanol) concentration did not appreciably change the generated syngas quality. However, increasing ethanol concentration was shown to enhance the glycerol conversion within the reactor. Note that elevating the glycerol feed concentration substantially increases the feedstock viscosity, imposing several operating challenges on the system.

Table 1.5. Main reactions involved in calcination in ethanol/glycerol

Reaction	Stoichiometry	$\Delta H_{25^\circ\text{C}} \text{ (kJ.mol}^{-1}\text{)}$
Limestone Calcination [18]	$\text{CaCO}_3 \rightleftharpoons \text{CaO} + \text{CO}_2$	178
Glycerol Decomposition [97]	$\text{C}_3\text{H}_8\text{O}_3 \rightleftharpoons 3\text{CO} + 4\text{H}_2$	251.18
Water-Gas Shift Reaction [97]	$\text{H}_2 + \text{CO}_2 \rightleftharpoons \text{CO} + \text{H}_2\text{O}$	41.17
Ethanol Dry Reforming [97]	$\text{C}_2\text{H}_5\text{OH} + \text{CO}_2 \rightleftharpoons 3\text{CO} + 3\text{H}_2$	296.7
Glycerol Calcination *	$\text{CaCO}_3 + \text{C}_3\text{H}_8\text{O}_3 \rightleftharpoons \text{CaO} + 4\text{CO} + 3\text{H}_2 + \text{H}_2\text{O}$	470.35
Ethanol Calcination *	$\text{CaCO}_3 + \text{C}_2\text{H}_5\text{OH} \rightleftharpoons \text{CaO} + 3\text{CO} + 3\text{H}_2$	474.4

* Standard heat of reactions were calculated by summing the heats of reaction of the reactions involved.

Although the concept of integrating limestone calcination with *in situ* CO₂ utilization is very attractive, more investigations are required to optimize these technologies for practical applications. The currently proposed processes are either highly endothermic (e.g. calcination in methane and ethanol/glycerol) or utilize costly gaseous feedstock (hydrogen). The required energy for thermal processing of these technologies should be supplied by a parallel oxy-fuel combustor, or by utilizing solar-concentrated power. Oxy-fuel combustors require an upstream air separation unit, while solar-concentrated power systems have not been fully developed, and suffer from low solar-to-chemical energy conversion efficiency (e.g. 7-10% [92]). Coke formation is another significant challenge in these processes, which must be avoided by controlling the gas inlet flow rate, reaction time or reactor temperature. Given the dynamic variation of solid composition in fluidized bed reactors, it would be practically difficult to eliminate coke formation by dynamically controlling the gas inlet flow rate or reaction time. Increasing the reactor temperature also imposes additional thermal penalty on the system, while also increasing the rate of pore sintering during cyclic operations.

1.6.2.5. *Oxy-Fuel Calciners*

Nearly 35-50% of the energy demand for post-combustion CaL carbon capture is attributed to the sorbent regeneration in the limestone calciner [98,99]. This includes energy input for:

- Increasing the feed (solid and gas) temperature
- Conducting highly endothermic limestone calcination

Indirect reactor heating can increase the heat loss and temperature gradient, while also enlarging the calciner to provide adequate heat transfer area. Instead, limestone calcination can be conducted in the presence of oxy-fuel feedstock, burning hydrocarbon fuels (e.g. coal and natural

gas) with oxygen inside the reactor. This eliminates the need for external heating supply, while also generating highly-concentrated CO₂ for carbon storage [99–102]. To date, most pilot-scale CaL systems are integrated with oxy-fuel limestone calciners [103–106]. Oxy-fuel calciners have also been studied for quick lime production in rotary kilns [107]. From a practical perspective, oxy-fuel calciners are most likely to be employed in emerging CaL technology, including post- and pre-combustion carbon capture processes.

One key challenge in oxy-fuel limestone calciners is the high energy penalty required for oxygen production *via* air separation units [108]. The power generation efficiency in coal-based power plants with post-combustion CaL carbon capture (depicted in Figure 1.10) is around 38.8%, with the CO₂ product compression and air separation being the main sources of efficiency penalty [102]. Therefore, it is desirable to minimize fuel burning inside the calciner, decreasing the process oxygen requirement and CO₂ productivity. One plausible approach is to recover the high-quality heat carried by the calciner solid and gas products, as shown in Figure 1.10. This can be achieved by different heat exchanger configurations (e.g. gas-gas and gas-solid), and by recycling a portion of the calciner off-gas into the reactor [108,109]. Flue gas recycle can also control the flame temperature spike, which occurs due to fuel combustion at high oxygen concentrations [107]. The heat carried by the calciner gas and solid products may also be used for preheating and/or high-pressure steam generation, with the produced steam being further used in steam cycles and electricity generation [99,108–111]. Note that “Power” and “Heat” labels in Figure 1.10 are complementary, with appropriate heat integration enhancing the power generation efficiency of the process.

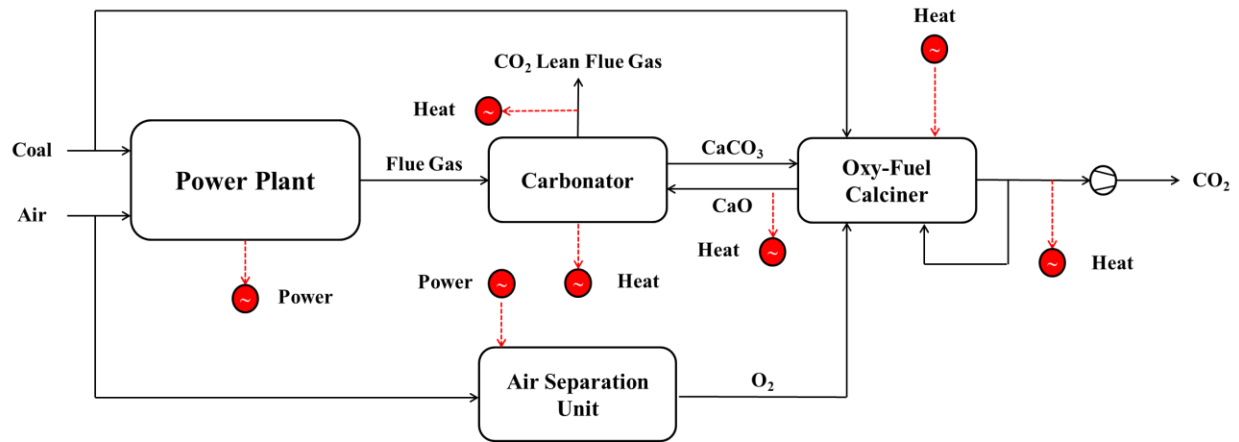


Figure 1.10. Schematic of coal-based power plant with post-combustion CaL carbon capture

The performance of oxy-fuel limestone calciners may depend strongly on the type of fuel applied for *in situ* heat generation. Coal and natural gas have been studied mostly, owing to their relatively low market price and wide geographical distribution [99,100,102–106,108–112]. Instead, biomass can be used to achieve “negative CO₂ emissions” within the system. However, biomass resources are limited, and cannot support the world’s growing demand for clean energy [59,77,102]. Another alternative is to burn hydrogen outside or inside the reactor, with the former case eliminating the need for an energy-intensive air separation unit [77]. Nevertheless, hydrogen is a precious gas, and burning it for energy production is not economically or environmentally attractive.

Despite its abundance and low cost, coal contains considerable impurities (e.g. S and Cl) which can adversely affect CaL performance. Both lime and limestone are highly favoured to be sulfated in the calciner range of operating conditions. This produces a CaSO₄ layer on the particle/pore surface, inhibiting limestone calcination by creating additional diffusional resistance to CO₂ evolution. Sulfated sorbents also lose their reactivity toward carbon capture, imposing the need for considerable sorbent make-up/purge flows [104,112,113]. Similarly, a

significant amount of HCl can be released by burning coal in power plants and oxy-fuel calciners. Nearly complete HCl removal can be achieved in the lime carbonator, with the chloride sorbent being fully regenerated in the calciner. This increases the HCl concentration within the calciner, resulting in equipment corrosion and failure if not addressed properly [59]. Ash deposition is another challenge linked to the coal-based oxy-fuel calciners, reducing sorbent reactivity for multi-cyclic operations. Coal ash can also agglomerate inside the calciner, leading to defluidization and reactor failure [106].

Compared to coal, natural gas is a cleaner fuel with no ash and very low sulfur content [109]. Lower CO₂ content of the flue gas in natural gas combustion can also offer lower calcination temperatures than in coal-based oxy-fuel calciners. However, the natural gas market price is currently higher than coal, and further economic analysis is required to assess economic feasibility.

In general, oxy-fuel calcination can eliminate the need for external heating supply, consequently increasing process thermal efficiency. Further enhancement can be achieved by utilizing alternative clean fuels (e.g. natural gas and biomass) and applying appropriate heat integration. Note that oxy-fuel calciners typically operate at higher reactor temperatures (e.g. >900°C at ambient pressure [102,106]) than those for calcination in inert-gases and steam. This is due to considerable CO₂ release by the fuel combustion, inhibiting limestone calcination at mild reactor temperatures. Elevating the calciner temperature adversely affects CO₂ capture capability of the calcined limestone, while also imposing an additional thermal penalty on the system. Several studies have suggested steam injection to reduce the CO₂ concentration within oxy-fuel calciners [101–103,105]. However, steam generation is energy-consuming, thereby steam dilution would only be preferred if steam comes from an available side-process (e.g. steam cycle [103]). Oxy-

fuel calciners may also operate with excess oxygen to ensure complete fuel combustion inside the reactor. This potentially dilutes the off-gas CO₂ concentration, while also resulting in catalyst oxidation/deactivation for some applications (e.g. sorbent-enhanced steam methane reforming).

1.7. Thesis Scope and Objectives

Limestone calciners are typically preferred to operate autothermally at reduced reactor temperatures, elevated pressures (depending on the carbonator pressure), and high CO₂ concentrations (or with CO₂ utilization). However, current technologies are incapable of meeting all these criteria simultaneously. The overarching objective of this thesis is to introduce a novel sorbent regeneration technology for low-temperature limestone calcination in calcium-looping. In addition, this project sought to investigate the effect of sorbent regeneration conditions, particularly partial limestone calcination, on the cyclic carbon capture capability of lime-based sorbents.

The effects of calcination temperature, duration, and extent (e.g. partial calcination) on the cyclic carbon capture capability of lime-based sorbents are examined in depth in Chapter 2 utilizing thermogravimetric analysis. Particular attention is given to the impact of partial/incomplete limestone calcination, where there is a major gap in prior scientific research. Some additional tests are also conducted to evaluate effects of heating rate and steam reactivation on the CO₂ capture capability of sorbents. However, these experiments could not be completed by the time of writing this thesis for reasons beyond the control of the author. The limited experimental results are therefore summarized and discussed in Appendices.

A novel sorbent regeneration technology is proposed in Chapter 3, combining methane reforming, combustion and limestone calcination (e.g. methane concentrated oxy-fuel

calcination) in a single reactor. Aspen Plus simulation is employed to evaluate the thermodynamic equilibrium of the proposed process at different operating conditions. It is shown that methane-concentrated oxy-fuel calciners can offer autothermal, coke-free and complete limestone calcination under certain circumstances. The proposed process also generates a highly valuable byproduct (syngas), utilizing a portion of the CO₂ released during limestone calcination.

Reactor simulations are carried out in Chapter 4, evaluating the kinetic performance of methane-concentrated oxy-fuel fluidized bed limestone calciners. The effects of operating conditions are assessed, and the results are compared to those for conventional steam calciners. A simple, yet effective, methodology is then suggested to determine the proper range of operating conditions and/or reactor dimensions for limestone calcination with this novel sorbent regeneration technology.

The performance of sorbent-enhanced steam methane reformers, integrated with steam and methane-concentrated oxy-fuel calciners, is evaluated in Chapter 5 for different operating conditions. The potential system performance is also assessed when hydrogen perm-selective membranes are installed inside the reformer. The methane-concentrated oxy-fuel calciner is shown to benefit from lower reactor temperature, higher hydrogen production yield and lower CO₂ emissions.

Additional thermodynamic/kinetic simulations are performed in Chapters 6 and 7 to shed light on some potential applications of this novel limestone calcination technology. In particular, Chapter 6 introduces an advanced lime hydration configuration, utilizing saturated steam as the sorbent reactivating reagent and direct-heat-removal medium. This enables controlling the lime hydrator temperature without internal heat-removal facilities, while also producing substantial

superheated steam as a by-product. The equilibrium performance of the methane-concentrated oxyfuel calciners is then extensively studied for co-calcining limestone and slaked-lime at different operating conditions.

Chapter 7 studies the equilibrium and kinetic performance of methane-concentrated air-fuel limestone calcination at elevated reactor pressures (up to 25 bars). The process syngas is shown to be mainly composed of H_2 , CO , and N_2 , which can be further used for ammonia synthesis without air separation. The equilibrium performance of the process is evaluated at different reactor pressures, operating temperatures, feeding ratios and air oxygen concentrations. A kinetic model is also employed to assess the system performance in turbulent fluidized bed reactors.

Chapter 8 summarizes the overall conclusions from this study and proposes some recommendations.

CHAPTER 2: Effects of Calcination Temperature and Extent on CO₂ Carrying Capacity of Lime-Based Sorbents

2.1. Introduction

One of the key challenges in calcium-looping technology is sorbent deactivation over multiple cycles. This leads to a significant reduction of CO₂ carrying capacity in the first few calcination-carbonation cycles, requiring substantial sorbent make-up flow for continuous operation. Sorbent utilization decay of lime-based sorbents is linked to the pore evolution (e.g. pore sintering) during limestone calcination [46–48,114–116]. Previous studies [51,52] have shown that increasing calcination temperature (e.g. to 850-1200°C) can accelerate pore sintering and sorbent deactivation in the first few reaction cycles. On the other hand, there have been contradictory observations regarding the effect of the duration of calcination on the cyclic performance of lime-based sorbents. Grasa and Abanades [51] observed no differences when calcination conditions were extended after reaction completion. In contrast, Manovic et al. [52] reported enhanced sorbent utilization when the duration of calcination was long (up to 4 h). Sun et al. [46] showed that extending the calcination period resulted in enhanced pore sintering, thereby, accelerating sorbent deactivation.

To date, there has not been a systematic study of the effect of incomplete (partial) limestone calcination on the cyclic performance of lime-based sorbents. Partial calcination is most likely to occur when there is limited sorbent residence time and a progressive increase of CO₂ concentration within a calciner. This chapter addresses cyclic (up to 100 cycles) performance of naturally-derived lime-based sorbents at different calcination temperatures and for various durations. A semi-empirical method is also introduced to estimate the fast-stage carbonation

extent as a function of the number of calcination-carbonation cycles, calcination temperatures, and calcination extent.

2.2. Experimental Details

Cyclic calcination-carbonation tests were conducted experimentally for two limestones (Strassburg from eastern USA, and Cadomin from western Canada), both screened to 500-710 μm . The tests were carried out in a TA Instruments SDT-Q600 thermogravimetric analyzer (TGA) in the department of Chemical and Biological Engineering. Approximately 15 mg of limestone particles was thinly spread on a ceramic pan for each test. The sweep gas flow rate was maintained at 300 ml (STD)/min in order to reduce the external mass transfer resistance around the sorbent particles and to decrease the time needed to switch the gas medium. Each test was initiated by 15-min of sorbent dehydration (initial pretreatment) at 105°C, and 90-min of secondary pretreatment (to decompose the MgCO_3 impurity of the limestone samples) at 450°C, both in a pure CO_2 atmosphere. The temperature was next raised quickly to the target calcination temperature. Calcination-carbonation cycles were then achieved by periodically varying the chamber gaseous medium and the operating temperature. Heating and cooling rates were maintained at 20°C/min, unless otherwise specified. Nearly pure (>99.5%: Praxair) CO_2 and N_2 were used to conduct the carbonation and calcination, respectively. This was to facilitate the performance evaluation and data interpretation when sorbents are partially calcined. The gaseous feed stream was switched as soon as the system reached the target reaction temperature.

Some limestone samples were reduced to the optimum grain-size range for quantitative X-ray analysis (<10 μm) by grinding under ethanol in a vibratory McCrone Micronizing Mill for 10 minutes. Continuous-scan X-ray powder-diffraction data were collected over a range of 3-80°2 θ

with CoK α radiation on a Bruker D8 Advance Bragg-Brentano diffractometer, equipped with a Fe filter foil, 0.6 mm (0.3°) divergence slit, incident- and diffracted-beam Soller slits, and a LynxEye-XE detector, located in the department of Earth, Ocean and Atmospheric Sciences, UBC. The long fine-focus Co X-ray tube was operated at 35 kV and 40 mA, using a take-off angle of 6°. The X-ray diffractograms were analyzed using the International Centre for Diffraction Database PDF-4 and Search-Match software by Bruker. X-ray powder-diffraction data of the samples were then refined with Rietveld program Topas 4.2 (Bruker AXS). The Rietveld-refined XRD results are presented in Table 2.1.

Table 2.1. XRD measurement results for different limestones

Limestone	Mineral Phase	Formula	wt%
Strassburg	Calcite	CaCO ₃	97.4
	Dolomite	CaMg(CO ₃) ₂	2.0
	Quartz	SiO ₂	0.6
Cadomin	Calcite	CaCO ₃	91.1
	Dolomite	CaMg(CO ₃) ₂	7.0
	Quartz	SiO ₂	1.5
	Pyrite	FeS ₂	0.1
	K-Feldspar	KAlSi ₃ O ₈	0.3

The dynamic variation of sorbent conversion was calculated as:

$$X(t) = \frac{m_0 - m(t)}{0.44m_0} \quad (2.1)$$

where m_0 is the weight of the limestone after the secondary pretreatment, and $m(t)$ is the instantaneous weight of the solid at time t during the reaction. Note that Equation (2.1) is based

on a 100% CaCO₃ sample after the secondary pretreatment, considering minor sorbent impurities (e.g. MgO, ~1 and 3 wt% for the Strassburg and Cadomin limestones, respectively) as inactive inert. The carbonation reaction was conducted at 650°C for 15 minutes, unless otherwise specified. The calcination temperature and duration were varied, with a summary of tested conditions presented in Table 2.2. These test conditions are governed by the factors investigated in this chapter, including effects of calcination temperatures (runs # 1-5), extended calcination duration (runs # 1, 3, 5, 7-9), exposing limestone to high temperature without reaction (runs # 8 and 10), partial limestone calcination (runs # 1, 6, 11-13), and the type of limestone sorbent (runs # 14-17). The extent of the fast reaction-controlled carbonation regime in each cycle was determined by:

1. Locating $\left. \frac{dX}{dt} \right|_{\max}$ (min⁻¹) and its corresponding time, t_{\max} (min);
2. Plotting $\bar{X}(t) = \left(\left. \frac{dX}{dt} \right|_{\max} \right) (t - t_{\max} - 0.3) + X(t_{\max})$ versus time;
3. Finding intersection of the experimental data and \bar{X} as the fast-stage carbonation extent.

Note that the 0.3 minutes offset was selected based on 2% of the carbonation duration in each 15 min cycle, similar to that typically applied for defining the offset of yield stress. Some tests were repeated to ensure reproducibility of the experimental results, as indicated in Table 2.2. Figure 2.1 confirms the reproducibility of the TGA test results, with very low standard deviations achieved by three-time repetition of a single cyclic test (run #3 in Table 2.2). Note that blue intervals in Figure 2.1 show +/- standard deviation at each calcination-carbonation cycle, calculated using the Excel built-in STDEV function.

Table 2.2. Summary of experimental conditions tested. (Measurement accuracy = +/- 5°C)

Test #	Limestone	Calcination Temperature (°C)	Calcination Time (min) *	# of Cycles	# of Test Repetitions
1	Strassburg	800	15	100	2 (Repeated for 20 cycles)
2	Strassburg	825	15	100	1
3	Strassburg	850	15	100	3 (Repeated for 20 cycles)
4	Strassburg	875	15	100	1
5	Strassburg	900	15	100	2 (Repeated for 20 cycles)
6	Strassburg	800	6	100	2 (Repeated for 20 cycles)
7	Strassburg	800	30	20	1
8	Strassburg	850	6	20	1
9	Strassburg	900	6	20	1
10	Strassburg	850	6	10 TS cycles in CO ₂ + 18 regular cycles	1
11	Strassburg	800	10 cycles at 4 min 10 cycles at 6 min 30 cycles at 15 min	50	1
12	Strassburg	800	10 cycles at 6.5 min 10 cycles at 6 min 10 cycles at 6.5 min 10 cycles at 7 min	40	1
13	Strassburg	Same as Run 11 with 30°C/min cooling ramp			1
14	Strassburg	Same as Run 3 except for carbonation temperature of 850°C		40	1
15	Strassburg	Same as Run 14 except for calcination duration of 5 minutes		40	1
16	Cadomin	Same as Run 14			1
17	Cadomin	Same as Run 15			1

* Time = 0 corresponds to when calcination temperature was reached.

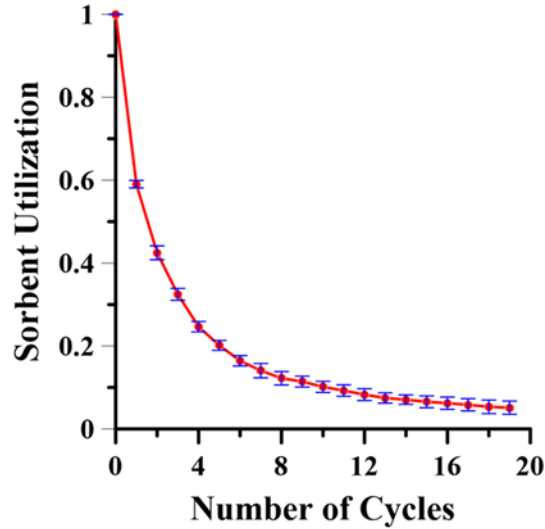


Figure 2.1. Reproducibility of the cyclic thermogravimetric analysis results. For test conditions, see run 3 in Table 2.2. Red points are the average sorbent utilization achieved by three-time repetition of the cyclic TGA test. Blue error bars show plus and minus the calculated standard deviation at each calcination-carbonation cycle.

Note that the range of limestone calcination temperature in Table 2.2 (800-900°C) was selected based on the typical range of sorbent regeneration temperature in calcium-looping processes. In fact, limestone calcination can be slow at temperatures <800°C, while temperatures >900°C are not practically attractive owing to the significant loss of sorbent utilization (i.e., high thermal pore sintering), high cost of material of construction, and low reactor thermal efficiency. On the other hand, the duration of limestone calcination (6-30 min, see Table 2.2) was chosen based on the preliminary tests to achieve complete, partial, and extended-duration (after completion) sorbent regeneration at different conditions.

2.3. Results and Discussion

2.3.1 *Effect of Calcination-Carbonation Cycling*

A typical sorbent conversion and temperature profile, obtained during the TGA experiments, is depicted in Figure 2.1. The stars in Figure 2.1(b) identify the sorbent conversion at the end of the

initial reaction-controlled carbonation stage, referred to henceforth as sorbent utilization. Calcined limestone rapidly lost its reactivity during the first few cycles, with utilization decay then decelerating with further calcination-carbonation cycling. This decay in sorbent utilization can be attributed to thermal pore sintering, a well-known phenomenon in calcium-looping processes [46–48,114–116]. Note that the transition from carbonation-to-calcination (by temperature swing, TS) was conducted in CO₂ to avert limestone calcination before reaching the target reaction temperature, at which the gas was switched to nitrogen. This led to a sudden jump in sorbent conversion (during the TS period), probably owing to enhanced CO₂ diffusion through the CaCO₃ product layer as the temperature increased. Similarly, the calcination-to-carbonation transition was conducted in N₂, preventing lime carbonation prior to reaching the target carbonation temperature. Therefore, limestone calcination progressed slowly during the TS period, especially if the isothermal calcination stage did not provide complete sorbent regeneration.

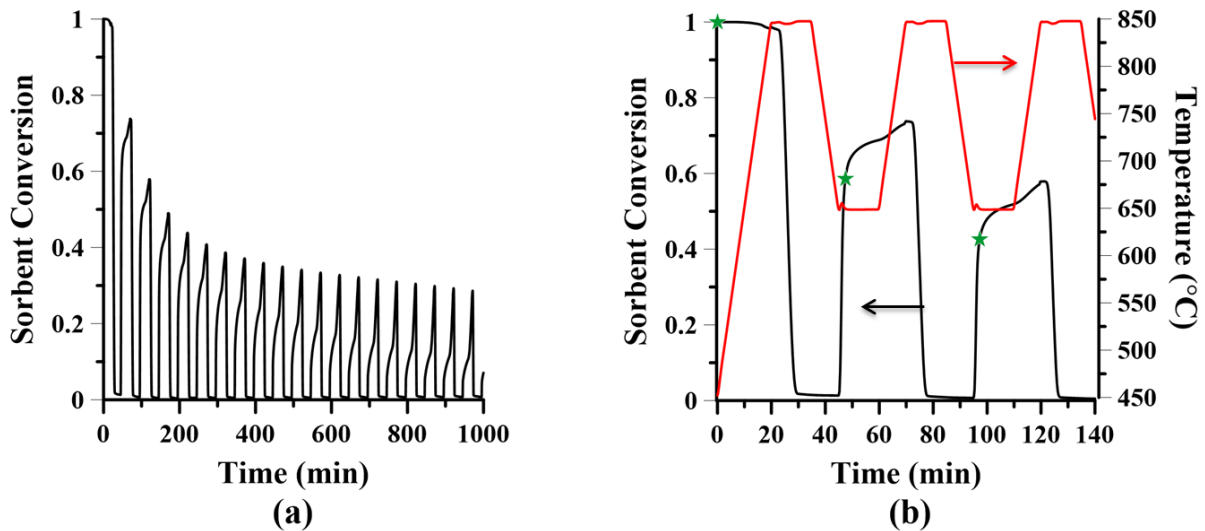


Figure 2.2. Typical sorbent conversion and temperature profile during cyclic calcination-carbonation tests. Stars show the fast-stage carbonation extent in each cycle. For test conditions, see run 3 in Table 2.2.

Both carbonation and calcination followed sigmoidal curves with respect to reaction time, as depicted in Figure 2.2. The existence of an induction period (time to start reaction) has been previously linked to the nucleation process on the particle surface [117]. In addition, the slow rate of gas replacement around sample particles might be responsible for the late initiation of reactions in TGA. This potentially explains the longer induction period observed for the limestone calcination than for lime carbonation; as the gaseous medium must be varied further to surpass the CaCO_3/CaO thermodynamic equilibrium. Note that Figure 2.2(a) plots the limestone calcination extent, normalized by the carbonate produced during the previous cycle:

$$X_{\text{Calc, Norm, N}} = \frac{X_{\text{Carb, N-1}} - (1 - X_{\text{Calc, N}})}{X_{\text{Carb, N-1}}} \quad (2.2)$$

where $X_{\text{Calc, Norm, N}}$ represents the normalized limestone calcination extent at cycle N, $X_{\text{Carb, N-1}}$ is the lime fast-stage carbonation extent at cycle N-1 relative to fully calcined particles, and $X_{\text{Calc, N}}$ is the limestone calcination extent at cycle N relative to fully carbonated particles. The deviation of the ultimate normalized calcination extent from unity at the higher numbers of cycles (Figure 2.2(a)) could be due to the sensitivity of Equation (2.2) at low carbonation extents. The CaCO_3 molar fraction profile during limestone calcination (Figure 2.3) confirms that nearly complete sorbent regeneration was achieved in all cycles of this TGA experiment.

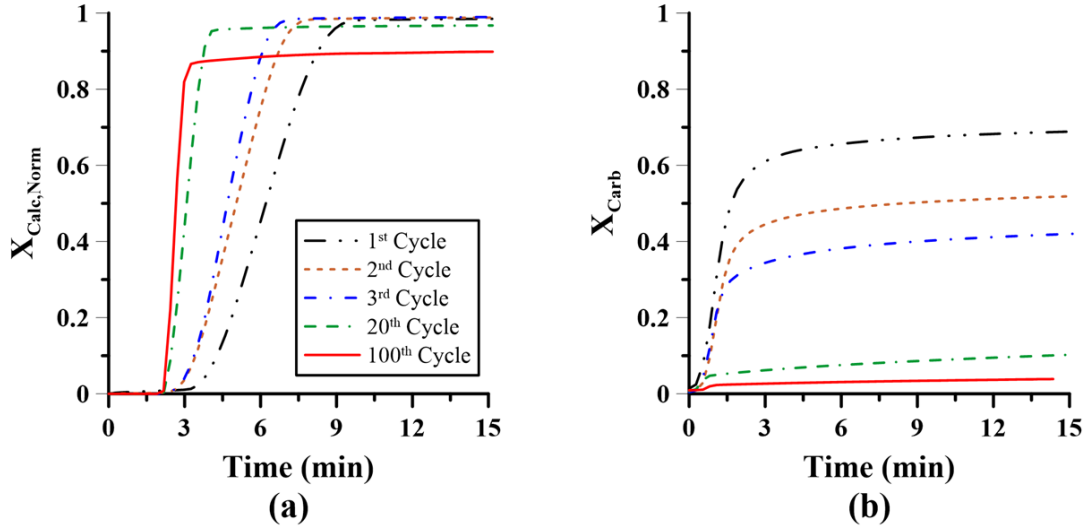


Figure 2.3. Normalized (a) calcination; and (b) carbonation profiles at different calcination-carbonation cycles. For test conditions, see run 3 in Table 2.2.

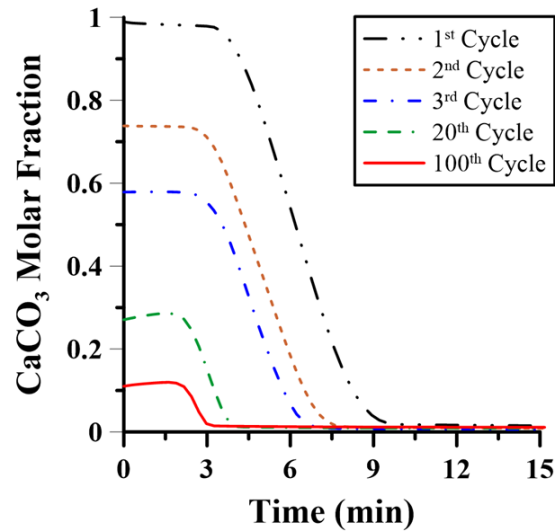


Figure 2.4. CaCO₃ molar fraction time variation during limestone calcination after different numbers of calcination-carbonation cycles. For test conditions, see run 3 in Table 2.2.

The limestone calcination rate appears to have increased over calcination-carbonation cycles, while the rate of fast-stage carbonation remained nearly independent of cycling. This can be observed from Figure 2.2, as well as from the dynamic variation of the reaction rates for different

cycles (Figure 2.4). It is widely accepted that pore sintering reduces active surface area within the sorbent, therefore decreasing the carbonation extent during cycling [46–48,114–116]. This leads to lower carbonate formation (mostly on the sorbent particle surface) during carbonation and, accordingly, less resistance for CO₂ outward diffusion during calcination. Thus, the rate of limestone calcination increases with increasing number of reaction cycles, with less increase in the calcination rate observed at higher numbers of cycles (Figures 2.2(a) and 2.4(a)). On the other hand, the rate of fast-stage lime carbonation appears to be independent of the number of reaction cycles, whereas the reaction-controlled carbonation extent substantially decreased during cycling. This could be attributed to the fact that the rate of fast-stage carbonation is dominated by the intrinsic reaction rate, while the fast-stage carbonation extent relies on the available surface area within the sorbent. Similar findings were also observed in other tests conducted for total calcination conditions (e.g. tests 1-5 in Table 2.2.).

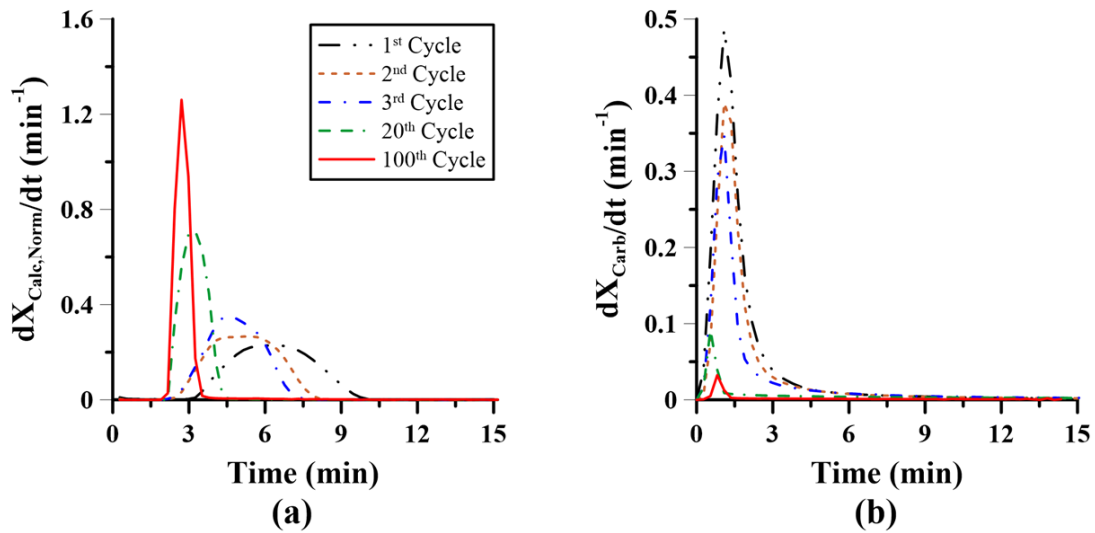


Figure 2.5. Normalized (a) calcination; and (b) carbonation rate profiles with different calcination-carbonation cycles. For test conditions, see run 3 in Table 2.2.

2.3.2 Effect of Calcination Temperature

Elevating the calcination temperature accelerates the sorbent utilization decay in the first few cycles, as shown in Figure 2.5(a). However, the residual sorbent utilization (after many cycles) at all calcination temperatures nearly approached zero. This observation is contrary to earlier studies where a non-zero sorbent utilization was observed [46,51]. The discrepancy may come from different applied carbonation temperatures, as well as different methodologies employed to determine the lime carbonation extent in each cycle. The present work determines the maximum sorbent conversion in the fast reaction-controlled carbonation regime, while previous studies mostly took the highest sorbent conversion at the end of each cycle. Note that the latter approach can depend highly on the reaction time, and may lead to sorbent being converted through both carbonation regimes. Accordingly, it may be concluded that the reaction-controlled carbonation extent nearly approaches zero after many cycles, while diffusion-controlled carbonation becomes dominant for highly sintered particles.

Raising the calcination temperature substantially enhanced the rate of limestone decomposition (Figure 2.5(b)) by increasing both the reaction rate constant and the driving force [118,119]. In addition, raising the calcination temperature led to a shorter induction period, confirming our earlier hypothesis on the significance of switching gaseous medium around sorbent particles. In fact, limestone can decompose at higher CO₂ partial pressures at elevated temperatures. Therefore, the composition of gaseous medium in the reaction chamber should vary less to initiate limestone calcination, corresponding to shorter induction periods at higher calcination temperatures.

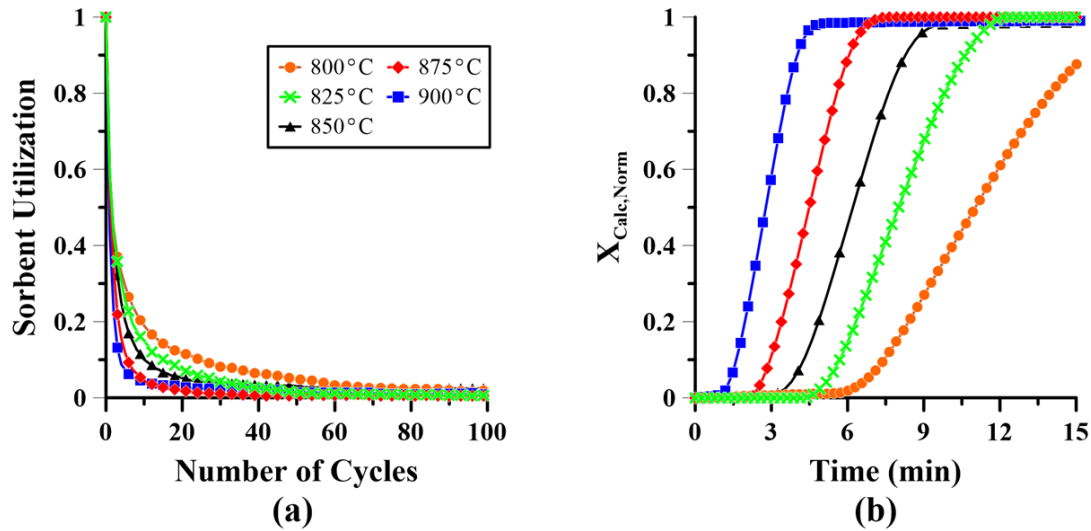


Figure 2.6. Effect of calcination temperature on: (a) cyclic sorbent (Strassburg) utilization; and (b) first-cycle calcination rate. Test conditions correspond to runs 1-5 in Table 2.2. Every third experimental data points is plotted in (a) for clearer presentation of the data.

2.3.3 Effect of Calcination Duration

The effect of the duration of calcination on the cyclic performance of the lime-based sorbent is depicted in Figure 2.6. Extending the calcination time from 6 to 15 minutes did not affect the sorbent performance at 850 and 900°C. Similarly, increasing the calcination duration from 15 to 30 minutes did not appreciably change the cyclic sorbent utilization at 800°C. It should be noted that the sorbent particles were fully calcined after 6 min at 850 and 900°C, as well as after 15 min at 800°C. Clearly, extending the calcination time after reaction completion had negligible impact on the sorbent cyclic performance, in agreement with findings of Grasa and Abanades [51]. On the other hand, reducing the duration of calcination from 15 to 6 minutes greatly altered the sorbent cyclic utilization at 800°C (Figure 2.6(b)). This was due to incomplete limestone calcination, leaving a portion of the sorbent uncalcined before entering the next carbonation stage. Note that the sorbent utilization in this case does not represent the CO₂ carrying capacity

of the sorbent since the uncalcined inner portion of the sorbents has not participated appreciably in capturing carbon.

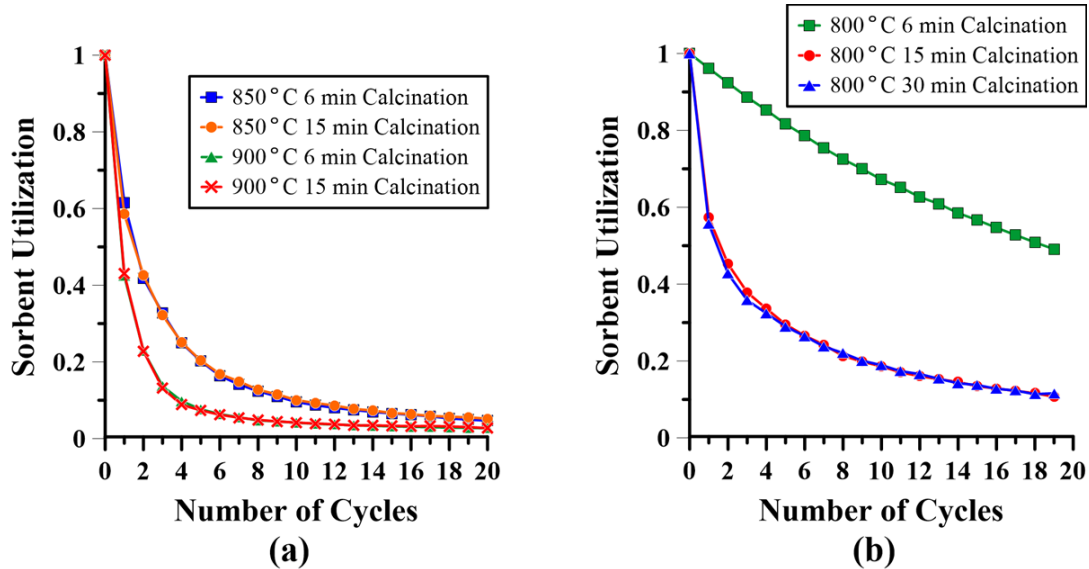


Figure 2.7. Effects of calcination temperature and duration on the cyclic performance of Strassburg sorbents. For test conditions, see runs 1, 3 and 5-9 in Table 2.2.

Two prolonged cyclic tests (100 cycles, runs 1 and 6 in Table 2.2) were conducted to evaluate the effect of partial calcination during extended calcination-carbonation cycles. A lower rate of sorbent utilization decay was achieved after partial calcination (Figure 2.7(a)), possibly due to gradual utilization of uncalcined sorbent when cycling. This can be confirmed by the progressive increase in limestone calcination extent with increasing number of cycles, as demonstrated in Figure 2.7(b). Note that the limestone calcination would have remained constant if there had been no decay in sorbent utilization. However, the loss of sorbent reactivity led to less sorbent re-carbonation and, consequently, the uncalcined portion of the sorbent being partially calcined during the next regeneration stage. Gradual utilization of the uncalcined sorbent is promising since it may offer a more stable CO₂ capture performance during multiple-cycle operation. Lower calciner temperatures and sorbent residence times are also needed for partial limestone

calcination, enhancing both the cyclic performance of the sorbent and the overall thermal efficiency of the process.

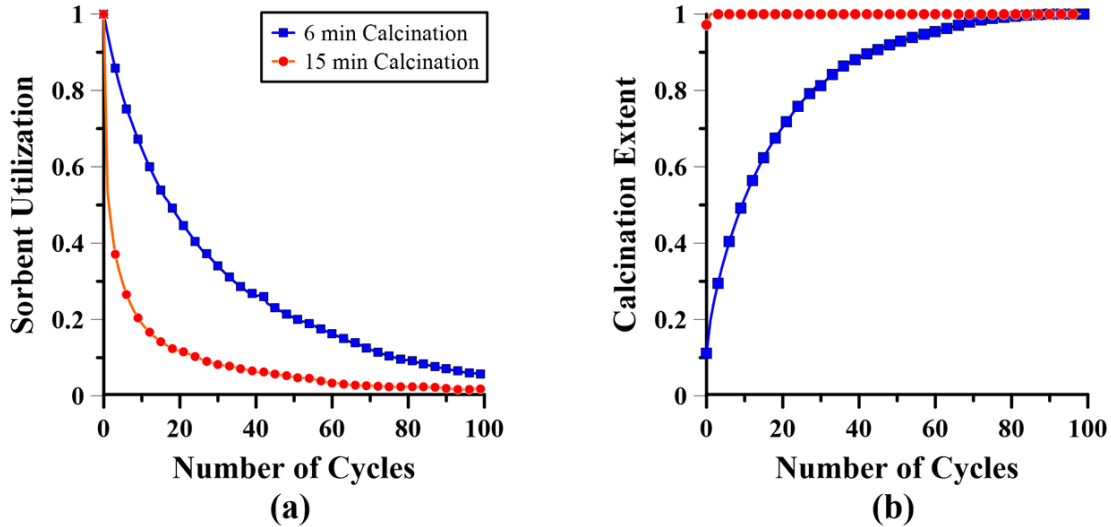


Figure 2.8. Effect of partial calcination on cyclic: (a) carbonation; and (b) calcination extents. For test conditions see runs 1 and 6 in Table 2.2. Every third experimental data point is plotted for better viewing.

Gradual utilization of the uncalcined sorbent would only be attractive if the preserved uncalcined portion maintains high CO₂ carrying capacity after being calcined. In other words, high operating temperatures should not adversely affect the reactivity of the uncalcined portion of the sorbent during cycling. As verification, a single test was conducted where sorbents were initially exposed to 10 successive temperature swing cycles in CO₂ (run 10 in Table 2.2, referred to henceforth as CO₂ pre-treatment). This virtually averted limestone calcination, while exposing the carbonated sorbent to high temperature. The carbonated sorbents were observed to maintain their reactivity after being exposed to a high operating temperature, as shown in Figure 2.8. Note that the small deviation could be due to slight variation of solid sample composition in the two tests, as well as minor limestone calcination during the CO₂ pre-treatment period. Sorbent utilization decay may be explained by means of pore evolution *via* three possible mechanisms:

1. Sintering of CaCO_3 before calcination
2. Pore sintering because of calcination
3. Sintering of CaO after calcination

Figures 2.6 and 2.8 clearly indicate that sintering of CaCO_3 and CaO (before and after calcination) did not appreciably affect the sorbent cyclic performance. Instead, pore sintering during limestone calcination is dominant, confirming that the sorbent utilization decay is predominantly due to material chemical and physical changes during limestone calcination. Therefore, partial limestone calcination remains helpful, since uncalcined sorbent, upon being calcined, behaves in a manner similar to freshly calcined sorbents.

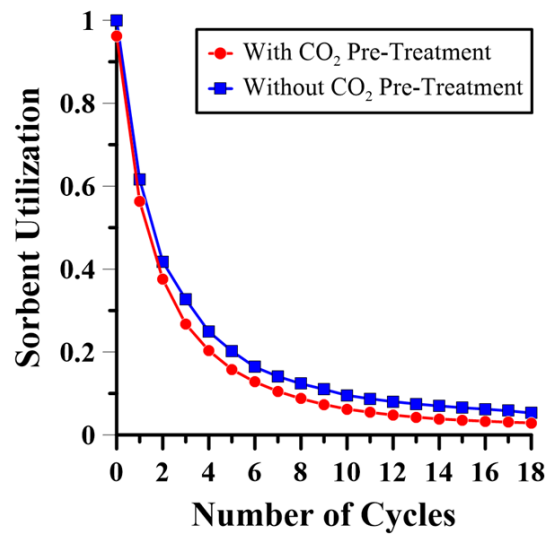


Figure 2.9. Effect of CO_2 pre-treatment on the cyclic performance of Strassburg sorbent. For test conditions, see runs 8 and 10 in Table 2.2.

As discussed above, sorbent utilization profiles alone cannot provide sufficient knowledge on the CO_2 carrying capacity of partially calcined sorbents. To address this, the CO_2 carrying capacity of partially calcined sorbents at different calcination extents may be calculated by

$$\text{Single-Cycle Carbon Capture}|_N = X_{\text{Carb},N} - (1 - X_{\text{Calc},N}) \quad (2.3)$$

Figure 2.9 compares the single-run and cumulative carbon capture capability of lime-based sorbents under partial and total calcination conditions (test conditions identical to those in Figure 2.7). These results show that partial calcination offers lower carbon capture capability for the first few cycles, but its results surpass those for total calcination at around the 17th cycle. This is due to progressive utilization of uncalcined sorbent, leading to a relatively stable performance from the 17th to the 40th cycle. The CO₂ carrying capacity of the partially calcined sorbents then slowly decreases, approaching that obtained for totally calcined particles. The higher CO₂ carrying capacity of the partially calcined sorbents (after 17 cycles) led to a faster increase in cumulative carbon capture, which eventually surpassed fully calcined particles at around the 50th cycle. Note that a portion of the sorbents in partial calcination tests was regenerated during the carbonation-to-calcination transition periods. This may also have led to enhanced sorbent utilization since a portion of the sorbent is calcined at reduced temperatures. Further discussion is provided in the next section.

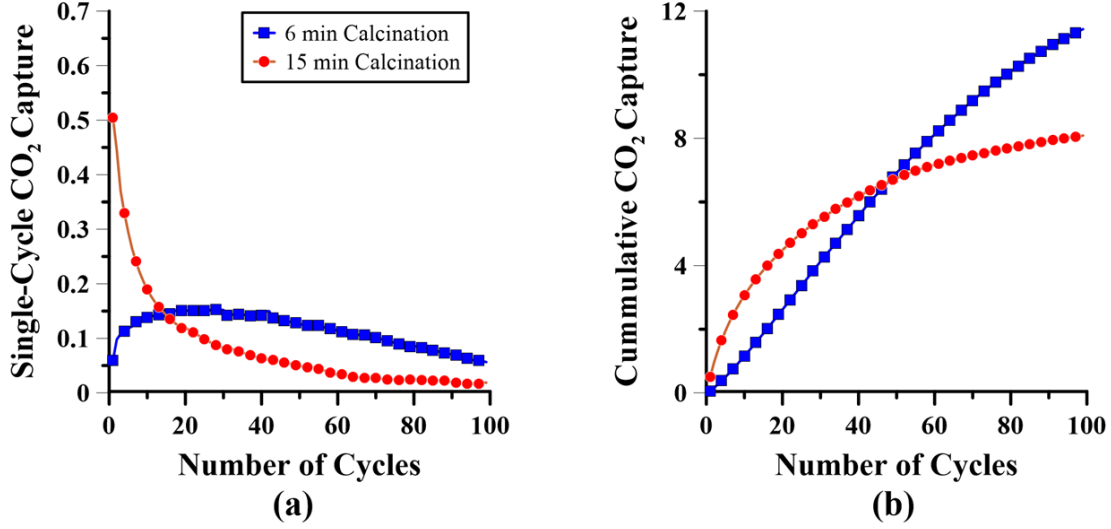


Figure 2.10. Effect of partial and total calcination on: (a) single-cycle; and (b) cumulative CO₂ capture capacity of Strassburg sorbent. For test conditions see runs 1 and 6 in Table 2.2. Every third experimental data point is plotted for better viewing.

2.3.4 Cyclic Sorbent Utilization in Equation Form

Grasa and Abanades [51] applied a 2nd-order surface reduction model to predict sorbent utilization as a function of the number of calcination-carbonation cycles:

$$-\frac{d\left(\frac{S_N}{S_0}\right)}{dN} = k_d \left(\frac{S_N - S_r}{S_0}\right)^2 \quad (2.4)$$

$$X_{Carb,N} = \frac{1}{\frac{1}{1 - X_r} + k_d N} + X_r \quad (2.5)$$

where k_d represents the surface reduction constant, S_N is the active surface area at cycle N , S_0 is the initial active surface area, S_r is the residual active surface area after many cycles, $X_{Carb,N}$ is the sorbent utilization at cycle N , and X_r is the residual sorbent utilization after many cycles. A

similar approach is employed here to estimate the sorbent cyclic performance for the complete calcination scenario. Equation (2.5) is rearranged to

$$d_N = \frac{X_{Carb,N-1} - X_{Carb,N}}{X_{Carb,N-1}} = \frac{k_d}{1 + k_d N} \quad N > 0 \quad X_r = 0 \quad X_{Carb,0} = 1 \quad (2.6)$$

where d_N is the normalized sorbent utilization decay. This normalizes the sorbent utilization decay with respect to lime carbonation from the previous cycle, simplifying performance evaluation when incomplete limestone calcination occurs during operation. Note that the reaction-controlled carbonation extent nearly approaches zero as the calcination-carbonation cycling proceeds. Therefore, the “residual sorbent utilization (X_r)” introduced by Grasa and Abanades [51] equals zero for the normalized sorbent utilization decay factor (d_N) in Equation (2.6).

Equation (2.6) is employed to fit the experimental data for the total calcination tests at different calcination temperatures. Curve fitting was conducted by maximizing the coefficient of determination (R^2) in each test. The surface reduction constant (k_d) was fitted by an Arrhenius relationship with respect to the absolute calcination temperature (Equation (2.7)), as seen in Figure 2.10. The cyclic sorbent utilization profile at each temperature can then be calculated by means of Equations (2.6) and (2.7). The predictions of the empirical equation are compared with experimental results in Figure 2.11, showing good agreement for all conditions investigated.

$$k_d = 10^6 \times \exp\left(\frac{-15678}{T_{Calcination}(K)}\right) \quad 1073 \leq T_{Calcination}(K) \leq 1173 \quad (2.7)$$

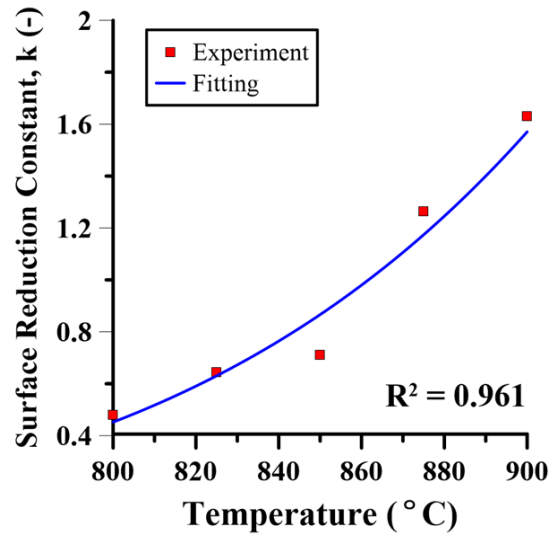


Figure 2.11. Arrhenius-type fitting of surface reduction constants (k) at different calcination temperatures.

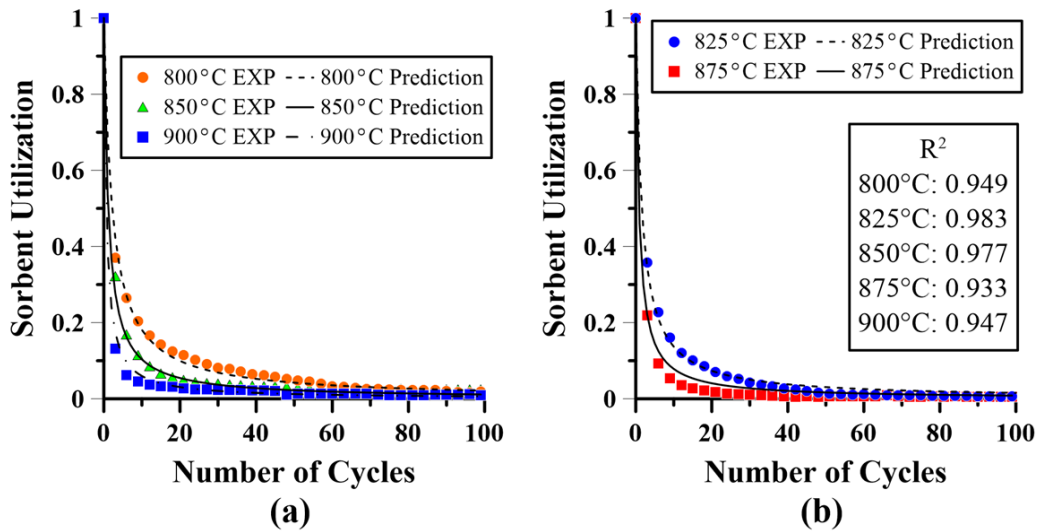


Figure 2.12. Comparison of experimental data for totally calcined Strassburg sorbents with predictions of Equations (2.6) and (2.7) at different calcination temperatures. Every third experimental data point is plotted to give clearer plots.

The Grasa and Abanades [51] equation (Equation (2.5)) is limited to calcium-looping systems with complete sorbent regeneration prior to each lime recarbonation stage. Accordingly, Equation (2.5) is not capable of predicting sorbent cyclic performance under partial calcination

conditions. Incomplete sorbent calcination can produce different regimes with different reaction history and cycling age for each sorbent particle. Therefore, a new equation is developed which considers the sorbent to be a mixture of CaCO_3 and CaO , with the CaO being composed of several sub-parts with different ages. The normalized sorbent utilization decay (d_N) in each CaO sub-part is assumed to be identical to those for total calcination (Equations (2.6) and (2.7)), neglecting possible mutual impact of CaO sub-parts on each other:

$$X_{\text{Carb},N} = (1 - X_{\text{Calc},N}) + \sum_{i=1}^N \left[(X_{\text{Calc},i} - X_{\text{Calc},i-1}) \left(\prod_{j=1}^{N-i+1} (1 - d_j) \right) \right] \quad X_{\text{Calc},0} = 0 \quad (2.8)$$

Equations (2.6)-(2.8) were used together to predict the sorbent cyclic utilization in run 6 (Table 2.2). The calcination extent in each cycle was read directly from the experimental data in Figure 2.7(b). Fair agreement is achieved between the predictions and experimental results, with more deviations observed as the number of calcination-carbonation cycles increased, as shown in Figure 2.12. This could be due to progressive limestone calcination during temperature transition periods, enhancing the sorbent utilization by calcining a portion of the sorbent at milder temperatures. A similar conclusion can be derived from the sensitivity analysis in Figure 2.12, where the predictions for 750°C calcination show better agreement with the experimental results than for limestone calcination at 800°C.

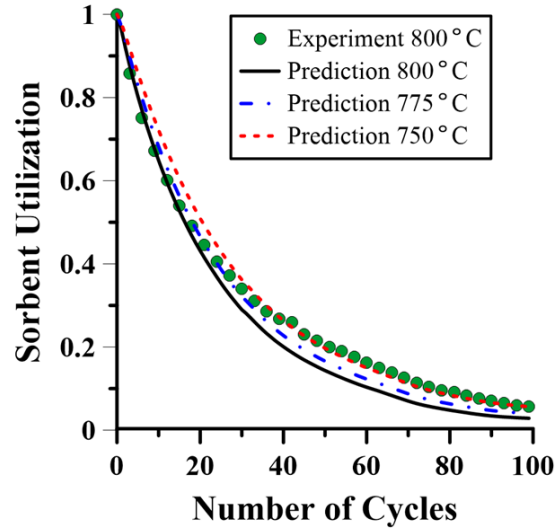


Figure 2.13. Comparison of experimental data with the predictions of Equations (2.6)-(2.8) for run 6. Every third experimental data point is plotted for clearer presentation.

Two cyclic tests (runs 11 and 12) were conducted next to evaluate the predictive method by periodically changing the calcination duration while cycling. It can be seen from Figure 2.13 that the predictions are in line with the experimental results, although there are some deviations at higher numbers of calcination-carbonation cycles. This could again be due to progressive limestone calcination during calcination-carbonation transition periods. To confirm this hypothesis, run 11 was repeated by increasing the cooling rate during the calcination-carbonation transition period. Better agreement was then observed between the predictions and experimental results, supporting our hypothesis regarding the impact of limestone calcination during the temperature swing period.

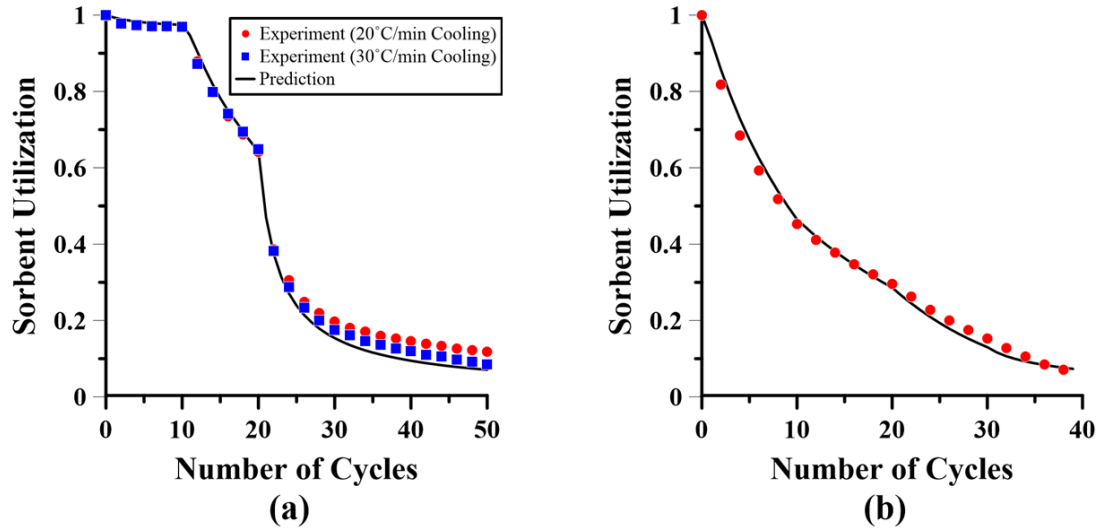


Figure 2.14. Comparison of experimental data and Equation (2.8) predictions for cyclic tests with periodically changing calcination duration during cycling (test conditions: (a) runs 11 and 13 (b) run 12 in Table 2.2). Every second experimental data point is plotted for better clarity.

The partial limestone calcination during the temperature swing (TS) transition period can be averted by using CO_2 as the gaseous medium during transition periods. However, this initiates lime carbonation above the target temperature, leading to inconsistency between testing conditions. Alternatively, isothermal calcination-carbonation cycling can be employed to eliminate the temperature swing transition period, thereby ensuring that limestone calcination occurs solely at the intended temperature. Two additional tests (runs 14 and 15 in Table 2.2) were conducted at isothermal calcination-carbonation cycling (850°C) to evaluate the method accuracy when the TS transition period does not exist. This also enables investigation of the sorbent performance at different carbonation temperatures, as the other tests conditions were identical to those for run 3 in Table 2.2.

Figure 2.14(a) indicates that increasing the carbonation temperature considerably enhanced the sorbent utilization in the reaction-controlled carbonation regime. Similar observations have been reported for cyclic lime carbonation at reaction temperatures of $450\text{-}725^\circ\text{C}$ [120]. This could be

due to enhanced CO_2 diffusion through the CaCO_3 product layer, with reduced diffusional resistance, thereby impeding the transition to the slow carbonation regime. Given the significant impact of lime carbonation temperature on the surface reduction constant, k_d , Equation (2.7) is not capable of predicting the surface reduction constant for run 14. Therefore, experimental results for run 14 (total calcination) were directly used to normalize the utilization decay in each calcination-carbonation cycle (Equation (2.6)). The normalized utilization decay profile was then used in conjunction with experimentally measured calcination extents after each cycle of run 15, predicting the cyclic sorbent utilization during partial calcination conditions (Equation (2.8)). Figure 2.14(b) shows that the predictions are in good agreement with the experimental results for run 15, confirming the ability of Equation (2.8) to predict sorbent cyclic utilization at different calcination extents. This also supports the earlier hypothesis on the source of deviations between the predictions and experimental results in temperature swing cyclic tests (Figures 2.12 and 2.13). Accordingly, it may be concluded that partial calcination does not enhance the carbon capture capability of the lime-based sorbents, but offers stable performance during extended cycles.

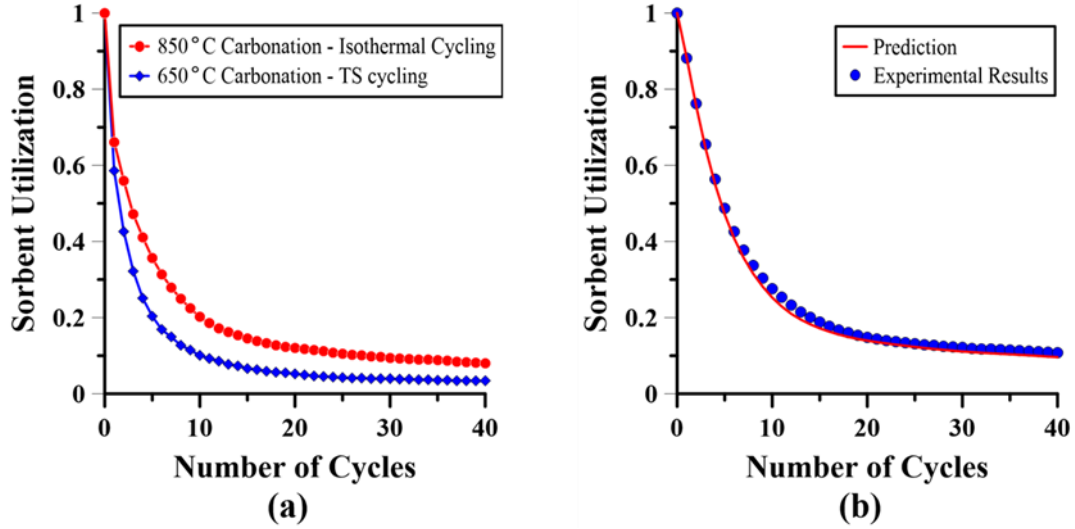


Figure 2.15. (a) Effect of carbonation temperature on the Strassburg sorbent cyclic performance; (b) Comparison of method predictions and experimental results for partial calcination during isothermal cycling (test conditions: (a) runs 3 and 14; (b) run 15 in Table 2.2).

To test the proposed predictive method further, isothermal calcination-carbonation tests were repeated for another naturally-derived limestone, Cadomin. Figure 2.15(a) indicates that the cyclic sorbent utilization of Cadomin and Strassburg limestones are similar when complete sorbent regeneration is achieved prior to all recarbonation stages. Note that the small deviations observed during the first few cycles could be due to slight differences in the compositions of these two sorbents (see Table 2.1).

The experimental results for totally calcined Cadomin particles (Figure 2.15(a)) were used in Equation (2.8) to predict the sorbent cyclic performance under partial calcination conditions (run 17 in Table 2.2). It can be seen from Figure 2.15(b) that the predictions are in good agreement with the experimental results, confirming the utility of the predictive method for an alternative limestone. Therefore, Equation (2.8) appears to be capable of predicting sorbent utilization for different calcination-carbonation cycles and calcination extents, with the model parameter (d_N) depending on the calcination and carbonation temperatures. Note that the sorbent utilization

alone does not represent the CO₂ carrying capacity of partially calcined sorbents. The proposed method should be used in conjunction with Equation (2.3) to estimate the overall CO₂ capture capability of lime-based sorbents at different conditions.

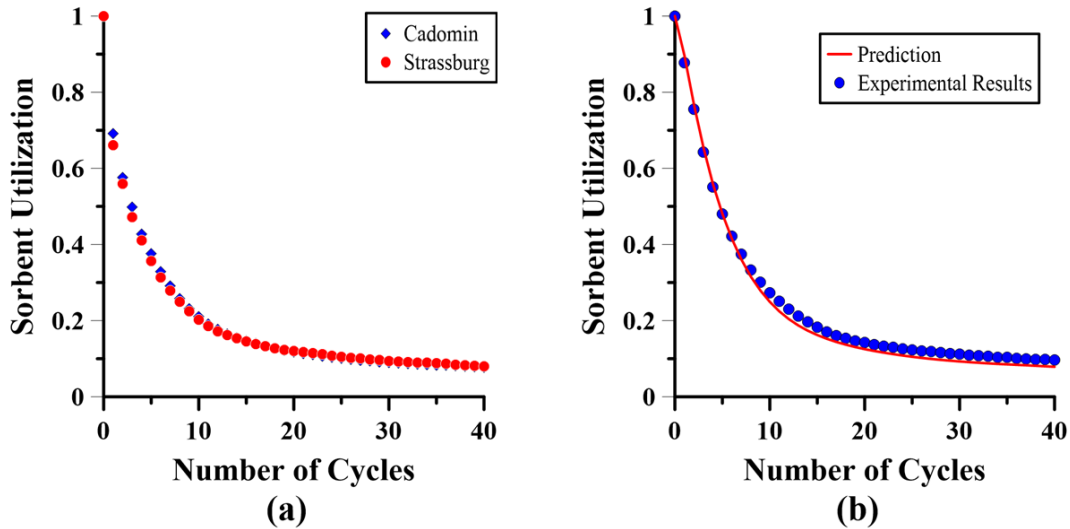


Figure 2.16. (a) Comparing cyclic performance of Strassburg and Cadomin limestones; (b) Comparing predictions and experimental results for partial calcination during isothermal cycling of Cadomin Limestone. (Test conditions: (a) runs 14 and 16; (b) run 17 in Table 2.2.)

2.4. Conclusion

Thermogravimetric analysis was employed to study the effect of calcination temperature, duration and extent on the performance of lime-based sorbents over prolonged cycling. Increasing the calcination temperature considerably accelerated the decay of sorbent utilization in the initial few cycles. On the other hand, extending the duration of calcination and exposing carbonated sorbents to high temperature did not greatly affect the sorbent performance. This indicates that the sorbent utilization decay is predominantly related to material physical and chemical changes during limestone calcination, which are further linked to the loss of active surface area due to thermal pore sintering.

Several tests were conducted to evaluate the sorbent performance when incomplete sorbent regeneration occurs during calcination-carbonation cycling. It was observed that uncalcined sorbents, upon being calcined, provide fresh CaO inside the sorbent and, hence, offer stable CO₂ capture capability over extended numbers of cycles. This could be promising since lower calcination temperatures would be required to achieve incomplete sorbent regeneration, resulting in enhanced sorbent performance in practical applications. A semi-empirical predictive method was introduced to determine the sorbent performance after different numbers of calcination-carbonation cycles, calcination temperatures and extents. This predictive method worked well with various testing procedures for two naturally-derived limestones.

CHAPTER 3: Combined Methane Reforming, Combustion and Limestone Calcination – Thermodynamic Analysis

3.1. Introduction

Limestone calcination is a highly endothermic reaction. It is typically conducted at low operating pressures and high reactor temperatures [3,37,98,118,119,121]. The energy required for calcination can be supplied by burning fuels *in situ* (direct) or *ex situ* (indirect) [122,123]. Direct heating is typically preferred by industry in order to enhance the system thermal efficiency (e.g. less heat losses and temperature gradient) and to reduce the reactor size. However, *in situ* oxy-combustion of carbonaceous fuels (e.g. coal and methane) increases the CO₂ concentration within the reactor, thereby reducing the rate and extent of limestone calcination. Oxyfuel calciners are normally operated at high temperatures (~900°C [123]) to ensure appropriate limestone calcination in a short solid residence time. However, increasing the calciner temperature promotes undesirable pore sintering of solids, imposing additional capital (more expensive material of construction) and operational (e.g. more sorbent make-up flow) costs on the system [4,43,46,47].

Alternatively, methane-concentrated oxyfuel feedstock can be used to achieve autothermal limestone calcination at reduced reactor temperatures. The gaseous feedstock of this calciner configuration is composed of methane and enriched-air (e.g. > 95% oxygen), with the methane feed concentration exceeding the combustion stoichiometric molar ratio (CH₄/O₂ > 0.5). Oxygen then becomes the combustion-limiting reactant, resulting in excess methane after initial rapid combustion. The excess methane then participates in endothermic dry and wet methane reforming, generating considerable syngas (H₂ and CO) inside the reactor. Simultaneously,

limestone calcination releases substantial CO_2 into the reactor gas, a portion of which reacts with the formerly-generated hydrogen (*via* the reverse water-gas shift reaction). This *in situ* CO_2 utilization feature of the process can potentially reduce the CO_2 concentration within the reactor, thereby decreasing the required calcination temperature.

A summary of the main reactions involved in combined methane reforming, combustion and limestone calcination (henceforth referred as MRC-CAL process) is depicted in Figure 3.1. This process can be operated autothermally if the heat released by the exothermic methane combustion can provide the energy needed for the endothermic methane reforming and limestone calcination. Therefore, the methane feed concentration plays a significant role in minimizing the absolute reactor heat duty and controlling the CO_2 concentration within the reactor. The MRC-CAL process can also produce a highly valuable byproduct (syngas), which can be used in various downstream applications (e.g. for methanol and ammonia production).

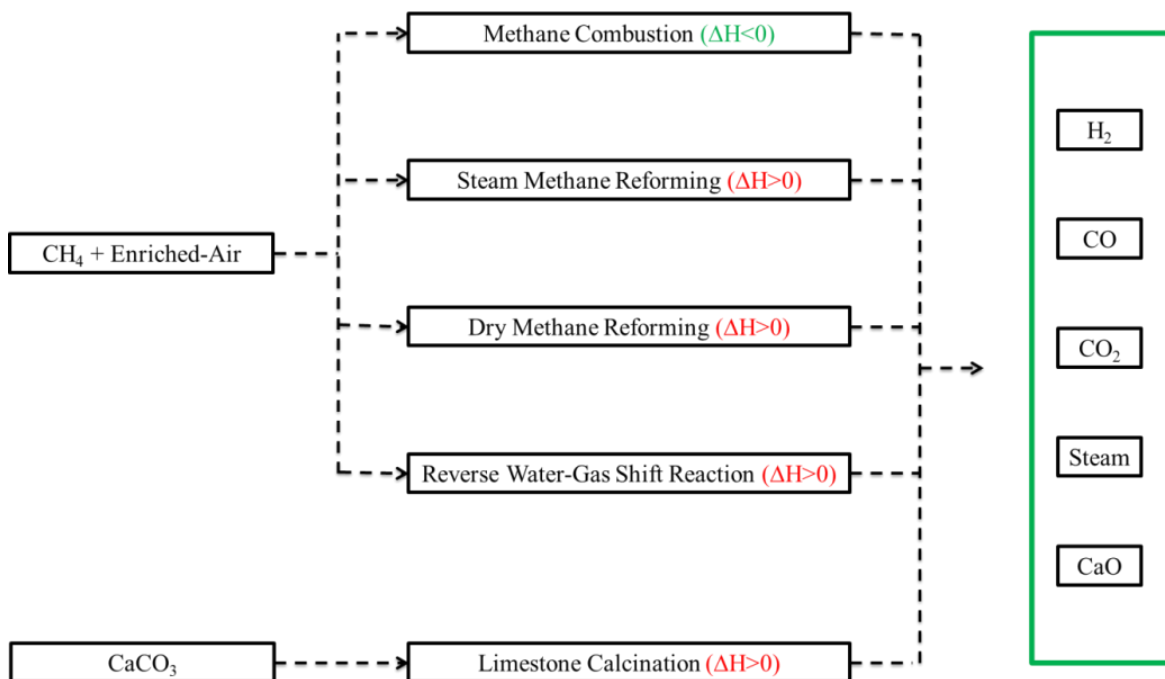


Figure 3.1. Reactions involved in the MRC-CAL process

This chapter evaluates the thermodynamic feasibility of autothermal syngas-producing limestone calcination based on the MRC-CAL process. Aspen Plus simulation is employed to investigate the effect of operating conditions (temperature, pressure and feeding ratios) on the equilibrium performance of isothermal MRC-CAL reactors. The simulation results are then used to develop an empirical correlation to estimate the gaseous feed concentrations required for autothermal, coke-free and complete limestone calcination. The variation of sorbent conversion, reactor heat duty, methane conversion and hydrogen yield with different operating conditions are also assessed and discussed. The system is then simulated under adiabatic conditions, demonstrating the non-isothermal performance of the MRC-CAL process for near-equilibrium operations.

3.2. Aspen Plus Simulation Setup

Aspen PlusTM software (V10.0, Peng-Robinson thermodynamic packages) was employed to evaluate the effect of operating conditions on the sorbent conversion, reactor heat duty, methane conversion and hydrogen yield of the MRC-CAL process. Figure 3.2 demonstrates the Aspen Plus simulation flowsheet, including gas mixer and splitter, solid and gas preheaters, calcination reactor and a solid-gas separator (cyclone). Note that RGibbs reactor was employed in Aspen Plus simulations, evaluating the process thermodynamic equilibrium by minimizing the Gibbs free energy. This enabled assessing the reactor performance without specifying the reactions involved, thereby considering all thermodynamically favoured reactions in the simulation. The gaseous feed flow rate to the reactor was fixed (via a splitter) at 0.2 mol.s^{-1} , while the system performance was assessed by varying the reactor pressure, temperature, and molar feed ratios ($\text{CaCO}_3/\text{total gas}$ and $\text{CH}_4/\text{enriched-air}$). A minimum $\text{CH}_4/\text{enriched-air}$ molar feed ratio of 0.5 was specified for all simulation runs, maintaining oxygen as the limiting reactant for methane combustion.

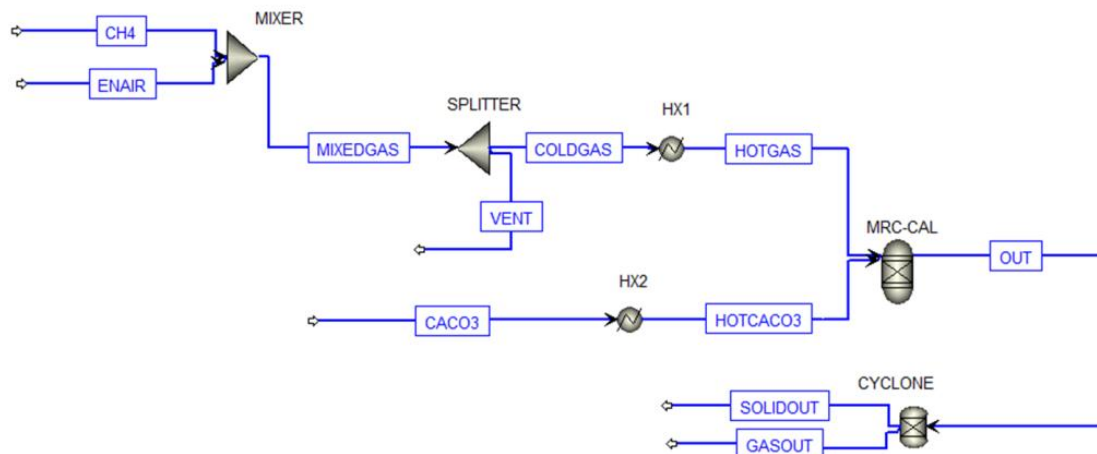


Figure 3.2. Aspen Plus process flow sheet for simulating the MRC-CAL process. Block and stream properties are listed below in Tables 3.1 and 3.2

Note that a pure oxygen stream is typically required to avoid diluting the MRC-CAL off-gas. However, cryogenic production of pure O₂ is extremely costly, affecting the economic viability of the process. Therefore, an enriched-air stream of 95% O₂ (balance nitrogen) was used to reduce both the production cost and the gas inert content. Such an oxygen concentration can be typically achieved *via* low-cost pressure-swing adsorption (PSA) process [124]. Tables 3.1 and 3.2 indicate the properties of the feed streams and blocks in the Aspen Plus simulation, respectively. Note that reactant streams were set to enter the system at the reactor pressure. A similar process flowsheet was employed to conduct adiabatic simulations, assuming MRC-CAL reactors with zero heat duty.

Table 3.1. Stream properties for Aspen Plus simulations

Stream	Temperature (°C)	Flow Rate (mol.s ⁻¹)	Composition
CH ₄	25	0.075-0.3	100% CH ₄
EnAir	25	0.15	95% O ₂ + 5% N ₂
ColdGas	25	0.2	CH ₄ /Enriched-Air: 0.5-2
CaCO ₃	25	0.01 - 0.3*	100% CaCO ₃

*Corresponding to CaCO₃/gas molar ratio of 0.05-1.5.

Table 3.2. Block properties in Aspen Plus simulations

Unit	Configuration & Notes	Temperature (°C)	Pressure (bars)
Mixer	Mixing Air and CH ₄	25	1-5
Splitter	Provide 0.2 mol.s ⁻¹ Gas Feed Flow	25	1-5
HX1	Electrical Heater	To Calciner Temperature	1-5
HX2	Electrical Heater	To Calciner Temperature	1-5
MRC-CAL	Gibbs reactor	750-900	1-5
Cyclone	Separator (for solid)	Calciner Temperature	1-5

3.3. Results and Discussion

3.3.1. Preliminary Performance Analysis

The effect of gaseous feed concentration on the sorbent conversion and reactor heat duty of the MRC-CAL process is depicted in Figures 3.3(a)-(e). Increasing the methane feed concentration results in a higher proportion of methane converted by endothermic dry/steam methane reforming and, hence, higher reactor heat duty. On the other hand, reactor temperature (with complete calcination) has negligible impact on the MRC-CAL off-gas concentration (Figure 3.3(f)) and thermal behaviour. Note that the kinks in these figures are due to a transition from incomplete to complete limestone calcination, resulting in abrupt slope changes in reactor heat duty.

Figures 3.3(a)-(e) also indicate that complete limestone calcination can be achieved at all studied methane feed concentrations ($\text{CaCO}_3/\text{total gas molar feed ration} = 0.5$, reactor pressure = 1 bars) if the reactor temperature exceeds 825°C. The minimum required methane feed concentration for complete limestone calcination then increases with decreasing reactor temperature below 825°C. This is due to lower calcination driving force at reduced temperatures, requiring higher methane

feed concentrations (thus less methane combustion) to surpass the CaCO_3/CaO thermodynamic equilibrium. Given also the higher reactor heat duty (more endothermicity) at elevated methane feed concentrations, complete and autothermal limestone calcination can only occur by exceeding a certain reactor temperature (e.g. 775°C for the operating conditions tested in Figures 3.3(a)-(e)).

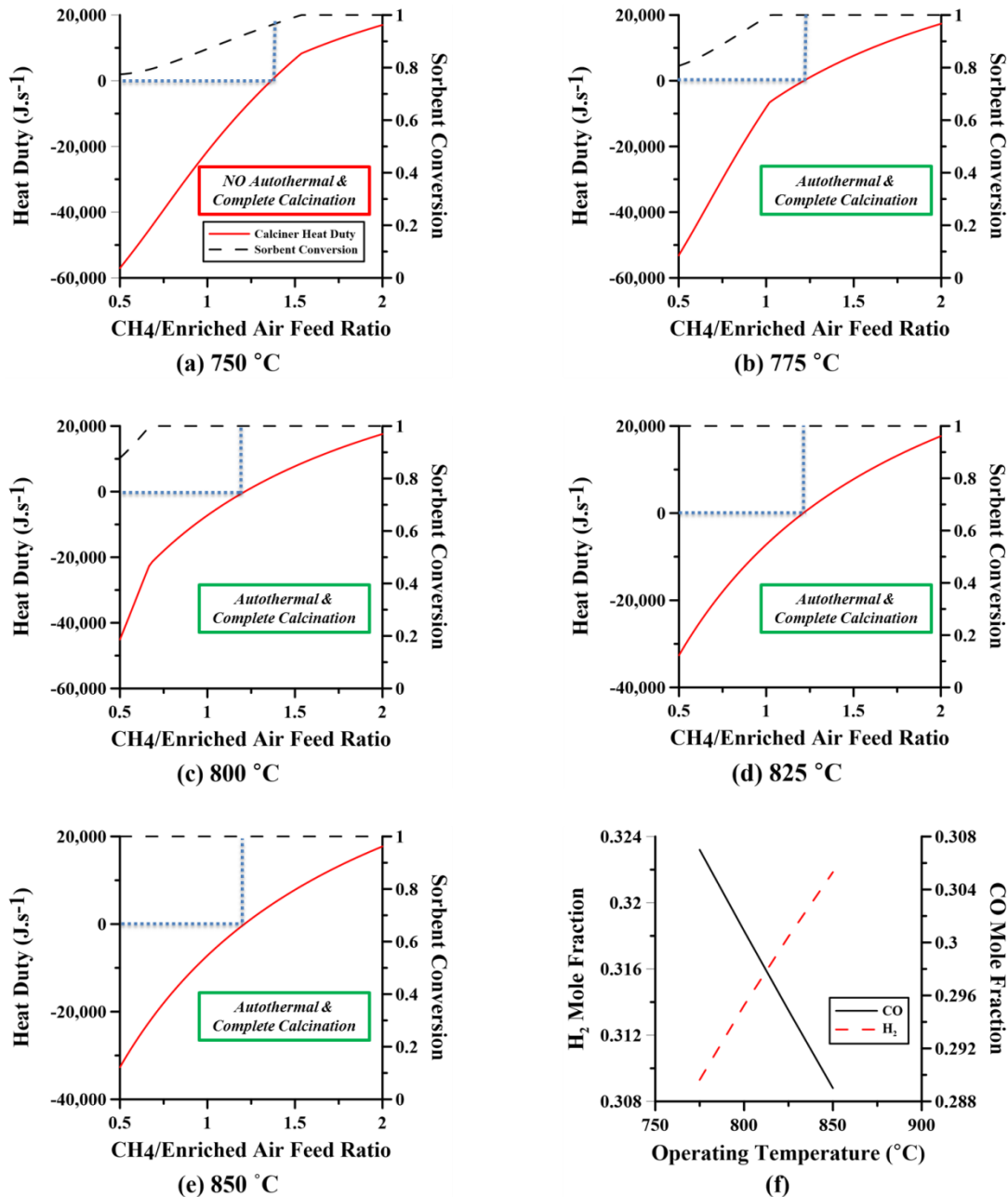


Figure 3.3. (a)–(e) Effect of temperature and feed concentration on MRC-CAL heat duty and sorbent conversion; (f) Effect of temperature on MRC-CAL off-gas H₂ and CO concentration. (All results are for atmospheric pressure and CaCO₃/total gas molar feed ratio of 0.5. Panel (f) is for a methane-to-air feed ratio of 1.21.)

The effect of methane feed concentration on the MRC-CAL heat duty is shown in Figure 3.4 for different CaCO₃/total gas molar feed ratios. Increasing the CaCO₃/total gas molar feed ratio (e.g. by increasing the sorbent feed flow rate) increases the energy required for limestone calcination,

thereby increasing the reactor heat duty. Hence, the required methane feed concentration for autothermal operation of the MRC-CAL process decreases with increasing CaCO_3 /total gas molar feed ratio. Note that the observed kinks in Figure 3.4(a) are due to incomplete limestone calcination at low operating temperatures with high CaCO_3 /total gas molar feed ratios. Further discussion is provided in Section 3.3.3.

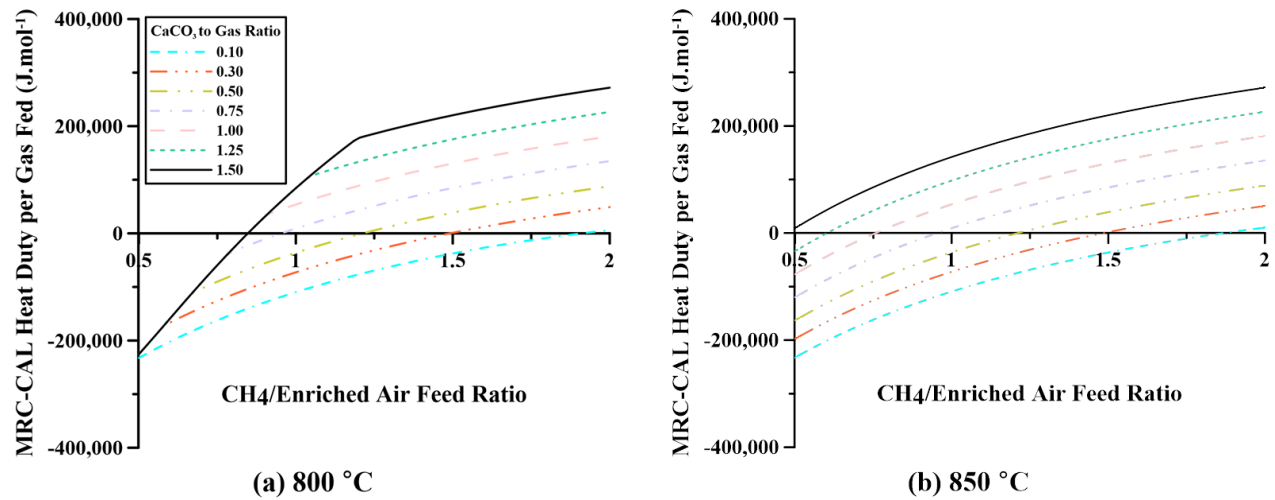


Figure 3.4. Effect of methane feed concentration on MRC-CAL heat duty at different CaCO_3 /gas feed ratios and at: (a) 800°C; (b) 850°C.

3.3.2. Correlation for Autothermal MRC-CAL Operation

Extensive simulation runs were employed next to determine the gaseous feed concentrations required for autothermal and complete limestone calcination by the MRC-CAL process. The MRC-CAL process combines exothermic methane combustion with endothermic methane reforming (steam and dry) and limestone calcination. Therefore, lower methane feed concentrations (more oxygen) would be needed if more energy were to be required within the reactor. Increasing the CaCO_3 /total gas molar feed ratio (e.g. by increasing the sorbent feed flow rate) can potentially increase the energy required for the calcination. Therefore, the required

methane feed concentration for autothermal MRC-CAL must decrease with increasing $\text{CaCO}_3/\text{total gas molar feed ratio}$. This is in agreement with the simulation results in Figure 3.5, demonstrating a sharp reduction in the methane/enriched-air molar feed ratio (β) with increasing $\text{CaCO}_3/\text{total gas molar feed ratio}$ (α). Note that increasing the $\text{CaCO}_3/\text{total gas molar feed ratio}$ also promotes reverse water-gas shift reaction between the CO_2 released by the limestone calcination and the hydrogen generated by methane reforming [119]. Although the latter potentially enhances the rate and extent of limestone calcination, the endothermicity of the reverse water-gas shift reaction suggests that further energy needs to be supplied to the reactor.

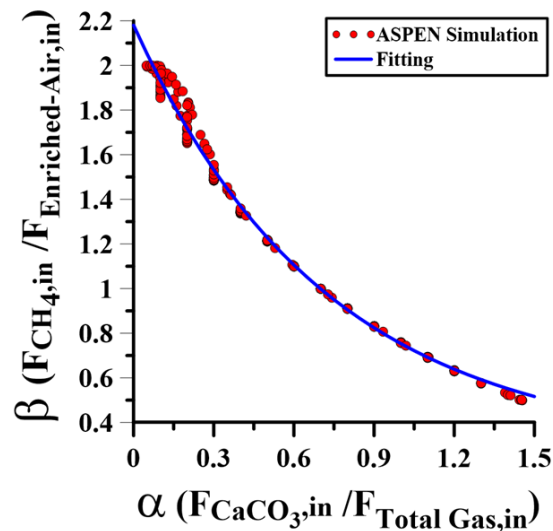


Figure 3.5. Required $\text{CH}_4/\text{Enriched-air}$ molar feed ratio for autothermal MRC-CAL at 1-5 bars and 800-900°C (Maximum error of $\pm 0.4\%$)

Equation (3.1) shows an empirical correlation used to estimate the gaseous feed concentrations required by the MRC-CAL process for autothermal and complete limestone calcination. This correlation is achieved by fitting the Aspen Plus predictions (red points in Figure 3.5) with an exponential function. Figure 3.5 confirms excellent fitting of the proposed correlation ($R^2 = 0.982$), while inevitable deviations exist for $\alpha < 0.3$. Increased deviation at reduced α is mainly

due to the variation of methane conversion, governed by the steam and dry methane reforming thermodynamic equilibrium. In fact, thermodynamic equilibrium of steam and dry methane reforming inhibits complete methane conversion, especially at reduced CaCO_3/gas molar feed ratios (see Section 3.3.4). This amplifies the effects of temperature and pressure on the reactor thermal behaviour, consequently reducing the accuracy of the fitted correlation (which is independent of reactor temperature and pressure). Note that steam and dry methane reforming are both favoured at reduced reactor pressures and elevated operating temperatures. Therefore, greater deviations between the correlation predictions and the Aspen Plus simulation results are expected at low operating temperatures and elevated reactor pressures.

$$\beta = 0.275 + 1.903e^{-\alpha/0.716} \quad 800^\circ\text{C} \leq T \leq 900^\circ\text{C} \ \& \ P = 1-5 \text{ bars} \quad (3.1)$$

3.3.3. Critical Limits of MRC-CAL Process

The overarching objective of the MRC-CAL process is to attain autothermal limestone calcination at reduced reactor temperatures. Therefore, it is crucial to determine the range of operating conditions to achieve complete and autothermal limestone calcination through this novel sorbent regeneration technology. In addition, the MRC-CAL process typically needs reforming catalysts (e.g. Ni-based) to ensure rapid methane conversion at practical temperatures. Catalyst deactivation by carbon deposition (coke formation) is a major challenge associated with methane reforming catalysts. Therefore, it is desirable to conduct the MRC-CAL process within a range of operating conditions where:

- reactor heat duty approaches zero;
- limestone fully calcines; and

- negligible carbon formation occurs.

As discussed above, lower methane feed concentrations are required to achieve autothermal MRC-CAL operation at elevated CaCO_3 /total gas molar feed ratios (Figure 3.5). However, increasing the CaCO_3 /total gas molar feed ratio (e.g. more CO_2 released by calcination) and reducing the methane feed concentration (e.g. more methane combustion) lead to higher CO_2 concentrations within the reactor, and consequently lowering the calcination rate and extent. On the other hand, increasing the methane/enriched-air molar feed ratio and reducing the CaCO_3 /total gas molar feed ratio can both increase coke formation, especially at mild reactor temperatures [119]. This is due to decreased steam and CO_2 generation (e.g. lower methane combustion and limestone calcination), resulting in lower average CO_2/CH_4 and $\text{H}_2\text{O}/\text{CH}_4$ molar ratios within the reactor [12,95,125]. Therefore, autothermal, coke-free and complete limestone calcination can be only attainable within a certain range of CaCO_3 /total gas molar feed ratios.

Figure 3.6 demonstrates the critical limits for autothermal, complete and coke-free limestone calcination in an atmospheric MRC-CAL reactor. The figure is split into three zones: (1) an endothermic/incomplete limestone calcination zone; (2) a potentially autothermal, coke-free, and complete limestone calcination zone (target zone); and (3) a coke formation zone. The upper CaCO_3 /gas molar feed ratio limit initially increases with increasing operating temperature, as shown in Figure 3.6. However, this upper limit nearly stabilizes at $\alpha \approx 1.45$ beyond an operating temperature of $\sim 837^\circ\text{C}$. Increasing the operating temperature potentially boosts the extent of limestone calcination by augmenting the calcination driving force [119]. Consequently, higher reactor CO_2 concentrations can be tolerated when calcining sorbents at elevated operating temperatures. In fact, more CaCO_3 can be calcined by a certain amount of gas (e.g. higher α)

when increasing the reactor temperature. However, at a temperature of roughly 837°C, the upper α limit reaches a value of nearly 1.45, corresponding to β (methane/enriched-air molar feed ratio) close to 0.5 (Figure 3.5). As mentioned above, lower β is required for autothermal and complete sorbent regeneration at elevated CaCO_3 /total gas molar feed ratios. However, reducing β to < 0.5 would result in switching the limiting combustion reactant from oxygen to methane, thereby reducing heat generation by methane combustion. In this situation, the MRC-CAL process reduces to that of conventional oxy-fuel calciners, and hence, the upper CaCO_3 /total gas molar feed ratio limit becomes insensitive to reactor temperature.

Increasing the methane/enriched-air molar feed ratio (β) and reducing the CaCO_3 /total gas molar feed ratio (α) both result in higher coke formation inside the reactor. This is due to decreased steam and CO_2 generation (less methane combustion and sorbent calcination), resulting in reduced average CO_2/CH_4 and $\text{H}_2\text{O}/\text{CH}_4$ ratios along the bed height [12,95,125]. As discussed above, reducing α results in a higher β required for autothermal MRC-CAL operation (Figure 3.5). Therefore, the chance of carbon formation increases when reducing the CaCO_3 /total gas molar feed ratio. This justifies the existence of a lower α limit to avert coke formation in the MRC-CAL process, as depicted in Figure 3.6. Previous studies [31,125] have also shown that increasing the operating temperature reduces the coke formation in methane reformers. This is in agreement with Figure 3.6, where the lower α limit slightly decreases with increasing reactor temperatures [118].

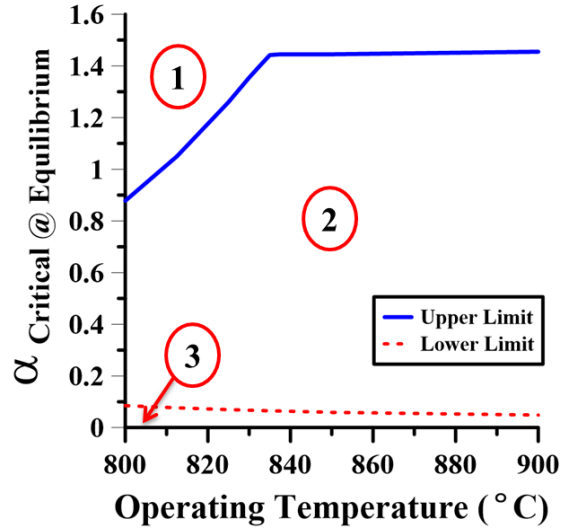


Figure 3.6. MRC-CAL critical limits for atmospheric reactor operation. (Zone 1: endothermic/incomplete sorbent regeneration zone; zone 2: potential autothermal, coke-free, and complete calcination zone; zone 3: carbon generating zone).

Pressurized limestone calcination is typically preferred by industry to reduce the cost of off-gas compression and increase reactor throughput. However, increasing the reactor pressure results in a lower calcination driving force and thus a lower rate and extent of limestone calcination [126]. The effect of reactor pressure on the critical limits of the MRC-CAL process is shown in Figure 3.7. Increasing the reactor pressure substantially reduces the upper α limit by decreasing the limestone calcination driving force. In addition, coke formation reactions (e.g. Boudouard reaction) are normally favoured at high reactor pressures, in agreement with Le Chatelier's principal. Therefore, increasing the reactor pressure narrows the range of applicable CaCO_3 /total gas molar feed ratio for autothermal, coke-free and complete limestone calcination, as depicted in Figure 3.7. Higher reactor temperatures and lower CaCO_3 /gas molar feed ratios are typically required to achieve appreciable limestone calcination in pressurized MRC-CAL reactors.

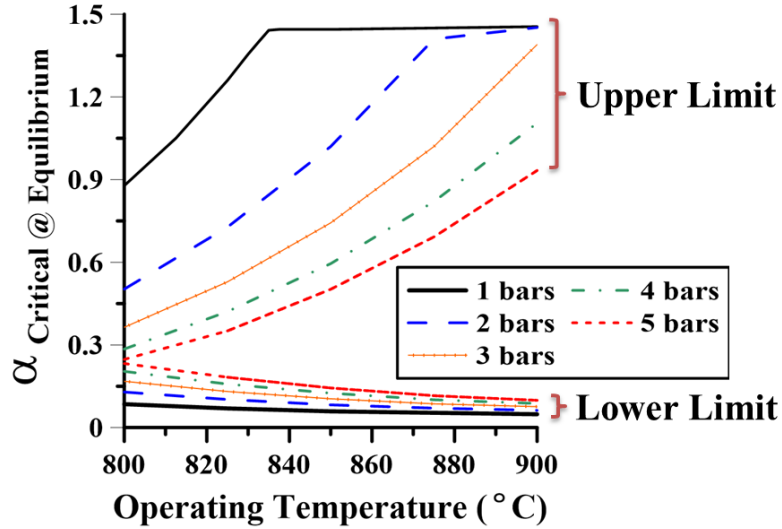


Figure 3.7. MRC-CAL critical limits at high reactor pressures

3.3.4. Performance Analysis for Isothermal Operation

The effects of reactor pressure and CaCO₃/total gas molar feed ratio (α) on the MRC-CAL sorbent conversion and heat duty are depicted in Figure 3.8. Note that the gaseous feed concentrations for these simulation runs are calculated based on Equation (3.1). These results indicate that incomplete limestone calcination can occur by exceeding a certain reactor pressure at $\alpha > 0.5$. In addition, the maximum reactor pressure for complete limestone calcination decreases with increasing CaCO₃/total gas molar feeding ratio. This is in agreement with the results presented in Figure 3.7, confirming the existence of an upper α limit for autothermal and complete limestone calcination. Figure 3.8(b) shows that the MRC-CAL heat duty is roughly zero when the CaCO₃/total gas molar feed ratio is lower than the upper α limit. Larger deviations are observed at reduced α , which could be due to low precision of Equation (3.1) at decreased CaCO₃/total gas molar feed ratios. Note that exceeding the α upper limit results in incomplete limestone calcination and hence, less energy consumption within the reactor. Accordingly,

isothermal MRC-CAL reactors tend toward exothermicity when the $\text{CaCO}_3/\text{total gas}$ molar feed ratio exceeds the upper α limit, as shown in Figure 3.8(b).

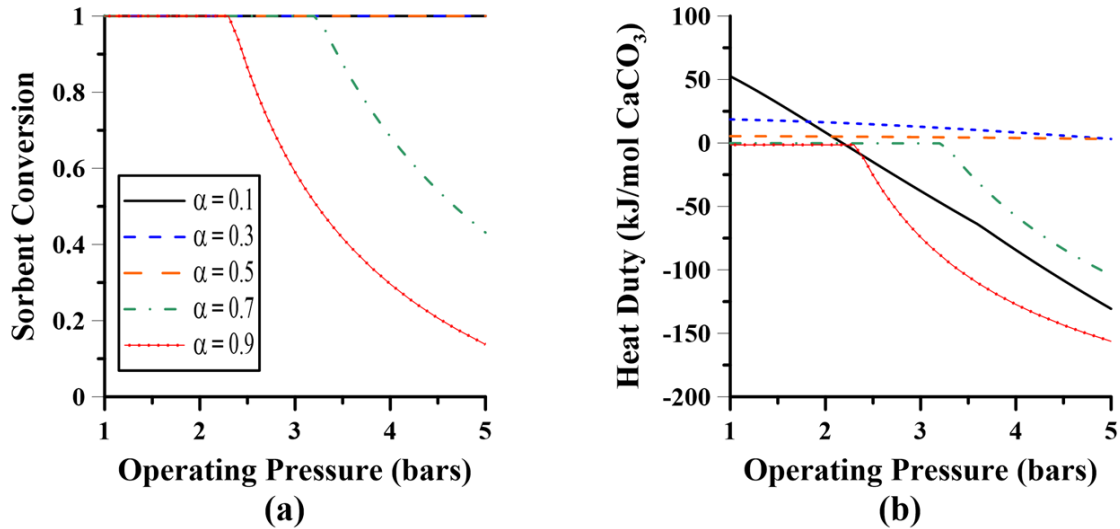


Figure 3.8. Effect of operating pressure on: (a) sorbent conversion; and (b) MRC-CAL heat duty at fixed temperature of 850°C and different $\text{CaCO}_3/\text{total gas}$ molar feed ratios.

Figure 3.9 shows the methane conversion and hydrogen yield of the MRC-CAL process at operating conditions identical to those applied in Figure 3.8. The MRC-CAL process offers relatively high methane conversion, especially at low reactor pressures and high $\text{CaCO}_3/\text{total gas}$ molar feed ratios. Increasing the reactor pressure inhibits the thermodynamic equilibrium of the steam and dry methane reforming, in agreement with Le Chatelier's principal. On the other hand, higher methane feed concentrations are required to achieve autothermal MRC-CAL operation at reduced $\text{CaCO}_3/\text{total gas}$ molar feed ratios (Figure 3.5). This corresponds to lower methane combustion within the reactor, and thereby, less initial steam and CO_2 generation. Reducing the $\text{CaCO}_3/\text{total gas}$ molar feed ratios also reduces the amount of CO_2 produced by the limestone calcination. Therefore, slightly lower methane conversion is expected when the $\text{CaCO}_3/\text{total gas}$ molar feed ratio decreases, as shown in Figure 3.9(a).

Figure 3.9(b) shows that increasing the CaCO_3 /total gas molar feed ratio substantially reduces the hydrogen productivity of the MRC-CAL process. This is due to lower methane feed concentration at elevated CaCO_3 /total gas molar feed ratios, as well as more hydrogen consumption by the reverse water-gas shift reaction. Note that exceeding the upper CaCO_3 /total gas molar feed ratio limit results in incomplete limestone calcination and consequently, less hydrogen consumption by the reverse water-gas shift reaction. This enhances the hydrogen productivity of the MRC-CAL process, as shown in Figure 3.9(b). On the other hand, increasing the reactor pressure slightly reduces the MRC-CAL hydrogen production yield, which could be due to the lower methane conversions at higher reactor pressures (Figure 3.9(a)).

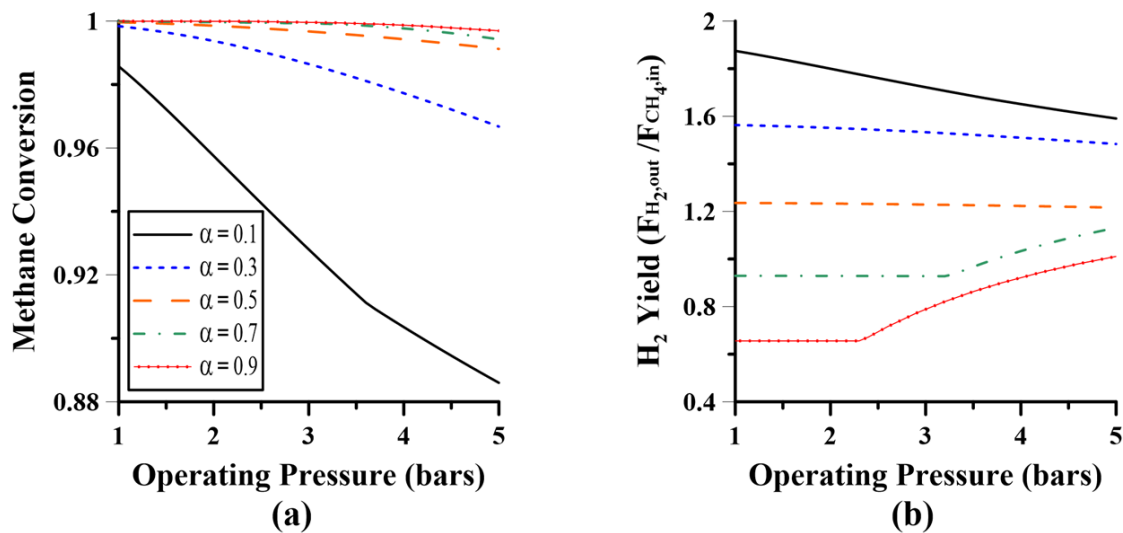


Figure 3.9. Effect of operating pressure at fixed reactor temperature of 850°C and different CaCO_3 /total gas molar feed ratios on the MRC-CAL: (a) CH_4 conversion; (b) H_2 yield.

A portion of the generated hydrogen could be recovered by implementing high-temperature hydrogen-selective membranes inside the reactor. The choice of the type of hydrogen-selective membranes depends strongly on the perm-selectivity and mechanical stability of the membrane material. Palladium-based membranes are known for their relatively high permeability and

nearly infinite hydrogen selectivity [22,127]. However, palladium can lose its selectivity and mechanical stability at temperatures above 550-620°C [22,23]. Nickel-based membranes can tolerate higher reactor temperatures, but typically offer lower hydrogen permeability and selectivity (e.g. 10 times less permeability compared to palladium) [22]. Further investigations are needed to identify alternative high-temperature hydrogen perm-selective membrane materials for the MRC-CAL process.

3.3.5. Performance Analysis for Adiabatic Operation

The sorbent conversion and off-gas temperature of a well-insulated MRC-CAL reactor are depicted in Figure 3.10 for different operating pressures and CaCO₃/total gas molar feed ratios. The feed streams in these simulations entered the reactor at 850°C, and the reactor heat duty was set to zero. The results show that the MRC-CAL off-gas temperature is roughly similar to the feed temperature at CaCO₃/gas molar feed ratios below the upper α limit. However, exceeding the upper α limit leads to a rapid jump in the reactor off-gas temperature, accompanied by a minor reduction in sorbent conversion. Exceeding the upper CaCO₃/total gas molar feed ratio limit results in a significant reduction of calcination extent and reactor heat duty (e.g. more exothermicity) in isothermal reactors. However, the excess energy in adiabatic mode would increase the reactor temperature, thereby enhancing the limestone calcination. In fact, the MRC-CAL process can offer a promising thermal-adaptability, maximizing the limestone calcination extent by naturally increasing the reactor temperature.

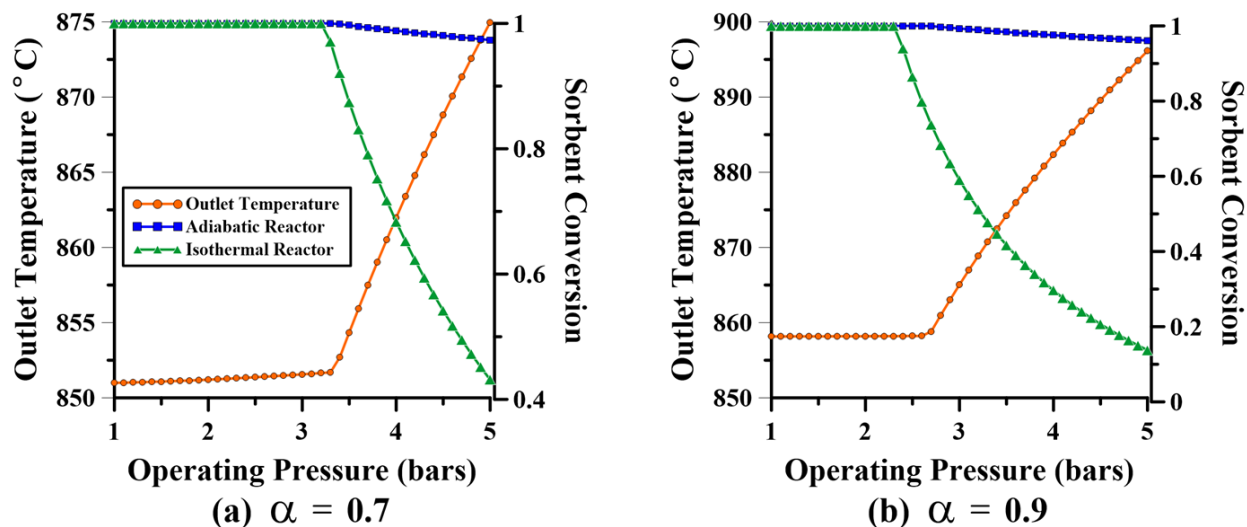


Figure 3.10. Adiabatic and isothermal performance of MRC-CAL at different reactor pressures: (a) $\alpha=0.7$ and (b) $\alpha=0.9$. (Feed temperature = 850°C)

Note that in practice the feed streams enter the limestone calciner at milder temperatures (e.g. sorbent circulating from a low-temperature carbonator). In this case, a portion of the MRC-CAL off-gas can be burned to supply the required excess energy inside or outside the reactor (Figure 3.11). The former case potentially inhibits limestone calcination since *in situ* syngas combustion releases CO₂ into the reactor gas. On the other hand, indirect heating reduces the system thermal efficiency and increases the reactor size.

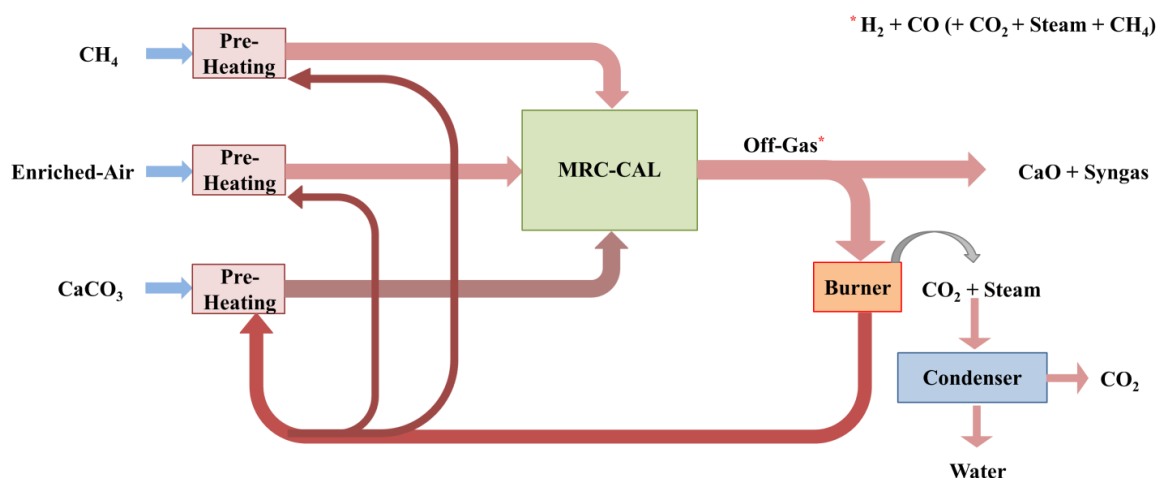


Figure 3.11. Sankey diagram of MRC-CAL process.

3.4. Conclusion

The performance of a process which combines methane reforming, combustion and limestone calcination was evaluated under thermodynamic equilibrium. A single correlation was developed to estimate the required gaseous feed concentration for autothermal reactor operation. The proposed correlation agrees well with the Aspen Plus simulation results, while larger deviations exist at lower CaCO_3 /total gas molar feed ratios. The applicable ranges of CaCO_3 /total gas molar ratio for autothermal, coke-free and complete limestone calcination were shown to narrow as the reactor pressure increases and as the temperature decreases.

The simulation results show a relatively high hydrogen yield, with higher hydrogen productivity at reduced CaCO_3 /total gas molar feed ratios. The hydrogen yield was also shown to be nearly insensitive to the reactor pressure and temperature, unless the critical limits for coke formation and/or complete limestone calcination are exceeded. It was also shown that the proposed technology can benefit from a promising thermal-adaptivity, maximizing the sorbent conversion by naturally increasing the reactor temperature.

CHAPTER 4: Simulation of Combined Methane Reforming, Combustion and Limestone Calcination in Turbulent Fluidized Bed Reactors

4.1. Introduction

Limestone calcination is conventionally conducted in the presence of air, steam, CO₂, or oxy-fuel media. Atmospheric air and steam calcination can be operated at temperatures above 850°C, while CO₂ and oxy-fuel calciners typically require higher reactor temperatures [122,123]. Higher reactor temperature undesirably affects the system thermal efficiency, sorbent cyclic performance and the cost of reactor materials of construction. On the other hand, air calcination produces a dilute CO₂ off-gas, requiring additional separation prior to sequestration. Although steam calciners produce a highly-concentrated CO₂ dry off-gas, steam generation is energy-consuming and, consequently, reduces the thermal efficiency of the process.

A novel configuration for limestone calcination was proposed in Chapter 3, where a methane-concentrated oxyfuel feedstock ($\text{CH}_4/\text{O}_2 > 0.5$) is fed into the reactor. Accordingly, oxygen becomes the combustion-limiting reactant, resulting in incomplete methane conversion by the exothermic methane combustion. The remaining methane is then catalytically reformed to hydrogen and CO, utilizing the steam and CO₂ generated by the methane combustion. Simultaneous limestone calcination then releases considerable CO₂ into the reactor gas, where a portion of this released CO₂ reacts with the formerly-generated hydrogen (reverse water-gas shift reaction). This potentially enhances the CO₂ partial pressure driving force for the limestone calcination and thereby, reduces the required calcination temperature.

The thermodynamic equilibrium of this combined process (referred as MRC-CAL process) was detailed in Chapter 3. A single correlation (Equation (4.1), identical to Equation (3.1)) was proposed to estimate the required gaseous feed concentration for autothermal and complete limestone calcination at different operating conditions. It was also shown that the MRC-CAL off-gas can contain substantial amount of hydrogen and carbon monoxide, to be used further in various downstream applications (e.g. chemical looping combustion, ammonia production and methanol synthesis). However, the thermodynamic analysis solely cannot provide any appreciable information on the process kinetics, and further simulation studies are imperative to evaluate the system performance under non-equilibrium conditions.

$$\beta = 0.275 + 1.903e^{-\alpha/0.716} \quad 800^{\circ}\text{C} \leq T \leq 900^{\circ}\text{C} \ \& \ P = 1-5 \text{ bars} \quad (4.1)$$

This chapter addresses the kinetic simulation of the MRC-CAL process in turbulent fluidized bed reactor. The turbulent fluidization flow regime was selected owing to supreme gas-solid contact, high solids hold-up [128], and relatively low solid-to-gas molar feed ratio. The effect of various operating conditions (temperature, pressure, CaCO₃/total gas molar feed ratio and sorbent residence time) on the sorbent conversion, methane conversion and hydrogen yield of the process are assessed. The system performance is also compared with conventional steam calciners (theoretically representative of any unreactive non-CO₂ calcination media), demonstrating superior performance of the proposed process under some circumstances. A simple, yet effective, design methodology is then introduced to help determine the proper range of operating conditions for this novel sorbent regeneration technology.

4.2. Simulation Setup

The steady-state and isothermal performance of the MRC-CAL process under turbulent fluidization conditions is investigated with a number of assumptions:

- i. One-dimensional, single phase (i.e. homogeneous without mass transfer constraints to separate bubbles/voids [129])
- ii. Isothermal operation
- iii. Steady-state condition
- iv. Axially dispersed plug flow reactor (ADPFR) model for gases [128–130]
- v. Continuous stirred tank reactor (CSTR) model for non-catalytic solid-gas reaction
- vi. Constant reactor cross-sectional area
- vii. Constant and homogenous solid properties
- viii. Constant and homogeneous bed voidage
- ix. Negligible segregation of particles of different species and properties.
- x. Ideal gas behaviour
- xi. Negligible carbon formation at studied range of conditions [119].
- xii. 100% sorbent activity (feed composed of pure CaCO_3).

Note that some of the applied assumptions are not precisely valid under practical conditions. For instance, solid particles can have non-uniform distributions of particle sizes and densities, while bed voidage can vary dynamically, axially, and radially within the bed. However, assumptions of this kind are helpful to minimize computation time. Also, overall conclusions and trends are unlikely to change due to minor divergences from these assumptions. Figure 4.1 demonstrates a schematic of the single-phase MRC-CAL reactor model for turbulent fluidized bed reactors. A summary of the governing equations, rate expressions and correlations applied are also presented in Tables 4.1-4.4. Note that the Xu and Froment kinetic model is employed for the steam methane reforming reactions. This model was developed for a Ni-based catalyst, which is typically used in industrial high-temperature steam methane reformers. Somewhat different

compositions of catalyst might result in minor changes in specific predictions of this chapter, but they are unlikely to affect the overall conclusions. Ideal gas law was used to calculate the local gaseous mixture densities, while the local gaseous mixture viscosities were estimated by averaging values from a linear dependency of the pure components and the Wilke method [12].

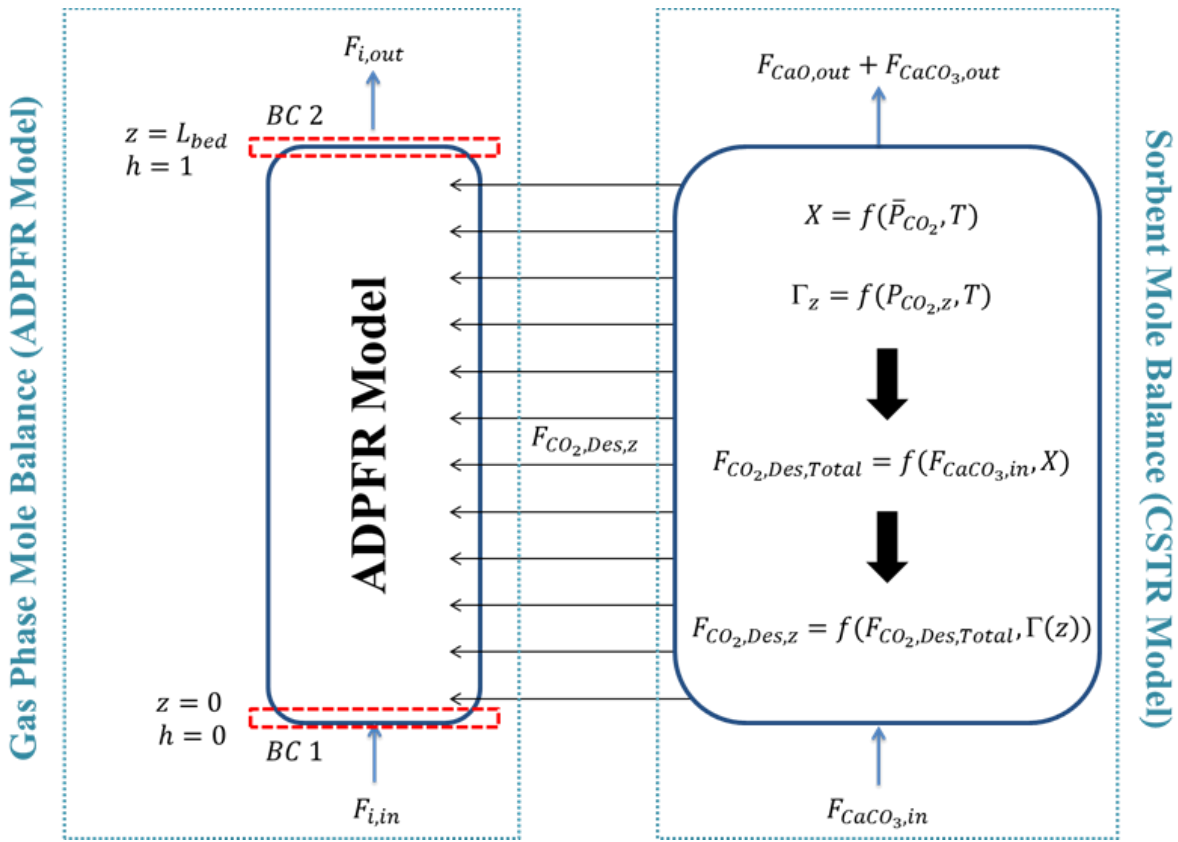


Figure 4.1. Schematic of MRC-CAL reactor model in turbulent fluidized bed reactors

Table 4.1. Governing equations for kinetic simulations

Dimensionless Form of Gas Phase Mole Balance	$h = \frac{z}{L_{\text{Reactor}}} \text{ and } Pe = \frac{U_{\text{Superficial}} L_{\text{Reactor}}}{D_a}$ $\frac{1}{Pe} \frac{d^2 F_i}{dh^2} - \frac{dF_i}{dh} + L_{\text{Reactor}} \left(\rho_{\text{Cat,bed}} \left(\sum_{j=1}^5 v_{i,j} r_j \right) A_{\text{Reactor}} \right) + \frac{dF_{\text{CO}_2, \text{Des},z}}{dh} = 0$ <p>BC1: $F_{i,h=0} - F_{i,in} = \frac{1}{Pe} \frac{dF_i}{dh} \Big _{h=0}$ BC2: $\frac{dF_i}{dh} \Big _{h=L} = 0$ i: CH₄, CO₂, CO, H₂, H₂O, O₂, N₂</p>
Sorbent Desorption Mole Balance	$X = \frac{-\bar{V}_6 \rho_{\text{CaCO}_3, \text{bed}} V_{\text{Reactor}}}{F_{\text{CaCO}_3, \text{Calciner Feed}}} \quad F_{\text{CO}_2, \text{Des}, \text{Total}} = F_{\text{CaCO}_3, \text{Calciner Feed}} X_{\text{Calc}}$ $\Gamma_{\text{Calc}}(z) = \frac{F_{\text{CO}_2, \text{Des},z}}{F_{\text{CO}_2, \text{Des}, \text{Total}}} \Rightarrow F_{\text{CO}_2, \text{Des},z} = F_{\text{CO}_2, \text{Des}, \text{Total}} \times \Gamma_{\text{Calc}}(z) \quad \Gamma_{\text{T,Calc}} = \sum_{i=1}^{N_{\text{Nodes}}} \left(1 - \frac{P_{\text{CO}_2,z}}{P_{\text{Eq,CO}_2}} \right)^{1.86} \quad \text{only if } P_{\text{CO}_2,z} \leq P_{\text{Eq,CO}_2}$ $\Gamma(z) = \frac{\left(1 - \frac{P_{\text{CO}_2,z}}{P_{\text{Eq,CO}_2}} \right)^{1.86}}{\Gamma_{\text{T}}} \quad \text{if } P_{\text{CO}_2,z} \leq P_{\text{Eq,CO}_2} \quad \Gamma(z) = 0 \quad \text{if } P_{\text{CO}_2,z} > P_{\text{Eq,CO}_2}$ $\frac{dF_{\text{CO}_2, \text{Des},z}}{dh} = \frac{F_{\text{CO}_2, \text{Des},z}}{\Delta h}$
Pressure Drop	$\frac{dP}{dz} = \rho_{\text{solid}} (1 - \varepsilon_{\text{bed}}) g + \rho_{\text{gas}} \varepsilon_{\text{bed}} g$
Solid Concentrations	$\rho_{\text{Cat,bed}} = (1 - \varepsilon_{\text{bed}}) \rho_{\text{Solid}} \frac{m_{\text{in,Cat}}}{m_{\text{in,Solid}}} (1 - X) \quad \rho_{\text{CaCO}_3, \text{bed}} = (1 - \varepsilon_{\text{bed}}) \rho_{\text{Solid}} \frac{m_{\text{in,Sorbent}}}{m_{\text{in,Solid}}} (1 - X_{\text{Calc}})$

Table 4.2. Reactions considered in kinetic simulations

Reaction	Stoichiometry	Rate Expression
Dry Methane Reforming (DMR) [95,131]	$\text{CH}_4 + \text{CO}_2 \rightleftharpoons 2\text{H}_2 + 2\text{CO}$	$r_1 = \frac{k_1 K_{\text{CH}_4,1} K_{\text{CO}_2,1} P_{\text{CH}_4} P_{\text{CO}_2}}{(1 + K_{\text{CH}_4,1} P_{\text{CH}_4} + K_{\text{CO}_2,1} P_{\text{CO}_2})^2} \left(1 - \frac{P_{\text{CO}}^2 P_{\text{H}_2}^2}{K_{\text{P},1} P_{\text{CH}_4} P_{\text{CO}_2}} \right)$
Reverse Water-Gas Shift Reaction (RWGS) [95,131]	$\text{H}_2 + \text{CO}_2 \rightleftharpoons \text{H}_2\text{O} + \text{CO}$	$r_2 = \frac{k_2 K_{\text{H}_2,2} K_{\text{CO}_2,2} P_{\text{H}_2} P_{\text{CO}_2}}{(1 + K_{\text{H}_2,2} P_{\text{H}_2} + K_{\text{CO}_2,2} P_{\text{CO}_2})^2} \left(1 - \frac{P_{\text{CO}} P_{\text{H}_2\text{O}}}{K_{\text{P},2} P_{\text{H}_2} P_{\text{CO}_2}} \right)$
Steam Methane Reforming (SMR) 1 [132]	$\text{CH}_4 + \text{H}_2\text{O} \rightleftharpoons 3\text{H}_2 + \text{CO}$	$r_3 = k_3 \left(\frac{P_{\text{CH}_4} P_{\text{H}_2\text{O}}}{P_{\text{H}_2}^{2.5}} - \frac{P_{\text{CO}} P_{\text{H}_2}^{0.5}}{K_3} \right) / \text{DEN}^2$
SMR 2 [132]	$\text{CH}_4 + 2\text{H}_2\text{O} \rightleftharpoons 4\text{H}_2 + \text{CO}_2$	$r_4 = k_4 \left(\frac{P_{\text{CH}_4} P_{\text{H}_2\text{O}}^2}{P_{\text{H}_2}^{3.5}} - \frac{P_{\text{CO}_2} P_{\text{H}_2}^{0.5}}{K_3 K_4} \right) / \text{DEN}^2$
Methane Combustion [26,133]	$\text{CH}_4 + 2\text{O}_2 \rightarrow 2\text{H}_2\text{O} + \text{CO}_2$	$r_5 = k_5 P_{\text{CH}_4} P_{\text{O}_2}$
Limestone Calcination [18]	$\text{CaCO}_3 \rightleftharpoons \text{CaO} + \text{CO}_2$	$\bar{r}_6 = \frac{1}{M_{\text{CaCO}_3}} \frac{dX_{\text{Calc}}}{dt} = \frac{1}{M_{\text{CaCO}_3}} \frac{dX_{\text{Calc}}}{dt} = k_6 (1 - X_{\text{Calc}})^{2/3} \left(1 - \frac{\bar{P}_{\text{CO}_2}}{P_{\text{Eq,CO}_2}} \right)^{1.86}$ $P_{\text{Eq,CO}_2} = 1.826 \times 10^7 \exp\left(\frac{-19680}{T(K)}\right)$

Table 4.3. Rate parameters for reactions considered in kinetic simulations

Reaction	Reaction Rate Parameters	
DMR [95,131]	$k_1 \left[\frac{\text{mol}}{\text{kg}_{\text{cat}} \cdot \text{s}} \right] = 1.29 \times 10^6 \text{Exp} \left(\frac{-102065}{RT} \right)$ $K_{\text{CH}_4,1} [\text{bar}^{-1}] = 2.566 \times 10^{-2} \text{Exp} \left(\frac{40684}{RT} \right)$	$K_{\text{CO}_2,1} [\text{bar}^{-1}] = 2.576 \times 10^{-2} \text{Exp} \left(\frac{37641}{RT} \right)$ $K_{\text{P},1} [\text{bar}^2] = 6.96 \times 10^{14} \text{Exp} \left(\frac{-259660}{RT} \right)$
RWGS [95,131]	$k_2 \left[\frac{\text{mol}}{\text{kg}_{\text{cat}} \cdot \text{s}} \right] = 0.35 \times 10^6 \text{Exp} \left(\frac{-81030}{RT} \right)$ $K_{\text{H}_2,2} [\text{bar}^{-1}] = 1.474 \text{Exp} \left(\frac{6025}{RT} \right)$	$K_{\text{CO}_2,2} [\text{bar}^{-1}] = 0.57 \text{Exp} \left(\frac{9262}{RT} \right)$ $K_{\text{P},2} [-] = 56.497 \text{Exp} \left(\frac{-36580}{RT} \right)$
SMR 1 [132]	$\text{DEN} = 1 + K_{\text{CO,SMR}} P_{\text{CO}} + K_{\text{H}_2,SMR} P_{\text{H}_2} + K_{\text{CH}_4,SMR} P_{\text{CH}_4} + \frac{K_{\text{H}_2\text{O,SMR}} P_{\text{H}_2\text{O}}}{P_{\text{H}_2}}$ $k_3 \left[\frac{\text{kmol} \cdot \text{bar}^{0.5}}{\text{kg}_{\text{cat}} \cdot \text{s}} \right] = 1.174 \times 10^{12} \text{Exp} \left(\frac{-240100}{RT} \right)$ $K_3 [\text{bar}^2] = \text{Exp} \left[\left(\frac{-26830}{T} \right) + 30.11 \right]$	$K_{\text{CO,SMR}} [\text{bar}^{-1}] = 8.23 \times 10^{-5} \text{Exp} \left(\frac{70610}{RT} \right)$ $K_{\text{H}_2,SMR} [\text{bar}^{-1}] = 6.12 \times 10^{-9} \text{Exp} \left(\frac{82900}{RT} \right)$ $K_{\text{CH}_4,SMR} [\text{bar}^{-1}] = 6.65 \times 10^{-4} \text{Exp} \left(\frac{38280}{RT} \right)$ $K_{\text{H}_2\text{O,SMR}} [-] = 1.77 \times 10^5 \text{Exp} \left(\frac{-88680}{RT} \right)$
SMR 2 [132]	$k_4 \left[\frac{\text{kmol} \cdot \text{bar}^{0.5}}{\text{kg}_{\text{cat}} \cdot \text{s}} \right] = 2.83 \times 10^{11} \text{Exp} \left(\frac{-243900}{RT} \right)$	$K_4 [-] = \text{Exp} \left[\left(\frac{4400}{T} \right) - 4.036 \right]$
Methane Combustion [26,133]	$k_5 \left[\frac{\text{mol}}{\text{kg}_{\text{cat}} \cdot \text{s} \cdot \text{bar}^2} \right] = 1.1 \times 10^{13} \text{exp} \left(\frac{-166000}{RT} \right)$	
Limestone Calcination [18]	$k_6 [s^{-1}] = 5.61 \times 10^5 \text{Exp} \left(\frac{-150000}{RT} \right)$	

Table 4.4. Correlations and supporting equations applied in kinetics simulations

Parameter	Correlations
Local Gas Velocity	$U_{\text{gas,mixture},z} = \frac{\sum F_{i,z} RT}{A_{\text{reactor}} P(z)}$
Peclet Number [129,130]	$Pe = \frac{U_{\text{Superficial}} L_{\text{Reactor}}}{D_a} = 3.472 Ar^{0.149} Re_{\text{Particle}}^{0.023} Sc_{\text{inlet}}^{-0.232} \left(\frac{L_{\text{Reactor}}}{d_{\text{Reactor}}} \right)^{0.285}$ $Re_{\text{Particle}} = \frac{\rho_{\text{Inlet-Gas}} U_{\text{Superficial}} d_{\text{Particle}}}{\mu_{\text{Inlet-Gas}}}$ $Sc_{\text{Inlet}} = \frac{\mu_{\text{Inlet-Gas}}}{D_{\text{Inlet-Gas}} \rho_{\text{Inlet-Gas}}}$ $Ar = \frac{d_{\text{Particle}}^3 \rho_{\text{Inlet-Gas}} (\rho_{\text{Solid}} - \rho_{\text{Inlet-Gas}}) g}{\mu_{\text{Inlet-Gas}}^2}$
Bed Voidage [130,134]	$\varepsilon_{\text{bed}} = \frac{U_{\text{Superficial}} + 1}{U_{\text{Superficial}} + 2}$

A single-phase axially dispersed plug flow reactor (ADPFR) model was employed for the gas mole balances, considering axial flow variation due to both concentration gradient (diffusive/dispersive flow) and reaction. This model has been widely accepted for the simulation of fluidized bed reactors operating in the turbulent fluidization regime [128–130]. Danckwerts boundary conditions (BC's) were applied, as suggested by others [128,129,135]. In summary, these BC's assume instant feed dilution by gas back mixing at the reactor entrance (as in a CSTR), with no reaction once gas leaves the top of the bed. The Peclet number ($=U_{\text{Superficial}} \cdot L_{\text{Reactor}} \cdot D_a^{-1}$) in the ADPFR model indicates the ratio of convective to dispersive mass flow rates within the reactor. Note that the ADPFR model reduces to CSTR and PFR models if the Peclet number approaches zero or infinity, respectively. Therefore, the ADPFR reactor model is theoretically capable of simulating a range, from complete (CSTR) to negligible (PFR), gas mixing behaviours. Considering that the Peclet number in turbulent fluidized bed reactors is roughly of order of magnitude 10 [135], appreciable gas axial dispersion is expected within the turbulent fluidized bed reactors.

The non-catalytic solid-gas limestone calcination was simulated using a continuous stirred tank reactor (CSTR) model. This corresponds to a uniform sorbent conversion within the bed, in agreement with previous studies on the simulation of lime-based solid-gas reactions in both reformers and calciners [17,98]. Accordingly, the mean sorbent conversion in each simulation run was based on the average calcination rate, calculated using the average CO₂ partial pressure within the reactor. The total desorbed CO₂ flow rate was then obtained using the limestone inlet flow rate and the calculated mean sorbent conversion. Simultaneously, the desorbed CO₂ enters the reactor gas, indicating the need for a desorbed gas distribution function. As the simplest approach, the desorbed CO₂ flow could be dispersed linearly, resulting in uniform CO₂ addition

into the reactor gas. However, the linear distribution approach would assume a constant calcination driving force throughout the reactor, while the CO₂ partial pressure varies along the bed height. Accordingly, the local CO₂ partial pressure calcination driving force in each node was used to develop a driving-force-weighted desorption distribution factor ($0 < \Gamma_z (P_{CO_2,z}) = F_{CO_2,des,z} / F_{CO_2,des,Total} < 1$, with $\sum \Gamma_z = 1$), as illustrated in Figure 4.1 and Table 4.1. The local desorbed CO₂ flow rate was then calculated by means of the total desorbed CO₂ flow rate and the local desorption distribution factor.

The single-phase ADPFR reactor model consists of a number of 2nd order two-point boundary value ordinary differential equations (TPBVDE). Accordingly, the ADPFR model was initially reduced to a system of 1st order ODE's, replacing dF_i/dh by a new parameter, arbitrary called G_i . The shooting method was then employed to solve the 1st order TPBVDE problem by iteratively modifying the species flow profiles using the Newton-Raphson method. This numerical solution technique requires an initial guess for the species flow profiles, with the convergence time/possibility strongly dependent on the precision of the applied initial guess. Accordingly, larger computation time is expected when the ADPFR model is applied than is required for the initial boundary value problem of the simpler PFR model [16].

A schematic diagram of the applied simulation algorithm for numerically solving the ADPFR kinetic model is depicted in Figure 4.2. The MRC-CAL reactor was discretized into 101 nodes, and the kinetic model was solved via the shooting method, programmed in MATLAB, with a minimum resolution of 10^{-4} mol.s⁻¹. Note that an orthogonal collocation technique could also be employed to solve this numerical problem [136]. Initial model assessments revealed that the shooting method is highly sensitive to the initial guess of the components' flow profiles, resulting in rapid divergence if the initial guess is imprecise. Accordingly, a reactivity coefficient

factor (λ) was considered for all calculated reaction rates (e.g. $r_j = \lambda r_{j,\text{calculated from rate expressions}}$) to ensure the convergence of the numerical solution. A λ of 10^{-14} and constant species flow profiles (equal to the components feed flow rates) were used to initiate each simulation run, while the resulting flow profiles (after solving the system with the initial λ) were used as the initial guess for the reactor simulation when λ reaches 10 times larger. The progressive calculation was then continued upon achieving a reactivity coefficient factor of unity.

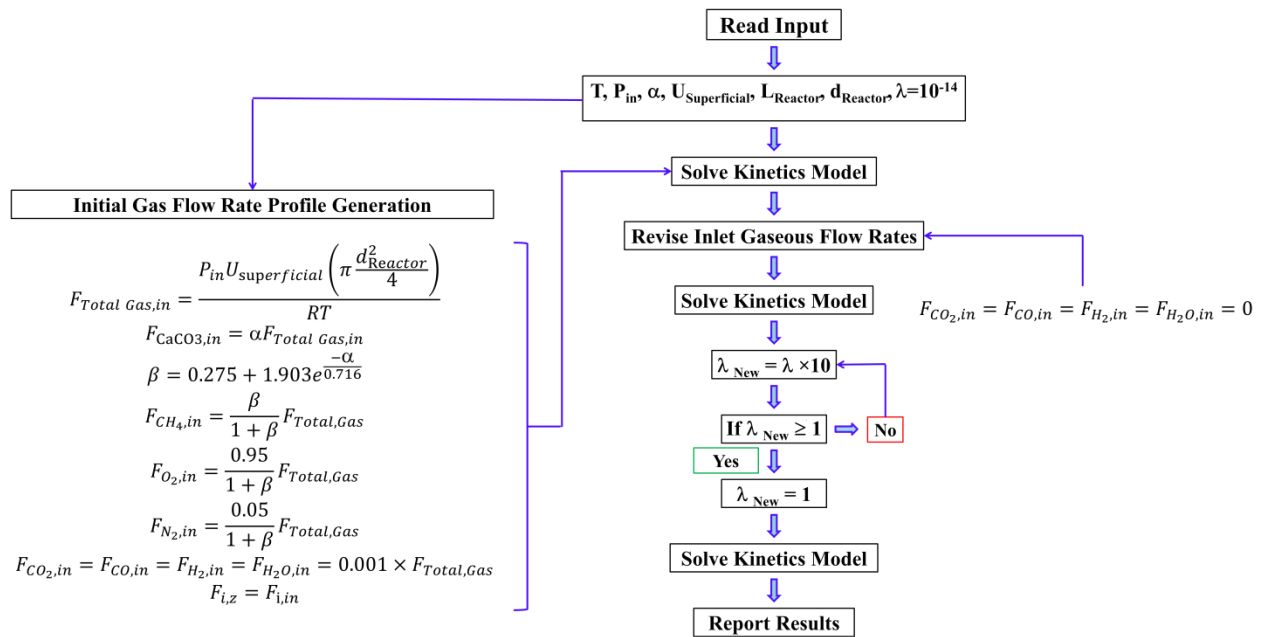


Figure 4.2. Simulation algorithm for kinetic simulation

Node independency was tested (up to 1001 nodes) and validated for the number of mesh points. Sensitivity analysis was also performed on some critical model parameters (CaO density, CaCO₃ density and average particle diameter) and no significant effect was observed on the reactor performance. The results of sensitivity analysis are briefly shown in Appendix C. Table 4.5 introduces some metric parameters which have often been employed to evaluate the MRC-CAL

performance in this chapter. Table 4.6 demonstrates the base inputs applied for the kinetic simulation of MRC-CAL process in turbulent fluidized bed reactor.

Table 4.5. Metrics for evaluating the MRC-CAL performance

Metric	Sorbent Conversion	Methane Conversion	H ₂ Yield
Definition	$\frac{F_{CaCO_3, \text{Calciner Feed}} - F_{CaCO_3, \text{Calciner Out}}}{F_{CaCO_3, \text{Calciner Feed}}}$	$\frac{F_{CH_4, \text{Calciner Feed}} - F_{CH_4, \text{Calciner Off-Gas}}}{F_{CH_4, \text{Calciner Feed}}}$	$\frac{F_{H_2, \text{Calciner Off-Gas}}}{F_{CH_4, \text{Calciner Feed}}}$

Table 4.6. Base inputs for kinetics simulations

Parameter/Variable	Values	Units
Reactor Diameter	0.1	m
Operating Temperature	850	°C
Sorbent Residence Time	10	min
Superficial Gas Velocity*	0.9	m/s
CaCO ₃ /Total Molar Gas Ratio	0.5	-
Catalyst/Solid Bed Mass Ratio	0.1	-
CaCO ₃ Density [15]	2200	kg/m ³
CaO Density [15]	1850	kg/m ³
Particle Diameter	200	µm
Enriched-Air Composition	95% O ₂ + 5% N ₂	

*Calculated at reactor operating temperature and pressure

4.3. Results and Discussion

4.3.1. Simulation Results in Base Inputs

The gases axial flow profiles for the base input data in Figure 4.3 show a substantial reduction in O₂ and CH₄ flow rates at the bottom of the reactor. This is in line with the predictions of an earlier PFR reactor model [119], corresponding to rapid methane combustion and reforming near the gas distributor. The hydrogen flow rate then decreases moderately along the bed, which could be due to enhanced reverse-water gas shift reaction (RWGS) by the limestone calcination. In

fact, limestone calcination releases considerable CO_2 into the reactor gas and consequently, shifts the RWGS reaction toward more hydrogen consumption. This also explains the moderate increase of the steam and CO flow rates along the bed height. Note that the remaining fraction of the desorbed CO_2 enters the reactor gas and consequently, increases the CO_2 flow rate within the reactor.

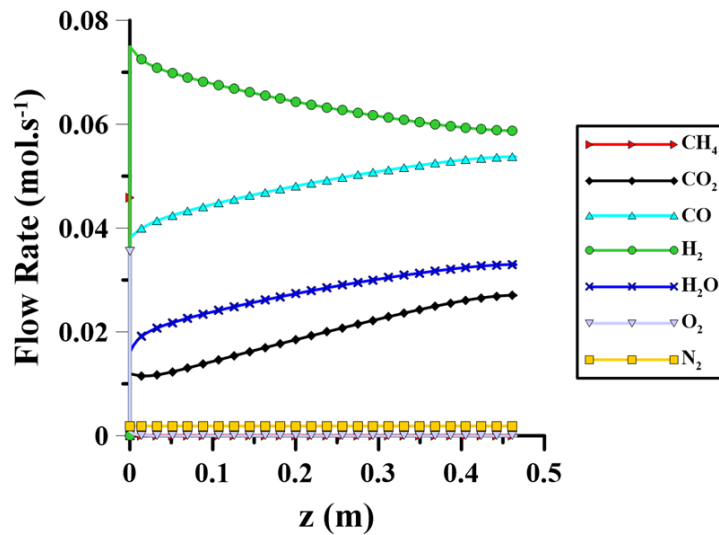


Figure 4.3. Simulated gases axial flow profiles at base input data in Table 4.6

4.3.2. Effect of Operating Temperature and Pressure

The effects of operating temperature and pressure on the sorbent conversion in the MRC-CAL and steam calcination units are shown in Figure 4.4. Note that steam in this study can theoretically be represented by other unreactive non- CO_2 calcination media such as air, argon and nitrogen. Increasing operating pressure in both calciner configurations results in lower sorbent conversion. On the other hand, more calcination can be achieved at elevated reactor temperatures. These observations can be explained by the effect of reactor pressure and temperature on the calcination rate and driving force. Increasing the reactor pressure leads to a lower calcination driving force, while elevating temperature enhances both the calcination rate

and the driving force. Accordingly, a higher reactor temperature is required to achieve a given sorbent conversion at elevated operating pressures. Note that these simulation results suggest that the MRC-CAL process offers faster sorbent regeneration only if the sorbent conversion exceeds roughly 20%. In fact, the initial combustion and reforming stages generate undesired CO₂ in the MRC-CAL gaseous medium and consequently, inhibiting limestone decomposition. However, the undesired impact of the initial CO₂ generation is alleviated at high sorbent conversions, owing to the promising *in situ* CO₂ utilization feature of the MRC-CAL process.

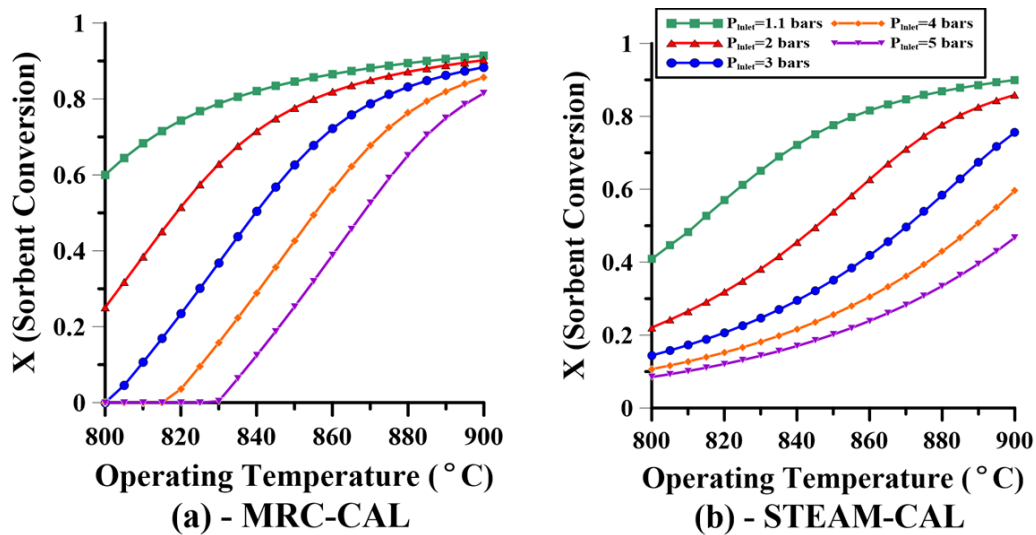


Figure 4.4. Effects of temperature and pressure on sorbent conversion in: (a) MRC-CAL process; and (b) STEAM-CAL units. Other input data are identical to those in Table 4.6

Overlaying the conversions shown in Figure 4.4 for MRC-CAL and STEAM-CAL identifies the sorbent conversions at which the MRC-CAL and steam calciner coincide, as exemplified in Figure 4.5. This “*critical conversion*” in each scenario was determined by finding the intercepts between the sorbent conversion in the MRC-CAL and STEAM-CAL reactors. The MRC-CAL process offers faster limestone calcination only if sorbent conversion exceeds this *critical conversion*. The resulting *critical conversions* plotted in Figure 4.6(a) indicate that increasing the

operating pressure at fixed CaCO_3 /total gas molar feed ratio (α) does not significantly affect the *critical conversion* ($\sim 19.5\% \pm 1\%$). However, the temperature required to achieve the *critical conversion* increases with increasing the reactor pressure, in agreement with the results presented in Figure 4.4. Note that Equation (4.1) is developed based on the MRC-CAL operating temperature of 800-900°C. However, the temperatures at which MRC-CAL and steam calciners show nearly identical sorbent conversion are lower than 800°C for pressures below 2 bars, and therefore, are omitted from Figure 4.6(a).

Figure 4.6(b) compares the *critical conversion* at fixed operating temperature and different CaCO_3 /total gas molar feed ratios (α). Increasing the operating pressure results in lowering the calcination extent in both the MRC-CAL and steam calcination reactors. Consequently, lower *critical conversion* is expected at elevated reactor pressures and fixed operating temperature. In addition, lower α is needed to achieve a given sorbent conversion at higher reactor pressures (see Section 4.3.3). Figure 4.6 suggests that the *critical conversion* depends mostly on the CaCO_3 /total gas molar feed ratio (α), with α values less than the *critical value* resulting in faster calcination by the MRC-CAL process (see Figure 4.5(b)). The latter can be explained by means of Equation (4.1), where the gaseous feed composition varies only with the solid to gas molar feed ratio. Note that incomplete limestone calcination in the MRC-CAL reactor may result in increasing the bed temperature, thereby further enhancing the calcination extent [137]. Accordingly, a well-insulated MRC-CAL reactor might show faster sorbent calcination than a steam calciner, even at α exceeding the *critical value*.

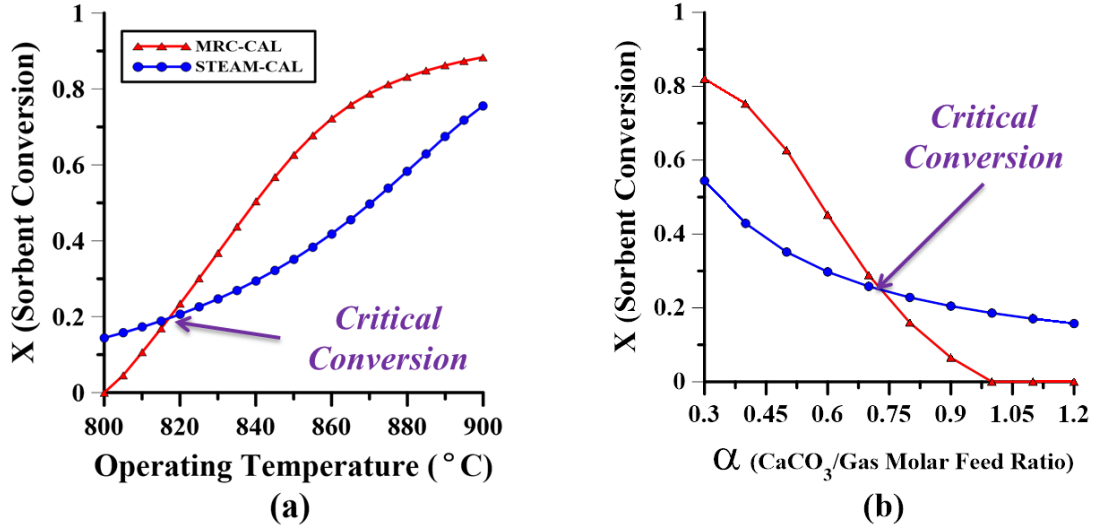


Figure 4.5. Determination of “critical conversion” at reactor pressure of 3 bars: (a) $\text{CaCO}_3/\text{total gas molar feed ratio } (\alpha) = 0.5$; and (b) reactor temperature of 850°C . Other input data are identical to those in Table 4.6

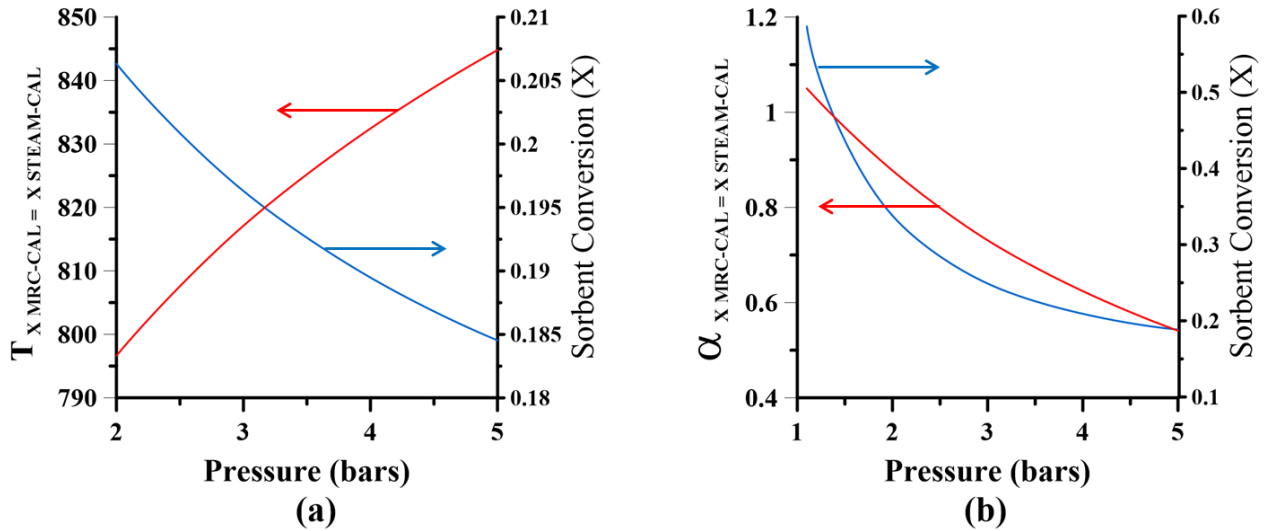


Figure 4.6. Effect of operating pressure on the “critical conversion” at: (a) $\text{CaCO}_3/\text{total gas molar feed ratio } (\alpha) = 0.5$; and (b) reactor temperature of 850°C . Other input data are identical to those in Table 4.6

The variation of methane conversion with operating temperature at different MRC-CAL pressures is depicted in Figure 4.7(a). It is seen that increasing the operating temperature results in higher methane conversion, while boosting the reactor pressure could reverse the behaviour.

These observations are consistent with Le Chatelier's principal for both reforming and calcination reactions. Note that the observed kinks at high reactor pressures are due to initiation of limestone calcination (Figure 4.4(a)), resulting in enhanced methane conversion by shifting the thermodynamic equilibrium of dry methane reforming.

Figure 4.7(b) compares the MRC-CAL hydrogen yield for operating conditions identical to those applied in Figure 4.7(a). The results show that the hydrogen yield decreases with increasing operating temperature at low reactor pressures. This is due to enhanced limestone calcination at elevated temperatures (Figure 4.4(a)), resulting in higher flow rates of released CO₂ and, consequently, increased *in situ* H₂ consumption *via* the reverse water-gas shift reaction. On the other hand, increasing the operating temperature at elevated reactor pressures initially increases the hydrogen yield, but exceeding a certain temperature results in a sharp reduction in hydrogen yield with further increasing in temperature. This may be due to the initiation of sorbent conversion, as illustrated in Figure 4.4(a). In fact, the hydrogen yield of the pressurized MRC-CAL reactors initially increases with increasing operating temperature since methane conversion is enhanced by increasing the reactor temperature (Figure 4.7(a)). However, initiating sorbent calcination (at a certain temperature for each pressure) results in substantial hydrogen consumption by the RWGS reaction, significantly diminishing the hydrogen production yield of the process. Note that the hydrogen yield for all operating pressures tested tends to a value of roughly 1.2 when the reactor temperature approaches 900°C. This observation is in line with the results in Figure 4.4(a), where the sorbent conversion was observed to be less sensitive to the reactor pressure at elevated temperatures. Accordingly, it can be concluded that the MRC-CAL hydrogen yield mostly relies on the sorbent conversion, with little influence of the operating temperature and pressure on hydrogen productivity.

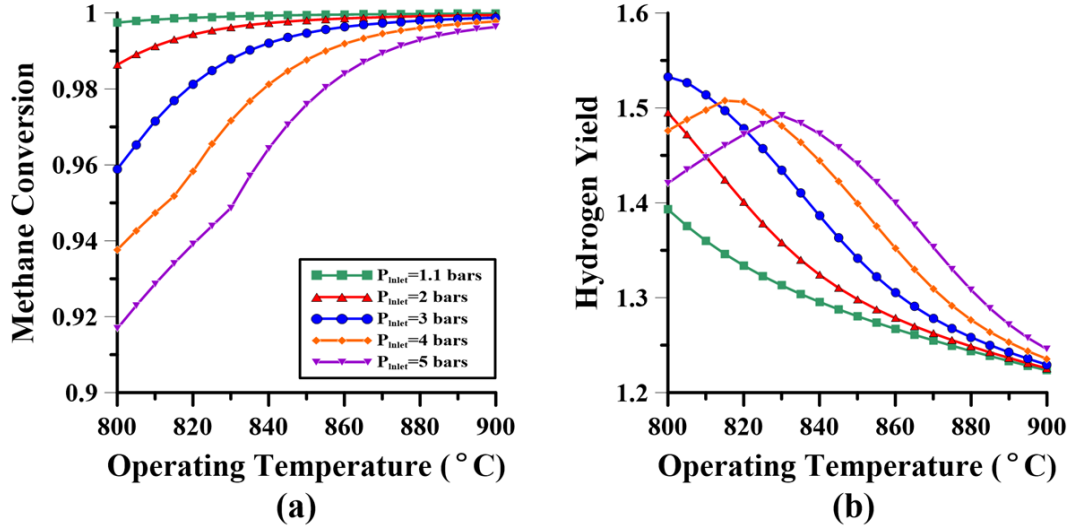


Figure 4.7. Effects of operating temperature and pressure on the MRC-CAL for: (a) methane conversion; and (b) hydrogen yield. Other input data are identical to those in Table 4.6

4.3.3. Effect of CaCO_3 /Total Gas Molar Feed Ratio

Figure 4.8 compares the sorbent conversion of the MRC-CAL and steam calciner units at fixed operating temperature and different CaCO_3 /total gas molar feed ratios (α). The simulations predict that increasing α results in substantial reduction of the sorbent conversion for both calciner configurations. In fact, increasing α (e.g. by increasing the CaCO_3 inlet flow rate) leads to a higher CO_2 flow rate entering the reactor gas. This increases the CO_2 partial pressure within the reactor and, consequently, inhibits limestone calcination. In addition, more methane combustion (due to enriched-air feed concentration, see Equation (4.1)) is required to maintain autothermal limestone calcination at elevated CaCO_3 /total gas molar feed ratios, producing more initial CO_2 within the reactor gas (MRC-CAL only). Consequently, the CO_2 partial pressure calcination driving force decreases with increasing α , resulting in lower sorbent conversion in both calciner configurations. Note that the MRC-CAL process reduces to a stoichiometric oxy-fuel calciner as the CaCO_3 /total gas approaches a value of roughly 1.45. Accordingly, increasing

α can substantially increase the required temperature at which a given sorbent conversion can be achieved by this novel sorbent regeneration process. Figure 4.8 also shows that increasing the reactor pressure leads to less limestone decomposition, as was also observed in Figure 4.4.

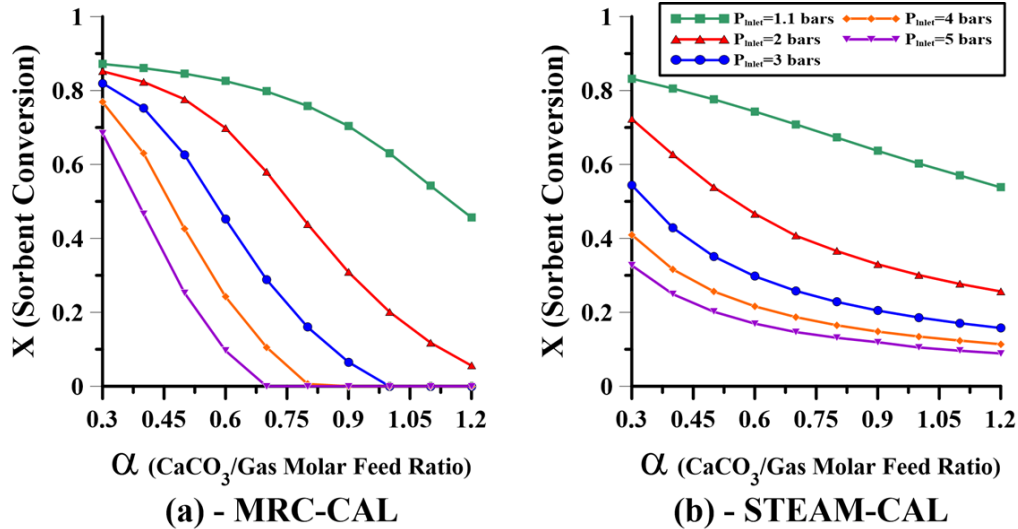


Figure 4.8. Effects of CaCO_3 /total gas molar feed ratio and reactor pressure on the sorbent conversion in: (a) MRC-CAL; and (b) STEAM-CAL units. Other input data are identical to those in Table 4.6

As mentioned above, the MRC-CAL process offers faster sorbent conversion than steam calciners for certain operating conditions. Figure 4.6(b) shows that increasing the reactor pressure leads to lower sorbent conversion and also lower corresponding α for identical calcination extent by the MRC-CAL and steam calciner units. The MRC-CAL offers faster sorbent regeneration only if the CaCO_3 /total gas molar feed ratio is less than the “critical value” in Figure 4.6(b). As the sorbent conversion increases with decreasing α , it can be concluded that the MRC-CAL is only preferred for high extents of limestone calcination.

Figure 4.9 demonstrates the effect of CaCO_3 /total gas molar feed ratio (α) on the methane conversion and hydrogen yield of the MRC-CAL process. Increasing α results in more CO_2 release into the reactor gas, and therefore, higher methane conversion due to enhanced dry

methane reforming. In addition, increasing α leads to lower methane/enriched-air molar feed ratio (see Equation (4.1)) and consequently, more methane conversion toward rapid and exothermic methane combustion. This also increases the initial CO_2 and steam generation, shifting the reforming thermodynamic equilibrium toward higher feedstock conversion. On the other hand, increasing the reactor pressure reduces the methane conversion, as discussed above with respect to Figure 4.7(a). Therefore, greater variation of the methane conversion with increased CaCO_3 /total gas molar feed is expected at higher reactor pressures, as confirmed by Figure 4.9(a).

Figure 4.9(b) shows that increasing the CaCO_3 /total gas molar feed ratio leads to lower hydrogen yield. This is due to increasing the *in situ* hydrogen consumption by the RWGS reaction (more CO_2 is added to the reactor gas) and lower methane conversion toward reforming (more oxygen fed, see Equation (4.1)). The simulation results also show that the MRC-CAL hydrogen yield at different reactor pressures approaches a similar value when the CaCO_3 /total gas molar feed ratio is substantially high or low. This observation is similar to those for the sorbent conversion in Figure 4.8(a). Accordingly, it can be concluded that the hydrogen yield of the MRC-CAL process is nearly independent of the reactor pressure, as also concluded from Figure 4.7(b). Instead, the hydrogen yield of the MRC-CAL process depends mainly on the CaCO_3 /total gas molar feed ratio and the sorbent conversion, with increases in both reducing the hydrogen yield.

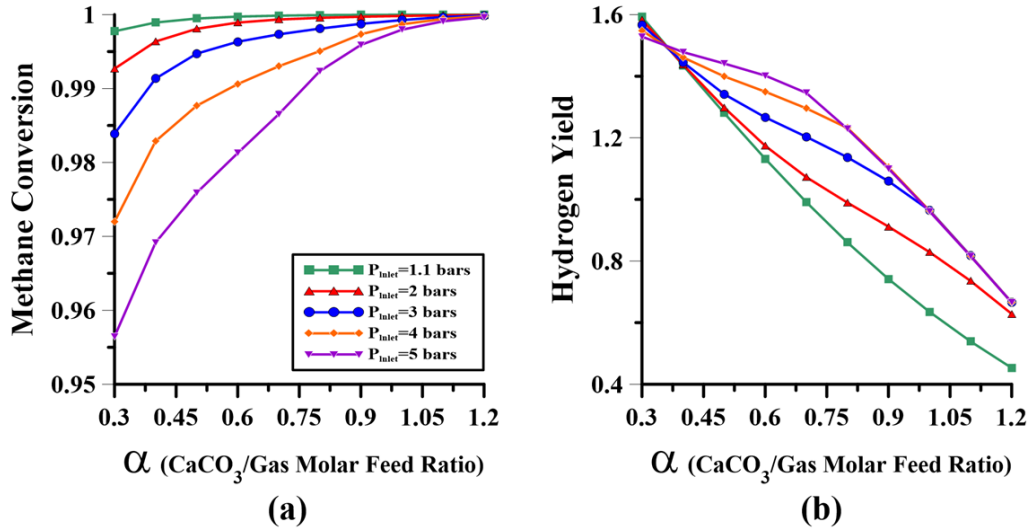


Figure 4.9. Effects of CaCO₃/total gas molar feed ratio and reactor pressure on MRC-CAL: (a) methane conversion; (b) hydrogen yield. Other input data are identical to those in Table 4.6

4.3.4. Effect of Sorbent Residence Time

The effect of sorbent residence time on the MRC-CAL sorbent conversion at different reactor pressures in Figure 4.10(a) demonstrates that higher sorbent residence time is required to achieve a given sorbent conversion at elevated reactor pressures. Increasing the sorbent residence time was also observed to have a less positive impact at higher operating pressures. This could be due to the reduction of calcination driving force at elevated reactor pressures. In addition, the variation of sorbent conversion with residence time decreases with increasing sorbent conversion. These results suggest that a sorbent residence time of 5-10 min could be optimal for the MRC-CAL process.

Figure 4.10(b) compares the required reactor length to achieve different sorbent residence times at operating pressures of 1 to 5 bars. As expected, greater bed height is needed to achieve higher sorbent residence times. In addition, increasing the reactor pressure at a constant superficial gas velocity leads to a higher gas molar inlet flow. Given a fixed CaCO₃/total gas molar feed ratio,

the CaCO_3 inlet flow rate must increase with increasing reactor pressure, resulting in a lower sorbent residence time at elevated pressures. Thus, increasing the reactor pressure requires a larger reactor to achieve a given sorbent residence time. Larger reactors would therefore be needed to obtain a given sorbent conversion at elevated reactor pressures.

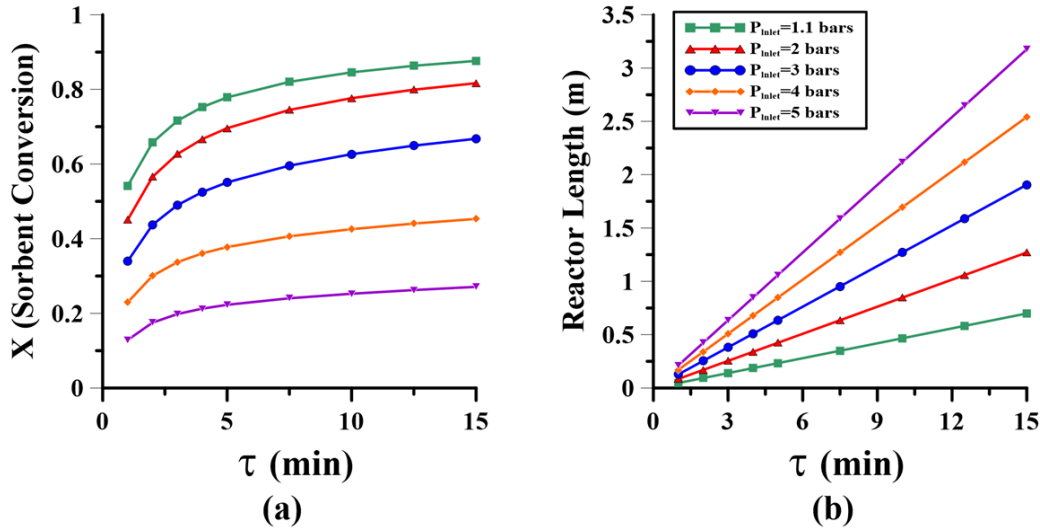


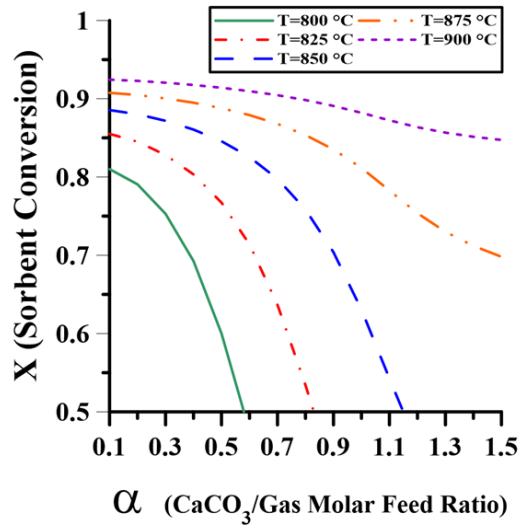
Figure 4.10. Effects of sorbent residence time and reactor pressure on: (a) sorbent conversion in MRC-CAL; and (b) reactor length. Other input data are identical to those in Table 4.6

4.3.5. Design Methodology

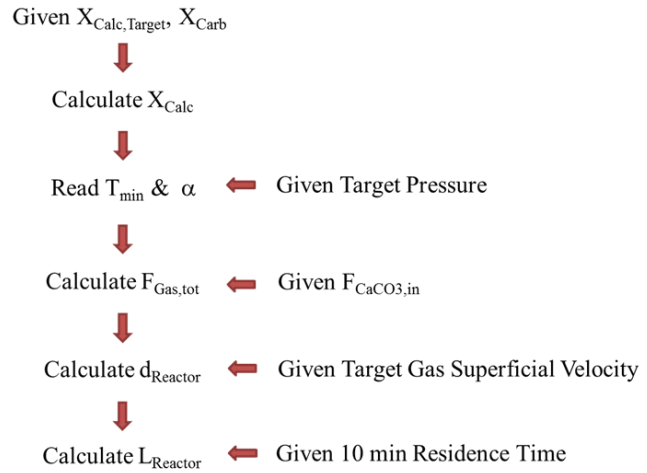
The performance of the MRC-CAL process has been shown to depend strongly on the reactor pressure, operating temperature and $\text{CaCO}_3/\text{total gas molar feed ratio}$ (α). It was also observed that a sorbent residence time of 10 minutes is optimal, with further increases in reactor length barely enhancing the sorbent conversion. In theory, a higher operating temperature, lower reactor pressure and smaller α are required to maximize the sorbent regeneration. However, increasing the calciner temperature results in serious operational challenges, including increased sorbent sintering, more thermal inertia and higher reactor cost. On the other hand, elevated reactor pressures are often preferred by industry due to higher reactor throughput and reduced need for

compression of the product. Fluidized bed sorbent-enhanced steam methane reformers (with or without *in situ* hydrogen perm-separation) are likely to be pressurized, resulting in a complicated solid circulation system when integrated with atmospheric calciners (e.g. for pressure swing adsorption). The CaCO_3 /total gas molar feed ratio is the most flexible influential factor, adjustable by varying the solid circulation rate, gas velocity and/or reactor cross-sectional area. In practice, larger CaCO_3 /total gas molar feed ratios are of interest to minimize the reactor size and gas requirement. Therefore, it is vital to simultaneously investigate the influential factors for the process, providing the lowest operating temperature and highest CaCO_3 /total gas molar feed ratio to achieve the desired sorbent conversion at the target reactor pressure.

Hence, the simulation results were extended to introduce a simple MRC-CAL design methodology for operating temperatures of 800-900°C and reactor pressures of 1-5 bars. Figures 4.11(a) and 4.12(a)-(d) were obtained, each demonstrating the variation of sorbent conversion (with limits of 50% - 100% for a 10 minute sorbent residence time) with CaCO_3 /total gas molar feed ratio at different operating temperatures and fixed reactor pressure. These figures can be further used for preliminary design of the MRC-CAL sorbent regenerators for calcium-looping technology. Figure 4.11(b) shows a schematic diagram of the MRC-CAL design methodology. The inputs, calculation methods and design outputs are summarized briefly in Table 4.7.



(a) - 1.1 bars

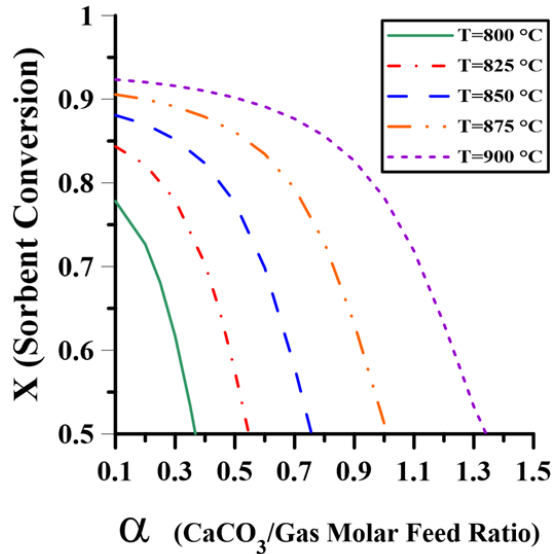


(b)

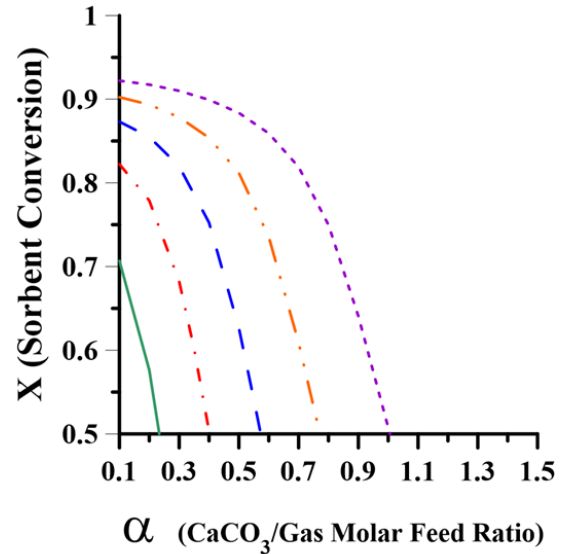
Figure 4.11. (a) MRC-CAL graph for determination of design parameters at 1.1 bars; (b) MRC-CAL reactor design steps ($\tau = 10$ min).

Table 4.7. MRC-CAL design methodology

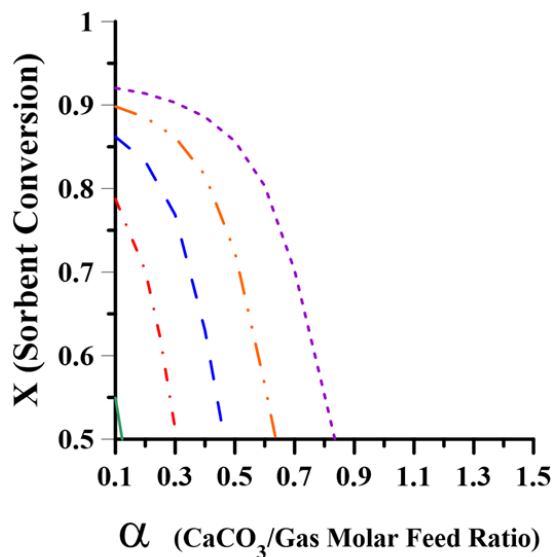
Inputs	$X_{Carb}, X_{Calc,Target}, P, F_{CaCO_3, Calciner Feed}, U_{Superficial, Target}, \tau, v_{CaCO_3, bed}$
Equations	$X_{Calc, Design} = \frac{1 - X_{Calc, Target}}{X_{Carb}}$ <p>α and $T_{min} \rightarrow$ Read from Design Parameters at P and $X_{Calc, Design}$</p> $F_{Gas, Calciner Feed} = \frac{F_{CaCO_3, Calciner Feed}}{\alpha} \rightarrow d_{Reactor} = \left(\frac{4F_{Gas, Calciner Feed}}{\pi U_{Superficial, Target}} \right)^{0.5}$ $\varepsilon = \frac{U_{Superficial, Target} + 1}{U_{Superficial, Target} + 2} \rightarrow L_{Reactor} = \frac{4F_{CaCO_3, in} M_{CaCO_3} \tau}{\pi \rho_{CaCO_3} d_{Reactor}^2 (1 - \varepsilon) v_{CaCO_3, bed}}$
Outputs	$d_{Reactor}, L_{Reactor}, T_{min}$



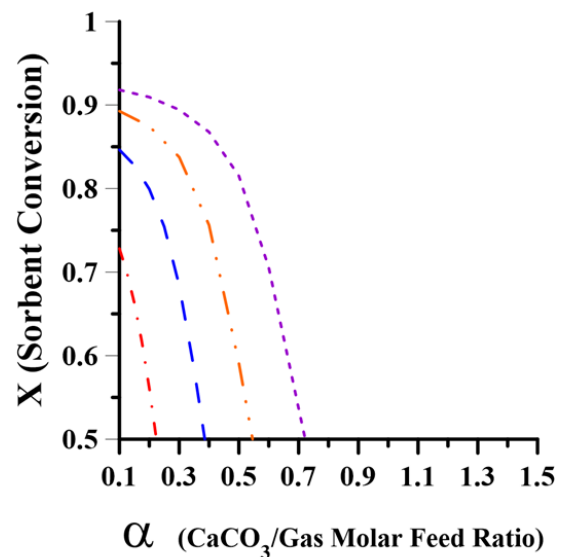
(a) - 2 bars



(b) - 3 bars



(c) - 4 bars



(d) - 5 bars

Figure 4.12. MRC-CAL graphs for determination of design parameters at: (a) 2 bars; (b) 3 bars; (c) 4 bars; and (d) 5 bars ($\tau = 10$ min.)

These results suggest that lower $\text{CaCO}_3/\text{total gas}$ molar feed ratio and higher operating temperature are required to achieve a given sorbent conversion at elevated reactor pressures, as also shown earlier in this chapter. The proposed design methodology can be employed to generate a rough estimate of the operating conditions and/or reactor dimensions for the MRC-

CAL process. Note that the MRC-CAL process should ideally operate autothermally, without the need for additional heating supply. However, the process thermal behaviour in practical applications may differ from the ideal scenario owing to:

1. Incomplete sorbent regeneration
2. Low gaseous feed temperature (normally preheated to 300-400°C)
3. Low solid circulation temperature (entering the calciner at reformer/carbonator temperature)
4. Low sorbent make-up flow temperature (normally fed at room temperature)
5. Heat losses through insulation

Note that solid attrition and pore sintering are major challenges in practical operation, requiring considerable sorbent make-up for continuous operation. This imposes additional energy penalty on the system, attributed to energy loss by solid replacement. Therefore, minor supply of heat may be required to maintain the reactor temperature in practical applications. A portion of the MRC-CAL higher heating value off-gas can be used as process fuel, providing the required excess energy inside (e.g. additional enriched-air feeding) or outside (e.g. fuel burning in the reactor shell) of the reactor. The additional enriched-air in the former case should preferably be fed above the gas distributor to burn syngas rather than methane. This would potentially reduce the temperature spike near the gas distributor, while more energy can be obtained by burning syngas, rather than methane (minimizing extra enriched-air flow). In addition, *in situ* syngas combustion reduces the hydrodynamic variations compared to mole-balanced methane combustion. In fact, reforming and calcination both increase the molar flow, thereby increasing the gas superficial velocity within the reactor. However, syngas combustion is mole-consuming and therefore, slightly reduces hydrodynamic variation within MRC-CAL reactors. Note that *in situ* combustion of syngas releases undesired CO₂ into the calciner gaseous medium. This can

potentially reduce the limestone calcination driving force, rate and extent. Accordingly, slightly higher temperature than predicted in the absence of heat loss may be required if a portion of syngas is burned inside the reactor.

The remaining MRC-CAL off-gas is mainly composed of H_2 , CO, CO_2 and steam, with minor constituent of nitrogen and unreacted methane. This can be further used in various applications, such as power generation, metal oxide reduction, Fischer-Tropsch processes and liquid fuel production. Note that certain H_2/CO ratios might be required for some of these processes, while the MRC-CAL syngas composition could vary based on the calciner operating conditions. An additional water-gas shift reactor (with excess steam) could be of interest to adjust the MRC-CAL off-gas composition prior to the next post-processing steps. Given the moderate temperature of the water-gas shift (WGS) reaction, palladium-based membranes may be implemented inside the reactor, shifting the thermodynamic equilibrium of the WGS reaction toward higher hydrogen production.

A relatively high methane conversion (e.g. >90%) can be achieved by the MRC-CAL process, as shown above in Figures 4.7(a) and 4.9(a). This is important as methane is considerably more potent as a greenhouse gas than carbon dioxide. Note that a pure methane feedstock was assumed in this work for simplicity. However, practical applications would use natural gas, which, although typically >95 % methane, contains minor constituents of H_2S , ethane, CO_2 and other trace gases. These impurities may adversely affect the system thermal behaviour, syngas composition, and the reactivity of calcined limestone for CO_2 capture. At a minimum, removal of almost all of the H_2S and other sulphur-containing compounds would be required to minimize degradation of the catalyst. Methane leakage could be another major challenge in the MRC-CAL process, resulting in serious environmental consequences if not addressed properly. Before the

process could be adopted commercially, comprehensive long-term performance and life cycle analyses would be imperative to assess and compare the economic and environmental impacts of the MRC-CAL process to other similar technologies.

The design parameters in this chapter (Figures 4.11(a) and 4.12) were obtained by assuming pure CaCO_3 feeding into the MRC-CAL reactor. However, the sorbent particles leaving the carbonator/reformer are likely to be only partially carbonated (mostly towards the outer surface) owing to the two-stage carbonation mechanism (fast stage reaction-controlled step, followed by the slow-stage diffusion-controlled carbonation) and thermal pore sintering [4,43,46,47]. This corresponds to an enhanced calcination rate compared to those for fully calcite particles. Therefore, higher sorbent conversion than predicted by the design methodology could be expected for sorbents circulating between the reformer and calciner.

Note that the methane feed concentration in the autothermal MRC-CAL process varies between 33 and 69%, corresponding to methane/enriched-air molar feed ratios of nearly 0.5-2.2 [137]. This slightly exceeds the methane upper flammability limit (UFL) in the oxy-fuel feedstock (~61% at 1 atm and 20°C [138]). However, increase in the operating temperature and pressure raise the UFL [139] and, hence, the MRC-CAL gaseous feedstock remains within the methane flammability limits. Appropriate reactor design and configuration would therefore be essential to ensure safe unit operation.

4.4. Conclusion

A kinetic reactor model is employed to compare the performance of combined methane reforming, combustion and limestone calcination with conventional steam calciners in isothermal turbulent fluidized bed reactors. This novel sorbent regeneration technique can offer faster

sorbent calcination under certain circumstances, especially if high sorbent regeneration extent is needed. This is due to favourable *in situ* CO₂ utilization behaviour of the proposed process, maintaining a high limestone calcination driving force within the reactor. In addition, this process can ideally be operated autothermally without external heating. Given the endothermicity of calcination, incomplete sorbent conversion results in increased bed temperature, thereby enhancing the sorbent calcination rate and extent. The proposed process is capable of adapting its thermal behaviour to maximize sorbent conversion, a promising feature for practical applications.

The effects of key operating factors on the reactor performance were investigated, with the results showing higher sorbent conversion at lower reactor pressure, higher operating temperature and lower CaCO₃/total gas molar feed ratios. Increasing the sorbent residence time also enhances the sorbent conversion, with 5-10 minutes sorbent residence time being optimal. The process produces higher heating values off-gas (syngas, H₂ + CO), with the hydrogen yield mostly dependent on the sorbent conversion and CaCO₃/gas molar feed ratio.

A design methodology is introduced for MRC-CAL units operating at 800-900°C and 1-5 bars pressure. This novel sorbent regeneration process has potential for pressurized limestone calcination in a practical range of operating temperatures. The proposed design methodology can be further used to determine the calciner range of operating conditions and reactor dimensions in calcium looping technology.

CHAPTER 5: Simulation of Sorbent-Enhanced Steam Methane Reforming and Limestone Calcination in Dual Turbulent Fluidized Bed Reactors

5.1. Introduction

Catalytic steam methane reforming (SMR) is the most important industrial hydrogen production route [140]. However, the thermodynamic equilibrium of the reversible SMR reactions prevents complete feedstock conversion, thereby limiting hydrogen production yield and product purity [141]. Previous studies have shown that *in situ* H₂ and CO₂ removal can favourably shift the thermodynamic equilibrium of the SMR reactions toward higher feedstock conversions [9,12,15,17–20]. *In situ* hydrogen removal can be achieved by installing hydrogen-permselective membranes (usually Pd-based) inside the reactor. Steam methane reforming can instead be integrated with calcium-looping technology, with lime-based sorbents assisting in capturing high-temperature CO₂ and in producing hydrogen [17,20,26,142,143].

Sorbent-enhanced steam methane reforming (SE-SMR) combines three major reactions; methane reforming, water-gas shift and lime carbonation. These reactions depend strongly on various factors, resulting in a complex system. The effects of different operating conditions on each individual reaction of the SE-SMR process are summarized in Table 5.1. The variation of SE-SMR performance with these operating conditions depends on their competitive effects for each individual reaction. Therefore, comprehensive performance analysis is crucial to determine the operating conditions in which optimal SE-SMR performance can be achieved.

Table 5.1. Effects of operating conditions on the reactions involved in the SE-SMR process

Reaction	SMR*	WGS*	Carbonation*
Temperature ↑	↑	↓	↓
Pressure ↑	↓	-	↑
Steam-to-Methane Feed Ratio ↑	↑	↑	-
Sorbent/Methane Feed Ratio ↑	-	-	↑
Membrane Addition ↑	↑	↑	-

* Upward and downward arrows indicate favourable and unfavourable, respectively.

Conventional SE-SMR processes consist of two interconnected fluidized bed reactors (FBR's), maintaining cyclic operation by circulating sorbent and catalyst particles back and forth between the reformer and calciner [41,144]. Ideally, hydrogen-enriched gas leaves the reformer, while a concentrated CO₂ stream is obtained from the sorbent calciner. The CO₂ concentration of the calciner off-gas depends mainly on the applied gaseous medium, with air, steam, CO₂, and oxy-fuel feedstock studied most in the literature. However, these processes suffer from several operational challenges, including external heating supply, dilute CO₂ off-gas, low thermal efficiency and high reactor temperature [118]. Alternatively, a methane-concentrated oxy-fuel calciner (MRC-CAL, detailed in Chapters 3 and 4) can be used to achieve autothermal syngas-producing sorbent regeneration at reduced reactor temperatures. A general schematic of the SE-SMR/MRC-CAL process in dual fluidized bed reactors is depicted in Figure 5.1, demonstrating the solid circulation and input/output of gaseous components, with gases in brackets representing minor constituents.

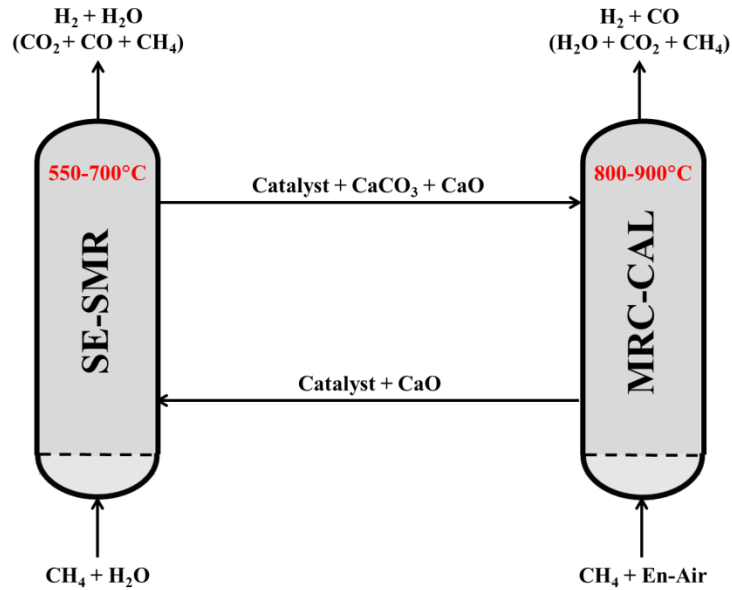


Figure 5.1. General schematic of integrated SE-SMR/MRC-CAL process in dual FBR's

Previous studies have mostly focused on the simulation of the SE-SMR process in fixed, bubbling and fast fluidized bed reactors [10,17,18,41,145–148]. However, industrial fluidized bed reactors often operate in the turbulent fluidization flow regime, owing to improved solids hold-up and gas-solid contact. This chapter addresses the steady-state simulation of the SE-SMR process in isothermal turbulent fluidized bed reactors. The variation of reformer performance is investigated for different operating conditions, in the presence and absence of hydrogen-permselective membranes. The effects of solid attrition and sorbent utilization decay are not included to avoid excessive simulation complexity. The required limestone calcination conditions are determined and compared for a SE-SMR reactor, integrated with steam and MRC-CAL sorbent regenerators.

5. 2. Simulation Setup

The methodology for kinetic simulation of the MRC-CAL process in turbulent fluidized bed reactors is detailed in Chapter 4. A similar approach is employed here, with minor modifications

to include the lime carbonation and *in situ* hydrogen separation. In summary, an axially dispersed plug flow reactor model is used for the gas phase mole balance, whereas lime carbonation is modeled by the continuous stirred tank reactor model. Mean sorbent conversion for each simulation run was obtained based on the average carbonation rate, estimated using the mean CO₂ concentration within the reactor. A local sorption distribution factor was then employed, taking the axial variation of the lime carbonation driving force into account. The governing equations, applied correlations, and the lime carbonation and H₂ permeation rate expressions are summarized in Tables 5.2-5.4. The other model parameters (e.g. methane reforming rate expressions and the Peclet number) are identical to those employed in Chapter 4.

Table 5.2. Governing equations for kinetic simulations

Dimensionless Form of Gas Phase Mole Balance	$h = \frac{z}{L_{\text{Reactor}}} \text{ and } Pe = \frac{U_{\text{Superficial}} L_{\text{Reactor}}}{D_a}$ $\frac{1}{Pe} \frac{d^2 F_i}{dh^2} - \frac{dF_i}{dh} + L_{\text{Reactor}} \left(\rho_{\text{Cat,bed}} \left(\sum_{j=1}^5 v_{i,j} r_j \right) A_{\text{Reactor}} + \pi N_{\text{Mem}} d_{\text{Mem}} J_{\text{H}_2,z} \right) + \frac{dF_{\text{CO}_2,\text{Des},z}}{dh} - \frac{dF_{\text{CO}_2,\text{Sorb},z}}{dh} = 0$ $\text{BC1: } F_{i,h=0} - F_{i,\text{in}} = \frac{1}{Pe} \frac{dF_i}{dh} \Big _{h=0} \quad \text{BC2: } \frac{dF_i}{dh} \Big _{h=L_{\text{Reactor}}} = 0 \quad i: \text{CH}_4, \text{CO}_2, \text{CO}, \text{H}_2, \text{H}_2\text{O}, \text{O}_2, \text{N}_2$
CaO Sorption Mole Balance	$X_{\text{Carb}} = \frac{-\bar{r}_7 \rho_{\text{CaO,bed}} V_{\text{Reactor}}}{F_{\text{CaO,Reformer Feed}}} \quad F_{\text{CO}_2,\text{Sorb,Total}} = F_{\text{CaO,in}} X_{\text{Carb}}$ $\Gamma_{\text{Carb}}(z) = \frac{F_{\text{CO}_2,\text{Sorb},z}}{F_{\text{CO}_2,\text{Sorb,Total}}} \Rightarrow F_{\text{CO}_2,\text{Sorb},z} = F_{\text{CO}_2,\text{Sorb,Total}} \times \Gamma_{\text{Carb}}(z) \quad \Gamma_{\text{T,Carb}} = \sum_{i=1}^{N_{\text{Nodes}}} \left(\frac{P_{\text{CO}_2,z}}{P_{\text{Eq,CO}_2}} - 1 \right)^{0.66} \quad \text{only if } P_{\text{CO}_2,z} \geq P_{\text{Eq,CO}_2}$ $\Gamma_{\text{Carb}}(z) = \frac{\left(\frac{P_{\text{CO}_2,z}}{P_{\text{Eq,CO}_2}} - 1 \right)^{0.66}}{\Gamma_{\text{T,Carb}}} \quad \text{if } P_{\text{CO}_2,z} \geq P_{\text{Eq,CO}_2} \quad \Gamma_{\text{Carb}}(z) = 0 \quad \text{if } P_{\text{CO}_2,z} < P_{\text{Eq,CO}_2}$
Permeation Flux	$J_{\text{H}_2,z} = \frac{\kappa_{\text{H}_2,\text{Pd}}}{\delta} \left(P_{\text{H}_2,\text{Film},z}^{0.5} - P_{\text{H}_2,\text{Permeate}}^{0.5} \right) = \frac{k_{g,\text{Mem}}}{RT} \left(P_{\text{H}_2,\text{Reformer},z} - P_{\text{H}_2,\text{Film},z} \right)$

Table 5.3. Correlations and supporting equation applied for kinetics simulations

Parameter	Correlations																		
External Mass Transfer Coefficient for Membrane Tubes [149]	$Sh_{Mem} = \frac{k_{g,Mem} d_{Mem}}{D_{H_2}}$																		
Sherwood Number for Membrane Tubes [12,149]	$Nu_{Mem} = B Re_{Mem}^n Pr_{Mem}^{1/3}$ Mass Transfer Analogy: $Sh_{Mem} = B Re_{Mem}^n Sc_{Mem}^{1/3}$ <table border="1" style="margin-left: auto; margin-right: auto;"> <thead> <tr> <th>Re_{Tube}</th> <th>B</th> <th>n</th> </tr> </thead> <tbody> <tr> <td>0.4-4</td> <td>0.989</td> <td>0.33</td> </tr> <tr> <td>4-40</td> <td>0.911</td> <td>0.385</td> </tr> <tr> <td>40-4,000</td> <td>0.683</td> <td>0.466</td> </tr> <tr> <td>4,000-40,000</td> <td>0.193</td> <td>0.618</td> </tr> <tr> <td>40,000 – 400,000</td> <td>0.027</td> <td>0.805</td> </tr> </tbody> </table>	Re_{Tube}	B	n	0.4-4	0.989	0.33	4-40	0.911	0.385	40-4,000	0.683	0.466	4,000-40,000	0.193	0.618	40,000 – 400,000	0.027	0.805
Re_{Tube}	B	n																	
0.4-4	0.989	0.33																	
4-40	0.911	0.385																	
40-4,000	0.683	0.466																	
4,000-40,000	0.193	0.618																	
40,000 – 400,000	0.027	0.805																	
Reynolds and Schmidt Number for Membrane Tubes [149]	$Re_{Mem} = \frac{\rho_{Gas} U_{gas,mixture,z} d_{Mem}}{\mu_{Gas}}$ $Sc_{Mem} = \frac{\mu_{Gas}}{D_{H_2} \rho_{Gas}}$																		
Effective Diffusivity in Lime Carbonation [149]	$D_{Eff} = D_{Eff,0} \left(\frac{1 + \bar{A} X_{Carb}}{1 + \bar{B} X_{Carb}} \right)$ $\bar{A} = \left(\frac{1 - \varepsilon_{Pore}}{\varepsilon_{Pore}} \right)$ $D_{Eff,0} = \left(\frac{1}{\varepsilon_{Pore}} \right) \left(\frac{1}{D_{Molecular}} + \frac{1}{D_{Knudsen}} \right)^{-1}$ $\bar{B} = \frac{AD_{eff,0}}{D_{PL}}$																		
Reactor Local Area	$A_{Reactor,z} = A_{Reactor} - A_{Occ,Mem} = \pi \frac{d_{Reactor}^2 - N_{Mem} d_{Mem}^2}{4}$ Node in membrane zone $= \pi \frac{d_{Reactor}^2}{4}$ Node out of membrane zone																		

Table 5.4. Rate expressions for lime carbonation and hydrogen permeation

Reaction/Permeation	Rate Expression
Lime Carbonation [12]	$\bar{r}_7 = \frac{1}{M_{CaO}} \frac{dX_{Carb}}{dt} = \frac{1}{M_{CaO}} \frac{\frac{6}{d_{Particle}} (1 - X_{Carb})^{2/3} (P_{CO_2} - P_{CO_2,eq})^{0.66}}{\frac{1}{k_7} + \frac{d_{Particle} \left((1 - X_{Carb})^{1/3} - (1 - X_{Carb})^{2/3} \right)}{2D_{eff}} + \frac{(1 - X_{Carb})^{2/3}}{k_{g,Particle}}}}{\rho_{CaO} RT}$ $k_7 \left[\frac{m}{s} \right] = 3.05 \text{Exp} \left(\frac{-32600}{RT} \right) \quad D_{PL} \left[\frac{m^2}{s} \right] = 7.7 \times 10^{-9} \quad \bar{\tau} [-] = 5 \quad r_{Pore} [m] = 10 \times 10^{-9} \quad \varepsilon_{Pore} [-] = 0.5$
H ₂ Permeation [17]	$\kappa_{H_2,Pd} \left[\frac{mol}{m.s.bar^{0.5}} \right] = 3.43 \times 10^{-5} \times \exp \left(\frac{-9180}{RT} \right)$

5.3. Results and Discussion

5.3.1. Hydrodynamic, Base Input Data and Performance Metrics

Turbulent fluidization is initiated in gas-solid fluidized beds by exceeding the superficial gas velocity demarcating an onset of turbulent fluidization (U_c), corresponding to the bubbling (or slugging)/turbulent fluidization boundary. Raising the superficial gas velocity further results in greater bed expansion, ultimately leading to transition to the fast fluidization flow regime. The range of gas superficial velocity for turbulent fluidization depends strongly on the particle properties (especially size, density and shape), reactor geometry (e.g. reactor diameter, height and configuration), and operating conditions (especially temperature and pressure) [128]. Bi et al. [150,151] proposed two empirical correlations to determine the lower and upper gas superficial velocities, respectively, for turbulent fluidized bed reactors:

$$Re_c = 0.565Ar^{0.461} \quad (5.1)$$

$$Re_{se} = 1.53Ar^{0.5} \quad (5.2)$$

The overarching objective of this chapter is to perform a preliminary simulation analysis on the performance of dual pilot-scale turbulent FBR's. As a case study, a pilot plant consisting of two interconnected reactor columns (inner diameter ~ 75 mm, expanded bed height of 3.5 m) is considered, capable of operating at high temperatures and pressures. Figure 5.2 illustrates the range of superficial gas velocities and gas molar flow rates needed to maintain turbulent fluidization in these pilot-scale dual fluidized bed reactors. A fixed gas inlet flow rate of 0.2 mol.s^{-1} is applied for all SE-SMR simulations. Table 5.5 shows the simulation base input data, together with the ranges of values investigated. Some performance metrics, frequently used to evaluate system performance for different scenarios, are defined in Table 5.6.

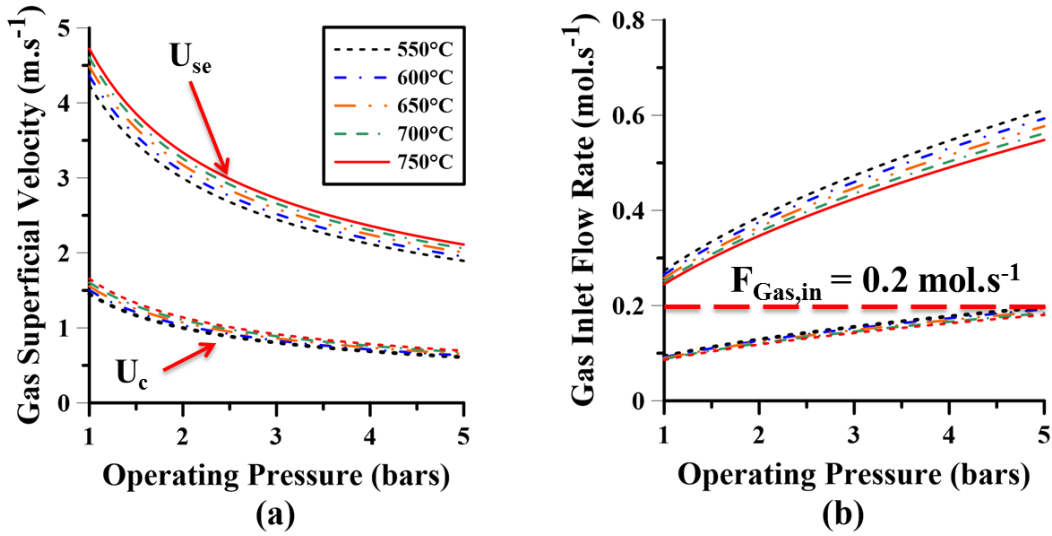


Figure 5.2. Boundaries of turbulent fluidization regime: (a) gas superficial velocity; (b) gas inlet flow rate for a reactor diameter of 75 mm.

Table 5.5. Base input data and ranges considered in kinetic simulations.

Parameter/Variable	Base Value	Range	Units
Reactor Diameter	0.075	-	m
Expanded Bed Height	3.5	-	m
Gas Inlet Flow Rate	0.2	-	mol.s ⁻¹
Catalyst Inlet Flow Rate	1.56	-	g/s
CaCO ₃ Particle Density [15]	2200	-	kg/m ³
CaO Particle Density [15]	1850	-	kg/m ³
Particle Diameter	100	-	μm
Membrane OD	10	-	mm
Membrane Thickness	25	-	μm
Membrane Length	3	-	m
Membrane Height Interval	0.25 – 3.25		m
Number of Membranes	0	0-3	-
Pressure in Membrane Permeate Side	0	-	bars
Operating Temperature	600	550-700	°C
Operating Pressure	1.3	1.3-5	bars
Steam/Methane Molar Ratio	3	3-4	-
CaO/CH ₄ Molar Ratio	3	0-5	-

Table 5.6. Metrics applied for SE-SMR performance evaluation

Methane Conversion	$\frac{F_{CH_4, \text{Reformer Feed}} - F_{CH_4, \text{Reformer Off-Gas}}}{F_{CH_4, \text{Reformer Feed}}}$
Sorbent Conversion	$\frac{F_{CaO, \text{Reformer Feed}} - F_{CaO, \text{Reformer Out}}}{F_{CaO, \text{Reformer Feed}}}$
Hydrogen Yield	$\frac{F_{H_2, \text{Permeated}} + F_{H_2, \text{Reformer Off-Gas}}}{F_{CH_4, \text{Reformer Feed}}}$
Dry Off-Gas Hydrogen Molar Fraction	$\frac{F_{H_2, \text{Reformer Off-Gas}}}{F_{\text{Reformer Off-Gas}} - F_{H_2O, \text{Reformer Off-Gas}}}$
Hydrogen Recovery by Membrane	$\frac{F_{H_2, \text{Permeated}}}{F_{H_2, \text{Permeated}} + F_{H_2, \text{Reformer Off-Gas}}}$

5.3.2. Simulation Results for Base Input Data

Figure 5.3(a) shows the gas axial flow profiles for the base input data in Table 5.5. The results show rapid methane reforming, which produces considerable H₂, CO₂ and CO near the gas distributor. Some of the generated CO₂ is then removed by the lime-based sorbents, resulting in further methane conversion and hydrogen production along the bed height. *In situ* CO₂ removal also leads to lower CO concentration, likely due to shifting the thermodynamic equilibrium of the water-gas shift reaction. Accordingly, the CaO sorbents lead to enhanced methane conversion, hydrogen yield and dry off-gas hydrogen molar fraction, as depicted in Figure 5.3(b).

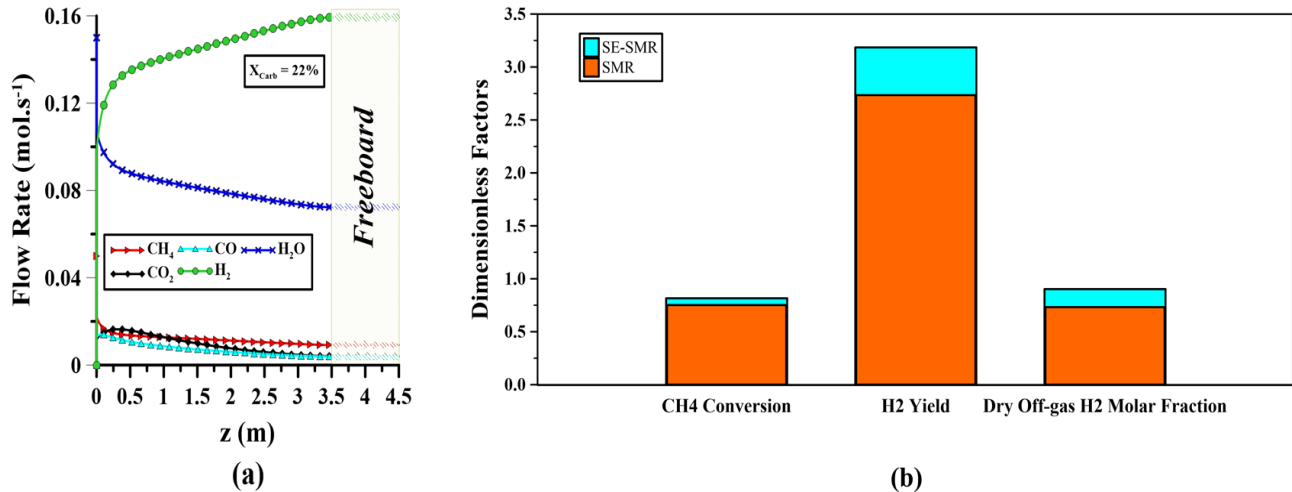


Figure 5.3. (a) Gas flow rate axial profiles in SE-SMR reactor; (b) Reformer performance metrics, as defined in Table 5.6, in the presence and absence of lime sorbents. Input data are identical to those in Table 5.5.

5.3.3. Effects of Operating Temperature and Pressure

Increasing the reactor temperature and reducing the operating pressure both enhance the methane conversion, as shown in Figure 5.4(a). The effect of reactor pressure on the methane conversion is less significant at mild temperatures. This could be due to the thermodynamic equilibrium of the steam methane reforming, together with more-pronounced impact of CO₂ removal at moderate reactor temperatures. Figure 5.4(b) shows that increasing the reactor temperature initially increases the sorbent conversion, while exceeding a “critical temperature” reduces the sorbent utilization by further raising the temperature. Boosting the reactor temperature typically enhances the methane conversion, while inhibiting the lime carbonation (Table 5.1). On the other hand, higher methane conversion results in more CO₂ generation, which increases the lime carbonation driving force. The variation of methane conversion with increasing temperature is significant at moderate reactor temperatures (Figure 5.4(a)), while the carbonation driving force (reverse function of $P_{\text{CO}_2,\text{eq}}$) barely changes at mild temperatures (Figure 1.5 in Chapter 1).

Therefore, increasing the reactor temperature initially enhances the sorbent conversion, while an opposite trend can be obtained if a certain “critical temperature” is exceeded.

The “critical temperature” depends strongly on the reformer operating pressure. Increasing the reactor pressure enhances lime carbonation, while inhibiting steam methane reforming. Simultaneously, increased lime carbonation can shift the reforming thermodynamic equilibrium toward more feedstock conversion. Given the positive impact of the reactor pressure on lime carbonation, higher reactor temperatures would be needed to optimize the performance of SE-SMR processes at elevated pressures.

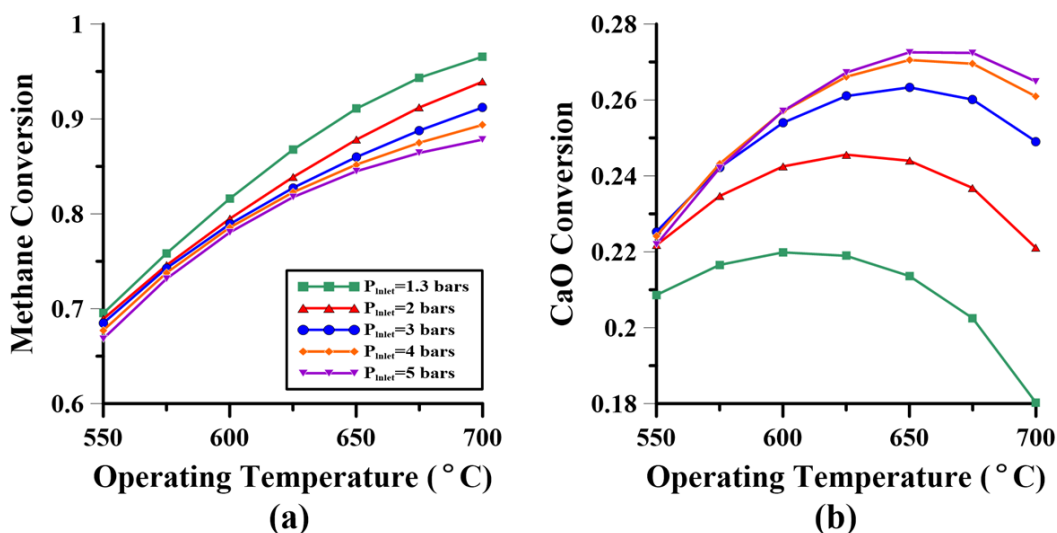


Figure 5.4. Effects of reactor temperature and pressure on conversion of: (a) methane; and (b) sorbent in SE-SMR reactor. The other input data are identical to those in Table 5.5.

The hydrogen productivity of the SE-SMR process depends mainly on the extent of methane conversion inside the reactor. This can be understood by comparing the simulation results in Figures 5.4(a) and 5.5(a). It is seen that both increasing the reactor temperature and reducing the operating pressure enhance the hydrogen productivity of the SE-SMR process. On the other hand, the hydrogen concentration of the reformer dry off-gas is a direct function of the methane

conversion and *in situ* CO₂ removal within the reactor. In fact, higher methane conversions result in less off-gas methane contaminant, while *in situ* CO₂ removal decreases the concentrations of both CO and CO₂ within the reactor (Figure 5.3(a)). Figure 5.5(b) indicates that the variation of the dry off-gas hydrogen molar fraction with changes in the reactor temperature and pressure is similar to those for the sorbent conversion in Figure 5.4(b). Therefore, the optimal operating conditions of the SE-SMR process are closely related to the extent of CO₂ removal by lime carbonation. The simulation results in Figure 5.5 suggest that the optimal SE-SMR operating temperature is approximately 625-675°C at reactor pressures of 1-5 bars. Higher temperatures would be needed to optimize the SE-SMR performance at higher operating pressures.

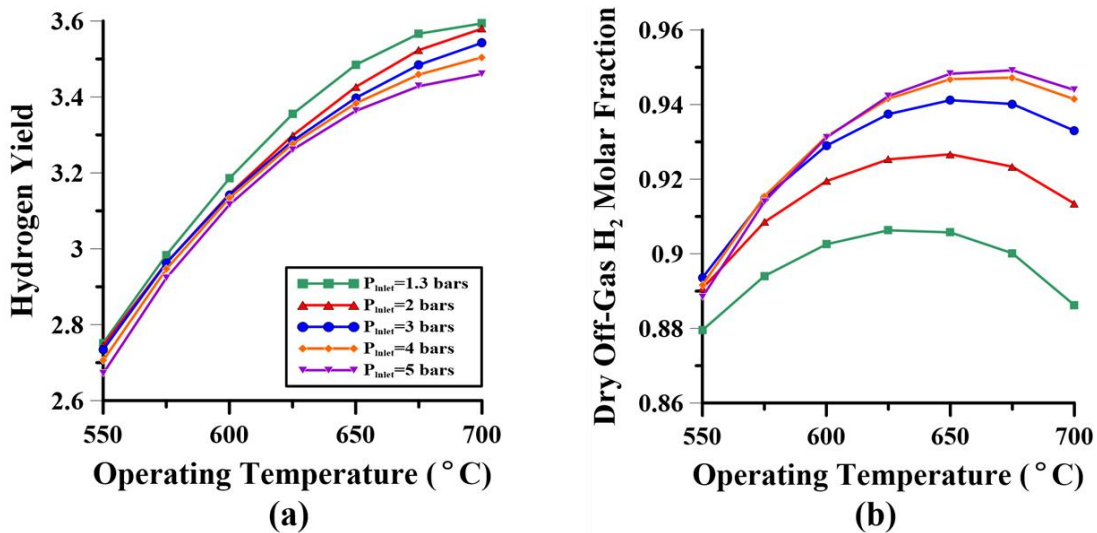


Figure 5.5. Effects of reactor temperature and pressure on: (a) hydrogen yield; and (b) dry off-gas hydrogen molar fraction in SE-SMR reactor. The other input data are identical to those in Table 5.5.

5.3.4. Effect of Gaseous Feed Concentration

The effect of gaseous feed concentration (e.g. steam/methane ratio) on the methane conversion and sorbent utilization of the SE-SMR process is depicted in Figure 5.6. Note that the gas inlet flow rate in these simulations is fixed, and different steam-to-methane molar feed ratios (S/C) are

obtained by changing the gaseous feed concentration. Increasing the S/C molar feed ratio substantially increases the methane conversion in the SE-SMR reactors, mainly due to excess steam, which can shift the reforming thermodynamic equilibrium toward more feedstock conversion. On the other hand, increasing the operating pressure reduces the feedstock conversion, in agreement with Figure 5.4(a). Less impact of reactor pressure is observed at higher S/C molar feed ratios, which indicates a feasible way to overcome the reduction in CH₄ conversion in pressurized SE-SMR reactors. Note that slightly lower sorbent utilization is also achieved when increasing the S/C molar feed ratio (Figure 5.6(b)). This is caused by the lower methane feed concentration, resulting in less CO₂ generation within the reactor. The excess steam also dilutes the reactor gas, thereby further reducing the lime carbonation driving force.

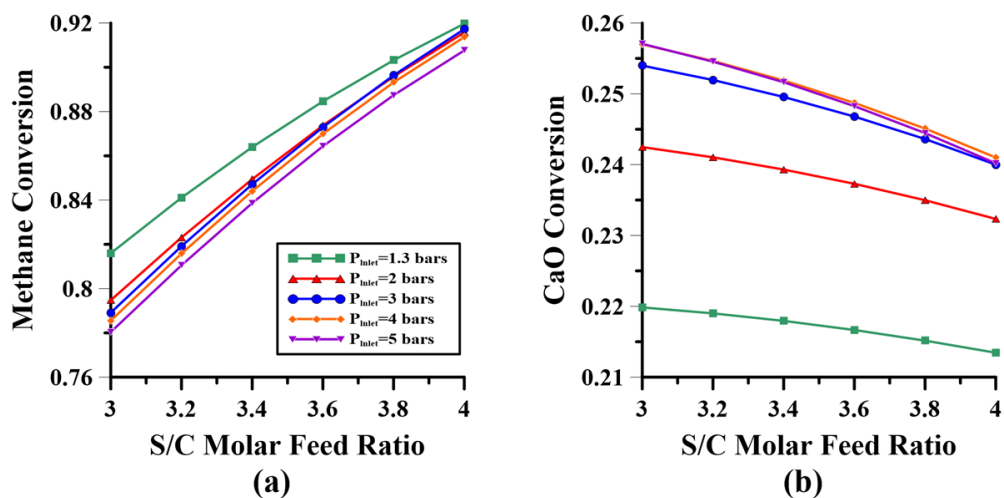


Figure 5.6. Effects of steam/methane ratio and operating pressure on: (a) methane conversion; (b) sorbent conversion in SE-SMR reactor. The rest of the input data are identical to those in Table 5.5.

The effects of the S/C molar feed ratio on the hydrogen yield and product purity of the SE-SMR process are shown in Figure 5.7. Increasing the S/C molar feed ratio leads to more methane conversion and, therefore, higher hydrogen production and less off-gas methane contamination.

In addition, higher steam feed concentration results in less CO generation by shifting the thermodynamic equilibrium of the water-gas shift reaction. Considering also *in situ* CO₂ removal, the reformer dry off-gas hydrogen concentration should increase with higher S/C molar feed ratio, as shown in Figure 5.7(b). However, increasing the S/C molar feed ratio likely leads to higher operating cost (due to more steam having to be generated) and lower reactor throughput (hydrogen production rate). This then leads to a trade-off between product quality (e.g. purity and hydrogen yield) and productivity (e.g. reactor throughput and operating costs). More detailed comparison is presented in Section 5.3.7.

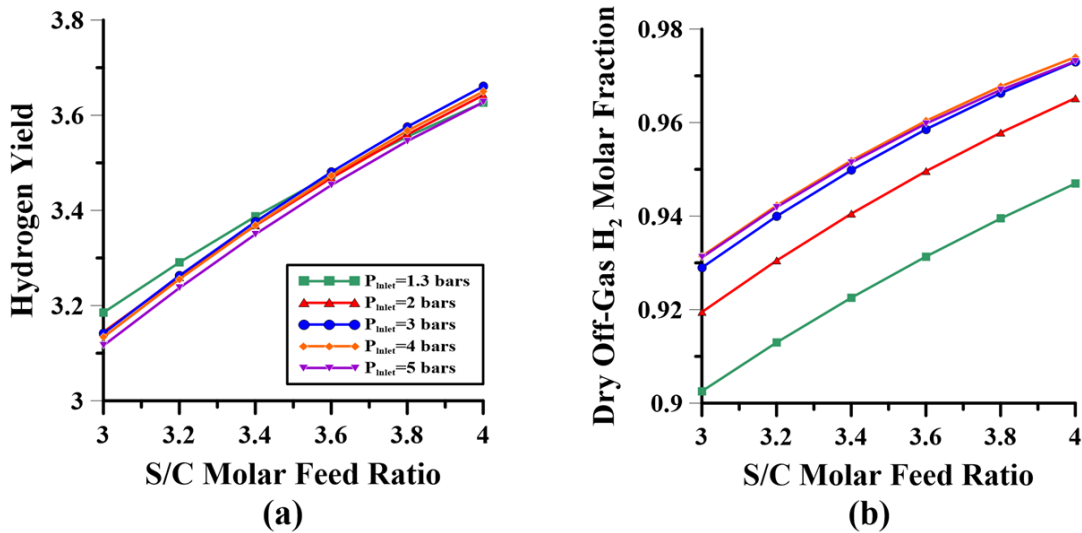


Figure 5.7. Effects of steam/methane and operating pressure on: (a) hydrogen yield; and (b) dry off-gas hydrogen molar fraction in SE-SMR reactor. The other input data are identical to those in Table 5.5.

5.3.5. Effect of CaO/Methane Feed Ratio

Lime carbonation occurs in two successive steps: a fast reaction-controlled regime, followed by slow diffusion-controlled carbonation [37,50,152–154]. The abrupt transition between these two carbonation stages is mainly due to the formation of a critical CaCO₃ product layer on the

surface of the sorbent material [155,156]. The interior unreacted surface of the porous particle then becomes inaccessible, restricting further carbonation by slowing down the diffusion of CO₂ through the product layer [4,87,120]. The kinetics of fast-stage carbonation is strongly dependent on the available active surface area within the sorbent [46,47]. On the other hand, diffusion-controlled carbonation relies on the morphology of the CaCO₃ product layer [37]. Note that CO₂ capture by slow-stage carbonation requires a much longer sorbent residence time and consequently, a larger reactor. Therefore, a practical SE-SMR process might be limited to fast-stage carbonation, requiring CaO/CH₄ molar feed ratios higher than the stoichiometric value (~1:1 CaO/CH₄ in the SE-SMR process).

The effect of the CaO/CH₄ molar feed ratio on the SE-SMR methane conversion is depicted in Figure 5.8(a). Note that the CaO feed flow rate in practice would be composed of fresh make-up flow and the re-circulated active lime from the calciner. However, the effect of sorbent utilization decay is neglected in this work and, therefore, the CaO inlet flow rate corresponds solely to the lime re-circulation. Increasing the CaO/CH₄ molar feed ratio results in higher methane conversion, with less improvement observed at elevated CaO/CH₄ molar feed ratios. This could be due to approaching the SE-SMR thermodynamic equilibrium. The positive impact of excess CaO feeding is more pronounced at elevated reactor pressures, indicating the significance of *in situ* CO₂ removal under pressurized conditions.

Boosting the CaO/CH₄ molar feed ratio (by increasing the sorbent inlet flow rate) also results in lower sorbent conversion, mainly due to excess sorbent entering the reactor (Figure 5.8(b)). Higher CaO inlet flow rates (e.g. by increasing the solids circulation rate) can also reduce the sorbent residence time for fixed reactor geometry. Although higher sorbent utilization is desired to minimize operating costs, excess sorbent feeding is imperative to maintain the lime

carbonation in the fast reaction-controlled regime. The results in Figure 5.8 suggest that a CaO/CH₄ molar feed ratio of 3-4 could be optimal for the SE-SMR processes, with less impact of excess CaO expected at CaO/CH₄ molar feed ratios > 4.

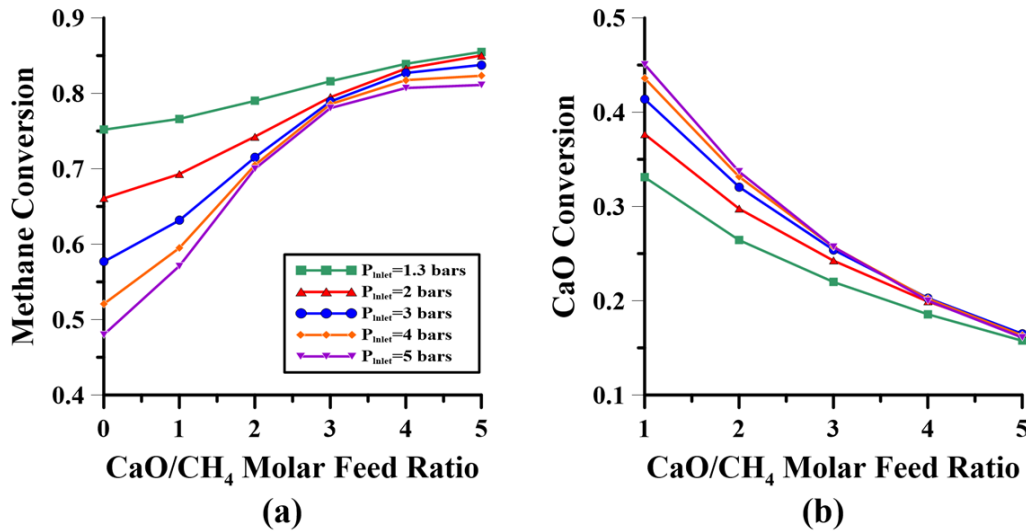


Figure 5.8. Effects of CaO/methane molar feed ratio and operating pressure on: (a) methane conversion; and (b) sorbent conversion in the SE-SMR reactor. The other input data are identical to those in Table 5.5.

Figure 5.9(a) indicates that increasing the CaO/CH₄ molar feed ratio results in higher hydrogen yield, attributable to the higher methane conversion at elevated CaO/CH₄ molar feed ratios. Note that the positive impact of excess CaO decreases with increasing CaO/CH₄ molar feed ratio. This could again be due to approaching the SE-SMR thermodynamic equilibrium, as discussed above. Elevating the CaO/CH₄ molar feed ratio also increases the dry off-gas hydrogen molar fraction, with higher enhancement achieved at elevated gas pressures (Figure 5.9(b)). Accordingly, higher CaO/CH₄ molar feed ratios (e.g. a higher solid circulation rate) would be required if the SE-SMR process were to be carried out at high pressure.

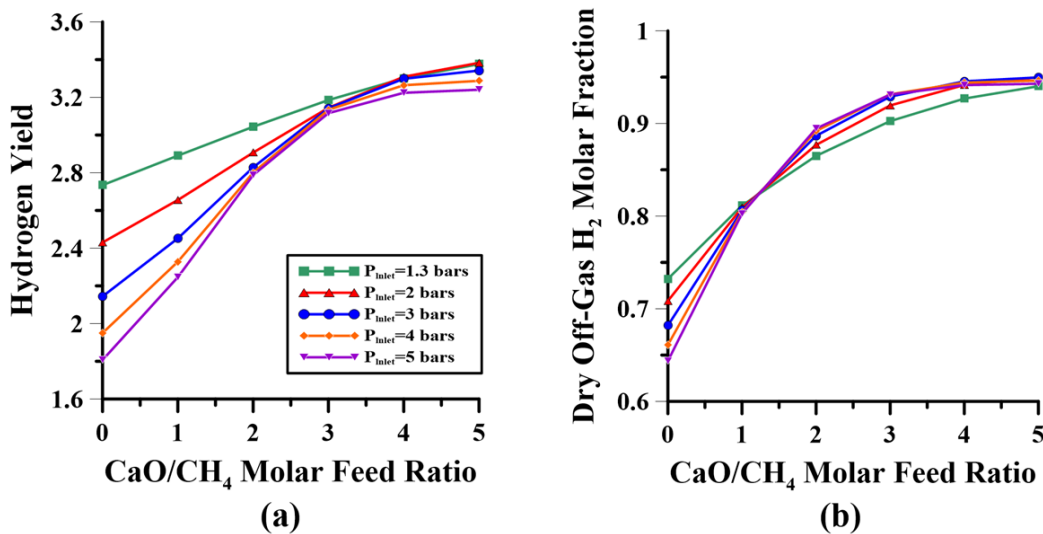


Figure 5.9. Effects of CaO/methane and operating pressure on: (a) hydrogen yield; and (b) dry off-gas hydrogen molar fraction in SE-SMR reactor. Other input data are identical to those in Table 5.5.

5.3.6. Effect of Membrane Implementation

The effect of inserting hydrogen perm-selective membranes on the methane conversion of the membrane-assisted sorbent-enhanced steam methane reforming (MA-SE-SMR) is depicted in Figure 5.10(a). *In situ* H₂ removal can shift the thermodynamic equilibrium of steam methane reforming, consequently enhancing methane conversion. Installing more membrane tubes leads to higher hydrogen permeation area and thus increased *in situ* hydrogen separation. Hence, the methane feedstock conversion can be substantially increased by adding more hydrogen perm-selective membrane tubes inside the reactor. The positive impact of membrane addition on the methane conversion is more pronounced at elevated reactor pressures due to the higher hydrogen permeation driving force, resulting in more hydrogen recovery at higher pressures (Figure 5.11).

The variation of sorbent conversion with an increase in the number of membrane tubes is shown in Figure 5.10(b). *In situ* hydrogen removal dilutes the reformer hydrogen concentration, thereby increasing the CO₂ concentration within the reactor. Increasing the number of membrane tubes

also enhances the methane conversion, resulting in further CO₂ generation. This leads to a higher lime carbonation driving force and consequently, higher sorbent utilization. Note that the H₂ permeation rate substantially increases with increasing reactor pressure. Accordingly, greater variation of sorbent utilization is expected in pressurized MA-SE-SMR reactors.

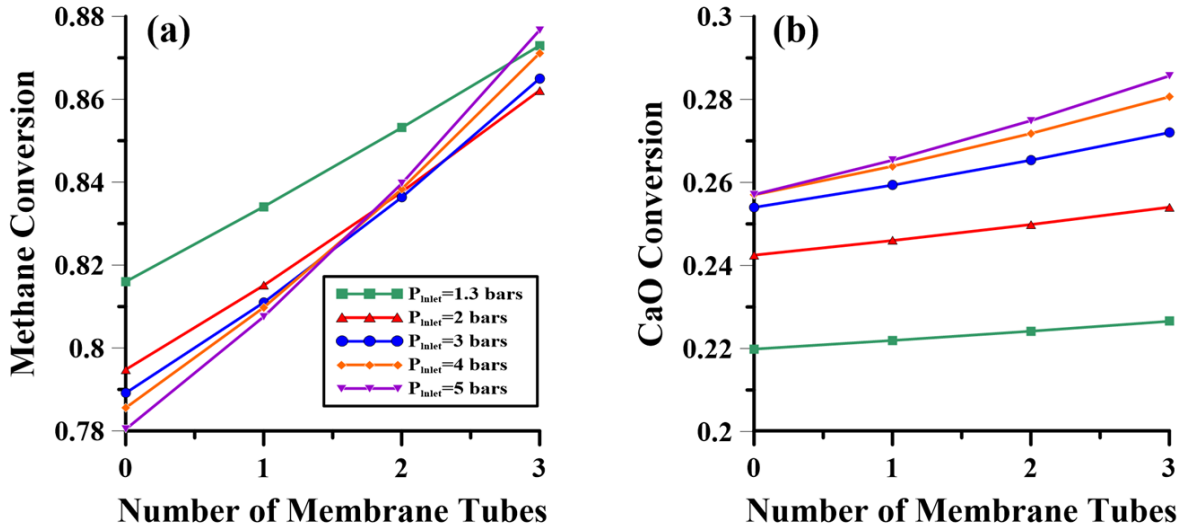


Figure 5.10. Effect of membrane addition on conversion of: (a) methane; and (b) sorbent in MA-SE-SMR reactor. The other input data are identical to those in Table 5.5.

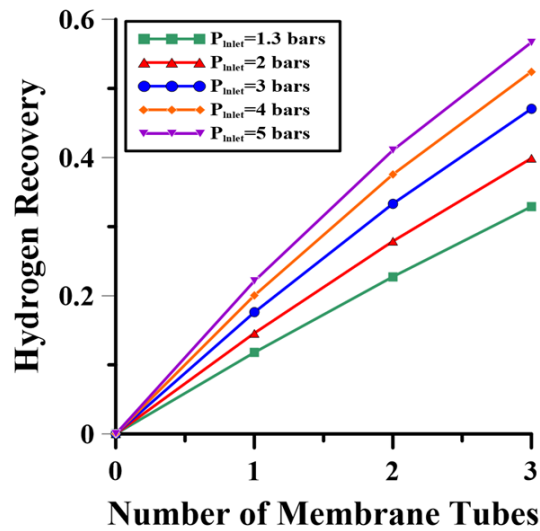


Figure 5.11. Variation of hydrogen recovery with number of membrane tubes and reactor pressure. Other input data are identical to those in Table 5.5.

As discussed above, increasing the number of membrane tubes results in higher permeation rates and, therefore, enhanced methane conversion. The hydrogen productivity of steam methane reforming depends mainly on the methane conversion within the reactor. Thus higher MA-SE-SMR hydrogen production yield can be achieved when more membrane tubes are inserted into the reactor (Figure 5.12(a)). On the other hand, *in situ* H₂ removal dilutes the hydrogen concentration within the reactor, while additional hydrogen can be generated by the enhanced methane reforming. Figure 5.12(b) indicates that increasing the number of membrane tubes results in slightly lower off-gas (i.e. reformer retentate gas) dry hydrogen concentration for the range of conditions studied. Further reduction of the off-gas purity is expected when more membrane tubes are provided inside the reformer.

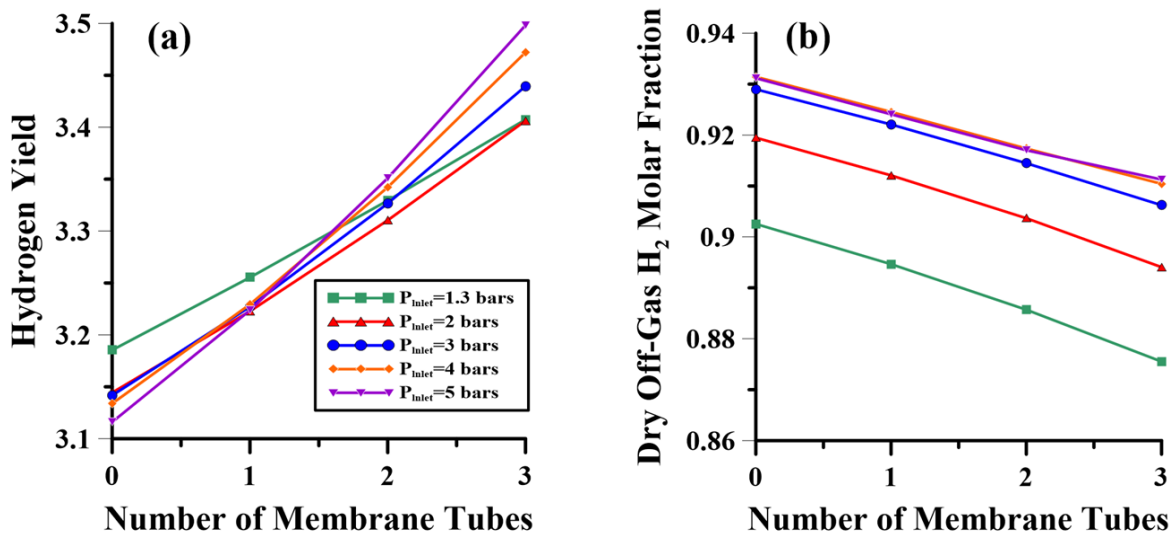


Figure 5.12. Effect of membranes on: (a) hydrogen yield; and (b) dry off-gas hydrogen molar fraction in MA-SE-SMR reactor. The other input data are identical to those in Table 5.5.

In summary, combining sorbent-enhanced steam methane reforming with *in situ* H₂ removal leads to higher hydrogen production yields and lower retentate off-gas hydrogen concentrations. Despite their advantages, high temperature hydrogen-permselective membranes are costly, and

difficult to maintain inside the reactor. Pd-based membranes are highly sensitive to the reactor conditions and can fail at temperatures above 550-625°C [22,23]. Harsh fluidization conditions could also damage the thin active layer of the membranes, resulting in small pinholes and, hence, loss of selectivity. Investigations are required to test alternative membrane materials with improved permeability, hydrogen selectivity and mechanical/thermal stability.

5.3.7. Selection of the SE-SMR Operating Conditions

The effect of different influential factors on the performance of sorbent-enhanced steam methane reforming was detailed in Sections 5.3.3-5.3.5. In general, higher operating temperatures, higher sorbent circulation/feeding rates and increased steam-to-methane molar feed ratios are required to enhance the system performance at elevated reactor pressures. Pressurized SE-SMR processes are desirable in industry to diminish the need for product compression and to increase the reactor throughput for a given size of reactor. In contrast, limestone calcination is favoured at low reactor pressures, and requires higher temperatures at pressurized conditions. However, increasing the calciner temperature leads to higher capital and operating costs, which undesirably affect the economic viability of the overall process. Therefore, it may be preferred to integrate pressurized SE-SMR reactors with atmospheric or sub-atmospheric limestone calciners. However, connecting two FBR's with different pressures needs difficult solid circulation infrastructure (e.g. multiple lock-hoppers), requiring complex process design and control.

Accordingly, a system pressure of 3 bars was selected here to evaluate the performance of SE-SMR/calciner system in simulated pilot-scale dual turbulent fluidized bed reactors. This offers the advantages of pressurized operation, while efficient sorbent regeneration may be achieved for a practical range of operating temperatures (e.g. < 900°C). The reformer was designed to operate

at 650°C, with a fixed sorbent (CaO) inlet flow rate of 0.21 mol.s⁻¹. The steam/methane molar feed ratio was then varied to determine the optimal gaseous feed concentration for this reformer configuration.

Figure 5.13(a) shows the effect of steam/methane (S/C) molar feed ratio on the hydrogen production yield and purity of the selected SE-SMR condition. Increasing the S/C molar feed ratio enhances both hydrogen production yield and purity, as also observed in Figure 5.7. However, increasing the S/C molar feed ratio (at a fixed gas inlet flow rate) results in lower methane feed concentration and, hence, a lower hydrogen production rate (Figure 5.13(b)). Higher methane feed concentration is normally desired to increase the hydrogen production rate, while a lower methane feed concentration enhances product quality. Given this trade-off, a new performance metric is defined by

$$\text{Hydrogen Production Index (HPI)} = \frac{H_2 \text{ Yield}}{4} \times Y_{H_2, \text{Dry Reformer Off-Gas}} \times \frac{3F_{H_2, \text{Reformer Off-Gas}}}{4F_{\text{Gas, Reformer Feed}}} \quad (5.3)$$

combining the hydrogen selectivity (hydrogen yield divided by 4), product purity (dry off-gas hydrogen concentration), and “normalized” hydrogen production rate. The latter was calculated by normalizing the hydrogen production rate with respect to the ideal reforming hydrogen productivity (4/3 of the total molar gas feed flow rate). This performance metric (henceforth called the “Hydrogen Production Index” or HPI) can vary between zero and unity, with a value of one being ideal.

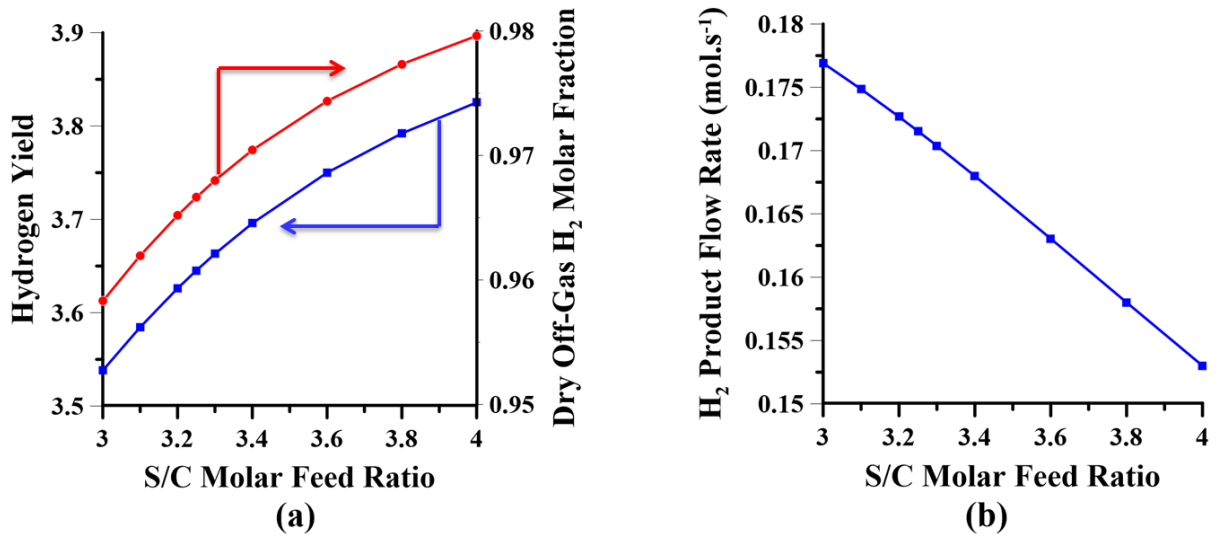


Figure 5.13. Effect of steam/methane molar feed ratio on SE-SMR: (a) hydrogen yield and dry off-gas hydrogen molar fraction; (b) hydrogen production rate, with $P = 3$ bars, $T = 650^{\circ}\text{C}$, $F_{\text{CaO},\text{in}} = 0.21 \text{ mol.s}^{-1}$. Other input data are identical to those in Table 5.5.

The effect of steam/methane molar feed ratio on the hydrogen production index (HPI) of the selected reformer configuration is plotted in Figure 5.14. Increasing the S/C molar feed ratio initially increases the HPI by enhancing the hydrogen production yield and purity (Figure 5.13(a)). However, exceeding a certain S/M molar feed ratio ($S/C \approx 3.25$) leads to a substantial drop in the HPI by reducing the hydrogen production rate (Figure 5.13(b)). Accordingly, an S/C molar feed ratio of 3.25 was selected for this reformer configuration, with a summary of simulation results presented in Table 5.7.

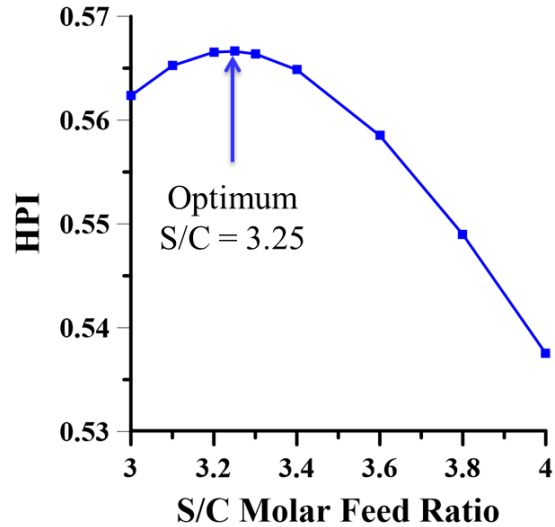


Figure 5.14. Effect of steam/methane molar feed ratio on SE-SMR hydrogen production index ($P = 3$ bars, $T = 650^{\circ}\text{C}$, $F_{\text{CaO},\text{in}} = 0.21 \text{ mol.s}^{-1}$). Other input data are identical to those in Table 5.5.

Table 5.7. Simulated SE-SMR performance at selected operating conditions

Selected Reformer Operating Conditions			
$P = 3$ bars	$T = 650^{\circ}\text{C}$	CaO/Methane: 4.46	Steam/Methane: 3.25
Reformer Performance at Selected Operating Condition			
Methane Conversion		91.7%	
Sorbent Utilization		19.6%	
Hydrogen Yield		3.65	
Dry Off-Gas Hydrogen Molar Fraction		96.7%	
Hydrogen Production Index (HPI)		0.57	

5.3.8. Design of Sorbent Regenerator

Given the complexity of pressure swing operations, it is often desirable to conduct sorbent regeneration and methane reforming at the same operating pressure. This potentially leads to higher calcination temperatures and, consequently, several operational challenges. It was shown

in Chapters 3 and 4 that a methane-concentrated oxy-fuel calciner can provide rapid limestone calcination under certain circumstances. In addition, this novel MRC-CAL process can be operated autothermally if proper feeding ratios are applied. A correlation was proposed in Chapter 3, estimating the methane/enriched-air molar feed ratio (β) for autothermal sorbent regeneration by the MRC-CAL process:

$$\beta = 0.275 + 1.903e^{-\alpha/0.716} \quad 800^{\circ}\text{C} \leq T \leq 900^{\circ}\text{C} \quad \& \quad P = 1-5 \text{ bars}$$

$$\alpha = \frac{F_{\text{CaCO}_3, \text{Calcliner Feed}}}{F_{\text{Gas, Calcliner Feed}}} \quad \beta = \frac{F_{\text{CH}_4, \text{Calcliner Feed}}}{F_{\text{Enriched-Air, Calcliner Feed}}} \quad y_{\text{O}_2, \text{Enriched-Air}} = 95\% \quad (5.4)$$

The calciner dimensions and operating pressure were assumed to be identical to those of the given SE-SMR reactor. Hence the CaCO_3 /total gas molar feed ratio (α) can vary between 0.1 and 0.3, based on the carbonated lime leaving the reformer, and the limits of gas inlet flow rate for turbulent fluidization (Figure 5.2). Higher α is often preferred to minimize the gas required by the sorbent regenerator. Therefore, a CaCO_3 /gas molar feed ratio of 0.3 was selected for the limestone calciner, integrated with the given SE-SMR reactor.

Chapter 4 proposed a simple design methodology for the MRC-CAL process, operating at reactor pressures of 1-5 bars and temperatures of 800-900°C. Figure 5.15(a) demonstrates the proposed design parameters for a reactor pressure of 3 bars. According to this figure, an operating temperature of ~825-850°C may be sufficient to obtain 75% CaCO_3 decomposition (corresponding to 95% CaO when sorbent is ~20% carbonated) at $\alpha = 0.3$ (shown by the star in the figure). Note that this design methodology is based on a 10 min residence time of fully calcite particles. However, sorbent residence time in this case is slightly greater than 10 min (~11 min), and particles are only partially carbonated on their surfaces. Therefore, reactor

temperatures lower than those predicted by Figure 5.15(a) might be required for sorbent regeneration by the MRC-CAL process.

The MRC-CAL process can be operated efficiently only if the CaCO_3/gas molar feed ratio remains within a certain range [118,137]. Exceeding a certain CaCO_3/gas molar feed ratio may result in incomplete/endothermic limestone calcination, while carbon formation can occur at low CaCO_3/gas molar feed ratios. Figure 5.15(b) shows the critical operating limits for the MRC-CAL process at 3 bars. This figure confirms that coke-free, complete and autothermal sorbent regeneration can be obtained at a CaCO_3/gas molar feed ratio of 0.3 and temperatures $> 800^\circ\text{C}$.

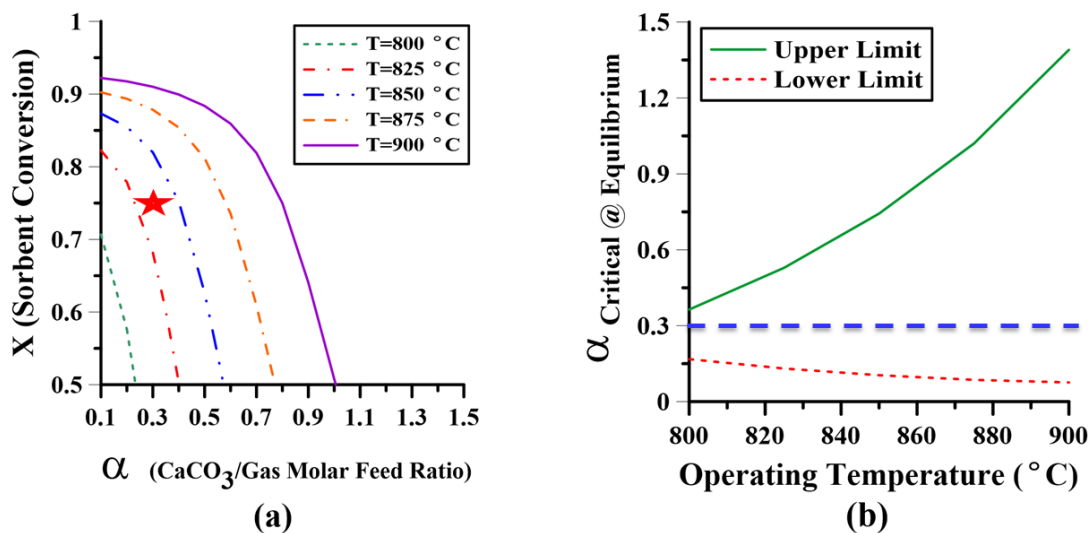


Figure 5.15. MRC-CAL (a) design parameters [69]; and (b) critical limits [137] at 3 bars.

Kinetic simulations identical to those applied for the Chapter 4 were employed next, to determine the minimum required MRC-CAL temperature for complete sorbent regeneration. This was achieved by tracking the calculated sorbent conversion at different reactor temperatures, starting from 800°C , with temperature intervals of 5°C . A similar procedure was followed to find the minimum sorbent regeneration temperature required by steam calciners. The

MRC-CAL process can offer complete sorbent regeneration at nearly 825°C, while a reactor temperature of roughly 880°C is needed by conventional steam calciners (Table 5.8). Note that the steam calciner can be theoretically representative of any unreactive non-CO₂ calcination medium, including air, nitrogen and oxygen. The MRC-CAL process also provides an off-gas of higher heating value, mainly composed of hydrogen and CO. This can be further used in various downstream applications such as metal oxide reduction and ammonia production.

Table 5.8. Performance of MRC-CAL and steam calciner for dual FBR's

Selected Calciner Operating Conditions													
P = 3 bars	CaCO ₃ /Gas Molar Feed Ratio: 0.3												
MRC-CAL Performance													
Minimum Required Temperature (°C)	825												
Off-Gas Flow Rate (mol.s ⁻¹)	0.289												
Off-Gas Molar Composition	<table border="1"> <tbody> <tr> <td>H₂</td> <td>43.7%</td> <td>CO</td> <td>33.1%</td> </tr> <tr> <td>CO₂</td> <td>9.1%</td> <td>CH₄</td> <td>0.6%</td> </tr> <tr> <td>H₂O</td> <td>12.6%</td> <td>N₂</td> <td>0.9%</td> </tr> </tbody> </table>	H ₂	43.7%	CO	33.1%	CO ₂	9.1%	CH ₄	0.6%	H ₂ O	12.6%	N ₂	0.9%
H ₂	43.7%	CO	33.1%										
CO ₂	9.1%	CH ₄	0.6%										
H ₂ O	12.6%	N ₂	0.9%										
STEAM-CAL Performance													
Minimum Required Temperature (°C)	880												
Off-Gas Flow Rate (mol.s ⁻¹)	0.178												
Off-Gas Molar Composition	<table border="1"> <tbody> <tr> <td>H₂</td> <td>0%</td> <td>CO</td> <td>0%</td> </tr> <tr> <td>CO₂</td> <td>23%</td> <td>CH₄</td> <td>0%</td> </tr> <tr> <td>H₂O</td> <td>77%</td> <td>N₂</td> <td>0%</td> </tr> </tbody> </table>	H ₂	0%	CO	0%	CO ₂	23%	CH ₄	0%	H ₂ O	77%	N ₂	0%
H ₂	0%	CO	0%										
CO ₂	23%	CH ₄	0%										
H ₂ O	77%	N ₂	0%										

Aspen Plus (V.10) was employed to estimate the reformer and calciner heat duties and fuel (methane) requirements for different scenarios. Isothermal Gibbs reactors were used to simulate each reactor, with the feed temperatures identical to those for the corresponding reactors. A sorbent feed flowrate of 0.041 mol.s^{-1} was applied for the SE-SMR and calciner units, corresponding to the amount of lime/limestone being carbonated/calcined in the dual FBR's. Good agreement was observed between the kinetic and Aspen Plus simulations, with the results summarized in Appendix D. The required process fuel (methane) for each case was then estimated based on the reactor heat duties and the methane heat of combustion. The latter was obtained by feeding stoichiometric ratio of methane and oxygen (at room temperature) into isothermal Gibbs reactors. The hydrogen yield and CO_2 emission for each process was then calculated based on Equations (5.5) and (5.6). Note that the MRC-CAL off-gas contains a substantial amount of CO, which could be further used in different applications. For instance, a downstream membrane-assisted water-gas shift reactor (MA-WGS) could be used to convert the CO content of the MRC-CAL off-gas to CO_2 , and produce an equimolar amount of hydrogen. Assuming complete CO conversion in a downstream MA-WGS, the hydrogen yield and CO_2 emission of the SE-SMR/MRC-CAL system can be calculated by Equations (5.7) and (5.8), henceforth referred to as “Ideal MRC-CAL” cases.

$$\text{H}_2 \text{ Yield} = \frac{F_{H_2, \text{Reformer Off-Gas}} + F_{H_2, \text{Calciner Off-Gas}}}{F_{CH_4, \text{Reformer Feed}} + F_{CH_4, \text{Calciner Feed}} + F_{CH_4, \text{Reformer Fuel}} + F_{CH_4, \text{Calciner Fuel}}} \quad (5.5)$$

$$\text{CO}_2 \text{ Emission} = \frac{F_{CO_2, \text{Reformer Off-Gas}} + F_{CO_2, \text{Calciner Off-Gas}} + F_{CO_2, \text{Reformer Fuel}} + F_{CO_2, \text{Calciner Fuel}}}{F_{H_2, \text{Reformer Off-Gas}} + F_{H_2, \text{Calciner Off-Gas}}} \quad (5.6)$$

$$\text{Ideal H}_2 \text{ Yield} = \frac{F_{H_2, \text{Reformer Off-Gas}} + F_{H_2, \text{Calciner Off-Gas}} + F_{CO, \text{Calciner Off-Gas}}}{F_{CH_4, \text{Reformer Feed}} + F_{CH_4, \text{Calciner Feed}} + F_{CH_4, \text{Reformer Fuel}} + F_{CH_4, \text{Calciner Fuel}}} \quad (5.7)$$

$$\text{Ideal CO}_2 \text{ Emission} = \frac{F_{\text{CO}_2, \text{Reformer Off-Gas}} + F_{\text{CO}_2, \text{Calciner Off-Gas}} + F_{\text{CO}_2, \text{Reformer Fuel}} + F_{\text{CO}_2, \text{Calciner Fuel}} + F_{\text{CO}, \text{Calciner Off-Gas}}}{F_{\text{H}_2, \text{Reformer Off-Gas}} + F_{\text{H}_2, \text{Calciner Off-Gas}}} \quad (5.8)$$

Figure 5.16 compares the performance of the SMR process with the sorbent-enhanced SMR processes, integrated with the MRC-CAL and steam calciner units. The SE-SMR/STEAM-CAL process results in higher hydrogen yield and CO₂ emission than the conventional SMR reactor. In addition, the SE-SMR generates highly purified hydrogen, while a concentrated CO₂ dry off-gas can be achieved from the steam calciners. This potentially eliminates downstream purification stages, enhancing the economic viability of the process. The SE-SMR/MRC-CAL process demonstrates similar hydrogen yield to those for the SMR process, but releases substantially less CO₂ per mole of hydrogen produced. This is due to *in situ* CO₂ utilization by the MRC-CAL process, consuming H₂ and CO₂ to produce steam and CO in the calciner. An ideal SE-SMR/MRC-CAL process (calciner integrated with downstream MA-WGS reactor) shows slightly higher hydrogen yields than the SE-SMR/STEAM-CAL process. In addition, the CO₂ emission of the ideal SE-SMR/MRC-CAL falls below that of the SE-SMR/STEAM-CAL process, resulting in more hydrogen production at lower environmental emissions. This is mainly due to the lower reactor temperature required by the MRC-CAL sorbent regenerators, as shown in Table 5.8. Note that the MRC-CAL off-gas can also be used for other applications (e.g. fuel reactors), and that the MA-WGS reactor was selected here for illustrative purposes.

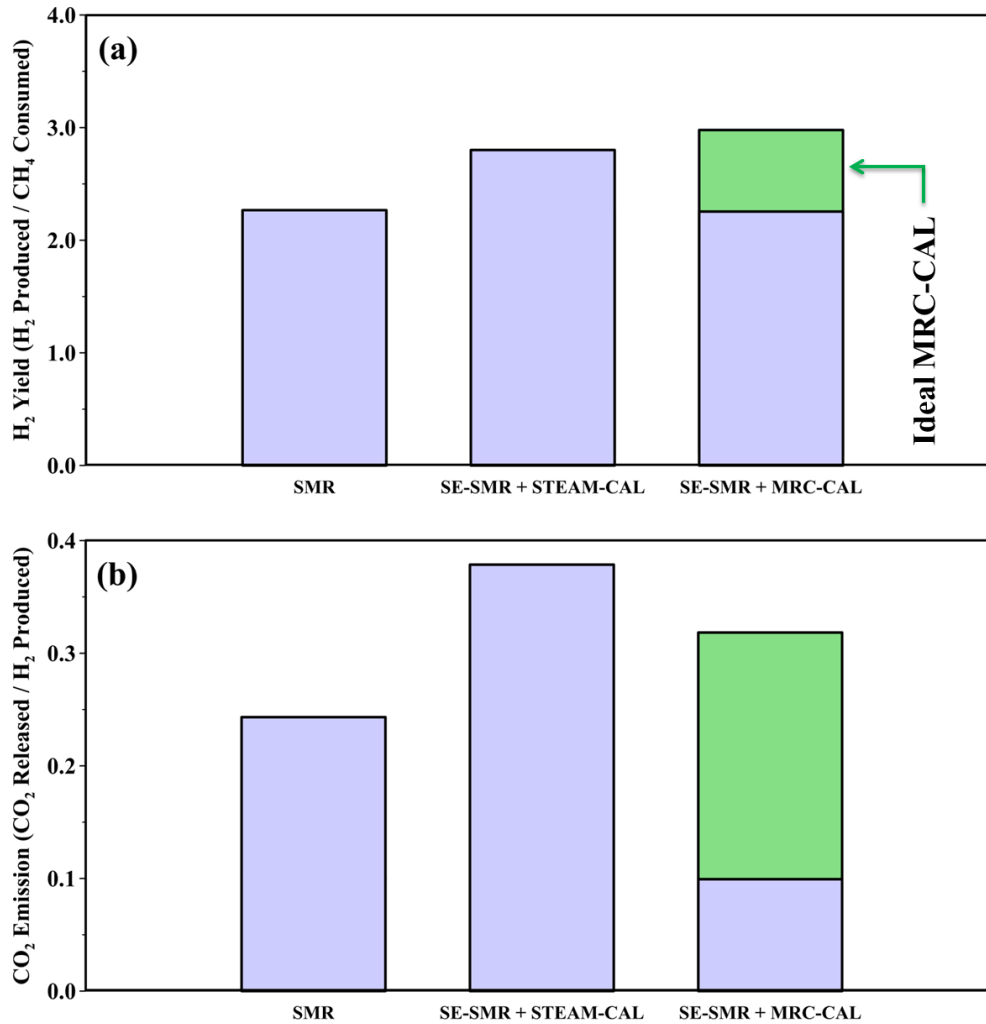


Figure 5.16. (a) Hydrogen yield; and (b) CO₂ emission of the SMR and SE-SMR processes, integrated with MRC-CAL and STEAM-CAL units. Reformer and calciner operating conditions are identical to those in Tables 5.7 and 5.8, respectively.

5.4. Conclusion

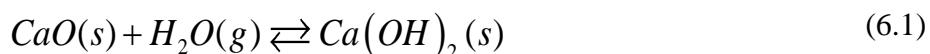
The performance of sorbent-enhanced steam methane reforming in dual turbulent fluidized bed reactors has been investigated for different operating conditions. It is shown that higher reactor temperatures, sorbent circulation/feeding rates and steam-to-methane molar feed ratios are required to optimize the system performance at elevated reactor pressures. Introducing hydrogen-permselective membrane tubes could also enhance the system performance by producing two hydrogen streams of different product purity.

The required sorbent regeneration conditions are determined for a given sorbent-enhanced steam methane reformer, integrated with steam and methane-concentrated oxy-fuel calciners. It is shown that the methane-concentrated oxy-fuel calciner can offer nearly autothermal sorbent regeneration at reduced reactor temperatures. This process also offers considerably lower CO₂ emissions, at the expense of lower hydrogen productivity. The latter could be resolved by means of a downstream membrane-assisted water-gas shift reactor, resulting in enhanced hydrogen production yield at moderate CO₂ emissions.

CHAPTER 6: Sorbent Steam Reactivation and Methane-Concentrated Calcination for Calcium-Looping Carbon Capture: Compatibilities and Limitations

6.1. Introduction

Sorbent deactivation is a major challenge for long-term operation of calcium-looping processes [39,51]. The high required operating temperature for efficient limestone calcination causes severe morphological changes to the sorbent, resulting in loss of active surface area and consequently, sorbent deactivation [157]. A significant amount of sorbent make-up flow would therefore be required to retain the sorbent reactivity. CaO hydration (Equation (6.1)) is a proven method to partially restore the CO₂ carrying capacity of the CaO sorbents over calcination/carbonation cycling [84,158]. In fact, the different molar volumes of CaCO₃ and Ca(OH)₂ create micro fractures during the sorbent hydration, enhancing the sorbent surface area upon dehydration [4].



Lime hydration is exothermic and favoured at operating temperatures of 250-500°C [84]. Therefore, the heat generated through sorbent hydration must be continuously removed in order to maintain the reactor temperature. One promising heat removal alternative is to use saturated steam as the hydrator feed, utilizing the excess energy for direct steam superheating. This potentially reduces the heat losses, therefore enhancing the thermal efficiency of the lime hydration process. In addition, the superheated steam can be used elsewhere, including in steam methane reformers, biomass gasifiers and steam-iron processes. On the other hand, slaked lime

dehydration is endothermic and releases an equimolar amount of steam. Although dehydration can occur either in the carbonator or the calciner, if in the carbonator, the desorbed steam dilutes the CO_2 concentration within the reactor, inhibiting lime carbonation. Alternatively, slaked lime can be dehydrated in the limestone calciner, where the operating temperature is substantially higher than the $\text{Ca}(\text{OH})_2$ decomposition temperature. Figure 6.1 presents a general schematic of the three interconnected fluidized bed reactors, continuously reactivating a portion of the carbonator solid product by steam. The hydrated sorbent is then directed to the MRC-CAL sorbent regenerator, where it calcines along with the circulating limestone.

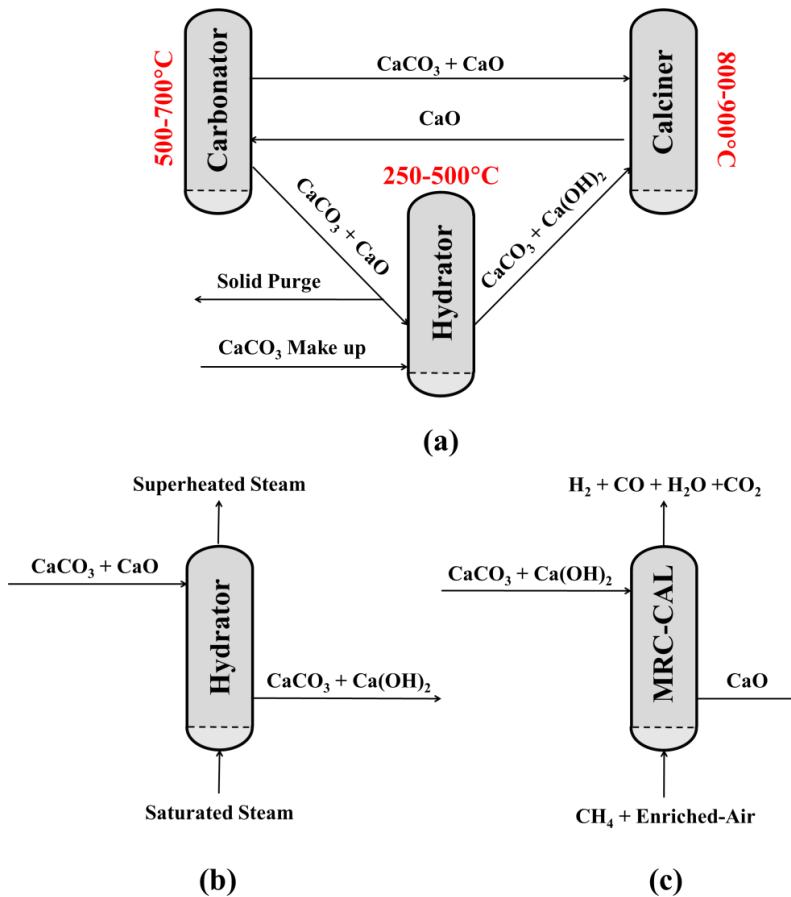


Figure 6.1 Schematics of calcium looping with sorbent hydrator/reactivation: (a) Three-integrated-reactors calcium looping; (b) Sorbent hydrator with steam superheater; and (c) MRC-CAL for $\text{CaCO}_3/\text{Ca}(\text{OH})_2$ co-calcination.

This chapter investigates the equilibrium performance of the lime hydrator and MRC-CAL sorbent regenerators at different operating conditions. The thermal behaviour of the lime hydration is investigated at different solid feed temperatures, system pressures and solid/water molar feed ratios. A detailed analysis of slaked lime calcination in the MRC-CAL sorbent regenerators is then performed in order to determine the required conditions for autothermal, coke-free and complete Ca(OH)_2 calcination. The simulation results are used in conjunction with Chapter 3 to propose a new correlation to estimate the required gaseous feed composition for autothermal co-calcination of limestone and slaked lime solid mixtures.

6.2. Simulation Setup

Aspen Plus V.10 was employed to investigate the equilibrium performance of the sorbent hydrator and MRC-CAL process with different operating conditions. The sorbent hydrator was modeled using an adiabatic Gibbs reactor, with saturated steam and CaO as the reactants. The pressure drop is neglected, with both feed streams at pressures equal to that of the reactor. The variation of hydrator off-gas temperature (superheated steam) with water/CaO molar feed ratio is then studied at different system pressures and solid inlet temperatures.

The simulation setup for the limestone calcination by the MRC-CAL process is detailed in Chapter 3. The simulation setup in this chapter is identical, with CaCO_3 , Ca(OH)_2 , or a mixture of both used as the solid feed. More than 300,000 simulation trials were conducted to determine the required conditions for autothermal, coke-free and complete sorbent regeneration at different reactor temperatures, pressures and feed compositions.

6.3. Results and Discussion

6.3.1. Sorbent Hydrator

The variation of hydrator off-gas temperature with the water/CaO molar feed ratio at different system pressures and solid feed temperatures is depicted in Figure 6.2. For a well-insulated system, the thermal behaviour of the sorbent hydrator depends on three main factors:

- Sensible heat carried by the solid feed;
- Heat released by exothermic CaO hydration;
- Energy consumed by steam superheating.

Assuming complete sorbent hydration, increasing the water/CaO molar feed ratio (e.g. by increasing the water inlet flow rate) would not affect the first two factors, whereas more energy would be removed *via* steam superheating. Accordingly, increasing the water/CaO molar feed ratio results in lower hydrator off-gas temperature, as observed in Figure 6.2. On the other hand, increasing the solid feed temperature and system pressure leads to slightly higher energy input, consequently elevating the off-gas temperature. The latter is due to the higher temperature of the pressurized saturated steam, carrying more sensible heat into the sorbent hydrator.

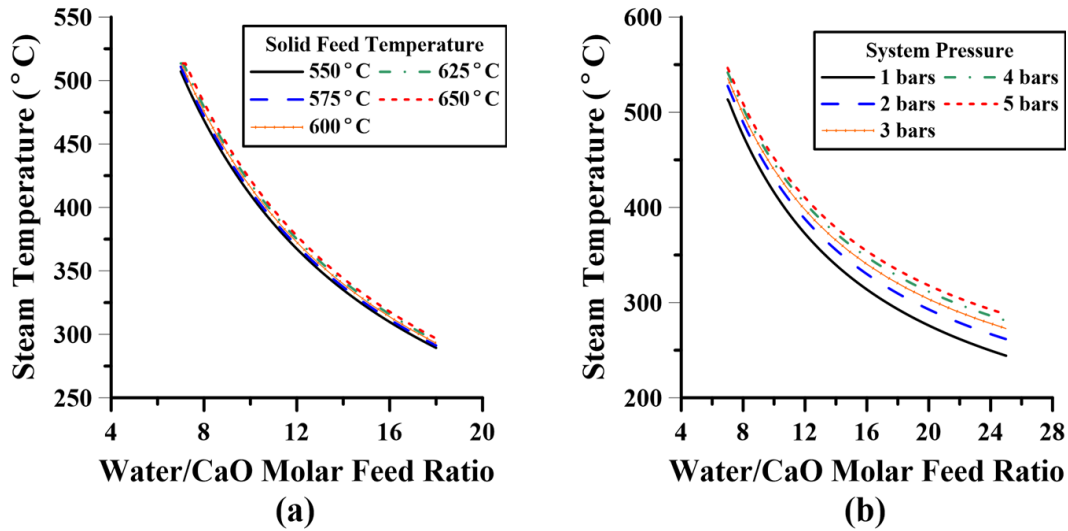


Figure 6.2. Effects of water/CaO molar feed ratio on the hydrator off-gas temperature at: (a) different solid feed temperatures and fixed reactor pressure of 1 bar; and (b) different pressures for a fixed solid feed temperature of 600°C.

These results confirm that the sorbent hydrator can simultaneously serve as a steam superheater unit. Given the typical range of lime hydration temperature (250-500°C, [84]), a substantial flow of saturated steam would be required to maintain the hydration temperature. The superheated steam could be used further in several applications, including in water-gas shift reactors, steam methane reformers, steam gasifiers, steam-iron reactors and steam turbines. Excess superheated steam could also be fed to a heat exchanger, supplying a portion of the energy required for water evaporation and gas pre-heating.

6.3.2. MRC-CAL Sorbent Regeneration

The gaseous medium fed into the MRC-CAL sorbent regenerator is at methane/oxygen molar ratio higher than the stoichiometric combustion value ($\text{CH}_4/\text{O}_2 > 0.5$). Accordingly, oxygen becomes the combustion limiting reactant, with the excess methane participating in endothermic dry and wet reforming reactions [118,119]. The MRC-CAL process can be operated autothermally only if the heat released by the methane combustion supplies enough energy for

endothermic methane reforming and limestone calcination. Equation (6.2) shows the correlation developed in Chapter 3 to estimate required methane to enriched-air (95% O₂ balanced with N₂) molar feed ratio (β) for autothermal limestone decomposition by the MRC-CAL process. Increasing the CaCO₃/total gas molar feed ratio (α) leads to a higher energy requirement and, therefore, more energy to be supplied inside the reactor. This corresponds to higher oxygen feed concentration (as the combustion limiting reactant), resulting in lower β for autothermal MRC-CAL operation at elevated α (Figure 6.3(a)):

$$\beta = 0.275 + 1.903e^{-\alpha/0.716} \quad 800^{\circ}\text{C} \leq T \leq 900^{\circ}\text{C}, P = 1-5 \text{ bars}, x_{\text{CaCO}_3} = 1 \quad (6.2)$$

Figure 6.3(a) also shows the required gaseous feed composition for autothermal decomposition of slaked lime at different Ca(OH)₂/total gas molar feed ratios. Calcination of slaked lime is less endothermic than the limestone decomposition. Therefore, a lower extent of methane combustion is required to calcine the Ca(OH)₂ particles in the MRC-CAL unit. This corresponds to a lower oxygen feed concentration and, consequently, a higher β than those for limestone calcination. Equation (6.3) correlates the required methane to enriched-air molar feed ratio for autothermal decomposition of slaked lime by the MRC-CAL unit. A molar weighted average of Equations (6.2) and (6.3) was used to estimate the required gas feed composition for autothermal co-calcination of limestone and slaked lime at different solid/gas molar feed ratios and solid feed compositions (Equation (6.4)). Figure 6.3(b) compares the Aspen Plus simulation results with those predicted by Equation (6.4), demonstrating the high precision of the proposed correlation ($R^2 = 0.992$) for autothermal co-calcination of CaCO₃/Ca(OH)₂ solid mixture using the MRC-CAL unit.

$$\beta = 0.23 + 2.07e^{-\alpha/1.46} \quad 800^{\circ}\text{C} \leq T \leq 900^{\circ}\text{C}, P = 1-5 \text{ bars}, x_{\text{CaCO}_3} = 0 \quad (6.3)$$

$$\beta = 0.23 + 2.07e^{-\alpha/1.46} + x_{\text{CaCO}_3} (0.045 + 1.903e^{-\alpha/0.76} - 2.07e^{-\alpha/1.46}) \quad (6.4)$$

$800^{\circ}\text{C} \leq T \leq 900^{\circ}\text{C} \ \& \ P = 1-5 \text{ bars}$

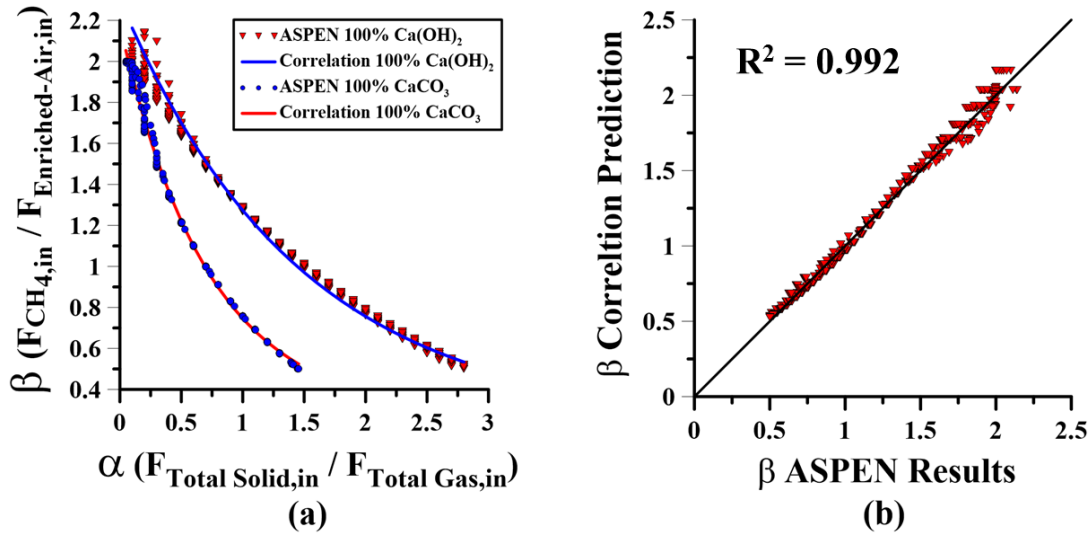


Figure 6.3. (a) Required gaseous feed composition for the autothermal MRC-CAL operation with unary solid feed; and (b) Comparison of the Aspen Plus simulation results and Equation (6.3) predictions

As discussed in Chapter 3, the MRC-CAL unit can offer autothermal, coke-free and complete sorbent regeneration within a certain range of solid/total gas molar feed ratio (α). In detail, exceeding an upper α limit leads to incomplete/endothermic sorbent calcination, while coke formation can occur below a certain α value. In addition, increasing the operating pressure and reducing the reactor temperature can narrow the applicable range of solid/gas molar feed ratio for effective MRC-CAL operation. Figure 6.4 shows the proper ranges of the MRC-CAL operating conditions for calcining limestone and slaked lime separately. Thermal decomposition of the slaked lime is less endothermic than of limestone and, hence, can be conducted at reduced reactor temperatures. In fact, Ca(OH)_2 decomposition is highly favoured at the operating

conditions of limestone calcination [159]. Accordingly, the upper α limit for slaked lime is considerably higher than for limestone, and, less sensitive to the reactor pressure and temperature (Figure 6.4 (a)). This corresponds to a wide applicable range of operating conditions for effective calcination of slaked lime by the MRC-CAL unit. On the other hand, the MRC-CAL lower α limit is roughly similar for the limestone and slaked lime, implying that carbon formation is nearly independent of the solid feed composition. Note that the limits of α for limestone calcination are well within those for slaked lime calcination, showing good compatibility of limestone and slaked lime co-calcination to achieve autothermal, coke-free and complete sorbent regeneration.

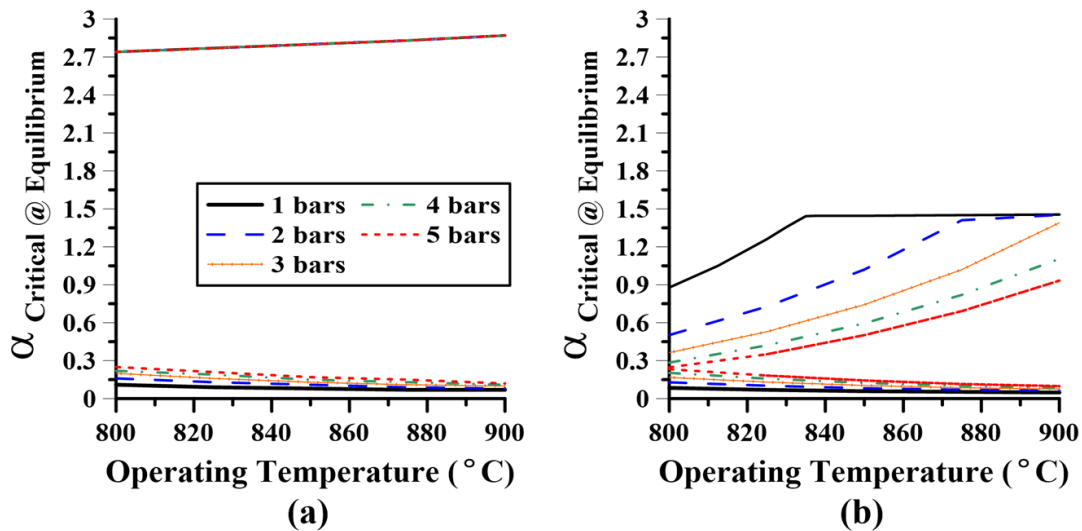


Figure 6.4. Critical α limits for (a) Ca(OH)_2 ; and (b) CaCO_3 decomposition via MRC-CAL process

The effect of solid feed composition on the MRC-CAL critical α limits in given operating conditions is shown in Figure 6.5(a). The gaseous feed compositions for these runs were obtained by means of Equation (6.4). Increasing the CaCO_3 solid feed fraction does not sensibly change the lower α limit for proper MRC-CAL operation. However, the upper α limit decreases

substantially with increasing CaCO_3 solid feed fraction. These results are in agreement with Figure 6.4 where it was observed that the α upper limit is higher for slaked lime, while the lower α limit is similar for both solid phases. Note that the Ca(OH)_2 decomposition releases steam into the MRC-CAL gaseous medium. This also reduces the CO_2 concentration within the reactor, potentially enhancing the rate and extent of limestone calcination.

Figure 6.5(b) compares the hydrogen and CO production yields of the MRC-CAL sorbent regenerator at different solid feed compositions. Increasing the CaCO_3 fraction in the total solid feed reduces the hydrogen yield, while enhancing CO production. In fact, increasing the CaCO_3 solid feed fraction leads to higher CO_2 addition into the reactor gas (more limestone calcination). The desorbed CO_2 then partially reacts with the hydrogen that was produced in the reforming stage, generating an equimolar amount of CO (reverse water-gas shift reaction). Simultaneously, calcination of the slaked lime produces steam, which shifts the thermodynamic equilibrium of the water-gas shift reaction toward more production of hydrogen. Accordingly, increasing the CaCO_3 solid fraction (accompanied by reducing the Ca(OH)_2 solid fraction) results in shifting the water-gas shift reaction toward more CO production, utilizing the CO_2 and the hydrogen content of the MRC-CAL gaseous medium.

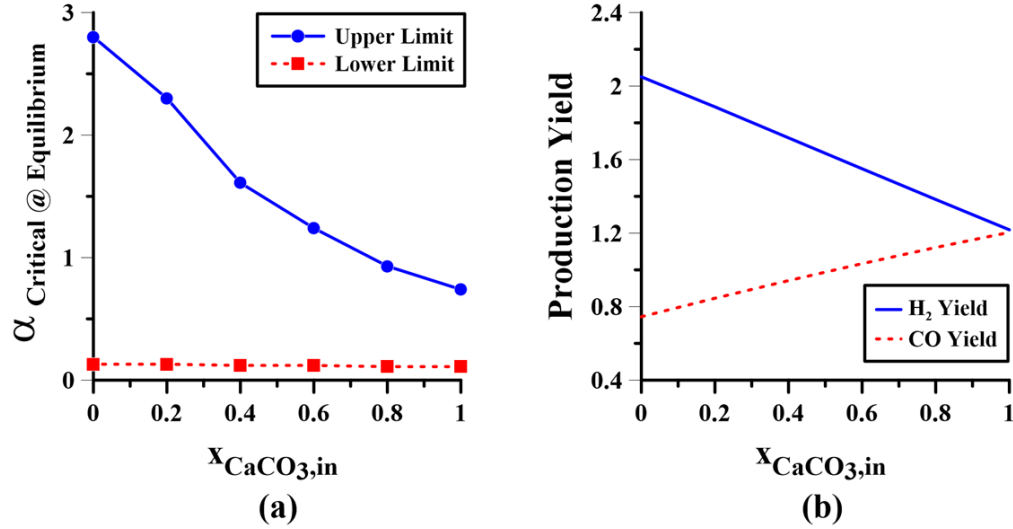


Figure 6.5. Effect of solid feed composition on the MRC-CAL: (a) critical operation limits; and (b) H₂ and CO production yields (Reactor Pressure: 3 bars, Operating Temperature 800°C, Solid/total gas molar feed ratio: 0.5 for panel (b), Gas feed composition calculated by Equation (6.4))

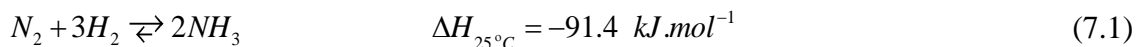
6.4. Conclusions

A novel lime hydration/reactivation setup is introduced, utilizing saturated steam as the hydration and direct heat-removal medium. It was observed that this configuration can produce significant amount of superheated steam, to be used in different industrial applications. The equilibrium performance of the limestone and slaked lime co-calcination was studied in a methane-concentrated oxy-fuel calciner. It was shown that increasing the slaked lime fraction in the solid feed increases the required methane feed concentration for autothermal sorbent regeneration using this novel sorbent regeneration technology. In addition, the process offers autothermal, coke-free and complete sorbent regeneration within a certain range of solid/gas molar feed ratios. The applicable range of solid/gas molar feed ratio was observed to narrow with increasing reactor pressure and limestone solid feed fraction, but expands when the operating temperature is raised. Increasing the CaCO₃ solid feed fraction also reduces the calciner hydrogen productivity, while increasing the CO production yield.

CHAPTER 7: Co-Production of Lime and Syngas for Ammonia Synthesis without Air Separation

7.1. Introduction

Ammonia is the second most widely produced chemical in the world, commonly used to produce nitrogen fertilizers [160,161]. It is industrially synthesised by the Haber-Bosch process, reacting hydrogen and nitrogen at moderate temperatures ($> 375^{\circ}\text{C}$) and high pressures (> 100 bars):



A general schematic of a conventional ammonia plant is depicted in Figure 7.1. Hydrogen is typically obtained by steam methane reforming (SMR), while cryogenic air separation unit (ASU) can be employed to generate nitrogen [160–162]. However, both the SMR and ASU processes are energy-intensive, imposing a considerable energy penalty on the overall integrated system.

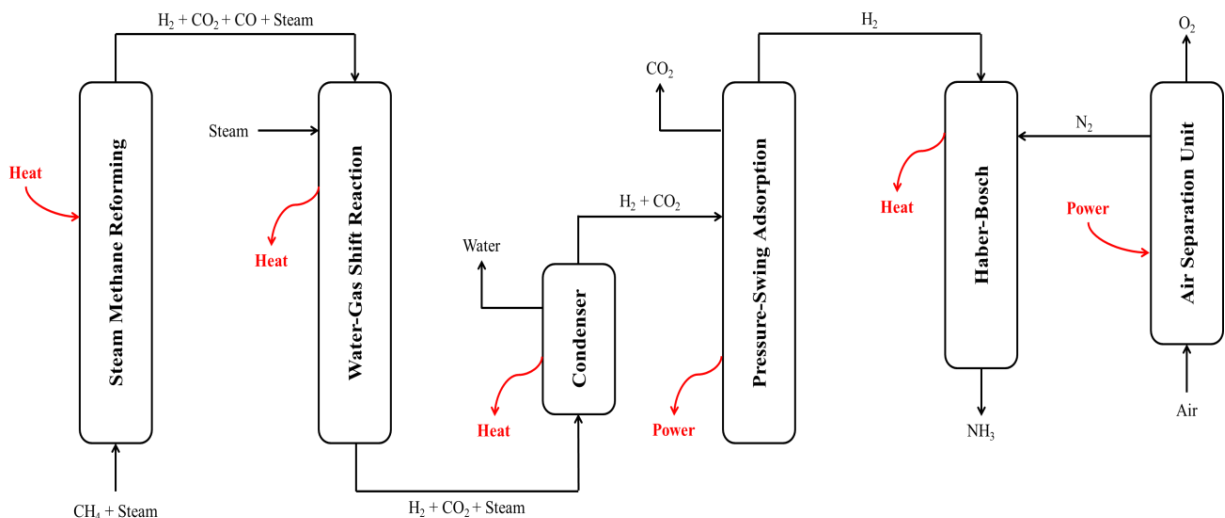


Figure 7.1. General schematic of a conventional ammonia plant

The hydrogen productivity of SMR process can be significantly enhanced by *in situ* CO₂ removal using lime-based sorbents. Exothermic carbonation of lime can also supply a large portion of the heat required for SMR thermal processing [12,15,18,20,163]. Sorbent-enhanced steam methane reforming (SE-SMR) is conventionally conducted in dual fluidized bed reactors, utilizing a parallel limestone calciner for continuous sorbent regeneration in a looping system [41,144]. Limestone calcination typically occurs in non-CO₂ gaseous media (e.g. air and steam), or oxy-fuel feedstock [39,122,123,164]. However, these processes suffer from several operational challenges, including external heating, high temperature, and dilute CO₂ off-gas [118].

A novel sorbent regeneration technology was introduced in Chapters 3 and 4, combining methane reforming, combustion and limestone calcination in a single reactor (called MRC-CAL process). This process utilizes methane-concentrated oxyfuel feedstock ($\text{CH}_4/\text{O}_2 > 0.5$), with the oxygen being supplied in a highly-concentrated form (e.g. 95 vol% O₂, balanced with N₂). It was shown in previous chapters that the MRC-CAL process can offer autothermal syngas-producing (H₂ and CO) limestone calcination at reduced temperatures. The process syngas can be further

used in many downstream applications, including metal oxide reduction, power generation and methanol production. Alternatively, the process off-gas can be used to supply the required feedstock for ammonia synthesis, as shown in Figure 7.2. This eliminates the need for highly-concentrated oxygen as the air nitrogen content can be further utilized in the Haber-Bosch process. Nitrogen dilution of the calciner gas may also enhance the limestone calcination and methane conversion within the MRC-CAL reactor.

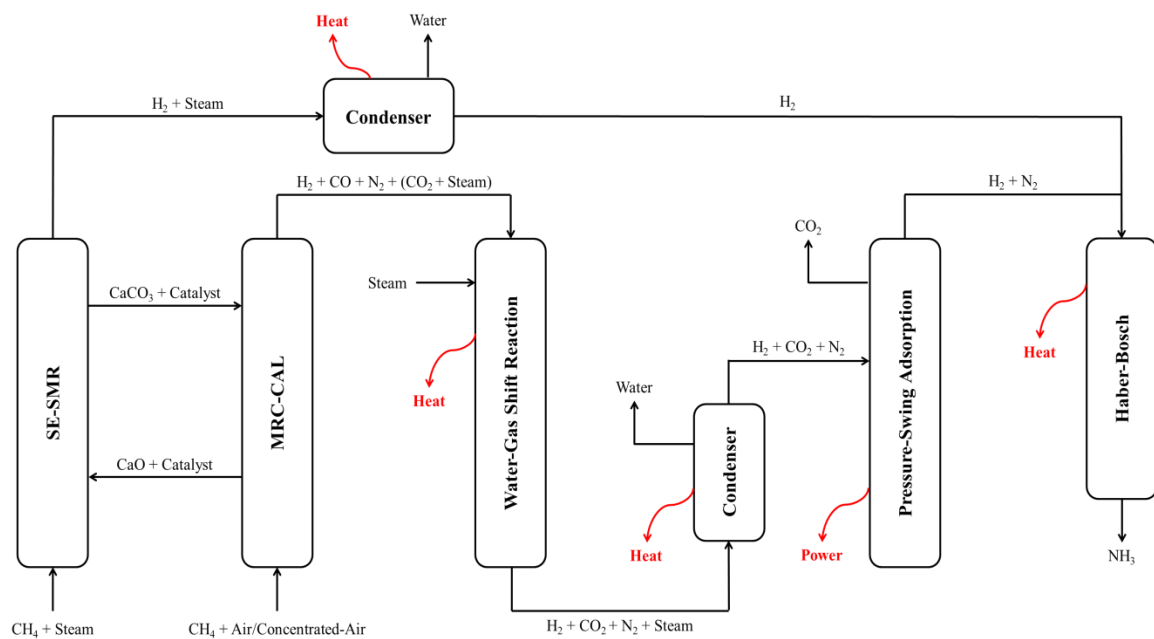


Figure 7.2. Schematic of the proposed ammonia plant

This chapter presents a thermodynamic analysis of the MRC-CAL process for co-production of lime and syngas, to be used for ammonia synthesis without cryogenic air separation. An empirical correlation is developed for estimating the required gaseous feed concentrations for autothermal air-fuel MRC-CAL reactors. Appropriate ranges of operating conditions for coke-free and complete limestone calcination are also assessed and discussed. The MRC-CAL equilibrium performance (syngas yield and quality) is evaluated at different reactor pressures (5-25 bars), operating temperatures (850-900°C), feed ratios and air oxygen concentrations. A

kinetic reactor model is then employed to analyze the system performance under turbulent fluidization conditions. The turbulent fluidization regime was selected owing to its superior solid-gas contact and high solids hold-up.

7.2. Correlation Development and Performance Metrics

Equation (7.2) was proposed in Chapter 3 for estimating the required gaseous feed concentrations for autothermal MRC-CAL operation. However, this correlation is based on 95 vol% O₂ in air, and cannot be used directly for different oxygen concentrations in the feed air.

$$\beta = 0.275 + 1.903e^{-\alpha/0.716} \quad 800^{\circ}\text{C} \leq T \leq 900^{\circ}\text{C}, P = 1-5 \text{ bars}$$

$$\alpha = \frac{F_{\text{CaCO}_3, \text{Calcliner Feed}}}{F_{\text{Gas, Calcliner Feed}}} \quad \beta = \frac{F_{\text{CH}_4, \text{Calcliner Feed}}}{F_{\text{Enriched-Air, Calcliner Feed}}} \quad y_{\text{O}_2, \text{Enriched-Air}} = 0.95 \quad (7.2)$$

Equation (7.2) was expanded to form Equation (7.3), which was further rearranged by introducing new dimensionless parameters (α^* and β^* , defined in Equation (7.4)). Note that minor impact of nitrogen dilution on shifting the equilibrium of steam and dry methane reforming is neglected in this derivation. Equation (7.4) can be used to provide a rough estimate of the required gaseous feed concentrations for autothermal MRC-CAL operation at different air oxygen concentrations. Some performance metrics to evaluate the syngas productivity of the process are defined in Table 7.1.

$$\frac{F_{\text{CH}_4, \text{Calcliner Feed}}}{F_{\text{O}_2, \text{Calcliner Feed}}} = 0.275 + 1.903e^{-\frac{\frac{F_{\text{CaCO}_3, \text{Calcliner Feed}}}{F_{\text{CH}_4, \text{Calcliner Feed}} + \frac{F_{\text{O}_2, \text{Calcliner Feed}}}{0.95}}{-0.716}} \quad (7.3)$$

$$\beta^* = 0.275 + 1.903e^{\left(\frac{-\alpha^*}{0.716}\right)\left(\frac{\beta^*}{\beta^*+1}\right)} \quad (7.4)$$

$$\alpha^* = \frac{F_{CaCO_3, \text{Calciner Feed}}}{F_{CH_4, \text{Calciner Feed}}} \quad \beta^* = \frac{0.95F_{CH_4, \text{Calciner Feed}}}{F_{Air, \text{Calciner Feed}} \times Y_{O_2, Air}}$$

Table 7.1. Metrics applied for SE-SMR performance evaluation

Syngas Yield	Syngas H ₂ /CO	Syngas Ideal H ₂ /N ₂ *
$\frac{F_{H_2, \text{Calciner Off-Gas}} + F_{CO, \text{Calciner Off-Gas}}}{F_{CH_4, \text{Calciner Feed}}}$	$\frac{F_{H_2, \text{Calciner Off-Gas}}}{F_{CO, \text{Calciner Off-Gas}}}$	$\frac{F_{H_2, \text{Calciner Off-Gas}} + F_{CO, \text{Calciner Off-Gas}}}{F_{N_2, \text{Calciner Off-Gas}}}$

* Assuming a downstream water-gas shift reactor to convert all CO to CO₂, generating an equimolar amount of H₂

7.3. Simulation Setup

7.3.1. Thermodynamics Simulation

Aspen Plus V.10 was employed to simulate the equilibrium performance of the MRC-CAL process at various operating conditions. An isothermal Gibbs reactor was used, with the reactant streams entering the system at the reactor temperature and pressure. Given the implicit nature of Equation (7.4), it was difficult to control the reactor gaseous feed concentration by a simple calculator block. A less complicated approach was employed instead, utilizing three gas streams (CH₄, Enriched-air, and N₂), two gas mixers and a gas splitter (Figure 7.3). The gaseous feed concentration for each simulation run was first estimated by a calculator block, assuming 95% O₂ in air (i.e., in Equation (7.2)). The resulting gas was then further diluted by an additional nitrogen stream in order to achieve the target air oxygen concentration for each simulation case.

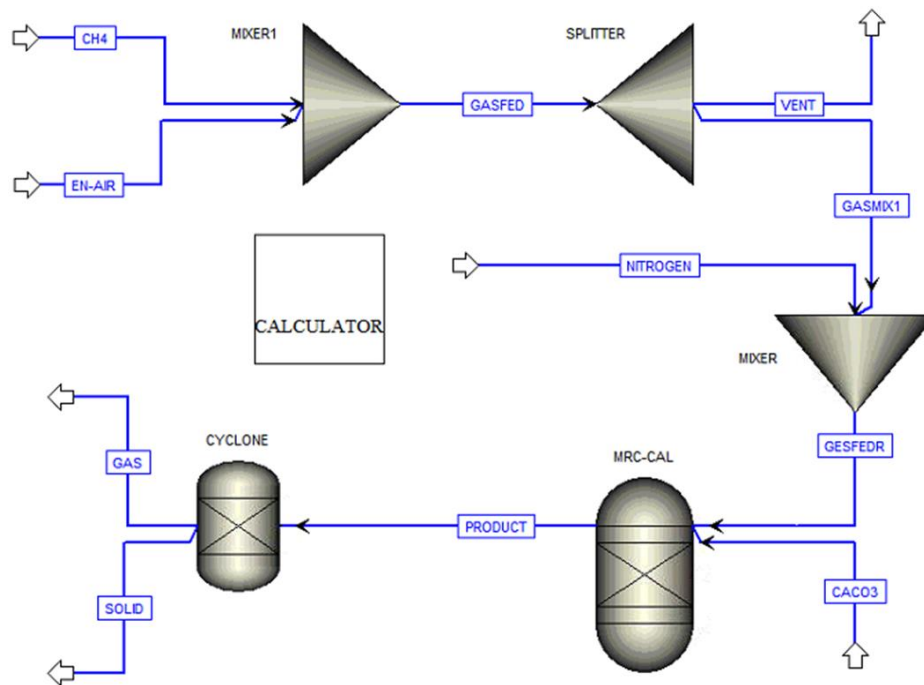


Figure 7.3. Process flowsheet for the Aspen Plus simulation

Enriched-air was set to contain 95% O_2 (balance nitrogen), similar to that in Equation (7.2). The methane inlet flowrate was fixed at 1 mol.s^{-1} , and different gaseous feed concentrations were achieved by controlling the flowrate of the enriched-air and nitrogen streams. A varying $CaCO_3$ /total gas (α) value was selected for each simulation case, and the required CH_4 /enriched-air molar feed ratio (β) was calculated *via* Equation (7.2). The enriched-air molar flow rate was then estimated based on the obtained CH_4 /enriched-air molar feed ratio and the methane inlet flow rate. The enriched-air and methane streams were then mixed, with 0.2 mol.s^{-1} of the resulting gas (GasMix1, taken *via* a gas splitter) taken to the reactor. The $CaCO_3$ inlet flowrate was calculated based on the selected α ($CaCO_3$ /total gas molar feed ratio) and GasMix1 total flowrate. The flowrate of nitrogen stream was then estimated based on the target air O_2 concentration, as well as O_2 and N_2 flowrates in the GasMix1 stream. A general schematic of the

calculation procedure is shown in Figure 7.4. A calculator block was used to solve these explicit equations in each simulation run.

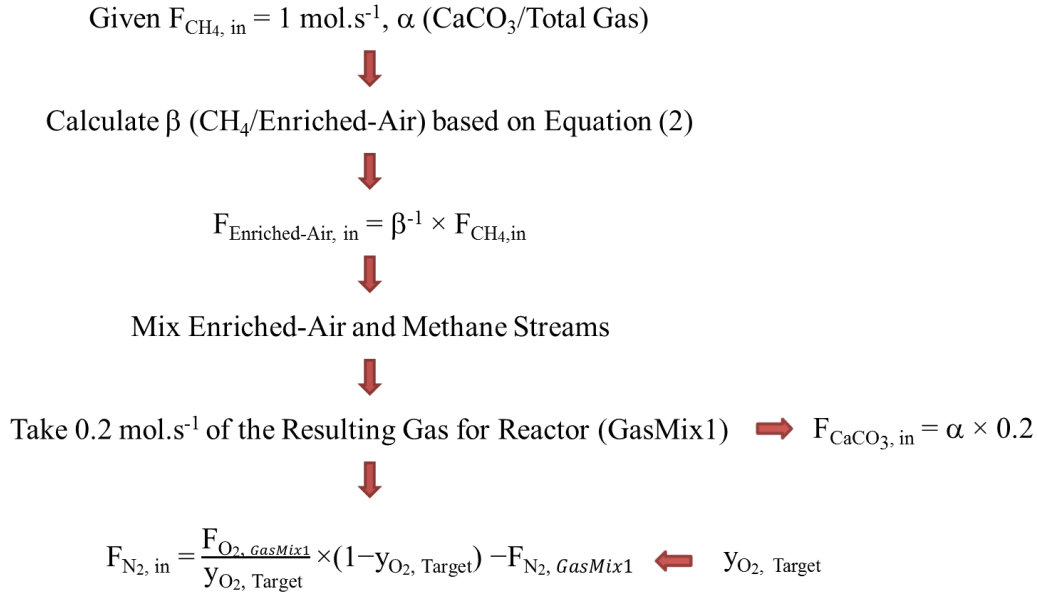


Figure 7.4. Flow chart of the applied calculation procedure in Aspen Plus simulation

7.3.2. Kinetic Simulation

The kinetic simulation of turbulent fluidized bed reactors for the MRC-CAL process is detailed in Chapter 4. In summary, an axially dispersed plug flow reactor model is used for the gas phase mole balance, whereas limestone calcination is modeled by the continuous stirred tank reactor model. Mean sorbent conversion for each simulation run was obtained based on the average calcination rate, estimated using the mean CO_2 concentration within the reactor. A local desorption distribution factor was employed, taking the axial variation of the limestone calcination driving force into account. The governing equations, rate expressions, applied correlations, and model parameters can be found in Chapter 4. The base input data for the reactor kinetics model is summarized in Table 7.2.

Table 7.2. Base inputs for kinetics simulations

Parameter/Variable	Values	Units
Reactor Pressure*	15	bars
Reactor Temperature*	900	°C
Reactor Diameter	0.1	m
Sorbent Residence Time	10	min
Superficial Gas Velocity**	0.9	m/s
CaCO ₃ /CH ₄ Molar Feed Ratio	0.2	-
Catalyst/Solid Bed Mass Ratio	0.1	-
Gaseous Feed Concentration	Calculated by Equation (7.4)	mol%
CaCO ₃ Density [15]	2200	kg/m ³
CaO Density [15]	1850	kg/m ³
Particle Diameter	200	μm

* Varied during the simulations

** Calculated at reactor operating temperature and pressure

7.4. Results and Discussion

7.4.1. Performance Analysis under Thermodynamic Equilibrium

The effects of different operating conditions on the reactor heat duty of the air-fuel MRC-CAL process (21 vol% O₂ in air) are depicted in Figure 7.5. Note that Equation (7.4) is indirectly employed to calculate β^* in these simulation runs. The calculated β^* is then used to estimate the gaseous feed concentration for each simulation case. Figure 7.5(a) shows that autothermal, coke-free, and complete limestone calcination can only occur within a certain range of CaCO₃/CH₄ molar feed ratios (α^*). In fact, coke formation can occur at low CaCO₃/CH₄ molar feed ratios, while exceeding a critical CaCO₃/CH₄ molar feed ratio results in incomplete limestone calcination. Incomplete limestone calcination also leads to lower energy consumption within the reactor, thereby shifting the reactor heat duty toward more exothermicity [137].

Reducing the reactor pressure, increasing the operating temperature and decreasing the air oxygen concentration lead to higher MRC-CAL reactor heat duty (i.e. stronger endothermicity),

as shown in Figures 7.5(b)-(d). This can be due to enhanced steam and dry methane reforming, resulting in more energy consumption within the reactor. Note that a significant deviation from autothermal reactor operation (heat duty ~ 0) is achieved at low $\text{CaCO}_3/\text{CH}_4$ molar feed ratios (α^*). This can be attributed to slight variation of steam and dry methane reforming extents at low limestone loadings. Therefore, Equation (7.4) can only be used to generate an initial estimation of the gaseous feed concentration, while detailed analysis has to be conducted for each case studied.

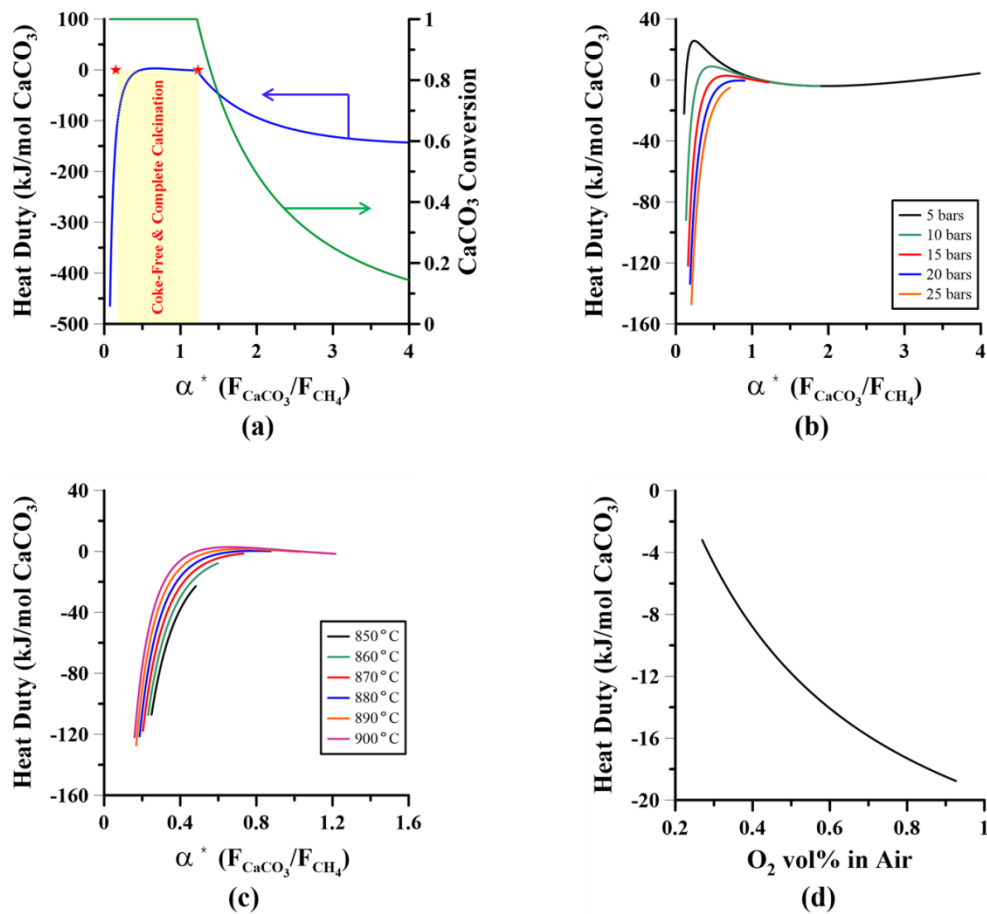


Figure 7.5. Variation of the MRC-CAL heat duty at (a) 900C, 15 bars, 21% O_2 in air and different α^* (b) 900C, 21% O_2 in air and different pressures and α^* (c) 15 bars, 21% O_2 in air and different temperatures α^* (d) 900C, 15 bars and $\alpha^* = 0.5$ and different O_2 level in air. Panels (b)-(d) are limited to complete and coke-free limestone calcination conditions.

The effects of operating temperature and pressure on the upper and lower critical limits of $\text{CaCO}_3/\text{CH}_4$ molar feed ratio (α^*) are depicted in Figure 7.6 for 21 vol% O_2 in air. Increasing the reactor pressure narrows the applicable range of α^* , whereas higher reactor temperature expands the appropriate operation zone. This is in agreement with the findings of our earlier study [137] for the oxy-fuel MRC-CAL process (95 vol% oxygen in air). Note that increasing the concentration of the nitrogen diluent in the reactor can potentially reduce the chance of coke formation, while also decreasing the CO_2 concentration within the reactor. The latter can potentially enhance the limestone calcination driving force, thereby elevating the upper critical α^* limit. Hence, higher air nitrogen concentrations can expand the applicable range of α^* for the MRC-CAL process, as shown in Figure 7.7.

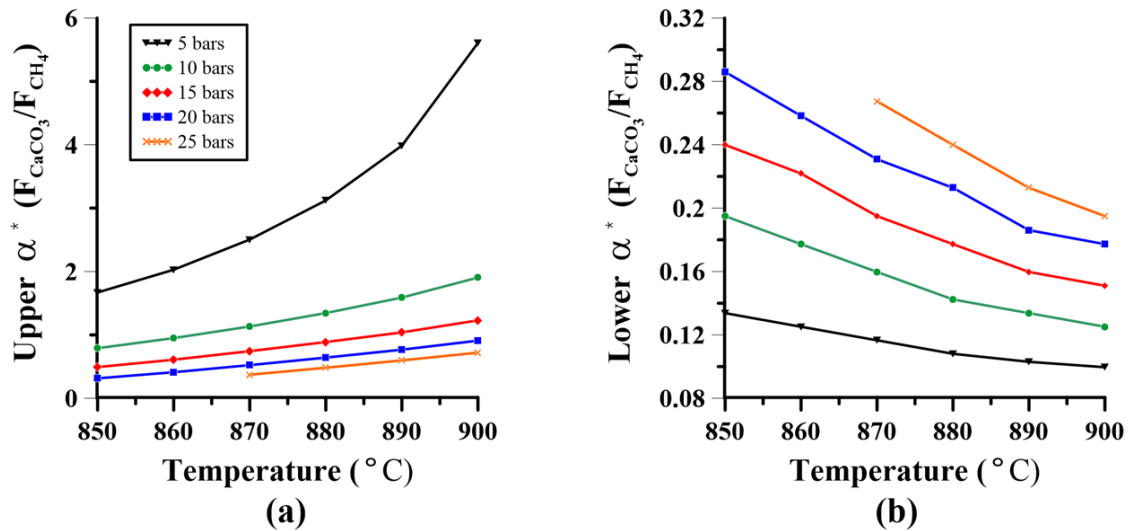


Figure 7.6. Effects of reactor temperature and pressure on the: (a) upper; and (b) lower α^* limits for complete and coke-free limestone calcination (21% O_2 in air).

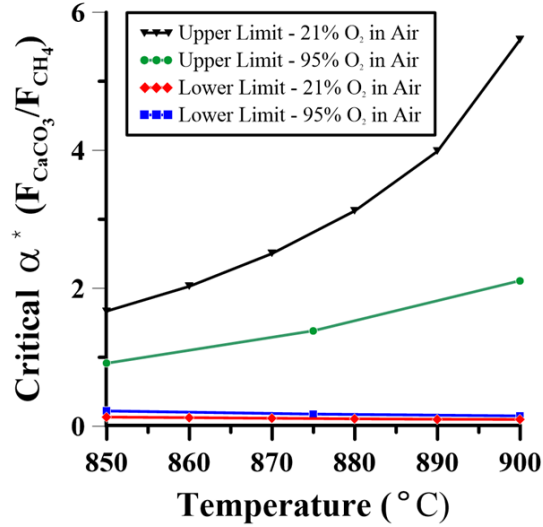


Figure 7.7. Effect of air oxygen concentration on the MRC-CAL critical α^* limits at 5 bars.

Increasing the operating temperature and reducing the reactor pressure both enhance the syngas yield of the MRC-CAL process, as shown in Figure 7.8. This could be explained by the effect of temperature and pressure on the thermodynamic equilibrium of the steam and dry methane reforming reactions. Increasing temperature shifts the thermodynamic equilibrium of the endothermic steam and dry methane reforming toward higher feedstock conversion. On the other hand, higher pressures hinder steam and dry methane reforming, in agreement with Le Chatelier's principle.

Increasing α^* ($\text{CaCO}_3/\text{CH}_4$ molar feed ratio) initially boosts the MRC-CAL syngas yield, as depicted in Figure 7.8. This could be attributed to enhanced dry methane reforming at higher limestone loadings. In fact, higher α^* (i.e. more CaCO_3 feeding) results in more CO_2 release into the reactor, consequently shifting the dry methane reforming toward higher methane conversion. On the other hand, the required methane feed concentration for autothermal MRC-CAL operation is significantly reduced when increasing the $\text{CaCO}_3/\text{CH}_4$ molar feed ratio (Equations (7.2)-(7.4)). This corresponds to a higher proportion of methane being combusted to maintain the

autothermal operation, resulting in a lower methane conversion by syngas-producing steam and dry methane reforming. Hence, exceeding a certain $\text{CaCO}_3/\text{CH}_4$ molar feed ratio leads to a substantial reduction of the MRC-CAL syngas yield, as shown in Figure 7.8. These simulation results suggest that $\text{CaCO}_3/\text{CH}_4$ molar feed ratios of less than 0.5 are required to maximize the syngas productivity of the air-fuel MRC-CAL process. Slightly higher $\text{CaCO}_3/\text{CH}_4$ molar feed ratios would then be needed if the reactor was to be operated at elevated pressures and low temperatures.

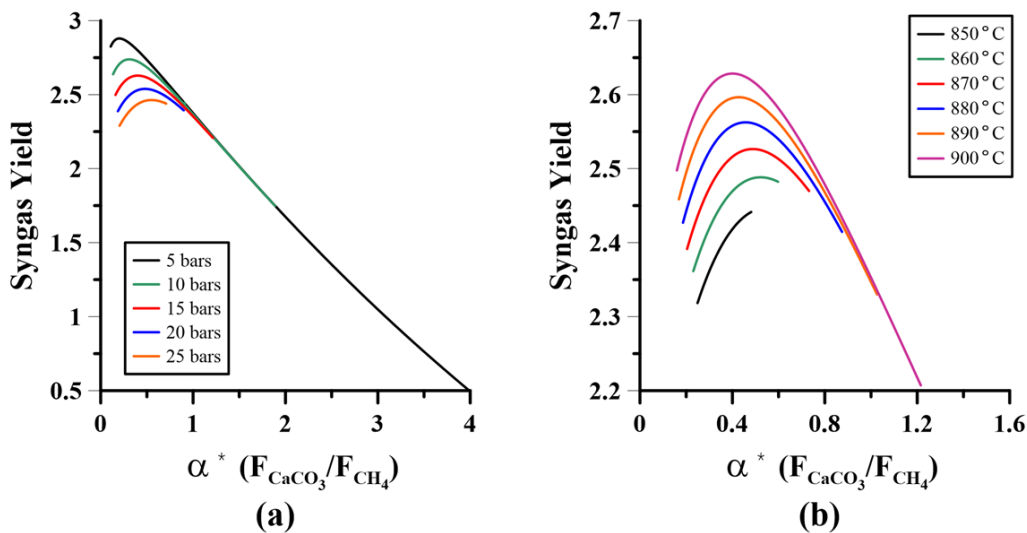


Figure 7.8. Effects of: (a) reactor pressure (at $T=900^\circ\text{C}$); and (b) reactor temperature (at $P=3$ bars) on syngas yield of the air-fuel MRC-CAL process at different $\text{CaCO}_3/\text{CH}_4$ molar feed ratios, for 21 vol% O_2 in air.

The variation of operating temperature and reactor pressure does not have an appreciable effect on the MRC-CAL syngas H_2/CO , as shown in Figure 7.9. However, increasing the $\text{CaCO}_3/\text{CH}_4$ molar feed ratio substantially reduces the syngas H_2/CO , likely due to shifting the water-gas shift reaction toward more hydrogen consumption. In fact, increasing the $\text{CaCO}_3/\text{CH}_4$ molar feed ratio (e.g. by more CaCO_3 feeding) releases excess CO_2 (released by limestone calcination) into the

reactor. This potentially shifts the water-gas shift thermodynamic equilibrium toward H₂ consumption, accompanied by production of more CO within the reactor.

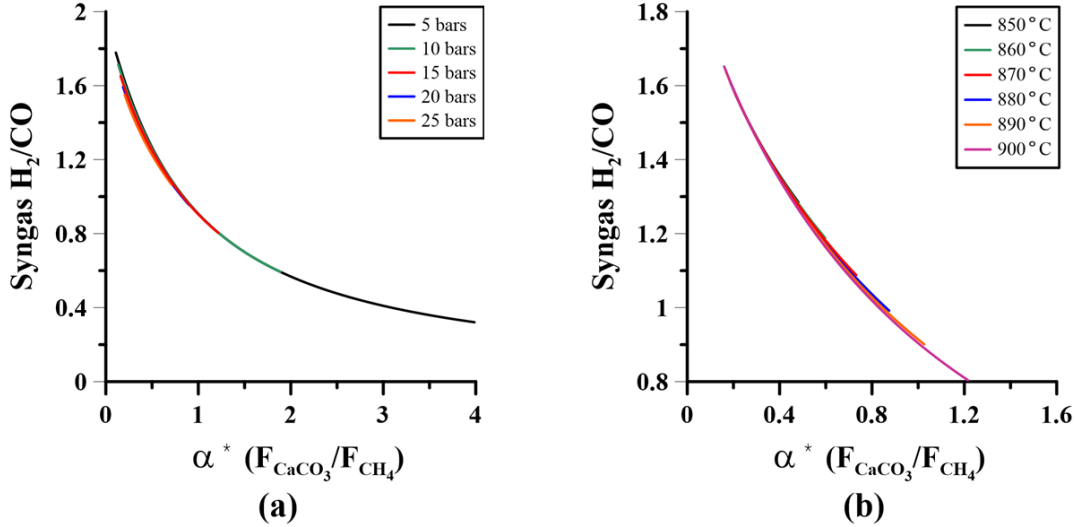


Figure 7.9. Effects of: (a) reactor pressure; and (b) reactor temperature on syngas H₂/CO ratio of the air-fuel MRC-CAL process at different CaCO₃/CH₄ molar feed ratios. Other operating conditions are identical to those in Figure 7.8.

Increasing the CaCO₃/CH₄ molar feed ratio (α*) reduces the MRC-CAL ideal H₂/N₂, as shown in Figure 7.10. This could be due to greater methane combustion at elevated CaCO₃/CH₄ molar feed ratios (Equations (7.2)-(7.4)), resulting in less methane reforming and, thereby, reduced syngas production. Lower methane feed concentration (at elevated CaCO₃/CH₄ molar feed ratios) also corresponds to a higher air feed concentration and, consequently, more nitrogen feeding. Hence, increasing the CaCO₃/CH₄ molar feed ratio can substantially reduce the ideal H₂-to-N₂ ratio in the MRC-CAL off gas. In addition, increasing the operating temperature and reducing the reactor pressure enhances the methane conversion at low CaCO₃/CH₄ molar feed ratios, thereby increasing the syngas ideal H₂/N₂. However, the effect of pressure and temperature becomes less significant at elevated α*, likely due to high methane reforming extent at elevated CaCO₃/CH₄ molar feed ratios.

Note that the Haber-Bosch process requires 3 moles of hydrogen per mole of nitrogen. Assuming that the MRC-CAL process is the only source for providing the gaseous feedstock for ammonia synthesis (e.g. no parallel sorbent-enhanced steam methane reformer installed), a H_2/N_2 molar ratio of 3 would be required out of the MRC-CAL reactor. However, Figure 7.10 suggests that air-fuel MRC-CAL process (21 vol% O_2 in air) is not capable of producing the syngas quality required for the Haber-Bosch process (H_2/N_2 molar ratio = 3), and higher air oxygen concentrations (e.g. lower nitrogen content) are therefore needed.

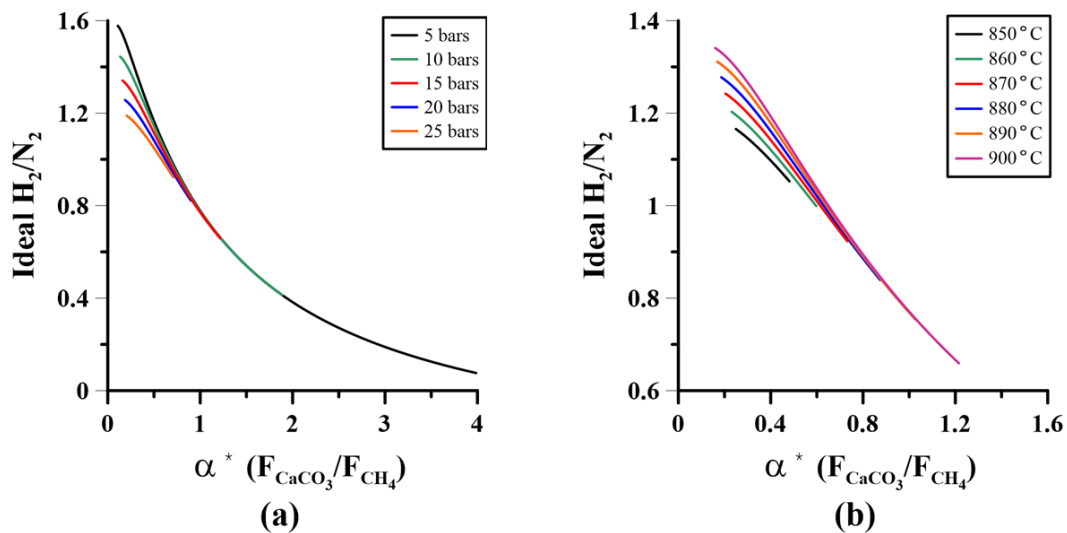


Figure 7.10. Effects of: (a) reactor pressure; and (b) reactor temperature on syngas H_2/N_2 of the air-fuel MRC-CAL process at different $CaCO_3/CH_4$ molar feed ratios. Other operating conditions are identical to those in Figure 7.8.

The required air oxygen concentration for achieving the Haber-Bosch syngas quality (ideal H_2/N_2 molar ratio = 3) is shown in Figure 7.11 for the MRC-CAL process. Increasing the $CaCO_3/CH_4$ molar feed ratio (α^*) substantially increases the required air oxygen level to meet the Haber-Bosch requirement. This is attributed to less syngas production at higher α^* (Figure 7.8), requiring a lower amount of nitrogen (e.g. air dilution) for ammonia synthesis. Note that increasing the $CaCO_3/CH_4$ molar feed ratio also reduces the reactor throughput, resulting in

lower ammonia production capacity of the plant. Figure 7.11 also indicates that the variation of reactor temperature and pressure has only a slight effect on the required air oxygen concentration, mainly at low α^* . This could be linked to the modest influence of temperature and pressure on the MRC-CAL syngas yield, as discussed earlier in Figure 7.8. The results in Figure 7.11 suggests that the MRC-CAL process can be optimized at air oxygen concentrations of around 40% and $\text{CaCO}_3/\text{CH}_4$ molar feed ratios of nearly 0.2-0.3 for the ranges of operating pressures and temperatures studied.

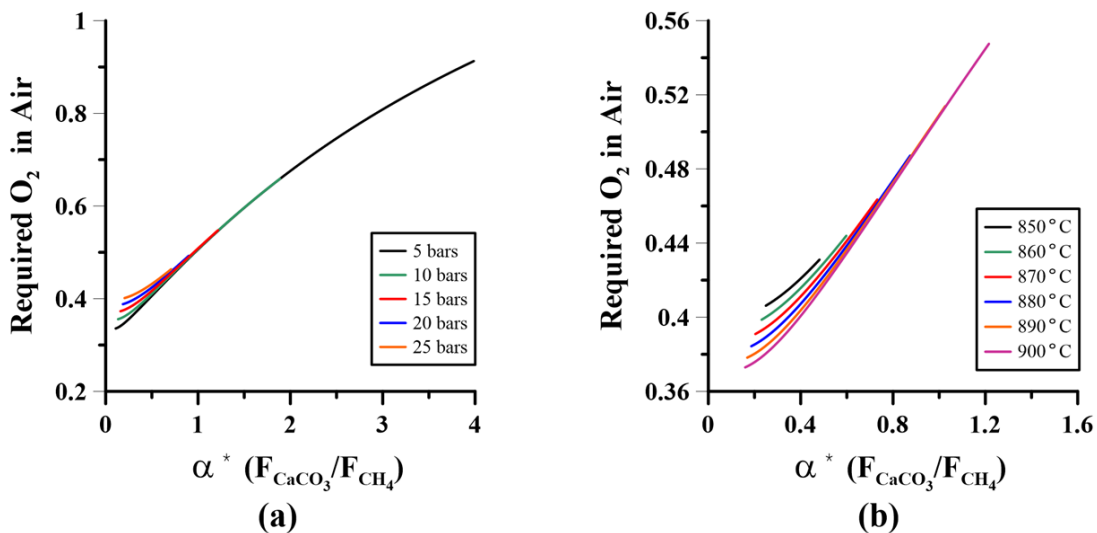


Figure 7.11. Effects of: (a) reactor pressure; and (b) reactor temperature on required air oxygen concentration to achieve the syngas quality for the Haber-Bosch process. Other operating conditions are identical to those in Figure 7.8.

7.4.2. Kinetic Performance Analysis in Turbulent Fluidized Bed Reactors

The effects of reactor temperature and pressure on the sorbent conversion of the MRC-CAL process are depicted in Figure 7.12 for different air oxygen concentrations. Increasing operating temperature and reducing the reactor pressure enhance the sorbent conversion at both air oxygen concentrations. Higher reactor temperatures are imperative to achieve an appreciable sorbent conversion at elevated pressures (e.g. at 25 bar). Figures 7.12 also indicates that increasing the

O₂ concentration in air (i.e., reducing the nitrogen concentration) can significantly reduce the sorbent conversion, especially at low operating temperatures and elevated reactor pressures. Increasing the air nitrogen concentration reduces the CO₂ concentration within the reactor, thereby enhancing the limestone calcination driving force. Therefore, higher reactor pressures and lower operating temperatures can be used to achieve a certain sorbent conversion at elevated air nitrogen concentrations.

Figure 7.12 suggests that the MRC-CAL process can offer relatively high sorbent conversion (e.g. > 60%) at elevated pressures (up to 25 bars) and moderate temperatures (<900°C). Note that sorbent particles in the CaL process are only partially carbonated in practice [69], whereas the current model assumes 100% CaCO₃ particles. This is mainly due to the formation of a CaCO₃ layer on the particle surface, inhibiting CO₂ diffusion into the particle unreacted core [155,156]. Therefore, higher sorbent conversion than those predicted in Figure 7.12 can be achieved in practical calcium-looping processes, including in sorbent-enhanced steam methane reformers.

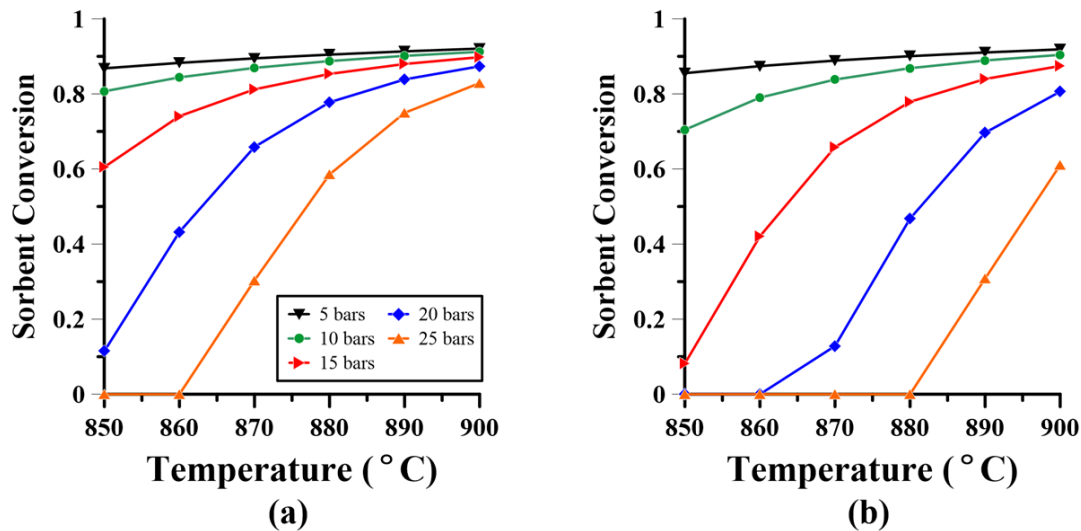


Figure 7.12. Effects of reactor temperature and pressure on the sorbent conversion of the MRC-CAL process at air oxygen concentration of: (a) 21 vol%; and (b) 40 vol%. Other input data are identical to those in Table 7.2.

Increasing the operating temperature and reducing the reactor pressure results in a higher MRC-CAL syngas ideal H_2/N_2 molar ratio, as shown in Figure 7.13. This is attributed to the higher methane conversion by steam and dry reforming at elevated temperatures and reduced pressures. Reducing the air oxygen concentration decreases the syngas H_2/N_2 , most likely due to increasing the amount of nitrogen fed to the reactor. Figure 7.13(a) indicates that the syngas ideal H_2/N_2 of an air-fuel MRC-CAL process (21 vol% O_2) is considerably lower than the required ratio for the Haber-Bosch process ($H_2/N_2=3$). This is in line with the thermodynamic equilibrium analysis presented in Figure 7.10. An air oxygen concentration of 40% can be used instead to achieve the syngas quality required for ammonia synthesis, as confirmed by Figure 7.13(b).

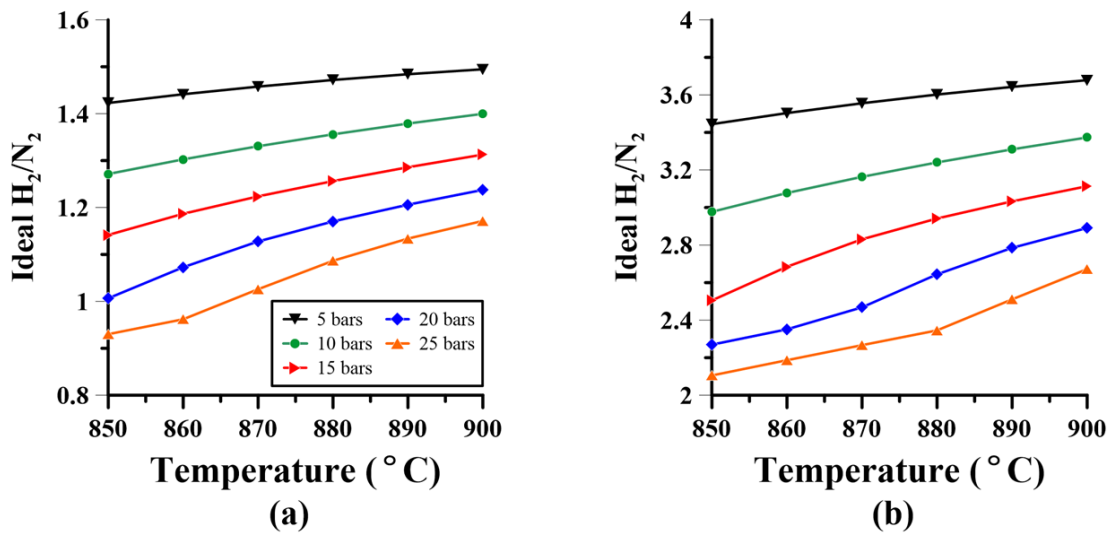


Figure 7.13. Effects of reactor temperature and pressure on the syngas H_2/N_2 of the MRC-CAL process at air oxygen concentration of: (a) 21 vol%; and (b) 40 vol%. Other input data are identical to those in Table 7.2.

In general, the air-fuel MRC-CAL process is capable of co-producing lime and syngas, which can be further used for ammonia synthesis without air separation unit. Increasing operating temperature and reducing the reactor pressure can considerably enhance the sorbent conversion and syngas quality of the process. However, higher pressures and lower temperatures are

typically preferred to enhance the system thermal efficiency and reduce the cost of downstream gas compression [69]. It was shown in Figures 7.12 and 7.13 that appreciable sorbent conversion can be achieved at practical ranges of operating conditions (pressures up to 25 bars and temperatures below 900°C), while an air oxygen concentration of nearly 40% is required to maintain the syngas quality for the downstream Haber-Bosch process.

Note that the optimal range of operating conditions may vary in practice due to several non-ideal circumstances. For instance, the solid and gas reactant streams typically enter the calciner at lower temperatures, whereas the current work assumes the feed streams to enter at the reactor temperature. Excess *in situ* fuel burning (e.g. methane or syngas) would then be inevitable for autothermal reactor operation, resulting in lower syngas yield and H₂/N₂ [69]. On the other hand, the generated lime by the MRC-CAL process can be used in a parallel sorbent-enhanced steam methane reformer, producing considerable hydrogen at relatively high concentrations (e.g. > 90%). This increases the amount of nitrogen required for the Haber-Bosch process, implying the need for lower air oxygen concentrations (i.e., increased air nitrogen concentrations).

The gaseous feed concentration in the oxy-fuel MRC-CAL process is typically within the methane flammability limits, resulting in major practical concerns with respect to safe operation. Increasing the nitrogen concentration in air can potentially narrow the methane flammability limit [138], thereby reducing operational challenges. Safe operation of highly pressurized Haber-Bosch reactor is another issue in this process, requiring specific material selection and reactor design.

7.5. Conclusions

The thermodynamic performance of methane-concentrated air-fuel calciner was investigated at different operating conditions. A correlation was introduced to generate an estimation of the required gaseous feed concentration for autothermal reactor operation at different operating temperatures, pressures, feed ratios and air oxygen concentrations. It was shown that autothermal, complete and coke-free limestone calcination can only occur within a certain range of $\text{CaCO}_3/\text{CH}_4$ molar feed ratios. Increasing the operating temperature and the air nitrogen concentration was shown to expand the applicable range of the $\text{CaCO}_3/\text{CH}_4$ molar feed ratios, while the opposite behaviour was predicted as the operating pressure increased.

The process syngas was shown to be mainly composed of H_2 , CO , and N_2 , which can be further used for ammonia synthesis without a cryogenic air separation unit. The syngas yield and quality (H_2/CO and H_2/N_2 molar ratios) were observed to be mainly functions of the $\text{CaCO}_3/\text{CH}_4$ molar feed ratio. Equilibrium analysis showed that the reactor temperature and pressure have less impact on the compositions of the generated syngas. However, operating temperature and pressure were observed to significantly affect the system kinetics in turbulent fluidized bed reactors.

CHAPTER 8: Conclusions and Recommendations

Massive emissions of greenhouse gases, especially CO₂, into the atmosphere are a major concern attributed to fossil fuel consumption for global energy supply. This has contributed to climate change, which is projected to continue if not addressed properly. Calcium-looping is an emerging carbon-capture technology, benefiting from low cost and toxic emissions. This process can be also integrated with steam methane reformers and biomass gasifiers, enhancing their hydrogen productivity by removing a portion of the generated CO₂ from the reactor. However, continuous operation of the calcium-looping process requires efficient sorbent regeneration (e.g. limestone calcination) at elevated reactor temperatures. This results in several practical challenges, including low thermal/energy efficiency, increased sorbent deactivation, and high cost of materials of construction.

In this thesis, the effect of limestone calcination conditions on the cyclic carbon capture capability of lime-based sorbents was evaluated using thermogravimetric analysis. Primary attention was given to incomplete/partial limestone calcination, a major gap in prior scientific works. A novel sorbent regeneration technology was then proposed for autothermal syngas-producing limestone calcination with *in situ* CO₂ utilization. The process was thoroughly assessed by means of kinetic and thermodynamic simulations. Simulation tests were also employed to screen the potential applications/integrations of the proposed process for hydrogen production *via* sorbent-enhanced steam methane reforming, ammonia synthesis without air separation unit, and Ca(OH)₂/CaCO₃ co-calcination in three-stage calcium-looping.

8.1. Conclusions

Thermogravimetric analysis of naturally-derived lime-based sorbents revealed that increasing the limestone calcination temperature undesirably reduces the sorbent reactivity for cyclic carbon capture. This could be attributed to higher pore sintering at elevated temperatures, reducing the active surface area for CO₂ capture. No significant variation in performance was observed when a sorbent remained at the calcination temperature after completing limestone decomposition. Similarly, exposing carbonated sorbents to high temperature did not greatly affect the sorbent performance. These results suggest that the loss of sorbent utilization is predominantly due to material physical and chemical changes during limestone calcination, which are further linked to the loss of active surface area by thermal pore sintering.

Significant efforts were made to assess the effect of partial limestone calcination on the cyclic CO₂ capture capability of lime-based sorbents. It was shown that partially calcined sorbents, upon being calcined, behave in a manner similar to freshly calcined sorbents. This could be promising, as partial limestone calcination can be achieved at relatively low reactor temperatures, significantly enhancing the system thermal/energy efficiency and the sorbent's cyclic performance. Partially calcined sorbents were also observed to offer smooth decay of sorbent reactivity, which can eventually offer stable CO₂ capture over extended numbers of cycles.

A simple predictive method was introduced to estimate the sorbent utilization of lime-based sorbents at different calcination-carbonation cycles, calcination temperatures, and extents. The predictive method worked well with various testing procedures, including a unique experimental design at which duration of limestone calcination was varied frequently over successive

calcination-carbonation cycles. The model parameters were observed to be significantly dependent on different factors, including calcination and carbonation temperatures.

A novel limestone calcination technology was proposed (referred as MRC-CAL process) which combines methane reforming, combustion, and limestone calcination in a single reactor. This process is shown to be capable of autothermal limestone calcination with *in situ* CO₂ utilization. Thermodynamic analysis revealed that the required methane feed (CH₄ + enriched-air) concentration for autothermal MRC-CAL operation significantly decreases as the CaCO₃/gas molar feed ratio increases. On the other hand, variation of temperature and pressure, upon complete and coke-free limestone calcination, had negligible impacts on the process thermal behaviour. An empirical correlation was developed to estimate the required gaseous feed concentrations for autothermal MRC-CAL operations. Extensive simulation tests were then employed to determine the required conditions (temperature, pressure, CaCO₃/gas molar feed ratio) for complete and coke-free limestone calcination by this novel sorbent regeneration technology. It was shown that increasing temperature expands the appropriate range of CaCO₃/gas molar feed ratios, whereas elevating pressure resulted in opposite behaviour.

An axially dispersed plug flow reactor model was applied to evaluate the performance of the MRC-CAL process in turbulent fluidized bed reactors. Turbulent fluidization regime was selected owing to its excellent gas-solid contact and high solids hold-up. It was observed that increasing temperature and sorbent residence time enhance the limestone calcination, whereas elevating pressure and CaCO₃/gas molar feed ratio resulted in opposite behaviour. A sorbent residence time of 5-10 minutes was found to be optimal, with further increases in reactor length barely enhancing the sorbent conversion. Extensive simulation runs were employed to obtain a simple design methodology for MRC-CAL units operating at 800-900°C and 1-5 bars pressure.

The proposed method can be further used for preliminary design of MRC-CAL sorbent regenerators for calcium looping systems. Note that the reactor diameter in this work is selected based on small-scale fluidized bed reactors (e.g. up to 0.1 m diameter). Although variation of reactor size can potentially alter the fluidization hydrodynamics, it is not likely to affect the overall conclusions (e.g. trends) obtained from simulation results.

The MRC-CAL process was found to offer faster sorbent regeneration than those for limestone calcination in non-CO₂ gases (e.g. steam and air). This is attributed to *in situ* CO₂ utilization capability of the process, enhancing the rate of limestone calcination by reducing the CO₂ concentration within the reactor. Therefore, lower calcination temperatures than those in currently developed technologies (e.g. limestone calcination in inert gases, steam, CO₂, and oxy-fuel feedstock) are required by the MRC-CAL process, especially at high sorbent conversions. This can potentially offer pressurized limestone calcination at temperatures <900°C, which are attractive for industrial applications.

Another promising feature of the MRC-CAL process is its ability to co-generate syngas (mainly H₂ and CO) as a valuable byproduct. Thermodynamic analysis showed that the process hydrogen yield is nearly insensitive to the reactor pressure and temperature, unless the critical limits for coke-free and complete limestone calcination are exceeded. Similarly, kinetic simulations revealed that the hydrogen yield of the MRC-CAL process depends mainly on the CaCO₃/total gas molar feed ratio and the sorbent conversion, with increases in both reducing the hydrogen yield.

The MRC-CAL technology could be highly attractive for industrial processes related to calcium-looping. This thesis presented a series of simulation studies for three possible applications, while

there are several other processes (e.g. fuel reactors, cement industry, and power generation) which could potentially be integrated with this novel sorbent regeneration technology:

1) Sorbent-enhanced steam methane reforming:

A kinetic reactor model was employed to investigate the effect of different operating conditions on the performance of sorbent-enhanced steam methane reforming in isothermal turbulent fluidized bed reactor. It was observed that increasing the sorbent/methane molar feed ratio and decreasing the methane feed concentration can enhance the methane conversion, hydrogen yield and product purity of the steam methane reformers. The reformer performance also depends strongly on the system pressure, with higher temperatures required for pressurized operation. *In situ* hydrogen removal by Pd-based membranes was also shown to enhance the methane conversion and hydrogen production yield, while reducing the hydrogen concentration in the reformer off-gas. A predictive model was used to determine and compare the operating conditions required for sorbent regeneration *via* steam and MRC-CAL sorbent regenerators. The reformer integrated with the MRC-CAL process was shown to benefit from lower calcination temperatures, higher overall hydrogen yield and lower CO₂ emissions.

2) Ca(OH)₂/CaCO₃ co-calcination in a three-stage calcium looping system:

A novel lime hydration configuration was proposed, utilizing saturated steam as the sorbent reactivating reagent and direct-heat-removal medium. Thermodynamic analysis showed that the proposed hydrator configuration can generate a substantial amount of superheated steam, for use elsewhere as required. The equilibrium performance of the MRC-CAL was evaluated when slaked lime (Ca(OH)₂) and limestone (CaCO₃) were to be calcined simultaneously in a single reactor. It was shown that increasing the slaked lime fraction in the solid feed increases the

required methane feed concentration for autothermal reactor operation. Higher slaked lime fraction in the solid feed also led to higher hydrogen yield, less CO generation, and expanded range of solid/gas molar feed ratios for coke-free and complete sorbent regeneration using this novel sorbent regeneration technology.

3) Ammonia synthesis without air separation:

The thermodynamics and kinetic performance of air/fuel MRC-CAL reactors were simulated at various operating conditions. A single correlation was proposed to estimate the required gaseous feed concentrations for nearly autothermal reactor operation at different reactor temperatures, pressures, feed ratios, and air oxygen concentrations. The process syngas was shown to be mainly composed of H₂, CO, and N₂, which can be further used (after a number of downstream post-treatments, e.g. water-gas shift reactor) for ammonia synthesis, without an expensive air separation unit. Increasing the air nitrogen concentration was observed to enhance the feedstock (limestone and methane) conversion, while also expanding the applicable range of CaCO₃/CH₄ molar feed ratios for autothermal, coke-free and complete sorbent regeneration. Kinetic reactor modelling confirmed the capability of the airfuel MRC-CAL process for appreciable limestone calcination at elevated reactor pressures (up to 25 bars) and at practical temperatures (<900°C). Moderate air oxygen concentrations (e.g. 40 vol% O₂) and relatively low CaCO₃/CH₄ molar feed ratios (e.g. 0.2-0.3) were found to be needed to achieve the syngas quality (H₂/N₂ = 3) required for ammonia synthesis by the MRC-CAL reactor.

8.2. Recommendations

Given the novelty of concepts presented in this thesis, significant scope remains for expanding the current knowledge through future research. Potential topics for future studies include:

- 1) Previous works have shown that the performance of lime-based sorbents depends strongly on the sorbent particle size, impurities, morphology, and porous structure. The effect of partial limestone calcination was studied in this thesis for two different naturally-derived lime-based sorbents (Strassburg and Cadomin). Future work should consider evaluating the performance of other natural and/or synthetic lime-based sorbents under partial calcination conditions, elucidating the effects of various sorbent characteristics on the carbon capture performance.
- 2) Given the promising performance of partially calcined sorbents in TGA environments, it would be of interest to evaluate their feasibility and limitations under more realistic conditions, especially in fluidized bed reactors. Note that a precise measurement of CO₂ concentration (at the reactor inlet and outlet) is imperative to determine the rate and extent of sorbent carbonation/calcination in fluidized bed reactors.
- 3) Partial limestone calcination can potentially reduce the sorbent CO₂ uptake in the first few calcination-carbonation cycles. On the other hand, incomplete limestone calcination can be achieved at milder reactor temperatures, which can eventually enhance the sorbent performance for extended cycles. Future studies may focus on optimizing the calciner operating conditions (e.g. temperature and duration), as well as developing simple carbonation and calcination kinetic models for reactor simulation.
- 4) The kinetic of MRC-CAL process was simulated in this work based on isothermal steady-state turbulent fluidized bed reactors. However, this process combines several endothermic and exothermic reactions, which may cause temperature variation along the bed height. Future works should consider non-isothermal and unsteady simulations of the

process in different fluidization flow regimes (e.g. bubbling and fast fluidization). Computational Fluid Dynamic (CFD) simulation could also be of interest in order to assess the reactor hydrodynamics, productivity, and thermal behaviour.

- 5) The simulation results in this thesis showed that the MRC-CAL process is capable of co-producing lime and syngas in a single reactor. The syngas was shown to be mainly composed of H_2 and CO , as well as some minor constituents of H_2O and CO_2 . Previous studies have shown that the calcination gaseous medium can significantly affect the pore sintering and cyclic carbon capture capability of lime-based sorbents. Future experimental studies should consider investigating the cyclic performance of lime-based sorbents when limestone calcination occurs in a syngas medium.

- 6) The MRC-CAL process was evaluated in this thesis based on thermodynamic and kinetic simulations. However, there might be several factors affecting the system performance/feasibility under practical conditions. Future studies may consider laboratory testing the MRC-CAL process, preferably in small-scale fluidized bed reactors. This also enables verifying the simulation results presented in this work, as well as improving the applied reactor model. Note that this process utilizes methane-concentrated oxyfuel feedstock, which can surpass the methane explosion limit in some circumstances. This can be potentially alleviated if air is used as the source of oxygen, as proposed in Chapter 7 for ammonia synthesis without an air separation. Specific process design and safety regulations must be then taken into account if the process is to be tested experimentally in the future.

- 7) The MRC-CAL process combines three major reactions of methane combustion, methane reforming, and limestone calcination in a single reactor. This complicates performance analysis in early experimental stages. Alternatively, one can split the process into partial methane oxidation and limestone calcination (in presence of syngas), evaluating each individually to reduce the system complexity and facilitate data interpretation. An additional CO₂ stream can be then used to virtually consider the effect of CO₂ release by limestone calcination in partial methane oxidation tests. Partial methane oxidation tests can be conducted in lab-scale fluidized bed reactors, investigating various aspects such as reactor performance (e.g. methane conversion and H₂ yield), fluidization hydrodynamic, and particle segregation/agglomeration/attrition. Fluidized bed reactors can be also used to experimentally study the effect of *in situ* CO₂ utilization on the rate of limestone calcination in a syngas medium. Note that the latter requires reforming catalyst along with limestone particles, ensuring rapid reverse water-gas shift reaction inside the reactor. Thermogravimetric analysis can be employed to investigate the sorbent cyclic carbon capture when limestone calcination is conducted in presence of syngas.
- 8) It was shown in this thesis that the MRC-CAL process can offer relatively high methane conversion, especially at elevated temperatures, reduced pressures, and high CaCO₃/total gas molar feed ratios. This is promising since methane is itself a potent greenhouse gas. Note that methane leakage, even at small extents, could be a significant challenge in practical MRC-CAL processes. Future studies should consider total GHG emissions and comprehensive life cycle analysis to assess and compare the environmental impacts of the MRC-CAL process to those of other related processes.

- 9) A pure methane feedstock was assumed in this work to simplify the evaluation of MRC-CAL process. However, practical applications would use natural gas, containing minor constituents of H₂S, ethane, CO₂, and other trace gases. Future studies should consider the effect of these natural gas impurities on the long-term performance of the MRC-CAL process, including reactor thermal behaviour and off-gas composition, as well as calcined limestone reactivity toward CO₂.
- 10) A highly-concentrated hydrogen stream can be produced if hydrogen perm-selective membranes are installed inside the MRC-CAL reactor. However, currently developed membrane materials are incapable of sustained hydrogen removal at elevated temperatures (e.g. 800-900°C). Future studies are needed to develop novel metallic membranes for high-temperature hydrogen separation, including from MRC-CAL reactors.
- 11) This work assumed Ni-based reforming catalyst for kinetic simulation of the MRC-CAL process. However, there are several other advanced reforming catalysts, especially for high temperature operation. Note that Ni-based reforming catalyst may encounter stability issues at temperatures above 800°C. Future work should consider screening and/or developing novel catalysts, applicable for methane reforming at MRC-CAL conditions.
- 12) A novel three-stage calcium-looping process was introduced in Chapter 6 based on thermodynamic analysis. This process co-utilizes steam as sorbent reactivation reagent and direct heat-removal medium. Future studies should consider evaluating the feasibility of this process under practical conditions.

13) The MRC-CAL process was thermodynamically analyzed for co-calcining limestone and slaked lime in a single reactor. This reactor configuration requires appreciable hydration and reactivation of partially carbonated sorbents in a timely manner. Future studies should consider assessing the efficiency of steam reactivation for partially carbonated, partially calcined, and totally calcined lime-based sorbents.

14) Several novel concepts were introduced in this thesis, including partial limestone calcination, MRC-CAL technology, and a three-stage calcium-looping process. Experimental and simulation analyses confirmed the promising performance of these processes under certain circumstances. Future works should consider techno-economic analysis of these technologies, including their exergy analysis, industrial costs and long-term revenue. Particular attentions must also be paid to safe operation of these processes, especially for the MRC-CAL technology.

Bibliography

- [1] Doremus H, Hanemann WM. Of babies and bathwater: Why the clean air act's cooperative federalism framework is useful for addressing global warming. *Ariz Law Rev* 2008;50:799.
- [2] Yang H, Xu Z, Fan M, Gupta R, Slimane RB, Bland AE, Wright I. Progress in carbon dioxide separation and capture: A review. *J Environ Sci* 2008;20:14–27. doi:10.1016/S1001-0742(08)60002-9.
- [3] Stanmore BR, Gilot P. Review-calcination and carbonation of limestone during thermal cycling for CO₂ sequestration. *Fuel Process Technol* 2005;86:1707–43. doi:10.1016/j.fuproc.2005.01.023.
- [4] Salaudeen SA, Acharya B, Dutta A. CaO-based CO₂ sorbents: A review on screening, enhancement, cyclic stability, regeneration and kinetics modelling. *J CO₂ Util* 2018;23:179–99. doi:10.1016/j.jcou.2017.11.012.
- [5] IEA. World Energy Balances 2019. <https://www.iea.org/subscribe-to-data-services/world-energy-balances-and-statistics>.
- [6] Zhao X, Ji G, Liu W, He X, Anthony EJ, Zhao M. Mesoporous MgO promoted with NaNO₃/NaNO₂ for rapid and high-capacity CO₂ capture at moderate temperatures. *Chem Eng J* 2018;332:216–26. doi:10.1016/j.cej.2017.09.068.
- [7] Owusu PA, Asumadu-Sarkodie S. A review of renewable energy sources, sustainability issues and climate change mitigation. *Cogent Eng* 2016;3:1–14. doi:10.1080/23311916.2016.1167990.
- [8] Avsec J. The production and use of hydrogen in the future. *AIP Conf. Proc.*, vol. 1866,

- 2017, p. 030001-1-030001–8. doi:10.1063/1.4994477.
- [9] Mahecha-Botero A, Chen Z, Grace JR, Elnashaie SSEH, Lim CJ, Rakib M, Yasuda I, Shirasaki Y. Comparison of fluidized bed flow regimes for steam methane reforming in membrane reactors: A simulation study. *Chem Eng Sci* 2009;64:3598–613. doi:10.1016/j.ces.2009.04.044.
- [10] Broda M, Manovic V, Imtiaz Q, Kierzkowska AM, Anthony EJ, Müller CR. High-purity hydrogen *via* the sorption-enhanced steam methane reforming reaction over a synthetic CaO-based sorbent and a Ni catalyst. *Environ Sci Technol* 2013;47:6007–14. doi:10.1021/es305113p.
- [11] Rakib M. Fluidized bed membrane reactor for steam reforming of higher hydrocarbons. University of British Columbia, Ph.D. Thesis, 2010.
- [12] Johnsen K. Sorption-enhanced steam methane reforming in fluidized bed reactors. Norwegian University of Science and Technology, Ph.D. Thesis, 2006.
- [13] International Energy Agency (IEA). The future of hydrogen. 2019.
- [14] Dincer I, Acar C. Review and evaluation of hydrogen production methods for better sustainability. *Int J Hydrogen Energy* 2015;40:11094–111. doi:10.1016/j.ijhydene.2014.12.035.
- [15] Johnsen K, Ryu HJ, Grace JR, Lim CJ. Sorption-enhanced steam reforming of methane in a fluidized bed reactor with dolomite as CO₂-acceptor. *Chem Eng Sci* 2006;61:1195–202. doi:10.1016/j.ces.2005.08.022.
- [16] Adris AEM. A fluidized bed membrane reactor for steam methane reforming: Experimental varification and model validation. University of British Columbia, Ph.D. Thesis, 1994.

- [17] Chen Y, Mahecha-Botero A, Lim CJ, Grace JR, Zhang J, Zhao Y, Zheng C. Hydrogen production in a sorption-enhanced fluidized-bed membrane reactor: Operating parameter investigation. *Ind Eng Chem Res* 2014;53:6230–42. doi:10.1021/ie500294k.
- [18] Li ZS, Cai NS. Modeling of multiple cycles for sorption-enhanced steam methane reforming and sorbent regeneration in fixed bed reactor. *Energy and Fuels* 2007;21:2909–18. doi:10.1021/ef070112c.
- [19] Grace J, Elnashaie SSEH, Lim J. Hydrogen production in fluidized beds with *in-situ* membranes. *Int J Chem React Eng* 2005;3:1–17. doi:10.2202/1542-6580.1303.
- [20] Anderson DM, Nasr MH, Yun TM, Kottke PA, Fedorov AG. Sorption-enhanced variable-volume batch-membrane steam methane reforming at low temperature: Experimental demonstration and kinetic modeling. *Ind Eng Chem Res* 2015;54:8422–36. doi:10.1021/acs.iecr.5b01879.
- [21] Moon S, Xu N, Su S, Li A, Grace JR, Lim CJ, Boyd T, Ryi S, Susdorf A, Schaadt A. Palladium/Ruthenium composite membrane for hydrogen separation from the off-gas of solar cell production *via* chemical vapor deposition. *J Memb Sci* 2017;541:1–8. doi:10.1016/j.memsci.2017.06.093.
- [22] Leimert JM, Karl J. Nickel membranes for *in-situ* hydrogen separation in high-temperature fluidized bed gasification processes. *Int J Hydrogen Energy* 2016;41:9355–66. doi:10.1016/j.ijhydene.2016.04.073.
- [23] Uemiya S. Brief review of steam reforming using a metal membrane reactor. *Top Catal* 2004;29:79–84. doi:https://doi.org/10.1023/B:TOCA.0000024930.45680.c7.
- [24] Ryi S, Li A, Lim CJ, Grace JR. Novel non-alloy Ru/Pd composite membrane fabricated by electroless plating for hydrogen separation. *Int J Hydrogen Energy* 2010;36:9335–40.

- doi:10.1016/j.ijhydene.2010.06.014.
- [25] Adris AM, Lim CJ, Grace JR. The fluidized-bed membrane reactor for steam methane reforming: Model verification and parametric study. *Chem Eng Sci* 1997;52:1609–22. doi:10.1016/S0009-2509(96)00511-8.
- [26] Chen Z, Po F, Grace JR, Jim Lim C, Elnashaie SSEH, Mahecha-Botero A, Rakib M, Shirasaki Y, Yasuda I. Sorbent-enhanced/membrane-assisted steam-methane reforming. *Chem Eng Sci* 2008;63:170–82. doi:10.1016/j.ces.2007.09.031.
- [27] Deshmukh SARK, Heinrich S, Mörl L, van Sint Annaland M, Kuipers JAM. Membrane assisted fluidized bed reactors: Potentials and hurdles. *Chem Eng Sci* 2007;62:416–36. doi:10.1016/j.ces.2006.08.062.
- [28] Arratibel Plazaola A, Tanaka P, Van Sint Annaland M, Gallucci F. Recent advances in Pd-based membranes for membrane reactors. *Molecules* 2017;22:1–53. doi:10.3390/molecules22010051.
- [29] Antonio J, Fernandez E, Melendez J, Parco M, Alfredo D, Tanaka P, van Sint Annaland M, Gallucci F. Pd-based metallic supported membranes : High- temperature stability and fluidized bed reactor testing. *Int J Hydrogen Energy* 2015;41:8706–18. doi:10.1016/j.ijhydene.2015.10.094.
- [30] Nayebossadri S, Fletcher S, Speight J, Book D. Hydrogen permeation through porous stainless steel for Palladium– based composite porous membranes. *Res Rev J Mater Sci* 2016;4:29–35.
- [31] Leimert JM, Karl J, Dillig M. Dry reforming of methane using a nickel membrane reactor. *Processes* 2017;5:1–13. doi:10.3390/pr5040082.
- [32] Wang M, Song J, Li Y, Tan X. Hydrogen separation at elevated temperatures using

- metallic Nickel hollow fiber membranes. *AIChE* 2017;63:3026–34. doi:10.1002/aic.
- [33] Park CY, Lee TH, Dorris SE, Balachandran UB. Palladium based film-type cermet membranes for hydrogen separation. *J Mater Chem* 2012;22:4904–9. doi:10.1039/c2jm14741f.
- [34] Balachandran UB, Lee TH, Park CY, Emerson JE, Picciolo JJ, Dorris SE. Dense cermet membranes for hydrogen separation. *Sep Purif Technol* 2014;121:54–9. doi:10.1016/j.seppur.2013.10.001.
- [35] Rothenberger KS, Howard BH, Cugini A V, Enick RM, Bustamante F, Ciocco M V, Morreale BD, Buxbaum RE. Tantalum-based membrane materials at elevated temperature and pressure. *Fuel Chem Div Prepr* 2002;47:814–5.
- [36] Li Y, Zhang M, Chu Y, Tan X. Design of metallic nickel hollow fiber membrane modules for pure hydrogen separation. *AIChE* 2018;64:3662–70. doi:10.1002/aic.16332.
- [37] Butler JW. Limestone as a sorbent for CO₂ capture and its application in enhanced biomass gasification. University of British Columbia, Ph.D. Thesis, 2013.
- [38] Hejazi B. Modeling of biomass steam gasification in a dual fluidized bed reactor with/without lime-based CO₂ capture. University of British Columbia, Ph.D. Thesis, 2017.
- [39] Kim JY, Ellis N, Lim CJ, Grace JR. Attrition of binary mixtures of solids in a jet attrition unit. *Powder Technol* 2019;352:445–52. doi:10.1016/j.powtec.2019.05.010.
- [40] Hejazi B, Grace JR, Bi X, Mahecha-Botero A. Steam gasification of biomass coupled with lime-based CO₂ capture in a dual fluidized bed reactor: A modeling study. *Fuel* 2014;117:1256–66. doi:10.1016/j.fuel.2013.07.083.
- [41] Johnsen K, Grace JR, Elnashaie SSEH, Kolbeinsen L, Eriksen D. Modeling of sorption-enhanced steam reforming in a dual fluidized bubbling bed reactor. *Ind Eng Chem Res*

- 2006;45:4133–44. doi:10.1021/ie0511736.
- [42] Manovic V, Anthony EJ. Lime-based sorbents for high-temperature CO₂ capture-A review of sorbent modification methods. *Int J Environ Res Public Health* 2010;7:3129–40. doi:10.3390/ijerph7083129.
- [43] Chen Z, Song HS, Portillo M, Lim CJ, Grace JR, Anthony EJ. Long-term calcination/carbonation cycling and thermal pretreatment for CO₂ capture by limestone and dolomite. *Energy and Fuels* 2009;23:1437–44. doi:10.1021/ef800779k.
- [44] Abanades JC. The maximum capture efficiency of CO₂ using a carbonation/calcination cycle of CaO/CaCO₃. *Chem Eng J* 2002;90:303–6. doi:10.1016/S1385-8947(02)00126-2.
- [45] Manovic V, Charland JP, Blamey J, Fennell PS, Lu DY, Anthony EJ. Influence of calcination conditions on carrying capacity of CaO-based sorbent in CO₂ looping cycles. *Fuel* 2009;88:1893–900. doi:10.1016/j.fuel.2009.04.012.
- [46] Sun P, Lim CJ, Grace JR. Cyclic CO₂ capture by limestone-derived sorbent during prolonged calcination/carbonation cycling. *AIChE J* 2008;54:1668–77. doi:10.1002/aic.
- [47] Sun P, Grace JR, Lim CJ, Anthony EJ. The effect of CaO sintering on cyclic CO₂ capture in energy systems. *AIChE J* 2007;53:2432–42. doi:10.1002/aic.11251.
- [48] Sun P, Grace JR, Lim CJ, Anthony EJ. Investigation of attempts to improve cyclic CO₂ capture by sorbent hydration and modification. *Ind Eng Chem Res* 2008;47:2024–32. doi:10.1021/ie070335q.
- [49] Chowdhury MBI, Quddus MR, DeLasa HI. CO₂ capture with a novel solid fluidizable sorbent: Thermodynamics and temperature programmed carbonation-decarbonation. *Chem Eng J* 2013;232:139–48. doi:10.1016/j.cej.2013.07.044.
- [50] Al-Jeboori MJ, Nguyen M, Dean C, Fennell PS. Improvement of limestone-based CO₂

- sorbents for Ca looping by HBr and other mineral acids. *Ind Eng Chem Res* 2013;52:1426–33. doi:10.1021/ie302198g.
- [51] Grasa GS, Abanades JC. CO₂ capture capacity of CaO in long series of carbonation/calcination cycles. *Ind Eng Chem Res* 2006;45:8846–51. doi:10.1021/ie0606946.
- [52] Manovic V, Anthony EJ. Parametric study on the CO₂ capture capacity of CaO-based sorbents in looping cycles. *Energy and Fuels* 2008;22:1851–7. doi:10.1021/ef800011z.
- [53] Borgwardt RH. Calcium oxide sintering in atmospheres containing water and carbon dioxide. *Ind Eng Chem Res* 1989;28:493–500. doi:10.1021/ie00088a019.
- [54] Fuertes AB, Alvarez A, Rubiera F, Pis JJ, Marban G, Palacios JM. Surface area and pore size changes during sintering of calcium oxide particles. *Chem Eng Commun* 1991. doi:10.1080/00986449108910974.
- [55] Manovic V, Anthony EJ. Carbonation of CaO-based sorbents enhanced by steam addition. *Ind Eng Chem Res* 2010;49:9105–10. doi:10.1021/ie101352s.
- [56] Ramkumar S, Fan LS. Thermodynamic and experimental analyses of the three-stage calcium looping process. *Ind Eng Chem Res* 2010;49:7563–73. doi:10.1021/ie100846u.
- [57] Blamey J, Anthony EJ, Wang J, Fennell PS. The calcium looping cycle for large-scale CO₂ capture. *Prog Energy Combust Sci* 2010;36:260–79. doi:10.1016/j.pecs.2009.10.001.
- [58] Valverde JM, Medina S. Limestone calcination under calcium-looping conditions for CO₂ capture and thermochemical energy storage in the presence of H₂O: An *in situ* XRD analysis. *Phys Chem Chem Phys* 2017;19:7587–96. doi:10.1039/c7cp00260b.
- [59] Symonds RT, Lu DY, Macchi A, Hughes RW, Anthony EJ. The effect of HCl and steam on cyclic CO₂ capture performance in calcium looping systems. *Chem Eng Sci* 2017.

- doi:10.1016/j.ces.2017.08.019.
- [60] Yan CF, Grace JR, Lim CJ. Effects of rapid calcination on properties of calcium-based sorbents. *Fuel Process Technol* 2010;91:1678–86. doi:10.1016/j.fuproc.2010.07.004.
- [61] Yu FC, Fan LS. Kinetic study of high-pressure carbonation reaction of calcium-based sorbents in the calcium looping process (CLP). *Ind Eng Chem Res* 2011;50:11528–36. doi:10.1021/ie200914e.
- [62] Basu P, Achayra B, Dutta A. Study of calcination-carbonation of calcium carbonate in different fluidizing mediums for chemical looping gasification in circulating fluidized beds. 10th Int. Conf. Circ. Fluid. Beds Fluid. Technol., 2013. doi:https://doi.org/10.1016/j.ces.2017.08.019.
- [63] Kaljuvee T, Trikkel A, Kuusik R. Decarbonization of natural lime-containing materials and reactivity of calcined products towards SO₂ and CO₂. *J Therm Anal Calorim* 2001;64:1229–40.
- [64] Ar I, Dogu G. Calcination kinetics of high purity limestones. *Chem Eng J* 2001;83:131–7.
- [65] Gupta H, Fan LS. Carbonation-calcination cycle using high reactivity calcium oxide for carbon dioxide separation from flue gas. *Ind Eng Chem Res* 2002;41:4035–42. doi:10.1021/ie010867l.
- [66] Fennell PS, Pacciani R, Dennis JS, Davidson JF, Hayhurst AN. The effects of repeated cycles of calcination and carbonation on a variety of different limestones, as measured in a hot fluidized bed of sand. *Energy and Fuels* 2007;21:2072–81. doi:10.1021/ef060506o.
- [67] Escardino A, García-Ten J, Feliu C, Saburit A, Cantavella V. Kinetic study of the thermal decomposition process of calcite particles in air and CO₂ atmosphere. *J Ind Eng Chem* 2013;19:886–97. doi:10.1016/j.jiec.2012.11.004.

- [68] Valverde JM, Sanchez-Jimenez PE, Perez-Maqueda LA. Limestone calcination nearby equilibrium: Kinetics, CaO crystal structure, sintering and reactivity. *J Phys Chem C* 2015;119:1623–41. doi:10.1021/jp508745u.
- [69] Ebneyamini A, Grace J, Ellis N, Lim CJ. Toward autothermal and hydrogen-producing sorbent regeneration for calcium-looping. *Can J Chem Eng* 2020.
- [70] Valverde JM, Miranda-Pizarro J, Perejón A, Sánchez-Jiménez PE, Pérez-Maqueda LA. Calcium-Looping performance of steel and blast furnace slags for thermochemical energy storage in concentrated solar power plants. *J CO₂ Util* 2017;22:143–54. doi:10.1016/j.jcou.2017.09.021.
- [71] Ortiz C, Chacartegui R, Valverde JM, Alovísio A, Becerra JA. Power cycles integration in concentrated solar power plants with energy storage based on calcium looping. *Energy Convers Manag* 2017;149:815–29. doi:10.1016/j.enconman.2017.03.029.
- [72] Manovic V, Anthony EJ. Integration of calcium and chemical looping combustion using composite CaO/CuO-based materials. *Environ Sci Technol* 2011;45:10750–6. doi:10.1021/es202292c.
- [73] Abanades JC, Murillo R, Fernandez JR, Grasa G, Martínez I. New CO₂ capture process for hydrogen production combining Ca and Cu chemical loops. *Environ Sci Technol* 2010;44:6901–4. doi:10.1021/es101707t.
- [74] Antzara A, Heracleous E, Bukur DB, Lemonidou AA. Thermodynamic analysis of hydrogen production via chemical looping steam methane reforming coupled with *in situ* CO₂ capture. *Energy Procedia* 2014;63:6576–89. doi:10.1016/j.egypro.2014.11.694.
- [75] Lyon RK, Cole JA. Unmixed combustion: An alternative to fire. *Combust Flame* 2000;121:249–61. doi:10.1016/S0010-2180(99)00136-4.

- [76] Perry, R.H., Green DW. Perry's Chemical Engineers' Handbook (8th rev. ed.). 2004. doi:10.1036/0071511245.
- [77] Acharya B, Dutta A, Basu P. Chemical-looping gasification of biomass for hydrogen-enriched gas. *Energy and Fuels* 2009;23:5077–83. doi:10.1021/ef9003889.
- [78] Garcia-Labiano F, Abad A, de Diego LF, Gayan P, Adanez J. Calcination of calcium-based sorbents at pressure in a broad range of CO₂ concentrations. *Chem Eng Sci* 2002;57:2381–93.
- [79] Wang Y, Lin S, Suzuki Y. Limestone calcination with CO₂ capture (II): Decomposition in CO₂/steam and CO₂/N₂ atmospheres. *Energy & Fuels* 2008:2326–31.
- [80] Wang C, Chen L. The effect of steam on simultaneous calcination and sulfation of limestone in CFBB. *Fuel* 2016;175:164–71. doi:10.1016/j.fuel.2016.02.028.
- [81] Wang Y, Thomson WJ. The effects of steam and carbon dioxide on calcite decomposition using dynamic X-ray diffraction. *Chem Eng Sci* 1995;50:1373–82. doi:10.1016/0009-2509(95)00002-M.
- [82] Giammaria G, Lefferts L. Catalytic effect of water on calcium carbonate decomposition. *J CO₂ Util* 2019;33:341–56. doi:10.1016/j.jcou.2019.06.017.
- [83] Coppola A, Allocca M, Montagnaro F, Scala F, Salatino P. The effect of steam on CO₂ uptake and sorbent attrition in fluidised bed calcium looping: The influence of process conditions and sorbent properties. *Sep Purif Technol* 2017;189:101–7. doi:10.1016/j.seppur.2017.08.001.
- [84] Rong N, Wang Q, Fang M, Cheng L, Luo Z, Cen K. Steam hydration reactivation of CaO-based sorbent in cyclic carbonation/calcination for CO₂ capture. *Energy and Fuels* 2013;27:5332–40. doi:10.1021/ef4007214.

- [85] Donat F, Florin NH, Anthony EJ, Fennell PS. Influence of high-temperature steam on the reactivity of CaO sorbent for CO₂ capture. *Environ Sci Technol* 2012;46:1262–9. doi:10.1021/es202679w.
- [86] Champagne S, Lu DY, MacChi A, Symonds RT, Anthony EJ. Influence of steam injection during calcination on the reactivity of CaO-based sorbent for carbon capture. *Ind Eng Chem Res* 2013;52:2241–6. doi:10.1021/ie3012787.
- [87] Chou YC, Cheng JY, Liu WH, Hsu HW. Effects of steam addition during calcination on carbonation behavior in a calcination/carbonation loop. *Chem Eng Technol* 2018;41:1921–7. doi:10.1002/ceat.201800133.
- [88] Reller A, Padeste C, Hug P. Formation of organic carbon compounds from metal carbonates 1987:55–6.
- [89] Jagadeesan D, Eswaramoorthy M, Rao CNR. Investigations of the conversion of inorganic carbonates to methane. *ChemSusChem* 2009;2:878–82. doi:10.1002/cssc.200900152.
- [90] Jagadeesan D, Sundarayya Y, Madras G, Rao CNR. Direct conversion of calcium carbonate to C1-C3 hydrocarbons. *RSC Adv* 2013;3:7224–9. doi:10.1039/c3ra40264a.
- [91] Belete TT, Van De Sanden MCM, Gleeson MA. Effects of transition metal dopants on the calcination of CaCO₃ under Ar, H₂O and H₂. *J CO₂ Util* 2019;31:152–66. doi:10.1016/j.jcou.2019.03.006.
- [92] Nikulshina V, Halmann M, Steinfeld A. Coproduction of syngas and lime by combined CaCO₃-calcination and CH₄-reforming using a particle-flow reactor driven by concentrated solar radiation. *Energy and Fuels* 2009;23:6207–12. doi:10.1021/ef9007246.
- [93] Kim SM, Abdala PM, Broda M, Hosseini D, Copéret C, Müller C. Integrated CO₂ capture and conversion as an efficient process for fuels from greenhouse gases. *ACS Catal*

- 2018;8:2815–23. doi:10.1021/acscatal.7b03063.
- [94] Dang C, Wu S, Cao Y, Wang H, Peng F, Yu H. Co-production of high quality hydrogen and synthesis gas *via* sorption-enhanced steam reforming of glycerol coupled with methane reforming of carbonates. *Chem Eng J* 2019;47–53. doi:10.1016/j.cej.2018.11.203.
- [95] Benguerba Y, Dehimi L, Virginie M, Dumas C, Ernst B. Numerical investigation of the optimal operative conditions for the dry reforming reaction in a fixed-bed reactor: Role of the carbon deposition and gasification reactions. *React Kinet Mech Catal* 2015;115:483–97. doi:10.1007/s11144-015-0849-9.
- [96] Dang C, Wu S, Yang G, Cao Y, Wang H, Peng F, Yu H. Syngas production by dry reforming of the mixture of glycerol and ethanol with CaCO_3 . *J Energy Chem* 2020;43:90–7. doi:10.1016/j.jechem.2019.08.002.
- [97] Wang W, Wang Y. Dry reforming of ethanol for hydrogen production: Thermodynamic investigation. *Int J Hydrogen Energy* 2009;34:5382–9. doi:10.1016/j.ijhydene.2009.04.054.
- [98] Martínez I, Grasa G, Murillo R, Arias B, Abanades JC. Modelling the continuous calcination of CaCO_3 in a Ca-looping system. *Chem Eng J* 2013;215–216:174–81. doi:10.1016/j.cej.2012.09.134.
- [99] Abanades JC, Grasa G, Alonso M, Rodriguez N, Anthony EJ, Romeo LM. Cost structure of a postcombustion CO_2 capture system using CaO . *Environ Sci Technol* 2007;41:5523–7. doi:10.1021/es070099a.
- [100] Shimizu T, Hiramata T, Hosoda H, Kitano K, Inagaki M, Tejima K. A twin fluid-bed reactor for removal of CO_2 from combustion processes. *Chem Eng Res Des* 1999;77:62–8.

doi:10.1205/026387699525882.

- [101] Lin S, Kiga T, Wang Y, Nakayama K. Energy analysis of CaCO₃ calcination with CO₂ capture. *Energy Procedia*, vol. 4, Elsevier Ltd; 2011, p. 356–61. doi:10.1016/j.egypro.2011.01.062.
- [102] Abanades JC, Anthony EJ, Wang J, Oakey JE. Fluidized bed combustion systems integrating CO₂ capture with CaO. *Environ Sci Technol* 2005;39:2861–6. doi:10.1021/es0496221.
- [103] Champagne S, Lu DY, Symonds RT, Macchi A, Anthony EJ. The effect of steam addition to the calciner in a calcium looping pilot plant. *Powder Technol* 2016;290:114–23. doi:10.1016/j.powtec.2015.07.039.
- [104] Sánchez-Biezma A, Paniagua J, Diaz L, Lorenzo M, Alvarez J, Martínez D, Arias B, Diego ME, Abanades JC. Testing postcombustion CO₂ capture with CaO in a 1.7 MWt pilot facility. *Energy Procedia*, vol. 37, Elsevier Ltd; 2013, p. 1–8. doi:10.1016/j.egypro.2013.05.078.
- [105] Erans M, Nabavi SA, Manović V. Pilot-scale calcination of limestone in steam-rich gas for direct air capture. *Energy Convers Manag X* 2019;1. doi:10.1016/j.ecmx.2019.100007.
- [106] Erans M, Jeremias M, Zheng L, Yao JG, Blamey J, Manovic V, Fennell PS, Anthony EJ. Pilot testing of enhanced sorbents for calcium looping with cement production. *Appl Energy* 2018;225:392–401. doi:10.1016/j.apenergy.2018.05.039.
- [107] Eriksson M, Hökfors B, Backman R. Oxyfuel combustion in rotary kiln lime production. *Energy Sci Eng* 2014;2:204–15. doi:10.1002/ese3.40.
- [108] Martínez A, Lara Y, Lisbona P, Romeo LM. Energy penalty reduction in the calcium looping cycle. *Int J Greenh Gas Control* 2012;7:74–81. doi:10.1016/j.ijggc.2011.12.005.

- [109] Romano MC, Martínez I, Murillo R, Arstad B, Blom R, Ozcan DC, Ahn H, Brandani S. Process simulation of Ca-looping processes: Review and guidelines. *Energy Procedia*, vol. 37, Elsevier Ltd; 2013, p. 142–50. doi:10.1016/j.egypro.2013.05.095.
- [110] Hanak DP, Biliyok C, Manovic V. Calcium looping with inherent energy storage for decarbonisation of coal-fired power plant. *Energy Environ Sci* 2016;9:971–83. doi:10.1039/c5ee02950c.
- [111] Lara Y, Lisbona P, Martínez A, Romeo LM. Design and analysis of heat exchanger networks for integrated Ca-looping systems. *Appl Energy* 2013;111:690–700. doi:10.1016/j.apenergy.2013.05.044.
- [112] Ylätaalo J, Parkkinen J, Ritvanen J, Tynjälä T, Hyppänen T. Modeling of the oxy-combustion calciner in the post-combustion calcium looping process. *Fuel* 2013;113:770–9. doi:10.1016/j.fuel.2012.11.041.
- [113] Chen L, Wang C, Yan G, Zhao F, Anthony EJ. The simultaneous calcination/sulfation reaction of limestone under oxy-fuel CFB conditions. *Fuel* 2019;237:812–22. doi:10.1016/j.fuel.2018.10.060.
- [114] Butler JW, Jim Lim C, Grace JR. Kinetics of CO₂ absorption by CaO through pressure swing cycling. *Fuel* 2014;127:78–87. doi:10.1016/j.fuel.2013.09.058.
- [115] Kuramoto K, Fujimoto S, Morita A, Shibano S, Suzuki Y, Hatano H, Shi-Ying L, Harada M, Takarada T. Repetitive carbonation–calcination reactions of Ca-based sorbents for efficient CO₂ sorption at elevated temperatures and pressures. *Ind Eng Chem Res* 2003;42:975–81. doi:10.1021/ie0207111.
- [116] Basinas P, Wu Y, Grammelis P, Anthony EJ, Grace JR, Jim Lim C. Effect of pressure and gas concentration on CO₂ and SO₂ capture performance of limestones. *Fuel*

- 2014;122:236–46. doi:10.1016/j.fuel.2014.01.038.
- [117] Khinast J, Krammer GFF, Brunner C, Staudinger G. Decomposition of limestone: The influence of CO₂ and particle size on the reaction rate. *Chem Eng Sci* 1996;51:623–34. doi:10.1016/0009-2509(95)00302-9.
- [118] Ebneyamini A, Grace JR, Lim CJ, Ellis N, Elnashaie SSEH, Mahecha-Botero A. Simulation of autothermal hydrogen-producing limestone calcination for calcium looping in turbulent fluidized bed reactors. *Chem Eng Sci* 2020;212:115353. doi:https://doi.org/10.1016/j.ces.2019.115353.
- [119] Ebneyamini A, Grace JR, Lim CJ, Ellis N, Elnashaie SSEH. Simulation of limestone calcination for calcium looping: Potential for autothermal and hydrogen-producing sorbent regeneration. *Ind Eng Chem Res* 2019;58:8636–55. doi:10.1021/acs.iecr.9b00668.
- [120] Criado YA, Arias B, Abanades JC. Effect of the carbonation temperature on the CO₂ carrying capacity of CaO. *Ind Eng Chem Res* 2018;57:12595–9. doi:10.1021/acs.iecr.8b02111.
- [121] Mikulčić H, von Berg E, Vujanović M, Priesching P, Perković L, Tatschl R, Duić N. Numerical modelling of calcination reaction mechanism for cement production. *Chem Eng Sci* 2012;69:607–15. doi:10.1016/j.ces.2011.11.024.
- [122] Sakadjian BB, Iyer M V., Gupta H, Fan LS. Kinetics and structural characterization of calcium-based sorbents calcined under subatmospheric conditions for the high-temperature CO₂ capture process. *Ind Eng Chem Res* 2007;46:35–42. doi:10.1021/ie060214a.
- [123] Romeo LM, Abanades JC, Escosa JM, Paño J, Giménez A, Sánchez-Biezma A, Ballesteros JC. Oxyfuel carbonation/calcination cycle for low cost CO₂ capture in existing

- power plants. *Energy Convers Manag* 2008;49:2809–14. doi:10.1016/j.enconman.2008.03.022.
- [124] Santos JC, Cruz P, Regala T, Magalhães FD, Mendes A. High-purity oxygen production by pressure swing adsorption. *Ind Eng Chem Res* 2007;46:591–9. doi:10.1021/ie060400g.
- [125] Steib M. Dry reforming of methane – understanding metal support interactions and evaluation of regeneration protocols. Technische Universität München, Ph.D. Thesis, 2018.
- [126] Kavosh M, Patchigolla K, Oakey JE, Anthony EJ, Champagne S, Hughes R. Pressurised calcination-atmospheric carbonation of limestone for cyclic CO₂ capture from flue gases. *Chem Eng Res Des* 2015;102:116–23. doi:10.1016/j.cherd.2015.06.024.
- [127] Ryi S, Xu N, Li A, Lim CJ, Grace JR. Electroless Pd membrane deposition on alumina modified porous Hastelloy substrate with EDTA-free bath. *Int J Hydrogen Energy* 2010;35:2328–35. doi:10.1016/j.ijhydene.2010.01.054.
- [128] Bi HT, Ellis N, Abba IA, Grace JR. A state-of-the-art review of gas-solid turbulent fluidization. *Chem Eng Sci* 2000;55:4789–825. doi:https://doi.org/10.1016/S0009-2509(00)00107-X.
- [129] Thompson ML, Bi H, Grace JR. A generalized bubbling/turbulent fluidized-bed reactor model. *Chem Eng Sci* 1999;54:2175–85.
- [130] Abba IA. A generalized fluidized bed reactor model across the flow regimes. University of British Columbia, Ph.D. Thesis, 2001.
- [131] Paripatyadar SA, Richardson JT. Carbon dioxide reforming of methane with supported Rhodium. *Appl Catal* 1990;61:293–309.
- [132] Xu JG, Froment GF. Methane steam reforming, methanation and water-gas shift. I.

- intrinsic kinetics. *AIChE J* 1989;35:88–96. doi:10.1002/aic.690350109.
- [133] Jin W, Gu X, Li S, Huang P, Xu N, Shi J. Experimental and simulation study on a catalyst packed tubular dense membrane reactor for partial oxidation of methane to syngas. *Chem Eng Sci* 2000;55:2617–25. doi:10.1016/S0009-2509(99)00542-4.
- [134] King DF. Estimation of dense bed voidage in fast and slow fluidized beds of FCC catalyst. *Fluid. VI* (eds. J.R. Grace, L.W. Schemilt, M.A. Bergougnou), New York: Engineering Foundation; 1989, p. 1–8.
- [135] Davis ME, Davis RJ. *Fundamentals of chemical reaction engineering*. New York: McGraw-Hill; 2003. doi:10.1021/ed043pA758.1.
- [136] Elnashaie SSEH, Uhlig F. *Numerical techniques for chemical and biological engineers using MATLAB*. New York: Springer-Verlag; 2007. doi:10.1007/978-0-387-68167-2.
- [137] Ebneyamini A, Cheng BL, Kim JY, Li ZJ, Grace JR, Lim CJ, Ellis N. Equilibrium analysis of the pressurized sorbent regeneration using combined methane reforming, combustion and calcination process. *CFB* 13, 2021.
- [138] Green MA. Hydrogen safety issues compared to safety issues with methane and propane. *AIP Conf Proc* 2006;823 I:319–26. doi:10.1063/1.2202431.
- [139] Vanderstraeten B, Berghmans J, Tuerlinckx D, Smit B, Van't Oost E, Vliegen S. Experimental study of the pressure and temperature dependence on the upper flammability limit of methane/air mixtures. *J Hazard Mater* 1997;56:237–46.
- [140] Di Giuliano A, Gallucci K, Giancaterino F, Courson C, Foscolo PU. Multicycle sorption enhanced steam methane reforming with different sorbent regeneration conditions: Experimental and modelling study. *Chem Eng J* 2019;377:119874. doi:10.1016/j.cej.2018.09.035.

- [141] Kim SM, Abdala PM, Hosseini D, Armutlulu A, Margossian T, Copéret C, Müller C. Bi-functional Ru/Ca₃Al₂O₆-CaO catalyst-CO₂ sorbent for the production of high purity hydrogen via sorption-enhanced steam methane reforming. *Catal Sci Technol* 2019;9:5745–56. doi:10.1039/c9cy01095e.
- [142] Mahecha-Botero A, Boyd T, Grace JR, Lim CJ, Gulamhusein A, Wan B, Kurokawa H, Shirasaki Y. *In-situ* CO₂ capture in a pilot-scale fluidized-bed membrane reformer for ultra-pure hydrogen production. *Int J Hydrogen Energy* 2011;36:4038–55. doi:10.1016/j.ijhydene.2010.09.091.
- [143] Alshafei FH, Minardi LT, Rosales D, Chen G, Simonetti DA. Improved sorption-enhanced steam methane reforming *via* calcium oxide-based sorbents with targeted morphology. *Energy Technol* 2019;7:1–13. doi:10.1002/ente.201800807.
- [144] Senthorselvan S, Gleis S, Hartmut S, Yrjas P, Hupa M. Cyclic carbonation calcination studies of limestone and dolomite for CO₂ separation from combustion flue gases. *J Eng Gas Turbines Power* 2009;131:011801–0118018. doi:10.1115/1.2969090.
- [145] Prasad P, Elnashaie SSEH. Novel circulating fluidized-bed membrane reformer using carbon dioxide sequestration. *Ind Eng Chem Res* 2004;43:494–501. doi:10.1021/ie030524i.
- [146] Chen Z, Grace JR, Jim Lim C, Li A. Experimental studies of pure hydrogen production in a commercialized fluidized-bed membrane reactor with SMR and ATR catalysts. *Int J Hydrogen Energy* 2007;32:2359–66. doi:10.1016/j.ijhydene.2007.02.036.
- [147] Abbas SZ, Dupont V, Mahmud T. Modelling of H₂ production *via* sorption enhanced steam methane reforming at reduced pressures for small scale applications. *Int J Hydrogen Energy* 2019;44:1505–13. doi:10.1016/j.ijhydene.2018.11.169.

- [148] Herce C, Cortés C, Stendardo S. Numerical simulation of a bubbling fluidized bed reactor for sorption-enhanced steam methane reforming under industrially relevant conditions: Effect of sorbent (dolomite and $\text{CaO-Ca}_{12}\text{Al}_{14}\text{O}_{33}$) and operational parameters. *Fuel Process Technol* 2019;186:137–48. doi:10.1016/j.fuproc.2019.01.003.
- [149] R. Welty J, E. Wicks C, E. Wilson R, Rorrer G. *Fundamentals of momentum, heat and mass transfer*. vol. 13. 1970. doi:10.1016/0017-9310(70)90063-3.
- [150] Bi HT, Grace JR. Effect of measurement method on the velocities used to demarcate the onset of turbulent fluidization. *Chem Eng J Biochem Eng J* 1995;57:261–71. doi:10.1016/0923-0467(94)02875-B.
- [151] Bi HT, Grace JR, Zhu J. Regime transitions affecting gas-solids suspensions and fluidized beds. *Chem Eng Res Des* 1995.
- [152] Wang S, Shen H, Fan S, Zhao Y, Ma X, Gong J. Enhanced CO_2 adsorption capacity and stability using CaO-based adsorbents treated by hydration. *AIChE J* 2013;59:3586–93. doi:10.1002/aic.
- [153] Manovic V, Fennell PS, Al-Jeboori MJ, Anthony EJ. Steam-enhanced calcium looping cycles with calcium aluminate pellets doped with bromides. *Ind Eng Chem Res* 2013;52:7677–83. doi:10.1021/ie400197w.
- [154] Chen H, Zhao C. Development of a CaO-based sorbent with improved cyclic stability for CO_2 capture in pressurized carbonation. *Chem Eng J* 2011;171:197–205. doi:10.1016/j.cej.2011.03.091.
- [155] Mess D, Sarofim AF, Longwell JP. Product layer diffusion during the reaction of calcium oxide with carbon dioxide. *Energy and Fuels* 1999;13:999–1005. doi:10.1021/ef980266f.
- [156] Alvarez D, Abanades JC. Determination of the critical product layer thickness in the

- reaction of CaO with CO₂. *Ind Eng Chem Res* 2005;44:5608–15. doi:10.1021/ie050305s.
- [157] Champagne S. Steam enhanced calcination for CO₂ capture with CaO. University of Ottawa, M.A.Sc Thesis, 2014.
- [158] Blamey J, Zhao M, Manovic V, Anthony EJ, Dugwell DR, Fennell PS. A shrinking core model for steam hydration of CaO-based sorbents cycled for CO₂ capture. *Chem Eng J* 2016;291:298–305. doi:10.1016/j.cej.2016.01.086.
- [159] Xie H, Yu Q, Zhang Y, Zhang J, Liu J, Qin Q. New process for hydrogen production from raw coke oven gas via sorption-enhanced steam reforming: Thermodynamic analysis. *Int J Hydrogen Energy* 2017;42:2914–23. doi:10.1016/j.ijhydene.2016.12.046.
- [160] Cinti G, Frattini D, Jannelli E, Desideri U, Bidini G. Coupling Solid Oxide Electrolyser (SOE) and ammonia production plant. *Appl Energy* 2017;192:466–76. doi:10.1016/j.apenergy.2016.09.026.
- [161] Aziz M, Oda T, Morihara A, Kashiwagi T. Combined nitrogen production, ammonia synthesis, and power generation for efficient hydrogen storage. *Energy Procedia* 2017;143:674–9. doi:10.1016/j.egypro.2017.12.745.
- [162] Licht S, Cui B, Wang B, Li FF, Lau J, Liu S. Ammonia synthesis by N₂ and steam electrolysis in molten hydroxide suspensions of nanoscale Fe₂O₃. vol. 345. 2014. doi:10.1126/science.1254234.
- [163] Wang Y, Chao Z, Jakobsen HA. CFD modelling of CO₂ capture in the SE-SMR process in the fluidized bed reactors 2010;21:601–6. doi:10.3303/CET1021101.
- [164] Kim JY, Ellis N, Lim CJ, Grace JR. Effect of calcination/carbonation and oxidation/reduction on attrition of binary solid species in sorption-enhanced chemical looping reforming. *Fuel* 2020;271:117665. doi:10.1016/j.fuel.2020.117665.

Appendices

Appendix A: Effect of Heating Rate on Cyclic CO₂ Capture of Lime-Based Sorbents

A TA Instruments TGA 5500 thermogravimetric analyzer, located at CanmetEnergy (Ottawa), was used to assess the effect of heating rate on the cyclic CO₂ capture capability of lime-based sorbents. Tests conditions were kept identical to that for run 3 in Chapter 2 (Table 2.2), while the carbonation-to-calcination transition was conducted at different heating rates. Increasing the heating rate slightly reduces the sorbent utilization of Strassburg limestone, as shown in Figure A.1. This could be due to shorter transition period, resulting in less carbonation during the calcination-to-carbonation temperature ramp. Therefore, high-temperature carbonation may slightly retain the sorbent reactivity over multi-cycling. Investigations are required to assess the effect of high-temperature carbonation on the carbon capture capability of lime-based sorbents.

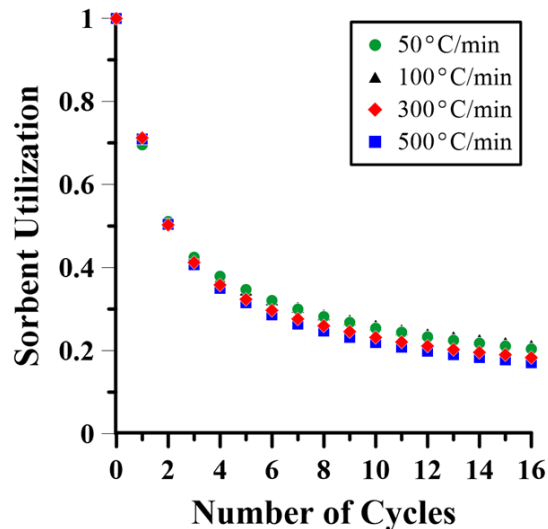


Figure A.1. Effect of heating rate on the cyclic carbon capture capability of lime-based sorbents. Other tests conditions are identical to that for run 3 in Chapter 2.

Appendix B: Effect of Steam Reactivation on Cyclic CO₂ Capture of Lime-Based Sorbents

The effect of lime hydration on the cyclic carbon capture capability of Strassburg limestone was investigated using a Thermax 700 thermogravimetric analyzer. The unit is located at CanmetEnergy (Ottawa), and was slightly modified for steam injection. Water was injected by Harvard PHD syringe pump, and evaporated in-line using heating tapes. The steam line was appropriately insulated to avert steam condensation before the reaction chamber. Calcination-hydration-carbonation tests were conducted up to 10 cycles, with the carbonation and calcination conditions being identical to that for run 3 in Chapter 2. Heating and cooling rate were kept at 30 and 10 °C/min, respectively. Lime hydration was carried out for 30 minutes at different temperatures and steam concentrations. Note that the initial experimental plan also covered the effects of hydration pressure, reactions sequence (calcination-hydration-carbonation vs. calcination-carbonation-hydration), sorbent material, temporary hydration (e.g. first 5 cycles only), periodic hydration, and calcination in syngas. However, those tests were not taken to completion due to failure of equipment and lack of time.

Increasing the hydration temperature and reducing the steam concentration adversely affect the sorbent reactivation of lime-based sorbents, as shown in Figures B.1 (a) and (b). This can be attributed to less sorbent hydration at these severe conditions (Figures B.2 (a) and (b)). Note that some experimental points are omitted from these figures due to failure of steam injection to the reaction chamber.

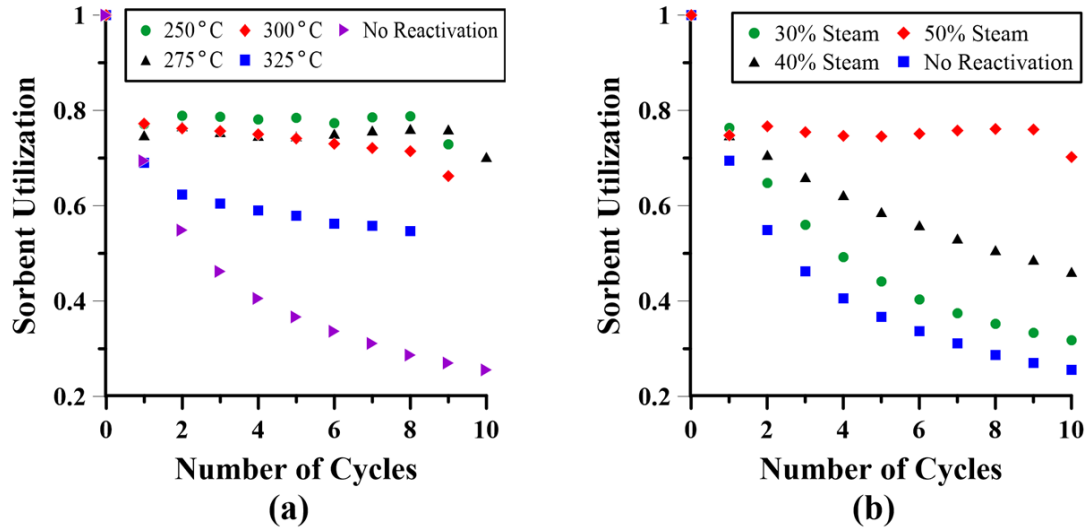


Figure B.1. Effects of: (a) hydration temperature; and (b) steam concentration on the cyclic carbon capture capability of Strassburg limestone.

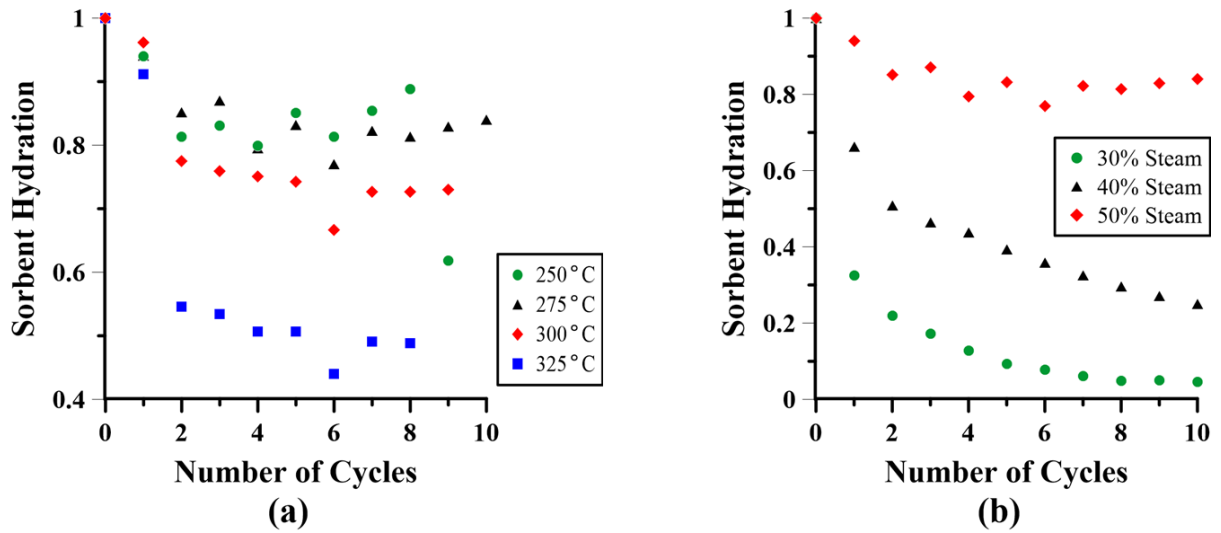


Figure B.2. Effects of: (a) hydration temperature; and (b) steam concentration on the cyclic sorbent hydration of Strassburg limestone.

Appendix C: Sensitivity Analysis of ADPFR Reactor Model

Figures C.1 to C.3 show the sensitivity of the ADPFR kinetic simulation to the CaO density, CaCO₃ density, and the average particle diameter. The simulation results demonstrate that the kinetic simulation is very slightly sensitive to all these parameters.

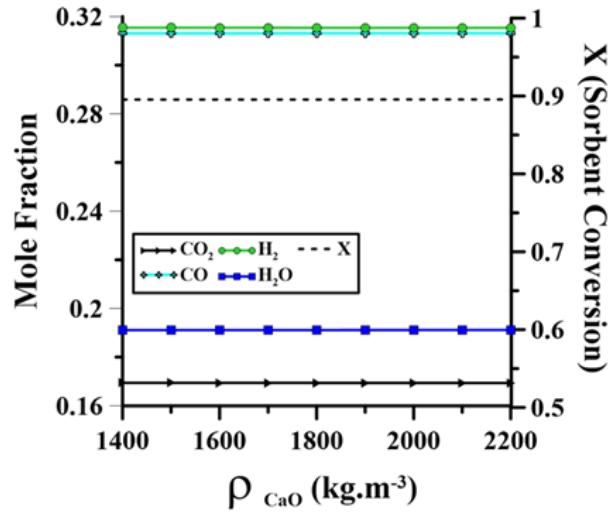


Figure C.1. Effect of CaO density on the MRC-CAL off-gas concentration and sorbent conversion

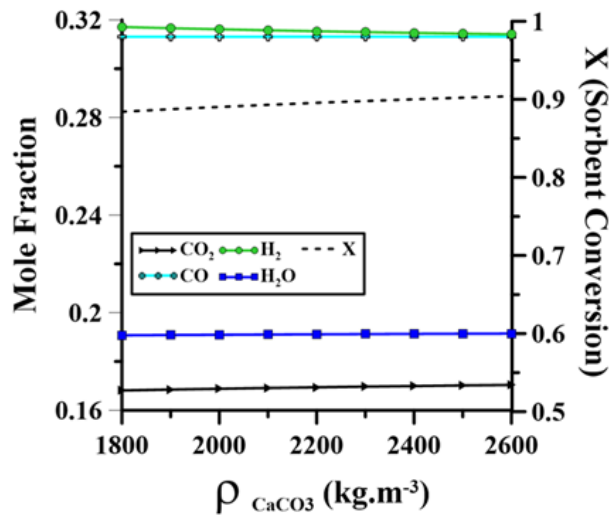


Figure C.2. Effect of CaCO₃ density on the MRC-CAL off-gas molar concentration and sorbent conversion

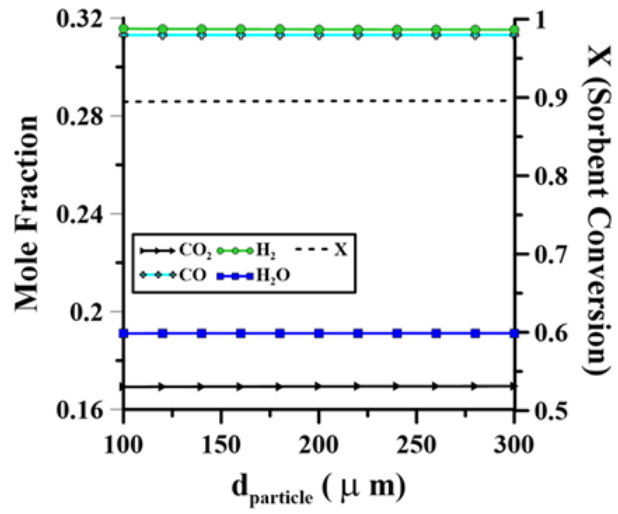


Figure C.3. Effect of the average particle diameter on the MRC-CAL off-gas molar concentration and sorbent conversion

Appendix D: Supplementary Results for SE-SMR/Calciner Simulation

Table D.1. Summary of Aspen Plus and kinetic simulation results for reformers

Summary of Operating Conditions								
	Aspen Plus Simulation				Kinetic Simulation			
Reactor Temperature (°C)	650				650			
Reactor Pressure (bars)	3				3			
Steam/Methane Molar Feed Ratio	3.25				3.25			
CaO Inlet Flow Rate (mol.s ⁻¹)*	0.041				0.21			
Steam Methane Reformer								
	Aspen Plus Simulation				Kinetic Simulation			
Off-gas Flow Rate (mol.s ⁻¹)	0.271				0.270			
Off-gas Molar Composition	H ₂	47.41%	CO	5.19%	H ₂	46.63%	CO	5.01%
	CO ₂	7.96%	CH ₄	4.19%	CO ₂	7.9%	CH ₄	4.55%
	H ₂ O	35.25%	N ₂	0%	H ₂ O	35.91%	N ₂	0%
Reactor Heat Duty (kW)	7.049							
Fuel Combustion Energy (kJ.mol ⁻¹)**	727.64							
Fuel Requirement (mol.s ⁻¹)	9.69×10 ⁻³							
Sorbent-Enhanced Steam Methane Reformer								
	Aspen Plus Simulation				Kinetic Simulation			
Off-gas Flow Rate (mol.s ⁻¹)	0.245				0.245			
Off-gas Molar Composition	H ₂	69.96%	CO	0.46%	H ₂	67.84%	CO	0.61%
	CO ₂	0.36%	CH ₄	1.59%	CO ₂	0.53%	CH ₄	2.12%
	H ₂ O	27.63%	N ₂	0%	H ₂ O	28.9%	N ₂	0%
Reactor Heat Duty (kW)	1.12							
Fuel Combustion Energy (kJ.mol ⁻¹)	727.64							
Fuel Requirement (mol.s ⁻¹)	1.54×10 ⁻³							

* CaO feed flow in Aspen Plus simulation was set to be equal to the carbonated lime predicted by the kinetic simulation (SE-SMR)

** Calculated using RGibbs (with stoichiometric CH₄ and O₂ feedstock at 25°C), operating at reformer temperature and pressure.

Table D.2. Summary of Aspen Plus and kinetic simulation results for calciners

Summary of Operating Conditions																												
	Aspen Plus Simulation		Kinetic Simulation																									
MRC-CAL Temperature (°C)	825		825																									
Steam Calciner Temperature (°C)	880		880																									
Reactor Pressure (bars)	3		3																									
Gas Feed Ratio (mol.s ⁻¹)	0.137		0.137																									
MRC-CAL Gas Feed Composition	60.5% CH ₄ + 37.5% O ₂ + 2% N ₂		60.5% CH ₄ + 37.5% O ₂ + 2% N ₂																									
Steam Calciner Gas Feed Composition	100% Steam		100% Steam																									
CaCO ₃ Inlet Flow Rate (mol.s ⁻¹)	0.041		0.041																									
MRC-CAL Calciner																												
	Aspen Plus Simulation		Kinetic Simulation																									
Off-gas Flow Rate (mol.s ⁻¹)	0.289		0.289																									
Off-gas Molar Composition	<table border="1"> <tr> <td>H₂</td> <td>43.67%</td> <td>CO</td> <td>32.94%</td> </tr> <tr> <td>CO₂</td> <td>9.35%</td> <td>CH₄</td> <td>0.66%</td> </tr> <tr> <td>H₂O</td> <td>12.44%</td> <td>N₂</td> <td>0.94%</td> </tr> </table>		H ₂	43.67%	CO	32.94%	CO ₂	9.35%	CH ₄	0.66%	H ₂ O	12.44%	N ₂	0.94%	<table border="1"> <tr> <td>H₂</td> <td>43.7%</td> <td>CO</td> <td>33.1%</td> </tr> <tr> <td>CO₂</td> <td>9.1%</td> <td>CH₄</td> <td>0.6%</td> </tr> <tr> <td>H₂O</td> <td>12.6%</td> <td>N₂</td> <td>0.9%</td> </tr> </table>		H ₂	43.7%	CO	33.1%	CO ₂	9.1%	CH ₄	0.6%	H ₂ O	12.6%	N ₂	0.9%
H ₂	43.67%	CO	32.94%																									
CO ₂	9.35%	CH ₄	0.66%																									
H ₂ O	12.44%	N ₂	0.94%																									
H ₂	43.7%	CO	33.1%																									
CO ₂	9.1%	CH ₄	0.6%																									
H ₂ O	12.6%	N ₂	0.9%																									
Reactor Heat Duty (kW)	0.325																											
Fuel Combustion Energy (kJ.mol ⁻¹) *	703.62																											
Fuel Requirement (mol.s ⁻¹)	0.461×10 ⁻³																											
Steam Calciner																												
	Aspen Plus Simulation		Kinetic Simulation																									
Off-gas Flow Rate (mol.s ⁻¹)	0.178		0.178																									
Off-gas Molar Composition	<table border="1"> <tr> <td>H₂</td> <td>0%</td> <td>CO</td> <td>0%</td> </tr> <tr> <td>CO₂</td> <td>23.08%</td> <td>CH₄</td> <td>0%</td> </tr> <tr> <td>H₂O</td> <td>76.92%</td> <td>N₂</td> <td>0%</td> </tr> </table>		H ₂	0%	CO	0%	CO ₂	23.08%	CH ₄	0%	H ₂ O	76.92%	N ₂	0%	<table border="1"> <tr> <td>H₂</td> <td>0%</td> <td>CO</td> <td>0%</td> </tr> <tr> <td>CO₂</td> <td>23.01%</td> <td>CH₄</td> <td>0%</td> </tr> <tr> <td>H₂O</td> <td>76.99%</td> <td>N₂</td> <td>0%</td> </tr> </table>		H ₂	0%	CO	0%	CO ₂	23.01%	CH ₄	0%	H ₂ O	76.99%	N ₂	0%
H ₂	0%	CO	0%																									
CO ₂	23.08%	CH ₄	0%																									
H ₂ O	76.92%	N ₂	0%																									
H ₂	0%	CO	0%																									
CO ₂	23.01%	CH ₄	0%																									
H ₂ O	76.99%	N ₂	0%																									
Reactor Heat Duty (kW)	7.06																											
Fuel Combustion Energy (kJ.mol ⁻¹)	695.83																											
Fuel Requirement (mol.s ⁻¹)	1.02×10 ⁻²																											

* Calculated using RGibbs (with stoichiometric CH₄ and O₂ feedstock at 25°C), operating at calciner temperature and pressure.

Appendix E: General Comparison and Suggested Range of Operating Conditions for MRC-CAL Process

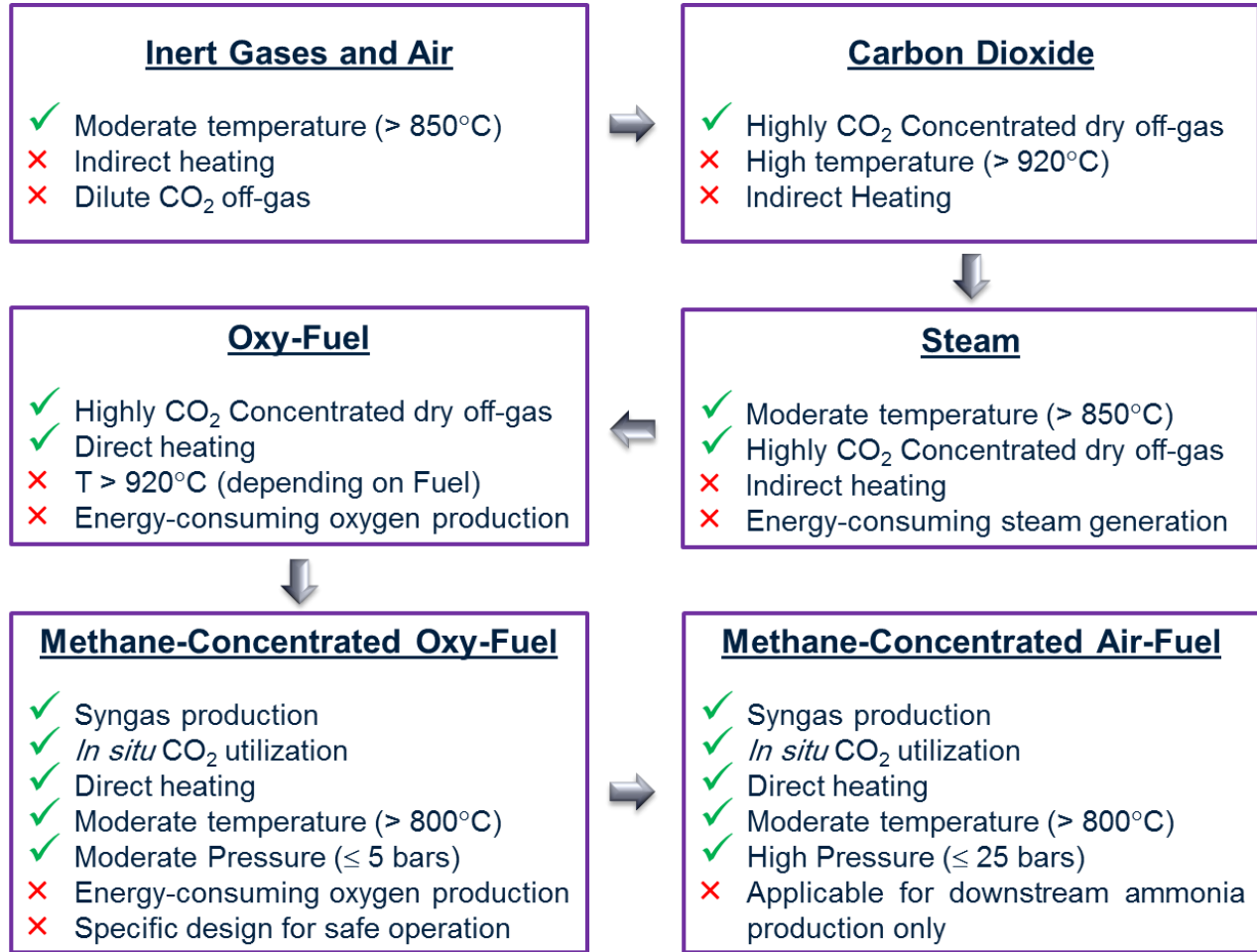


Figure E.1. Comparison of different gaseous media for limestone calcination

Table E.1. Suggested range of operating conditions for oxy/air-fuel MRC-CAL processes

	Oxy-Fuel MRC-CAL	Air-Fuel MRC-CAL
Temperature ($^{\circ}\text{C}$)	800-900	800-900
Pressure (bars)	1-5	1-25
Air Oxygen Concentration (vol %)	$>95\%$	$\sim 40\%$
Optimal CaCO_3/Gas Molar Feed Ratio	$\sim 0.1-0.3$	-
Optimal $\text{CaCO}_3/\text{CH}_4$ Molar Feed Ratio	-	$\sim 0.2-0.3$
Gaseous Feed Concentration	Equation (3.1)	Equation (7.4)